Cracow University of Technology
Civil Engineering Department

Doctoral dissertation

INTERFACE MODEL INFLUENCE ON SIMULATED BEHAVIOUR OF CONCRETE-CONCRETE COMPOSITE PRE-STRESSED GIRDER WITH INSIGHT INTO TIME EFFECTS AND CRACKING

WPŁYW MODELU INTERFEJSU NA SYMULOWANE ZACHOWANIE SIĘ ZESPOLONYCH DŹWIGARÓW SPRĘŻONYCH TYPU BETON-BETON Z UWZGLĘDNIENIEM EFEKTÓW REOLOGICZNYCH I ZARYSOWANIA

Author:

mgr inż. Łukasz Jarno

Supervised by:

prof. dr hab. inż. Jerzy Pamin

August 25, 2022

This work is dedicated to the person who started it all and did everything to make it possible - this person is my dad. I also dedicate this dissertation to my mother and to the whole family and loved ones who supported and motivated me in this long journey. However, separate and biggest thanks go to my supervisor, Professor Jerzy Pamin - his endless patience, understanding, help and motivation is something without which I would absolutely never complete this work.

Contents

1 Introduction 5

1.1 Aim and scope of the work 5
1.2 Statements 10

2 Experiments on concrete-concrete composite girders 11

2.1 Introduction 11
2.2 Composite structures – general description 12
2.3 Main properties of composite structures 14
2.4 Experimental research by Choi 14
  2.4.1 High-strength concrete girders 16
  2.4.2 Normal-strength concrete deck 16
  2.4.3 Manufacturing of test specimens 17
  2.4.4 Instrumentation used 18
  2.4.5 Testing procedure and set-up 21
2.5 Results and discussion 21
2.6 Conclusions 24

3 Physical phenomena in contact zone 27

3.1 Adhesion 27
3.2 Friction between two surfaces 29
3.3 Stitching reinforcement 31
3.4 Different code recommendations 34
  3.4.1 Eurocode 2 34
  3.4.2 Model Code 2010 37
  3.4.3 ACI code 38
3.5 Summary 40

4 Finite element formulation of interface elements 41

4.1 Introduction and interpolation 41
4.2 Point interface element 43
4.3 Line interface element 44
4.4 Surface interface element 45
4.5 FEM equations for interface elements 45

5 Interface behaviour – benchmark and calibration 51

5.1 Coulomb friction model 51

5.2 Aggregate interlock model 57

5.3 Indented connection 61

5.4 Stitching reinforcement 64

5.4.1 Stitching reinforcement – 3D modelling 64

5.4.2 Stitching reinforcement – bar in solid 70

6 Generalized Maxwell model for creep 73

6.1 Introduction to linear visco-elasticity 73

6.2 Visco-elastic behaviour under continuous loading 75

6.3 Visco-elastic Maxwell models 76

6.3.1 Simple spring-dashpot model 76

6.3.2 Generalized Maxwell model 77

6.4 Implementation of Generalized Maxwell model in 3D 79

6.5 Tests of Generalized Maxwell model 80

6.5.1 1D benchmark 80

6.5.2 3D test 81

7 Numerical model and cracking analysis 85

7.1 Geometry, material and mesh 85

7.2 Reinforcement 86

7.3 Pre-stressing 86

7.4 Boundary conditions and loads 88

7.5 Analysis cases 89

7.6 Cracking behaviour analysis – Total Strain Crack model 91

8 Construction stage analysis results 95

8.1 First stage – concrete girder with reinforcement 95

8.2 Second stage – pre-stressing of the girder 95

8.3 Third stage – slab casting – wet concrete load 97

8.4 Fourth stage – composite girder 98

8.5 Fifth stage – external load 99

8.6 Final results without construction stage analysis 101

9 Construction stage analysis with time-dependent effects 103

9.1 Third stage – casting the slab – wet concrete load 103

9.2 Fourth stage – composite girder 103

9.3 Fifth stage – external load 104

9.4 Sixth stage – long term behaviour (10000 days) 105

9.5 Input data for Generalized Maxwell model 106

9.6 Third stage – casting the slab (Maxwell model) 107

9.7 Fourth stage – composite girder (Maxwell model) 108

9.8 Fifth stage – external load (Maxwell model) 109

9.9 Sixth stage – long term behaviour (Maxwell model) 111

10 Construction stage analysis with interface elements 113

10.1 Bending behaviour for frictional interface 113

  10.1.1 Model data 113

  10.1.2 Fourth stage – composite girder 114

  10.1.3 Fifth stage – external load 116

10.2 Longitudinal shear behaviour for frictional interface 117

10.3 Stitching reinforcement in connection zone 125

11 Summary and conclusions 131

Appendix A 150

A.1 Total Strain Crack model 150

A.2 Concrete properties 151

A.3 Crack strain transformation 152

A.4 Stiffness matrix 153

A.5 Tangent stiffness matrix 153

A.6 Tension models 154

A.7 Compression models 155

A.8 Shear models 155

Appendix B 156

B.1 Isoparametric shape functions for surface interface element 156

Appendix C 158

C.1 Source code of subroutine for Generalized Maxwell model in Midas FEA 158

Appendix D **167**

D.1 Algorithm of stress update in CS analysis 167

Summary **170**

Streszczenie **172**

1 Introduction

1.1 Aim and scope of the work

Nowadays, the environment and form of construction that architects shape require from engineers more efforts to analyze and design sophisticated structural and material solutions. In the modern world of civil engineering it is often required to combine advanced concepts like composition, pre-stressing, high-strength materials etc. with one another to meet high requirements for structures.

One of such complex engineering solutions is a prefabricated pre-stressed bridge girder made of high-strength concrete (HSC) combined with a normal-strength concrete (NSC) bridge deck cast in-situ. This kind of girder combines the best features of composite, pre-stressed structures and advanced materials.

The composite concrete member is an element which is built by connecting two different parts of concrete, bonded with each other with various types of connections. The purpose of designing and constructing such elements is to provide the best possible cooperation between two concretes in load-bearing aspects. This is the reason why this research is focused on load-bearing parameters of the contact zone, which have a significant influence on the behaviour of the whole composite member under loading.

Concrete designed with special additions, admixtures and with proper proportions of ingredients is a modern material that allows one to reach the compressive strength greater than 100 MPa. Advanced mixture of normal concrete components and suitable additions as well as high quality control allow one to produce such concrete called high-strength concrete (HSC). It is a material enabling engineers to design bridges with longer spans without changing the dimensions of the girder cross-section or even to reduce the number of those girders.

In the thesis, after a short presentation of concrete-concrete composite structures, experimental studies carried out by Choi at State University of North Carolina, Raleigh are described [Choi et al., 2008, Choi, 2006] in Chapter 2. The aim of this doctoral project is to build a family of complex finite element models of the pre-stressed composite bridge girder made of HSC with bridge deck made of NSC in order to examine its transient and long-term behaviour. Today, the finite element method (FEM) is considered as a well-established and convenient technique for computer simulation of complex problems in different fields of engineering: civil engineering (including geomechanics), mechanical engineering, nuclear engineering, biomedical engineering, hydrodynamics, heat conduction, etc. This is because FEM is a powerful tool for the approximate solution of differential equations describing different physical phenomena and processes, see for instance [Zienkiewicz et al., 2000, Zienkiewicz et al., 2005, de Borst et al., 2012, Rakowski and Kacprzyk, 2016, Smarzewski, 2009].

The main part of the dissertation is thus dedicated to the finite element analysis of the pre-stressed bridge girder including construction stages, specific composite structure behaviour and rheological effects. In the context of the present research, the accuracy of the initial model is validated by experimental findings (thereby cracking idealization is employed) and then more advanced computational simulations are performed to examine complex phenomena, in particular the contact zone model influence on the load-bearing capacity of the beam and the creep influence on its life-cycle response.

To reach the aims described above the scope of the doctoral thesis is as follows:

1. *Literature overview* – the development of the research program is preceded by a literature overview, covering the state of scientific studies carried out in the world on the considered class of pre-stressed concrete composite structures, including the modelling of such engineering solutions using FEM; as already mentioned, the experimental research on the investigated composite beams was carried out in [Choi et al., 2008, Choi et al., 2008] and it is presented in Chapter 2; the physical phenomena occurring in the concrete-concrete contact zone are described in Chapter 3; the relevant part of the FEM technology, namely interface elements, is discussed in Chapter 4; other components of the simulation strategy, namely the construction stage analysis, time-dependent phenomena, cracking and failure are briefly reviewed in further chapters and appendices.

2. *Implementation of advanced creep model* – in Chapter 6 an incremental rheological model based on the visco-elasticity theory and Generalized Maxwell equations is described, which is implemented in the employed finite element package to be used for more accurate creep representation; some verification tests are also discussed.

3. *Numerical analysis* – before the actual analysis of the composite girder which is

the main object of interest in this work, a benchmark of interface behaviour is analyzed in Chapter 5, thereby the influence of different models of the connection zone are examined (Coulomb friction, aggregate interlock behaviour, indented connection, dowel action); then a series of finite element models of the pre-stressed composite girder are examined:

- a pre-stressed composite girder model is built taking into account the discrete character of the reinforcement and the pre-stressing,
- cracking and failure modelling of the girder is performed for comparison with experiments,
- a construction stage analysis is carried out to represent the actual life-cycle of the composite bridge girder assuming full bond between the two beam parts (HSC girder and NSC deck) and neglecting rheological effects,
- the Generalized Maxwell model implemented to examine the influence of creep on the mechanical response of concrete is used and the results are compared with the predictions of standard code models of creep,
- the influence of the type of construction of the contact zone is examined in the construction stage analysis of bending and longitudinal shear.

The experimental research performed by W. Choi is used in the assessment of the composite girder model. The study evaluated the flexural behaviour of pre-stressed composite girders combining high- and normal-strength concrete. The study used three types of girders: with 1.5m wide NSC deck, with 0.3m-wide cast deck and without the cast deck. For testing, the girders were set up as simply supported beams and loaded at two points. The results of the experimental analysis, summarized in Chapter 2, are taken into account during the current investigation.

Thus, the object of this doctoral project is the pre-stressed bridge girder made of HSC composite with the bridge deck made of NSC [Jarno, 2012a], [Jarno, 2012b]. The contact zone in the concrete-concrete composite structure is the crucial aspect of the analysis. This is a key issue when it comes to load-bearing capacity of the composite girder.

The connection analysis is started in Chapter 3 by discussing the main properties of a composite cross-section and the phenomena that occur in the contact zone. First, the most important phenomena of adhesion and friction are described. After that, the behaviour of the reinforcement bars (so-called stitching reinforcement) acting against longitudinal shear transfer in a composite zone is analyzed. Considering the connection of composite components, directions included in related standards are summarized [Jarno, 2013a].

Next, interface-type finite elements employed in the modeling of composite structures are presented in Chapter 4 and options of their properties are discussed. Interface elements were introduced into the finite element method to represent a relationship between a relative displacement vector, a stiffness matrix and a traction vector. Choosing the right type of interface behaviour is important for a proper simulation of concrete-concrete contact.

In order to determine an appropriate representation of the contact, in Chapter 5 a simple calculation model is created which consists of two solid elements with plane interface elements between them. Different types of interface constitutive models are applied in the interface elements to check their behaviour in this simple test. A non-linear static analysis is performed. First, the Coulomb friction model which is derived from Mohr-Coulomb plasticity for continuum elements is used. An aggregate interlock model is the next contact model to be analyzed. The concept of this model is that the strength of adhesion is increased by aggregate used in the concrete mixture. To describe this numerically, a two-phase Walraven model is used. The last model that is checked involves the use of the stitching reinforcement. The steel bar with 8 mm diameter is placed in the middle of the boxes and connected to them. Finally, some options of the stitching reinforcement model are checked.

To account for rheological effects (which are very important due to different ages of the connected concretes) a concrete visco-elastic model is implemented. As described in Chapter 6, using a Generalized Maxwell spring-dashpot model, superposition principle for the visco-elastic behaviour of concrete under continuous loading and a spectral form of the characteristic function representing material properties, an incremental formulation of linear visco-elasticity for a non-ageing material is derived and programmed in the employed 3D FE software package Midas. The model is tested in 1D and 3D, and then the results of simulations for the analyzed composite girder are compared with the results obtained using creep functions defined in CEB-FIP and EC recommendations (shrinkage is not considered).

The finite element model of the composite beam under consideration is presented in Chapter 7. To evaluate the cracking behaviour of the beam model the so-called Total Strain Crack model is employed. It is a robust smeared fixed crack model with secant stiffness. The tested girder contains stirrups and it is pre-stressed. It is modelled as simply supported and loaded up to the yielding of pre-stressing strands and then to failure. The main analysis is performed for the beam model with 1.5 meter broad deck and the span of 12.5 m between supports.

A series of computations are carried out for the girder model. The influence of the building process is evaluated by the construction stage analysis in Chapter 8. For the simulation of concrete creep the construction stage analysis with time-dependent effects is performed in Chapter 9. To show the long-term behaviour of the model there is also an additional stage with 10000 days duration time. More information about the construction stage analysis can be found in [Ates, 2011, Wang et al., 2020a].

After performing the rheological analysis, in Chapter 10 the results are evaluated in subsequent stages for the model with the connection zone represented by interfaces. Based on the analysis maximum deflection and maximum tension stress are checked. Longitudinal shear behaviour is also analyzed. All results are carefully assessed and conclusions are drawn in the final Chapter 11 on the behaviour of the model under the given loads.

The scope of this thesis is established based on the literature review and the description of the experimental research performed by Choi. To see the predictive abilities of the finite element approximation of the problem the Total Strain Crack (TSC) model, summarized in Appendix A, is applied to the initial model to check failure modes, crack patterns etc. The results of this simulation are compared with the results of experiments performed by Choi.

The main purpose of the thesis is to evaluate to influence of the interface numerical model on the flexural and shear behaviour and on the load-bearing capacity of the composite pre-stressed girder made of high-strength concrete connected with normal-strength concrete.

In Chapter 10 the construction stage analysis with interface elements is shown and discussed to investigate the influence of different types of contact zone modelling for composite concrete structures.

Linear kinematic relations, elastic reinforcement and tendons are assumed. Unfortunately, in the software used for the study it is not possible to combine all nonlinear effects (e.g. phased analysis and cracking) in the life-cycle analysis of the problem.

In Chapter 11 one can find summary and conclusions of the thesis as well as statements verification.

The thesis includes four appendixes: Appendix A contains a brief description of the Total Strain Crack model, Appendix B presents isoparametric shape functions for surface interface elements used in the beam model, Appendix C is the source code of the user supplied subroutine implemented for the Generalized Maxwell model in Midas FEA, and finally Appendix D contains a brief discussion of the algorithm of stress update in the construction stage analysis.

1.2 Statements

The following statements are considered in the course of the research:

- **Statement 1** – The consideration of construction stages in the FEM analysis has a significant influence on the analysis results of pre-stressed concrete-concrete composite beams.

- **Statement 2** – The load bearing capacity of composite (HSC-NSC) bridge girders depends strongly on the type of contact zone construction.

- **Statement 3** – To accurately examine the behaviour of the pre-stressed concrete composite of two different types of concrete it is advisable to implement an advanced rheological constitutive model (for instance, Generalized Maxwell model based on visco-elasticity theory) rather than use a simple function for creep, based on standards.

2 Experiments on concrete-concrete composite girders

2.1 Introduction

One of the most important problems in the analysis of load-bearing capacity of concrete composite structures is the contact zone load-transfer calculation because only full co-operation between the two materials, i.e. primary and subsidiary concretes, ensures well-designed load-bearing system. This chapter presents ways of forming and calculation of the contact zone in composite structures which consist of two different concrete components. A collection of approaches and codes are taken into account.

Technical and utility features of elements and structures result from the properties of the materials from which they were built. Mechanical properties such as the strength of a material, pliability, rheological properties, but also durability and resistance to environmental factors, which are derivatives of the internal structure of each material, can have influence on the features of designed structures, cf. [Roller et al., 1993,Stallings et al., 2003,Wollmann et al., 2003,Bilal et al., 1990,Troitsky et al., 1989,Hewson, 2012, Pipinato and De Miranda, 2016,Benaim, 2008,Stewart and Rosowsky, 1998,Ducret and Lebet, 1999,Malm and Sundquist, 2020,Hambly, 1990,Menn, 2011]. The rational design of structures means maximization of positive features of materials and minimization of bad influence factors. This can be achieved applying composite structures which consist of well-chosen and properly connected materials [Halicka, 2007].

An example of this kind of structures are reinforced concrete composite structures, see for instance Fig. 2.1. They connect the advantages of precast structures such as high quality due to production in a prefabrication factory, with formability and homogeneity of monolithic concrete cast on the building site. Despite these benefits concrete-concrete composite structures are not as popular as steel-concrete composite structures which are well-recognized in calculation methods and design procedures.

It is obvious that the determination of the behaviour of the connection zone between these two materials is very important from the point of view of load-bearing capacity of the composite girder and therefore this issue is a significant part of the research.

This chapter describes such characteristics of composite structures and gives fundamental definitions related to the composite structures. Then the experimental research

Fig. 2.1: Composite concrete-concrete girder [Halicka, 2007]

of pre-stressed composite girders, performed by Choi [Choi, 2006], which is the starting point of the current study, is presented. Important parameters which have influence on the load-bearing capacity of the contact zone, as well as physical and chemical phenomena which take place on the contact surface between two different concretes are described in the next Chapter 3.

2.2 Composite structures – general description

First of all, it is necessary to define what a composite structure is. According to [Kamiński and Kmiecik, 2010] a reinforced concrete composite structure is an engineering solution where the cross-section is composed of at least two subsections of structural elements. Usually one of them is an earlier prepared prefabricated part and another one is a concrete subsection cast on the building site, see Fig. 2.2. The two parts of a reinforced concrete structure made at distant time moments should be connected in such a way (usually by means of staple reinforcement) that it is possible to treat such structural element as one member. According to [Halicka and Franczak, 2009] a composite concrete element is the structural member which is built as a result of connection of two concretes: primary and subsidiary. The main purpose of construction of this element is to provide the best possible co-operation between two different concretes to achieve the best effective load-bearing properties of the whole composite cross-section of the member, cf. [Cholewicki, 2001, Gromysz and Starosolski, 2003, Halicka, 2001, Jarek, 2004, Król and Tur, 2001, Król et al., 2001, Kuś et al., 1999, Wilczyński, 2003, Bruyneel et al., 2009]. Similar or different materials or technology can be used for the parts of composite cross-section. The cooperation of the parts is provided by an appropriately designed connection zone.

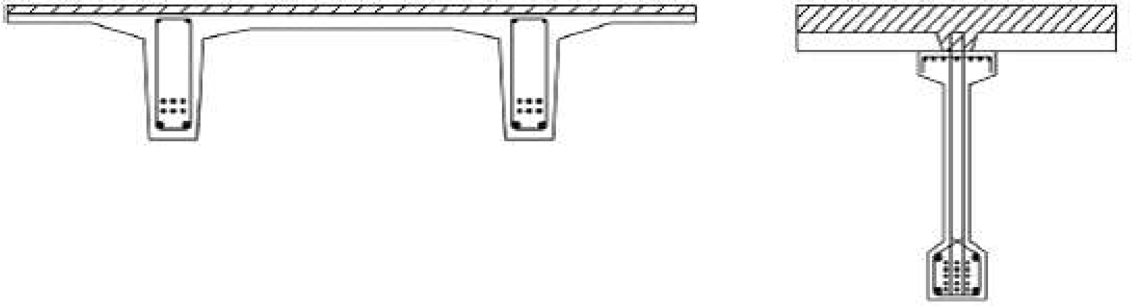

Fig. 2.2: Examples of composite element cross sections [Halicka, 2007]

Most precast elements used in composite structures [Kamiński and Kmiecik, 2011b] are proprietary types offered by manufacturers and produced under factory conditions. Three types of composite sections can be specified, cf. [fib, 2010]:

- precast soffit elements mainly used for floors in buildings, available in many different shapes. The main feature is that in situ concrete is in uniform contact over the entire area in the form of a topping to the precast units;
- hollow block composite elements. Similarly, the principal application is floor slabs. Many different systems have been developed and used in different countries;
- the most interesting from the view point of the thesis are beam and slab sections which could be used either for buildings, bridges or superstructures. Shear stress at the interface between the precast beam and the in situ concrete are relatively high comparing to the above mentioned types of sections, which could result in a necessity of the application of reinforcement at the interface.

2.3 Main properties of composite structures

In composite cross-section there are two or more connected elements, made of concretes with different mechanical properties, pliability and also in age, which results in different behaviour when rheological effects are considered, cf. [Furtak, 2006, Sououshian et al., 1987, Wang et al., 2020b, Zhou et al., 2018, Hou et al., 2016, Lorenc and Kubica, 2016, Kim et al., 2011, Lou and Karavasilis, 2019, Lorenc and Kubica, 2020, Shiming and Ping, 2005, Hamid et al., 1989, Saadatmanesh et al., 1989, Wang et al., 2011, Bradford and Gilbert, 1992, Ranzi and Bradford, 2006, Roberts, 1985, Bryson and Carpenter, 1970, Kim et al., 2018, Evans and Parker, 1955]. The main features of composite members are:

- non-uniformity of cross-section which causes regrouping of internal forces due to casting monolithic concrete part and transforms the structure from statically determinate to statically indeterminate,
- redistribution of internal forces in the cross-section as a result of geometry changes (in the first phase only the prefabricated part works, and in the second phase the whole composite element),
- presence of interface between two materials, which has a significant influence on the distribution of internal forces in the cross-section and also along the element,
- redistribution of internal forces due to rheological parameter changes of connected concrete parts which are loaded at different age of hardening.

When considering a composite cross-section it should not be forgotten that the erection of this kind of structure is divided into several phases and in every phase there can be a different static scheme and distribution of internal forces which should be taken into account in the design process [Halicka, 2007], [Jarno and Dyba, 2013a], [Jarno and Dyba, 2013b].

2.4 Experimental research by Choi

The application of HSC to pre-stressed composite bridge girders shown in Fig. 2.3 and the experimental examination of their flexural behaviour performed are summarized in this section.

Fig. 2.3: HSC composite girder [Choi, 2006]

The advantages of using high-strength concrete (HSC) allow an engineer to improve a structure capacity, see [Portland Cement Association, 1994, Building and Construction Authority, 2008, Biliszczuk and Rajski, 2002, Carrasquillo et al., 1981a, Carrasquillo et al., 1981b, Chin et al., 1997, French and Mokhtarzadeh, 1993, Gupta et al., 2009, Hueste et al., 2004, Iravani, 1996, Khan et al., 1995, Khan et al., 1996, Logan et al., 2009, Magureanu et al., 2012, Mokhtarzadeh and French, 2004, Mokhtarzadeh and French, 2000, Ngab et al., 1981b, Ozbakkaloglu and Saatcioglu, 2004, Polski Komitet Normalizacyjny, 2002, Sengul et al., 2002, Shah and Ahmad, 1985, Weiss, 2000, Wiegrink et al., 1996]. It is now possible to design and build bridges with girders having longer spans and the same cross-section area or to reduce the weight of the structure.

Concrete with the compressive strength greater than 60MPa is commercially available. This kind of concrete is a result of using chemical and mineral admixtures such as fly ash, silica fume, slag and water reducing agents. Every admixture has an influence on the properties of concrete, in particular compressive strength, hardening rate, workability and durability [Jarno, 2013b].

The behaviour of high-strength concrete is different than of normal-strength concrete. Codes used for NSC cannot be applied to describe stress-strain relationship for

HSC. The properties of HSC depend to a large extent on the used aggregate, admixtures etc., so it is still an open field for scientific research.

The experimental study presented in this section [Choi, 2006] was carried out by Wonchang Choi at the State University of North Carolina, Raleigh, to evaluate the flexural behaviour of pre-stressed composite girders combining high and normal-strength concrete. The prefabricated girders were made of three different types of high-strength concrete, they were pre-stressed with different strands configuration and then combined with normal-strength concrete deck. This kind of prefabricated girders can reduce the time necessary to build a structure and has economic benefits. All figures and tables used in this section are quoted from [Choi, 2006].

The purpose of investigation of this experimental research is to calibrate the initial FEM model to obtain similar results in the same conditions as the laboratory test. When the model is calibrated properly, further modelling and the analysis of other phenomena will be more accurate.

2.4.1 High-strength concrete girders

Nine 12-meters long pre-stressed girders were designed and tested. Concrete used for those girders was designed to give the compressive strength of 69 MPa, 97 MPa and 127 MPa. Concrete mixture properties are shown in Table 2.1.

Shear reinforcement was constituted by stirrups with 75mm spacing near the end blocks and 150mm spacing along the whole girder. The strands used to pre-stress concrete were made of 1860 MPa pre-stressing steel. The strands were straight and fully bonded over the entire length. More detailed specification is shown in Table 2.2.

All girders were designed based on the code [American Association of State Highway and Transportation Officials, 2017], but some details were modified to prevent premature failure in shear or bond slip due to flexural failure.

For each test specimen fifteen cylinders with dimensions of 100mm x 200mm and nine 150mm x 150mm x 500mm prisms were made to determine the HSC elastic modulus, modulus of rapture and compressive strength.

2.4.2 Normal-strength concrete deck

The tests were divided into three parts, the first girder with a 1.5m wide NSC deck, the second girder with a 0.3m-wide cast deck and the third girder without a deck cast

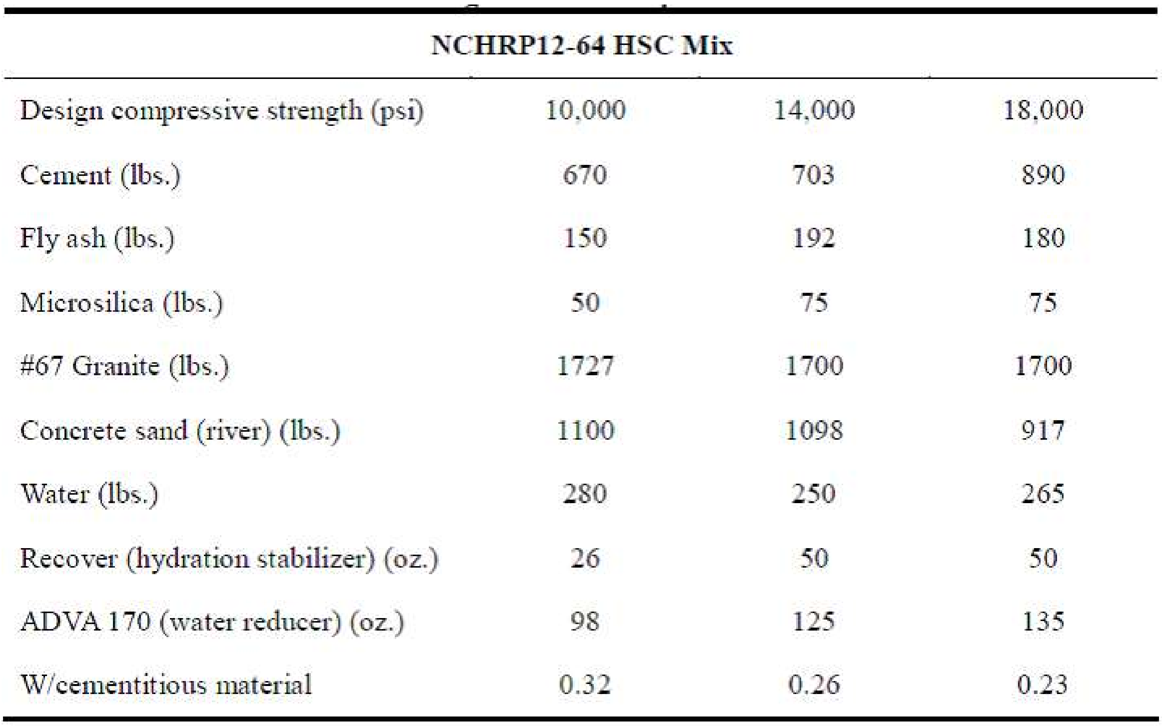

NCHRP12-64 HSC Mix			
Design compressive strength (psi)	10,000	14,000	18,000
Cement (lbs.)	670	703	890
Fly ash (lbs.)	150	192	180
Microsilica (lbs.)	50	75	75
#67 Granite (lbs.)	1727	1700	1700
Concrete sand (river) (lbs.)	1100	1098	917
Water (lbs.)	280	250	265
Recover (hydration stabilizer) (oz.)	26	50	50
ADVA 170 (water reducer) (oz.)	98	125	135
W/cementitious material	0.32	0.26	0.23

Table 2.1: Design mixture properties for 3 types of HSC, table quoted from [Choi, 2006]

on it. The deck was 200mm thick and made from concrete mixture shown in Table 2.3.

2.4.3 Manufacturing of test specimens

The fabrication of the pre-stressed high-strength concrete composite girders with different deck widths consist of two steps. Firstly, the girders were fabricated at a pre-cast pre-stress plant and then decks with variable configuration were cast in the laboratory.

All nine pre-stressed girders were produced by Standard Concrete Products pre-stressing plant in Savannah, GA. All measuring devices, load cells, strain gauges were placed before tensioning of the pre-stressing strands. All 20 strands were placed on the pre-stressing bed simultaneously and tensioned individually (it is shown in Fig. 2.4). All strands were tensioned to 75 percent of their ultimate strength. After that, the reinforcement and form were installed (Fig. 2.5).

For each mixture strength design the girders were cast using four batches of the same concrete mix (Fig. 2.6). The girders were vibrated using internal vibrator, top surface was roughened, which has influence on the behaviour of the interface between the girder and the deck. After casting concrete, each girder was protected with a plastic

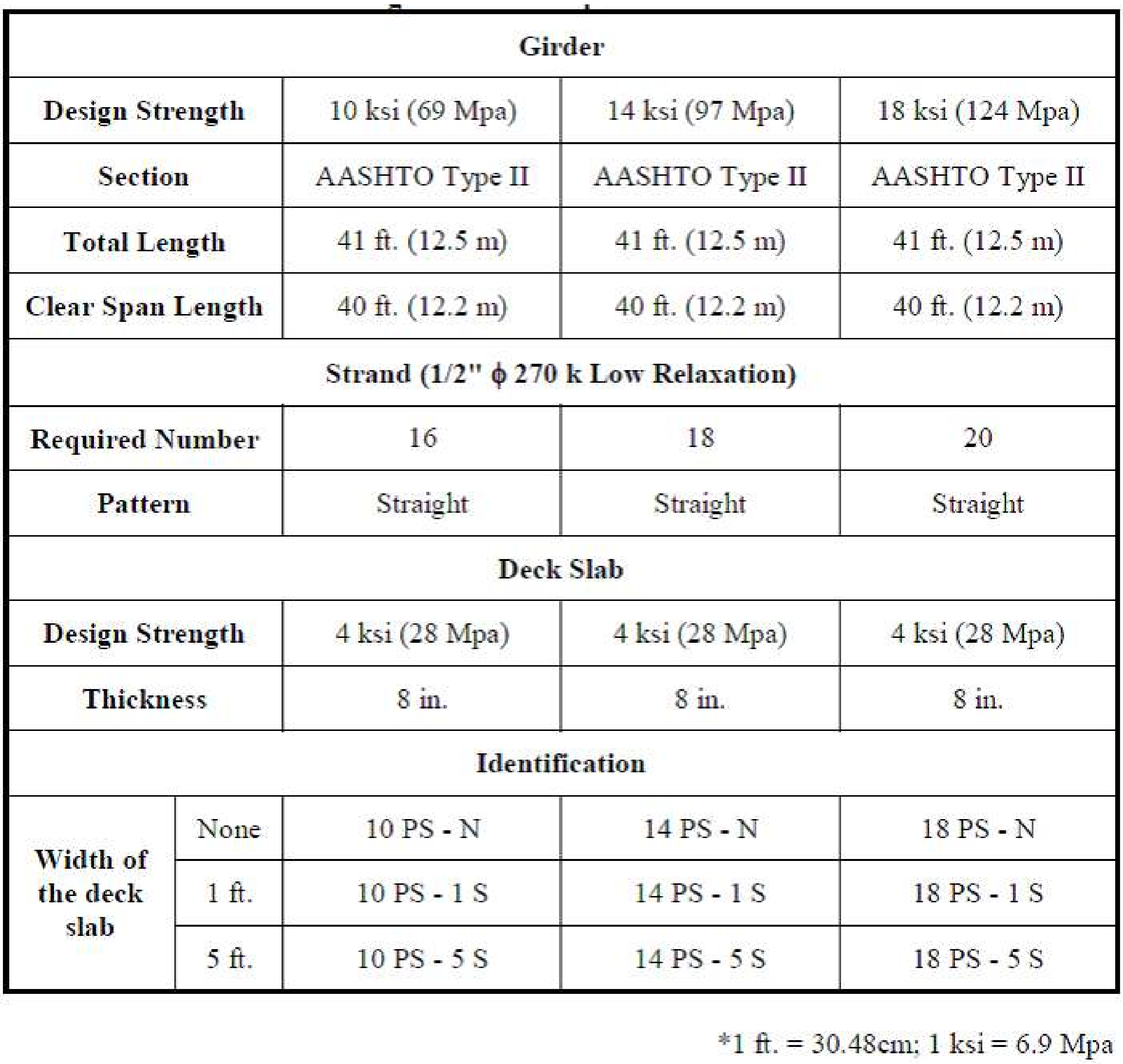

Girder				
Design Strength		10 ksi (69 Mpa)	14 ksi (97 Mpa)	18 ksi (124 Mpa)
Section		AASHTO Type II	AASHTO Type II	AASHTO Type II
Total Length		41 ft. (12.5 m)	41 ft. (12.5 m)	41 ft. (12.5 m)
Clear Span Length		40 ft. (12.2 m)	40 ft. (12.2 m)	40 ft. (12.2 m)
Strand (1/2" ϕ 270 k Low Relaxation)				
Required Number		16	18	20
Pattern		Straight	Straight	Straight
Deck Slab				
Design Strength		4 ksi (28 Mpa)	4 ksi (28 Mpa)	4 ksi (28 Mpa)
Thickness		8 in.	8 in.	8 in.
Identification				
Width of the deck slab	None	10 PS - N	14 PS - N	18 PS - N
	1 ft.	10 PS - 1 S	14 PS - 1 S	18 PS - 1 S
	5 ft.	10 PS - 5 S	14 PS - 5 S	18 PS - 5 S

*1 ft. = 30.48cm; 1 ksi = 6.9 Mpa

Table 2.2: Detailed design of test specimens, table quoted from [Choi, 2006]

cover and a water hose was placed on top to enable curing.

After fabrication of the nine pre-stressed girders they were stored at the plant. About 56 days after manufacturing three girders with the weakest strength were shipped from the plant to CFL for testing. The other girders were moved 3 months after the fabrication process and stored in the laboratory.

2.4.4 Instrumentation used

The pre-stressing force, strain during pre-stressing, elongation and end slip were measured during the fabrication process. To measure the elongation of strands during the construction of the girders two internal strain gauges were welded to chosen strands at the bottom of the girder near the middle of the span. The gauges were used to show pre-stressing losses and strand strains during the entire testing procedure. Fig. 2.7

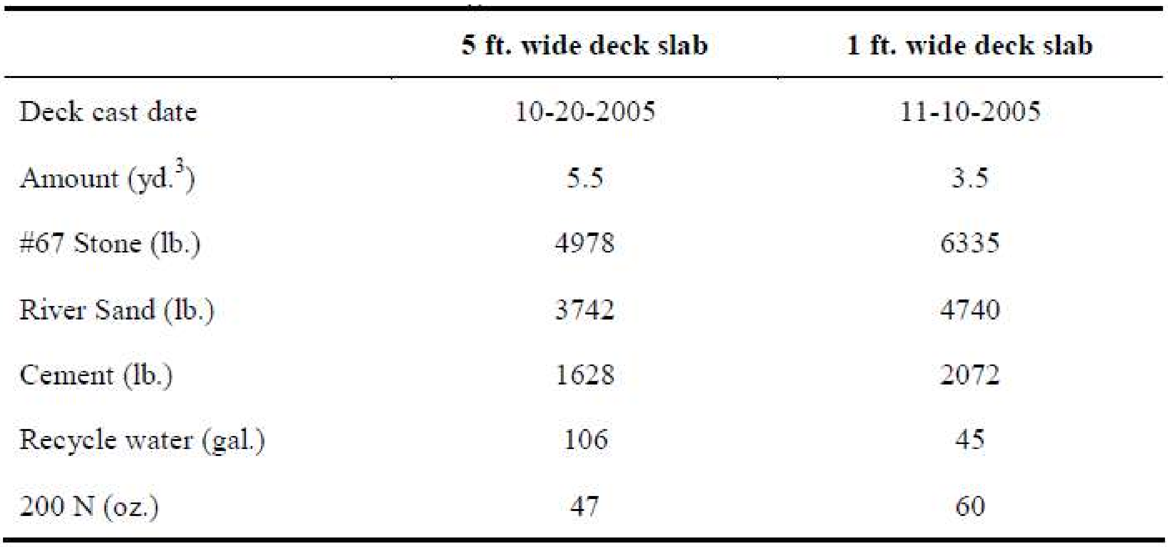

	5 ft. wide deck slab	1 ft. wide deck slab
Deck cast date	10-20-2005	11-10-2005
Amount (yd.^{3})	5.5	3.5
#67 Stone (lb.)	4978	6335
River Sand (lb.)	3742	4740
Cement (lb.)	1628	2072
Recycle water (gal.)	106	45
200 N (oz.)	47	60

Table 2.3: Concrete mix design for NSC slab, table quoted from [Choi, 2006]

Fig. 2.4: Strand lay-out [Choi, 2006]

shows the location of these gauges.

Before testing, all the specimens, 1.5-meter-wide, 0.3-meter-wide, and without the

Fig. 2.5: Reinforcement installation [Choi, 2006]

Fig. 2.6: Casting of concrete [Choi, 2006]

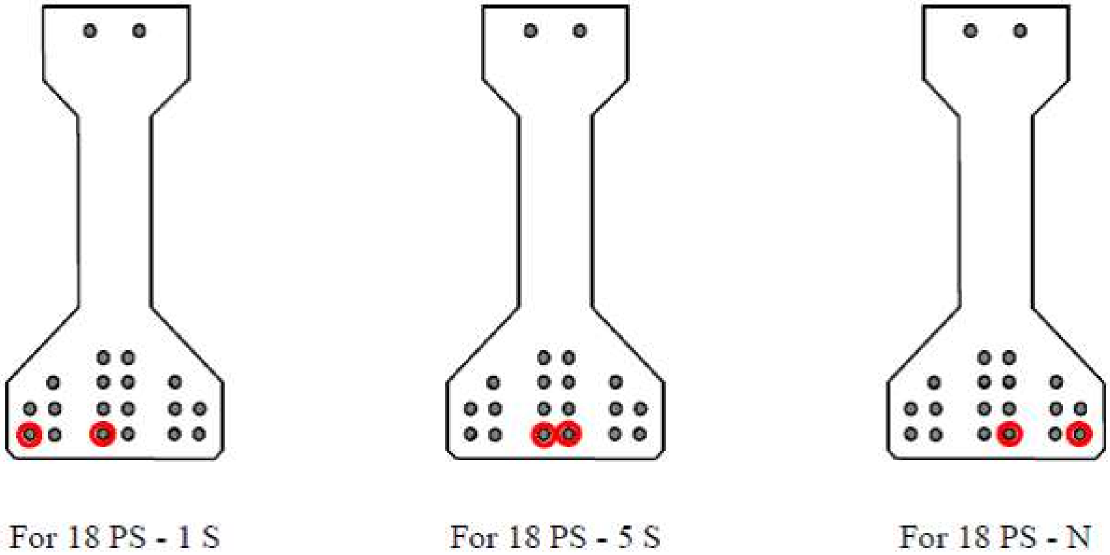

Fig. 2.7: Locations of welded strain gauges [Choi, 2006]

deck, were instrumented for the measurement of displacements and strains at several locations along the beam. Linear motion transducers (LMTs) were used to measure deflections at the ends, at quarter-span and mid-span location. Moreover, two conventional linear transducers at the end were used to determine the relative deflection between the concrete girder and the neoprene pad (Fig. 2.8).

To measure the strain, electrical resistance strain gauges and PI gauges were installed on the top, bottom and side surface of concrete girders. These devices measured the strain at various loading stages. Strain gauges were also placed at the top of the deck slab. For more details, see [Choi et al., 2008].

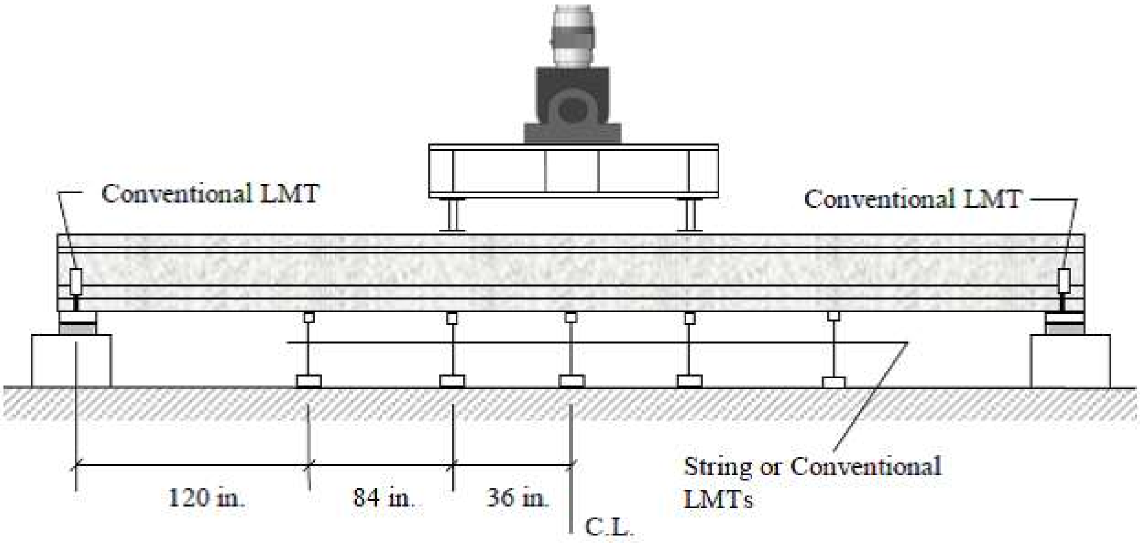

Fig. 2.8: Locations of LMTs to measure deflections [Choi, 2006]

2.4.5 Testing procedure and set-up

The girders placed on steel plates above neoprene pads worked as simply supported beams. The load was applied to every girder at two points spaced 6 ft. at the mid-span. The girders were loaded and unloaded using a stroke control at a rate of 0.1 in./min. due to cracking, and reloaded with the same stroke control rate up to the yielding of the pre-stressing strands. After the strands yielded, the girders were loaded to failure. Fig. 2.9 shows a typical set-up for the described test.

2.5 Results and discussion

All results were divided into: material properties obtained in the experimental study, pre-stressing losses measured using internal strain gauges, measured end slip used to determine the transfer length and, most important, flexural response of the girders, cracking strength, load-deflection relationships, failure modes etc. In this section only the flexural response is presented, for more details see [Choi et al., 2008].

The three composite girder groups with 1.5-meter-wide deck slab, 0.3-meter-wide slab and without the slab were tested under static loading conditions. As mentioned before, these composite girders were made from two different materials, having different stiffness, which has an influence on the interaction between them. Next, load-deflection relationships, cracking and ultimate loads are presented for each group of girders.

Fig. 2.9: Test set-up for girder with 1.5 meter wide slab [Choi, 2006]

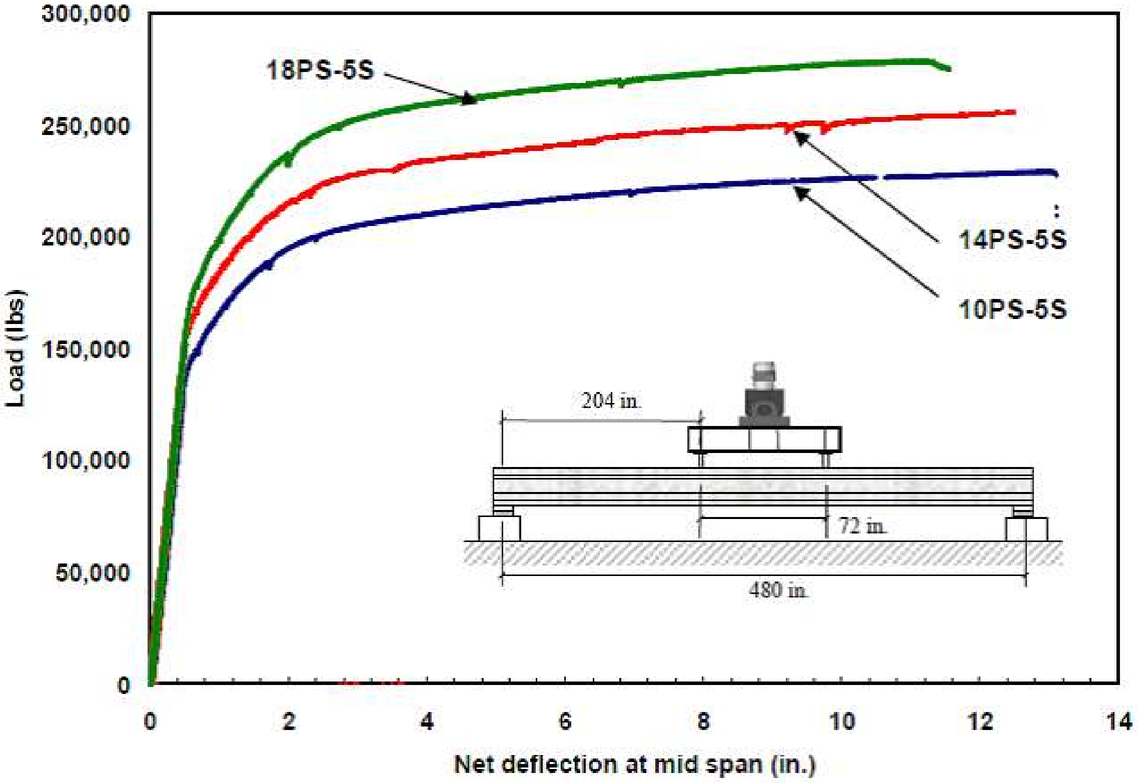

Fig. 2.10: Load-deflection diagrams for girders with 1.5-meter-wide deck [Choi, 2006]

As we can see in Fig. 2.10, the deflection at the mid-span of the group of girders with 1.5 meter deck at the time of failure was relatively large. After a beam cracks, the load-deflection behaviour becomes non-linear. The observed cracking load and ultimate load for each of these girders are given in Table 2.4.

Identification	Cracking Load (kips)	Ultimate Load (kips)
10PS-5S	129	229.0
14PS-5S	149	255.5
18PS-5S	162	278.4

Table 2.4: Test results for girders with 1.5 meter wide deck, table quoted from [Choi, 2006]

Next, the load-deflection relationship (Fig. 2.11) as well as thr cracking and ultimate load (Table 2.5) for the group of girders with 0.3 meter deck width are presented. In the load-deflection diagram a softening behaviour is observed.

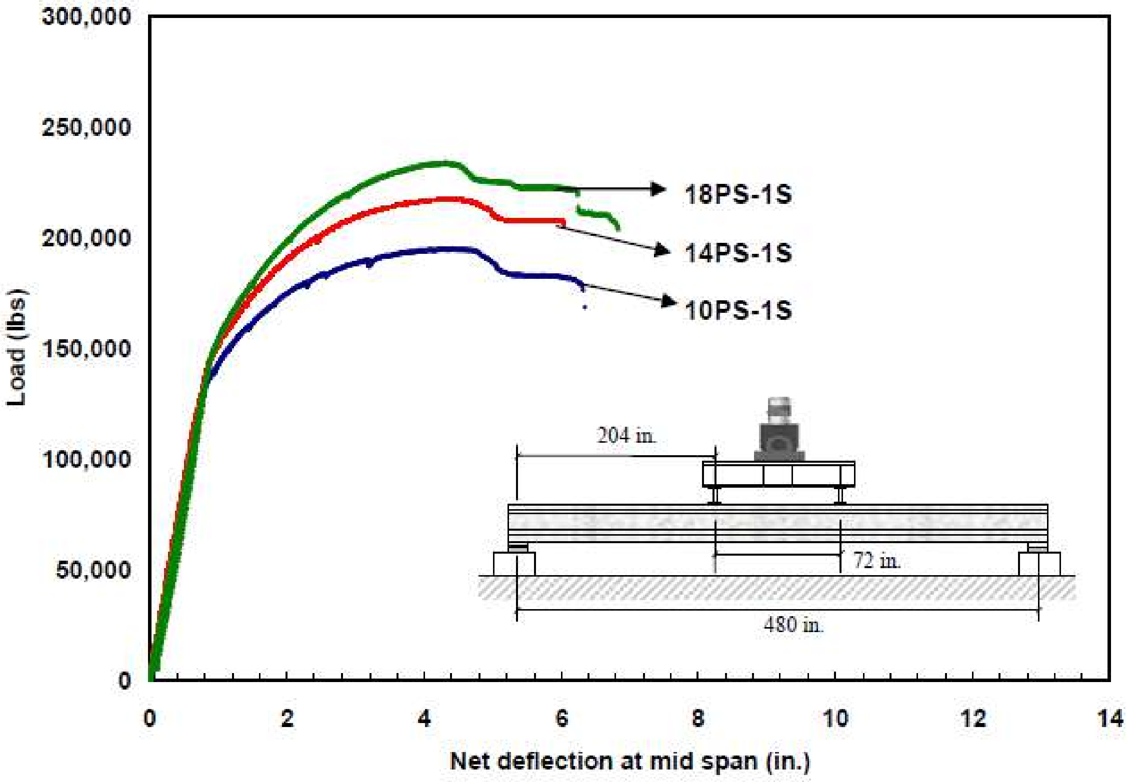

Fig. 2.11: Load-deflection behaviour for girders with 0.3-meter-wide deck [Choi, 2006]

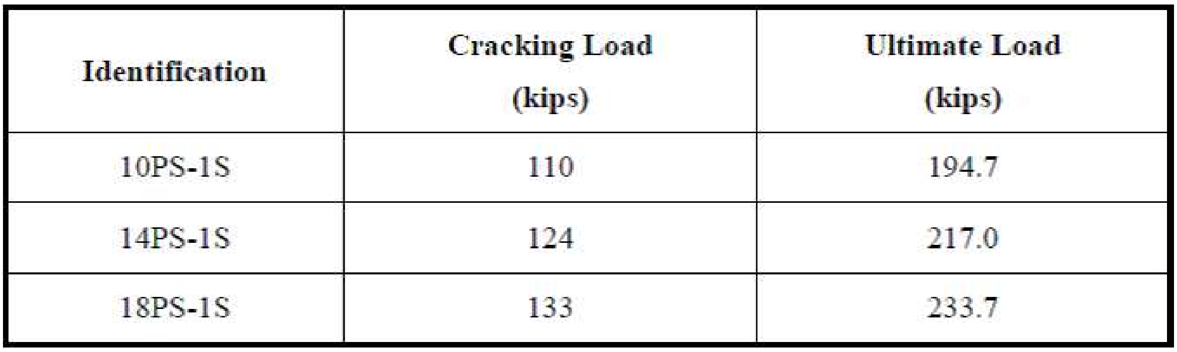

Identification	Cracking Load (kips)	Ultimate Load (kips)
10PS-1S	110	194.7
14PS-1S	124	217.0
18PS-1S	133	233.7

Table 2.5: Test results for girders with 0.3-meter-wide deck [Choi, 2006]

Finally, the load-deflection relationship (Fig. 2.12) and the values of cracking and ultimate load (Table 2.6) for the last group of girders without the cast deck are presented. The failure is less ductile in comparison to what is observed for the other six composite girders with normal-strength concrete slab.

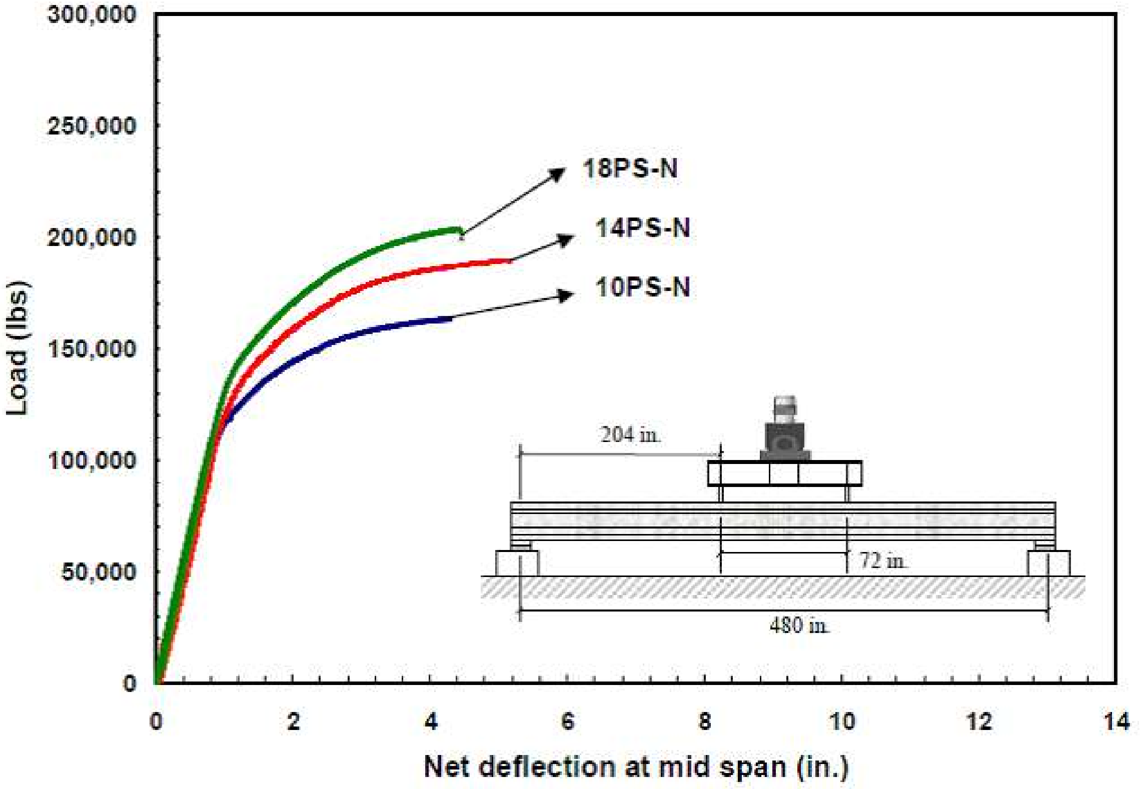

Fig. 2.12: Load-deflection behaviour for girders without deck [Choi, 2006]

2.6 Conclusions

Three groups of composite girders, pre-stressed high-strength concrete beam with normal-strength concrete deck, were tested by [Choi, 2006]. The first group of girders

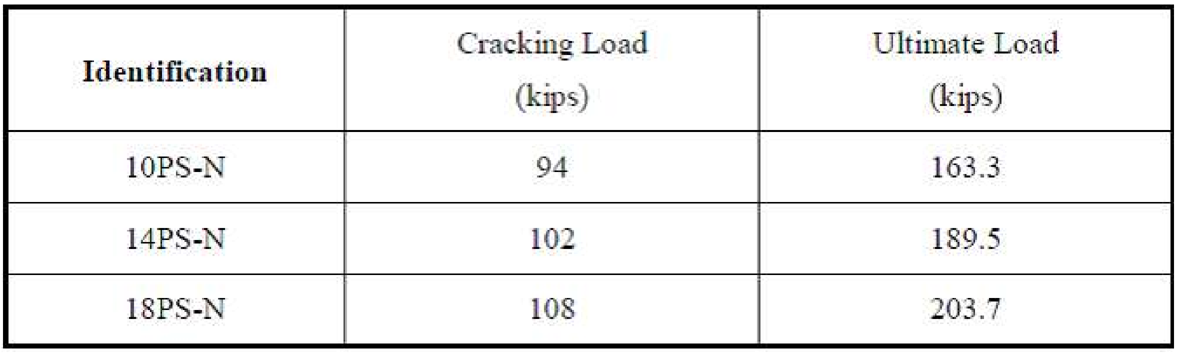

Identification	Cracking Load (kips)	Ultimate Load (kips)
10PS-N	94	163.3
14PS-N	102	189.5
18PS-N	108	203.7

Table 2.6: Test results for girders without deck [Choi, 2006]

with 1.5-meter slab width exhibits linear initial stiffness and then cracking of concrete, the load-displacement relation becomes non-linear and a significant deflection at mid-span is observed before failure due to yielding of pre-stressing strands. For the second group of girders with 0.3 meter slab width, after the initial linear behaviour and non-linear cracking progress leading to the strand yield strength, a small drop in load level is observed due to softening of concrete. The last group of specimens without composite deck shows the initial linear behaviour and then non-linear response as well, but the failure mode observed is brittle crushing of concrete. It is obvious that the existence and width of the composite slab has a significant influence on the cracking load, load-bearing capacity at ultimate limit state and on the failure mode of flexural response.

The tests carried out by Choi show the static flexural behaviour for composite pre-tensioned high-strength concrete girders. However, it is necessary to investigate the flexural response accounting for time effects, in particular the influence of creep. The method of joining the two different materials, HSC and NSC, should also be examined.

3 Physical phenomena in contact zone

To represent the phenomena occurring in the contact zone, several non-linear interface models can be used:

- adhesion,
- Coulomb friction,
- aggregate interlock,
- stitching reinforcement,
- indented connection.

They are described in this chapter.

3.1 Adhesion

Load-bearing co-operation between two parts of concrete which constitute a composite cross-section is possible thanks to the phenomena of adhesion and friction on the contact surface [Jarno et al., 2014]. Adhesion is understood as a range of phenomena on the edge between two different materials, which bond them to each other. There are many theories describing adhesion and its factors which have influence on the bond strength. Fig. 3.1 shows a classification of adhesion types.

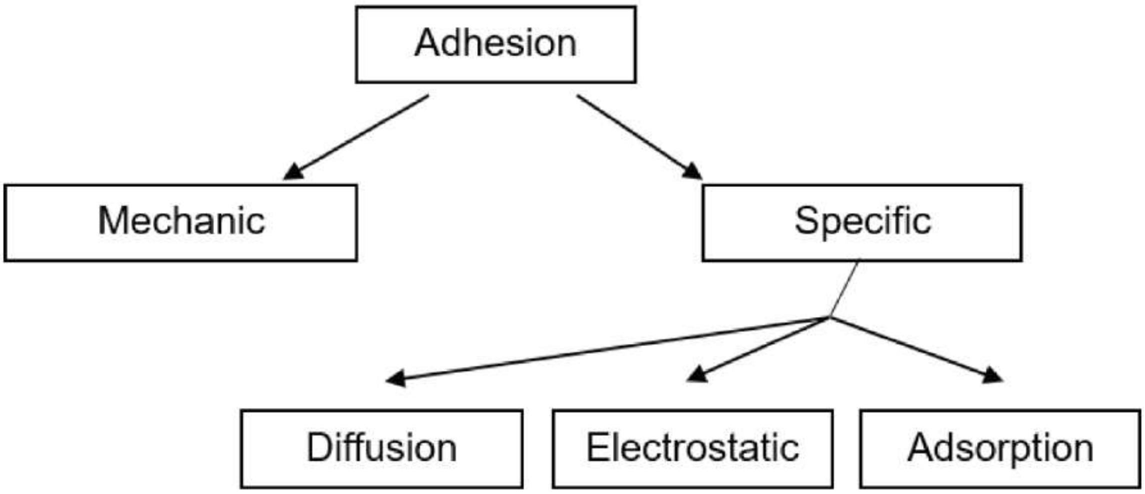

Fig. 3.1: Classification of adhesion types

Mechanical adhesion is a result of the penetration of new cast in-situ grout into the pores of old precast concrete (prefabricated girder) and into surface irregularities, which after grout hardening provides mechanical interlock. Since there is aggregate involved, this phenomenon is called *aggregate interlock* (Fig. 3.2).

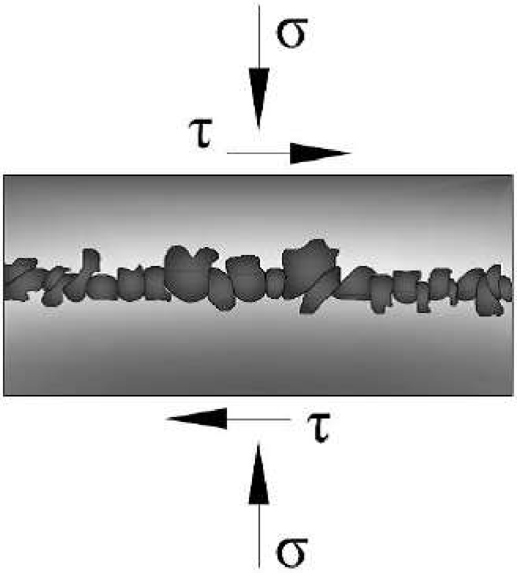

Fig. 3.2: Illustration of aggregate interlock [Halicka, 2007]

When the phenomenon of aggregate interlock occurs, the contact surface increases because of irregular shape of aggregate. There are a few theories which describe specific adhesion, like Dieriagin electrostatic adhesion theory, Vojucki diffusion theory, theories based on Van der Waals forces or chemical bonds [Halicka, 2007,Kamiński and Kmiecik, 2010]. While connecting concretes, grout of the new concrete plays the role of *glue* and the connected parts have the same chemical composition. The most important factor in adhesion formation between the new and old concrete are inter-molecular forces. They enable grout to penetrate pores and irregularities of the old concrete.

The adhesion effect of joining two concretes depends on:

- roughness of the surface,
- additives to improve adhesion,
- contamination of the contact surface,
- hydration treatment of the old concrete surface,
- air bubbles,
- water lens,
- segregation of grout.

After joining two concretes a chemical reaction can take place between the compounds of the new concrete and non-hydrated parts of cement in the old concrete, so this is specific adhesion resulting from chemical bonds. A measure of the adhesion is a force which is needed to disconnect the two materials. Load-bearing capacity of the interface is related to the tensile strength but also to the shear strength or torsion strength [Halicka, 2007].

3.2 Friction between two surfaces

When considering adhesion, the tractions perpendicular to the contact surface are considered. The existence of these forces is related with the friction phenomenon which is described by friction coefficient μ. The friction coefficient is a ratio of shear traction τ to normal traction σ_N on the interface surface (Fig. 3.3). There are a few theories describing the friction phenomenon:

- molecular-mechanical theory which assumes friction as an effect of deformation of thin surface layers and the friction coefficient is a sum of parts related to adhesion and deformation:
$$\mu = \mu_{adh} + \mu_{def} \tag{3.1}$$
- according to the Dieriagin theory the force perpendicular to the contact surface can be treated as a sum of external load N and adhesion force N_0 to produce the shear force:
$$T = \mu \cdot (N + N_0) \tag{3.2}$$
- in the Kregielski theory the friction coefficient is calculated according to the formula:
$$\mu = \frac{\tau_{j,0}}{\sigma_N} + \beta + k \cdot \alpha_H \cdot \sqrt{\frac{h}{R}} \tag{3.3}$$

where:

- $\tau_{j,0}$ - initial adhesion stress on a contact surface without any external loads,
- β - specific adhesion coefficient,
- k - roughness and shape coefficient,
- α_H - histeresis loss with volumetric deformation,

- h - depth of irregularities,
- R - curvature radius of a particular irregularity.

When analysing the described formulas, it can be noticed that the friction force is treated as resistance to movement of the materials in contact. The resistance is a result of adhesion (independent of external stress) and friction.

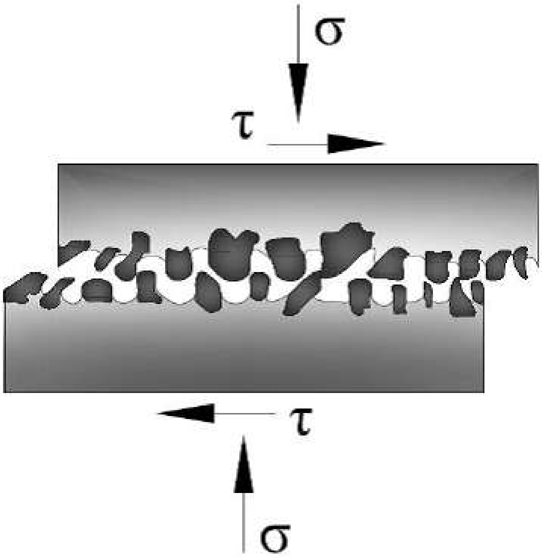

Fig. 3.3: Friction in contact zone [Halicka, 2007]

In the Kregielski theory the description of appropriate friction is improved by adding two effects: specific adhesion forces dependent on the value of external load and aggregate interlock mechanism resulting from the characteristics of the surface and its roughness. On the other hand friction is related to the shear forces on the contact surface. Friction is a phenomenon which determines the behaviour of the contact zone between two concretes. To determine the load bearing capacity of the shear-loaded contact zone the Coulomb hypothesis is used:

$$\tau_{Rd,j} = C + \mu \cdot \sigma_N \tag{3.4}$$

where:

- $\tau_{Rd,j}$ – effective friction stress
- C – adhesion stresses in contact zone without external loads,
- $\mu \cdot \sigma_N$ – specific friction, where μ is a friction coefficient which can be interpreted as a sum of the specific adhesion and the aggregate interlock effect [Halicka and Franczak, 2009, Halicka and Franczak, 2012, Halicka, 2007].

[Seeber, 2004] proposed an effective friction coefficient to the describe shear in the friction behaviour [Tanner, 2008]. It is stated that according to ACI the effective friction coefficient should approach the friction coefficient as the capacity of the interface is reached. However, [Seeber, 2004] proposes modifications shown in Table 3.1.

Interface condition	**Recommended μ**	**Maximum μ_e**	$V_{n,max}$
Concrete to concrete cast monolithically	1.4 λ	3.4 λ	$0.30\ \lambda\ f_c \cdot A_c < 1000 \cdot \lambda\ A_{cr}$
Concrete to concrete with roughened surface	1.0 λ	2.9 λ	$0.25\ \lambda\ f_c \cdot A_c < 1000 \cdot \lambda\ A_{cr}$
Concrete to concrete	0.6 λ	2.2 λ	$0.2\ \lambda\ f_c \cdot A_c < 800 \cdot \lambda\ A_{cr}$
Concrete to steel	0.7 λ	2.4 λ	$0.2\ \lambda\ f_c \cdot A_c < 800 \cdot \lambda\ A_{cr}$

Table 3.1: Modification of friction coefficient according to [Seeber, 2004]

Here, A_{cr} is the area of shear crack interface, f_c is the specified compressive strength of concrete, μ is a friction coefficient, μ_e is an effective friction coefficient, $V_{n,max}$ is a maximum nominal shear capacity. Moreover, λ is a modification factor related to concrete density, which equals 1.0 for normal-weight concrete, 0.85 for sanded lightweight concrete, 0.75 for all-lightweight concrete [Tanner, 2008].

3.3 Stitching reinforcement

In the situation when the longitudinal shear stress in the plane of bond is higher than the total load-carrying capacity resulting from adhesion and friction, the lateral reinforcement is required (Fig. 3.4). When the cross-section strain increases, adhesion and friction forces are overcome and a longitudinal slip of the surfaces occurs, then the stitching reinforcement is a decisive component of the capacity [Kamiński and Kmiecik, 2011b, Kamiński and Kmiecik, 2011a].

The behaviour of the reinforcement bars acting against longitudinal shear transfer in a composite zone was tested in [Bass et al., 1989, Fowler et al., 1999a, Fowler et al., 1999b, Hanswille et al., 1998, Lindig, 2007, Menkulasi and Roberts-Wollmann, 2005,

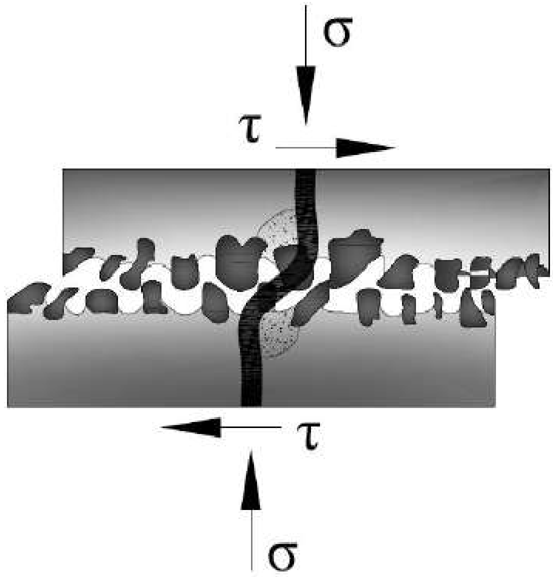

Fig. 3.4: Stitching reinforcement [Halicka, 2007]

Randl et al., 2008, Tan et al., 1999, Valluvan et al., 1999].

The horizontal shear resistance of the connection between precast concrete bridge deck and pre-stressed concrete girders was tested in [Menkulasi and Roberts-Wollmann, 2005]. The connection was formed by isolated shear bars extending from the precast I-girder into a block-out pocket in the precast deck panel. The block-out and haunch between the panel and the beam were grouted. To check the strength and the behaviour of the contact zone, 36 push-off tests were carried out. The main parameters tested were the type of grout and the area of reinforcing steel crossing the interface. Several shear connector details were tested as well. All of the results were compared with the equations given by [American Association of State Highway and Transportation Officials, 2017]. The deck panels were full depth 180 mm to 230 mm and 18 m to 30 m long in the direction of traffic and the full width of the bridge was up to 14 m. The decks were equipped with pockets over the girders for shear connectors. The research programme was calibrated to investigate the horizontal shear capacity of full-depth precast panels on pre-stressed concrete I-girders. Three aspects of the horizontal shear transfer mechanism are quite different from typical cast-in-place decks on pre-stressed girders. The first is that there are two possible shear planes – one between the girder and the haunch and the other between the haunch and the deck panel. The second is that the grout has no coarse aggregate, so no aggregate interlock phenomenon is observed. The third is that the connectors are clustered in the block-out pockets. To study the influence of these factors a series of push-off tests were performed and compared with code provisions [ACI Committee 363, 1997, ACI Committee 363, 2007, American Association of State Highway and Transportation Officials, 2017]. Beside the measurement of horizontal shear strength, haunch height etc., different types of shear connectors other than conventional stirrups, e.g. post-installed hooked reinforcing bars or Dayton-Richmond anchors were tested and load vs slip curves were determined.

Another way to use the stitching reinforcement is the application of powder-driven nails. The tests in [Fowler et al., 1999a] were performed to examine the shear transfer behaviour between new and existing concretes using large powder-driven nails. The nails (120 mm long and 10 mm in diameter) fabricated from high-strength steel were installed into predrilled holes with a special powder-driven actuator. The authors of the paper tested eight concrete slabs (4 m long, 1.4 wide and 0.2 m deep), with four different combinations of concrete compressive strength and coarse aggregate. During pull-out and push-off tests the strength and the relation of the load with the slip of nails were examined. To test the interface horizontal shear behaviour a cubic sample with contact area of 230 cm^2 and one nail was prepared. The results were divided into two sets, concerning the push-off behaviour of bonded and unbonded interface. They can be summarized as follows:

- the mean interface shear strength of all specimens with a bonded-rough interface was 2930 kPa,
- there was no significant difference between specimens with different preparation of the contact surface,
- the specimens with 0.38 percent interface shear reinforcement had 10 to 16 percent higher interface strength than those without nails for the same contact area,
- due to redistribution of stresses across the interface which was provided by nails the maximum displacement at the peak load was higher for specimens with nails,
- the specimens with the unbonded-rough interface with nails effectively resisted shear and limited slip,
- the shear stress vs slip relations for unbonded-smooth and unbonded-rough interfaces were significantly different.

A similar series of experiments was performed in [Issa et al., 2003]. 28 full-scale push-out specimens were tested under static loading. Each of them was composed of a steel beam and a precast slab which was attached to the top flange of the steel beam using welded studs. The number of pockets and number of studs per pocket were the parameters of the tests. Similarly to other papers, several push-out tests were carried out. The results of the experiments presented a trend of increasing the horizontal shear strength with the number of studs and pockets. However, the load capacity was not proportional to the number of studs in the shear pocket.

The following set of variables which have influence on the shear capacity of the contact zone were proposed in [Bass et al., 1989]:

- amount of interface reinforcement,
- embedment depth of interface reinforcement,
- compressive strength of existing member and new material,
- concrete interface surface preparation,
- reinforcement detailing,
- casting procedures,
- concrete interface area.

The minimum required reinforcement for horizontal shear in composite structures was investigated in [Hanswille et al., 1998] and [Lindig, 2007].

3.4 Different code recommendations

3.4.1 Eurocode 2

According to the code a structure can be considered as a composite structure when the following conditions are met:

- the longitudinal shear load capacity of prefabricated and cast parts of concrete is maintained
- the continuity in transmission of normal forces is maintained by co-operating parts,
- the cast in-situ concrete class is not lower than C16/20,

- the thickness of the cast concrete layer is not lower than 40 millimetres.

According to Eurocode 2 the design shear capacity per unit of interface surface of two different hardening concretes is given by the formula:

$$\nu_{Rdi} = c \cdot f_{ctd} + \mu \cdot \sigma_n + \rho \cdot f_{yd} \cdot (\mu \cdot \sin\alpha + \cos\alpha) \leqslant 0.5 \cdot \nu \cdot f_{cd} \tag{3.5}$$

where:

- f_{ctd} – design tensile strength of concrete,
- c – coefficient dependent on type of surface of precast concrete,
- σ_n – stress perpendicular to the plane of the joint,
- μ – shear friction coefficient,
- ρ – degree of reinforcement,
- f_{yd} – design tensile strength of steel,
- α – angle between joint plane and reinforcement,
- ν – Poisson's ratio,
- f_{cd} – design compressive strength of concrete.

The shear stresses on the contact surface depend on a coefficient which is related to the thickness of subsidiary concrete as a result of using the classical model based on a Moersch truss. Concrete in phase II works only in the compressive stress state so the value of shear stress along the tension zone is constant.

Both adhesion and friction depend on the surface preparation. Taking into account different technologies of this operation, the codes distinguish the following types of surface to determine the adhesion coefficient (Table 3.2):

- very smooth surface is steel, plastic or wooden casting formwork,
- smooth surface is prepared using slide or press formwork,
- rough surface is defined as the application of concrete with grooves at least 3 mm deep and with spacing less than 40 mm,
- indented construction joint – a specially prepared connection (Fig. 3.5).

Type of surface	**Eurocode 2**	**PN-B-03264:2002**	**Model Code 2010**	**CEB-FIP**
Very smooth	0.025÷0.10	0.02	0.025	0.10
Smooth	0.20	0.35	0.35	0.20
Rough	0.40	0.45	0.45	0.40
Indented	0.50	0.50	0.45	0.40

Table 3.2: Adhesion coefficient values according to codes

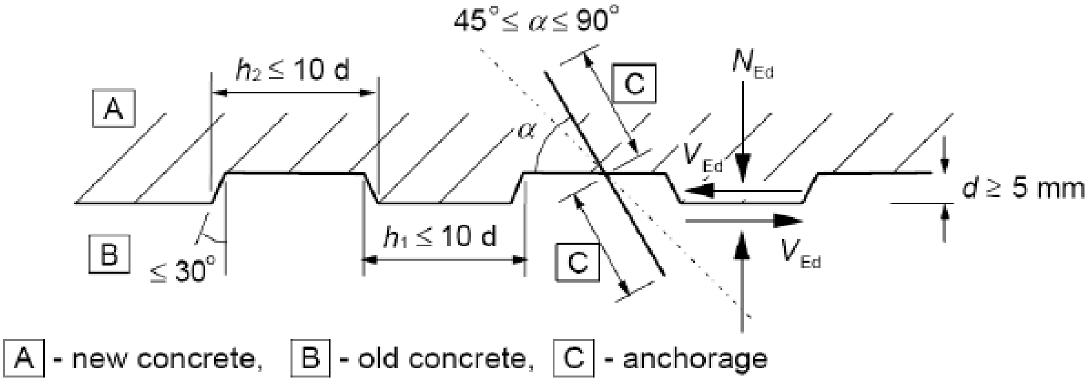

Fig. 3.5: Indented construction joint [European Committee for Standardization, 2004]

Thanks to the above classification it is possible to assume the adhesion coefficient for different types of surface, which allows one to determine the ultimate longitudinal shear stress resulting from adhesion. A part of the natural adhesion of the rough joint is characterized by an aggregate blocking mechanism on the cracked surface. It is related to the phenomenon called aggregate interlock. It occurs together with adhesion, but after adhesion breaking it plays a more significant role.

Friction between the two parts is described by friction coefficient μ which mainly depends on the preparation of the surfaces.

Eurocode 2 also limits the normal stresses to 60% of the design value of the compressive strength of concrete. In the case when longitudinal shear stresses reach a value above the sum of adhesion and friction capacity, it is necessary to design additional stitching reinforcement [European Committee for Standardization, 2004,Kamiński and Kmiecik, 2011a].

Surface preparation	$\boldsymbol{k_c}$	$\boldsymbol{\kappa}$	$\boldsymbol{\alpha_F}$	$\boldsymbol{\beta_c}$	$\boldsymbol{\mu}$ $(\boldsymbol{f_{ck}} > 20MPa)$	$\boldsymbol{\mu}$ $(\boldsymbol{f_{ck}} > 35MPa)$
Water under pressure	2.3	0.5	0.9	0.5	0.8	1.1
Prepared with sand	0	0.5	1.0	0.4	0.7	0.7
Without preparation	0	0	1.4	0.4	0.5	0.5

Table 3.3: Coefficients for calculation of load-carrying capacity according to Model Code 2010

3.4.2 Model Code 2010

Model Code 2010 for reinforced concrete structures gives rules and conditions for design and calculation but also proposes the direction of research in the discussed field. The description of the structural behaviour of composite concrete is based on the phenomena of adhesion, aggregate interlock, friction and the presence of additional reinforcement which can be designed.

The design formula reads:

$$\nu_{Rdi} = 0.09 \cdot k_c \cdot f_{ck}^{\frac{1}{3}} + \mu \cdot \left(\kappa \cdot \rho \cdot f_{yd} + \frac{\sigma_n}{\gamma} \right) + \alpha_F \cdot \sqrt{f_{yd} \cdot f_{cd}} \leqslant \beta_c \cdot f_{cd} \cdot b_i \tag{3.6}$$

where b_i is width of the cross-section and γ is safety factor.

The first part of the sum is due to adhesion and aggregate interlock, the second is due to shear friction and further there is an additional part representing dowel action which is bending capacity of the stitching reinforcement related to a slip in the interface. The coefficients for formula (3.6) are given in Table 3.3.

In spite of the fact that Model Code 2010 defines the load-carrying capacity of the contact zone very precisely, one should not sum the effects of all interface phenomena in a simple way because these particular phenomena reach their maximum at different values of bond slip and they are mutually dependable. For interfaces reinforced in a proper way and anchored in prefabricated or cast parts, the model presented in Model Code 2010 coincides with the model described in Eurocode 2 [Kamiński and Kmiecik, 2011a, fib, 2010].

The friction coefficient depends on the surface preparation and in Eurocode 2, Model Code 2010 as well as Polish code PN-B-03264:2002 it has the same values given below:

- very smooth surface: 0.5,

- smooth surface: 0.6,
- rough: 0.7,
- indented: 0.9.

German code DIN 1045-1 gives the same values except for the indented connection, for which it has the value 1.0 [Kamiński and Kmiecik, 2011a, fib, 2010, Polski Komitet Normalizacyjny, 2002].

3.4.3 ACI code

The evaluation of [ACI Committee 318, 1995] shear-friction provisions was performed in [Valluvan et al., 1999]. Section 11.7 of [ACI Committee 318, 1995] includes design recommendations for conditions where direct shear transfer through friction should be considered. One of those conditions concerns the interface between concretes cast at different times. Shear friction capacity is defined as a function of steel reinforcement area placed in the interface and of preparation of the surface of old concrete before the new part is cast. The ACI code also defines an upper limit on the interface shear capacity. The tests carried out in [Valluvan et al., 1999] were used to verify and extend the application of the shear friction provisions of [ACI Committee 318, 1995]. In the experimental program sixteen test specimens were prepared. Each of them consisted of two reinforced concrete elements, the first representing the old part of concrete and the second representing the new one. The cross-section at the interface was constructed to obtain the area of 128 square inches for direct shear transfer. The test specimens were subjected to monotonic and cyclic loading in direct shear. The applied shear and normal compressive load as well as the interface slip and uplift were measured by pressure transducers and strain gauges. The measurements allowed for evaluation of the peak shear capacity, interface displacements and failure mode of each specimen. The results of the test are given in Table 3.4.

Four different failure modes were observed: failure of existing concrete, of aggregate interlock or interface grout, or dowels pull-out. The results and comparison between experiments and ACI provisions are shown in Table 3.5.

Discussing the upper limit on shear strength of a plane given by ACI that should not be taken greater than $0.2f_c \cdot A_c$ nor $A_c \cdot 800$, where A_c is the area of concrete section resisting shear transfer, the test results indicate that the limit is overly conservative,

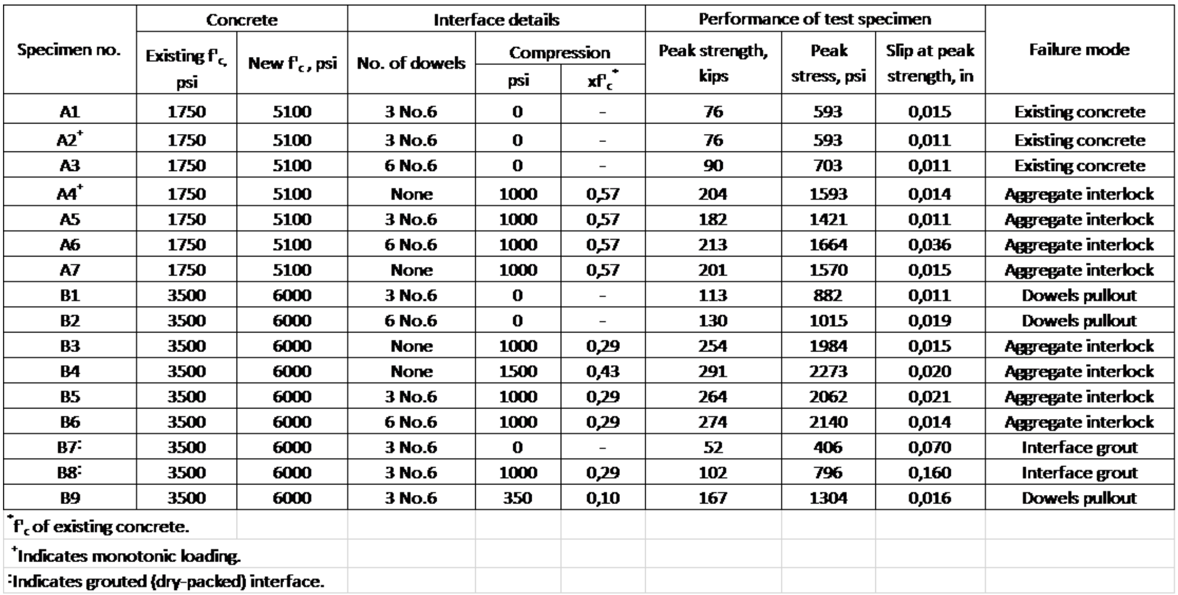

Specimen no.	Concrete		Interface details			Performance of test specimen			Failure mode
	Existing f'_c, psi	New f'_c, psi	No. of dowels	Compression		Peak strength, kips	Peak stress, psi	Slip at peak strength, in	
				psi	$xf'_c{}^*$				
A1	1750	5100	3 No.6	0	-	76	593	0,015	Existing concrete
A2$^+$	1750	5100	3 No.6	0	-	76	593	0,011	Existing concrete
A3	1750	5100	6 No.6	0	-	90	703	0,011	Existing concrete
A4$^+$	1750	5100	None	1000	0,57	204	1593	0,014	Aggregate interlock
A5	1750	5100	3 No.6	1000	0,57	182	1421	0,011	Aggregate interlock
A6	1750	5100	6 No.6	1000	0,57	213	1664	0,036	Aggregate interlock
A7	1750	5100	None	1000	0,57	201	1570	0,015	Aggregate interlock
B1	3500	6000	3 No.6	0	-	113	882	0,011	Dowels pullout
B2	3500	6000	6 No.6	0	-	130	1015	0,019	Dowels pullout
B3	3500	6000	None	1000	0,29	254	1984	0,015	Aggregate interlock
B4	3500	6000	None	1500	0,43	291	2273	0,020	Aggregate interlock
B5	3500	6000	3 No.6	1000	0,29	264	2062	0,021	Aggregate interlock
B6	3500	6000	6 No.6	1000	0,29	274	2140	0,014	Aggregate interlock
B7:	3500	6000	3 No.6	0	-	52	406	0,070	Interface grout
B8:	3500	6000	3 No.6	1000	0,29	102	796	0,160	Interface grout
B9	3500	6000	3 No.6	350	0,10	167	1304	0,016	Dowels pullout

$^*f'_c$ of existing concrete.

$^+$Indicates monotonic loading.

:Indicates grouted (dry-packed) interface.

Table 3.4: Test measurements (peak shear capacity, interface displacements and failure mode) [ACI Committee 318, 1995]

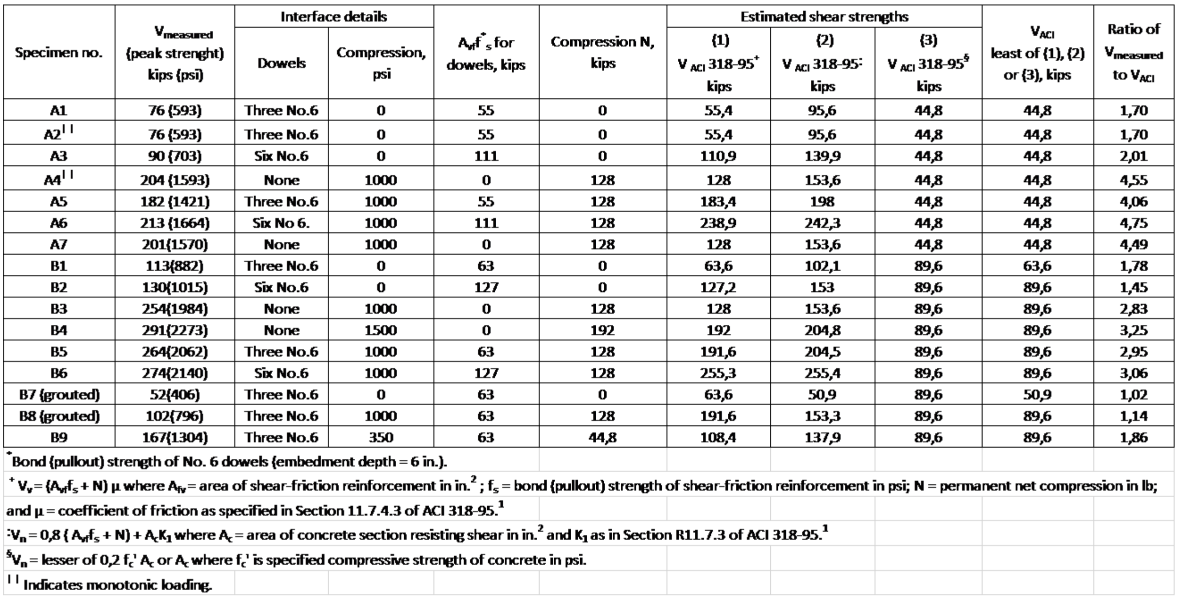

Specimen no.	$V_{measured}$ (peak strenght) kips (psi)	Interface details		$A_{vf}f^*_s$ for dowels, kips	Compression N, kips	Estimated shear strengths			V_{ACI} least of (1), (2) or (3), kips	Ratio of $V_{measured}$ to V_{ACI}
		Dowels	Compression, psi			(1) V_{ACI} 318-95$^+$ kips	(2) V_{ACI} 318-95: kips	(3) V_{ACI} 318-95§ kips		
A1	76 (593)	Three No.6	0	55	0	55,4	95,6	44,8	44,8	1,70
A2$^{\vert\vert}$	76 (593)	Three No.6	0	55	0	55,4	95,6	44,8	44,8	1,70
A3	90 (703)	Six No.6	0	111	0	110,9	139,9	44,8	44,8	2,01
A4$^{\vert\vert}$	204 (1593)	None	1000	0	128	128	153,6	44,8	44,8	4,55
A5	182 (1421)	Three No.6	1000	55	128	183,4	198	44,8	44,8	4,06
A6	213 (1664)	Six No 6.	1000	111	128	238,9	242,3	44,8	44,8	4,75
A7	201(1570)	None	1000	0	128	128	153,6	44,8	44,8	4,49
B1	113(882)	Three No.6	0	63	0	63,6	102,1	89,6	63,6	1,78
B2	130(1015)	Six No.6	0	127	0	127,2	153	89,6	89,6	1,45
B3	254(1984)	None	1000	0	128	128	153,6	89,6	89,6	2,83
B4	291(2273)	None	1500	0	192	192	204,8	89,6	89,6	3,25
B5	264(2062)	Three No.6	1000	63	128	191,6	204,5	89,6	89,6	2,95
B6	274(2140)	Six No.6	1000	127	128	255,3	255,4	89,6	89,6	3,06
B7 (grouted)	52(406)	Three No.6	0	63	0	63,6	50,9	89,6	50,9	1,02
B8 (grouted)	102(796)	Three No.6	1000	63	128	191,6	153,3	89,6	89,6	1,14
B9	167(1304)	Three No.6	350	63	44,8	108,4	137,9	89,6	89,6	1,86

*Bond (pullout) strength of No. 6 dowels (embedment depth = 6 in.).

$^+$ $V_v = (A_{vf}f_s + N)\,\mu$ where A_{fv} = area of shear-friction reinforcement in in.^{2}; f_s = bond (pullout) strength of shear-friction reinforcement in psi; N = permanent net compression in lb; and μ = coefficient of friction as specified in Section 11.7.4.3 of ACI 318-95.[1]

:$V_n = 0{,}8\,(A_{vf}f_s + N) + A_cK_1$ where A_c = area of concrete section resisting shear in in.^{2} and K_1 as in Section R11.7.3 of ACI 318-95.[1]

$^§V_n$ = lesser of 0,2 f_c' A_c or A_c where f_c' is specified compressive strength of concrete in psi.

$^{\vert\vert}$ Indicates monotonic loading.

Table 3.5: Results and comparison between experiments and ACI provisions [ACI Committee 318, 1995]

especially when the shear planes are subjected to permanent compression. In American code [ACI Committee 318, 2008] the friction coefficient does not depend on surface preparation and has the value 0.6. The indented interface involves coefficient 1.0 which was considered as appropriate in tests done by [Valluvan et al., 1999].

3.5 Summary

All codes dedicated to the design of composite reinforced concrete structures allow one to treat a composite member as homogeneous cross-section if the contact zone is properly formed and the conditions for longitudinal shear strength are met. Structures made of elements with different strengths should be transformed into homogeneous cross-section according to properly chosen ratio of their design strengths. Majority of the models are based on the phenomenon called shear friction which occurs when there is a movement in the contact zone according to the shear stress direction, which implies opening of the contact interface in the case of surface irregularity. The stitching reinforcement is then in tension while compressive stresses in concrete additionally increase friction. The horizontal shear capacity depends on preparation of the contact surface, its roughness, types of materials connected (strength, age), and the area of reinforcement resisting the horizontal shear [Tan et al., 1999].

4 Finite element formulation of interface elements

4.1 Introduction and interpolation

Interface elements are widely used for modelling mechanical behaviour of discontinuity zones in various structures, especially in composite structures which are made of two or more materials with different mechanical properties (strength, stiffness) and rheological properties. There is a large number of phenomena occurring in connection zones which can be represented by interface elements in the finite element analysis, such as discrete cracking (including crack dilatancy), bond slip, dowel action, aggregate interlock or friction [Schellekens, 1990, de Borst et al., 2012]. Especially in the case when failure of the contact zone has a significant influence and the zone is comparable in dimensions with the structure, a cohesive-zone model should be used to simulate properly the interface response. In such cases interface elements should be implemented in the finite element mesh during the initial stage of modelling of the structure. Inserting interface elements into connection zones can capture the kinematics of the failure mode in a proper way [Schellekens and de Borst, 1993, de Borst et al., 2012]. More information about interface elements and examples of computational modelling of interface phenomena can be found in [Bfer, 1985, Rots, 1988, Schellekens, 1990, Gens et al., 1989, Pantano and Averill, 2007, Wisnom, 2010, de Borst, 2018, de Borst, 2018].

Interface elements can be divided into two classes. In the first class, continuous interface elements in the form of a line or surface are formulated and nodal or point elements belong to the second class. In fact, the second class elements are identical to spring elements [Schellekens, 1992]. General finite element formulation is applied to describe interface elements, but usually zero thickness is assumed. According to the definition of interface element with zero thickness, penalty stiffness should be assigned to the interface element which can cause numerical problems [Midas IT, 2020].

Interface elements are introduced into a finite element mesh to represent the following relationship between the relative displacement vector $\boldsymbol{\Delta u}$, stiffness matrix $\mathbf{D}_I$ and traction vector $\boldsymbol{t}$

$$\boldsymbol{t} = \boldsymbol{D}_I \boldsymbol{\Delta u} \tag{4.1}$$

For a two-dimensional problem the traction, the stiffness matrix and relative displacement are expressed as:

$$\boldsymbol{t}=\begin{bmatrix} t_n \\ t_t \end{bmatrix}, \quad \boldsymbol{D}_I=\begin{bmatrix} k_n & 0 \\ 0 & k_t \end{bmatrix}, \quad \boldsymbol{\Delta u}=\begin{bmatrix} \Delta u_n \\ \Delta u_t \end{bmatrix} \tag{4.2}$$

For a three–dimensional model they are as follows:

$$\boldsymbol{t}=\begin{bmatrix} t_n \\ t_s \\ t_t \end{bmatrix}, \quad \boldsymbol{D}_I=\begin{bmatrix} k_n & 0 & 0 \\ 0 & k_s & 0 \\ 0 & 0 & k_t \end{bmatrix}, \quad \boldsymbol{\Delta u}=\begin{bmatrix} \Delta u_n \\ \Delta u_s \\ \Delta u_t \end{bmatrix} \tag{4.3}$$

where t_n is the normal traction, t_s and t_t are tangential tractions. The same indices are used for relative displacements. It should be noted that the relationships between respective tractions and displacements are for simplicity fully uncoupled. The relative displacement vector at an integration point is computed by dividing the interface element into upper and lower parts (nodes, faces). The displacements of the top nodes are denoted by:

$$\boldsymbol{u}_{\boldsymbol{i}}^{\mathrm{t}}=\left[u_i^{\mathrm{t}} \;\; v_i^{\mathrm{t}} \;\; w_i^{\mathrm{t}}\right]^T \tag{4.4}$$

The displacements and coordinates within the element are expressed as:

$$\begin{gathered} \boldsymbol{u}^{\mathrm{t}}=\sum_{i=1}^{W} N_i^{\mathrm{t}} u_i^{\mathrm{t}}, \quad \boldsymbol{v}^{\mathrm{t}}=\sum_{i=1}^{W} N_i^{\mathrm{t}} v_i^{\mathrm{t}}, \quad \boldsymbol{w}^{\mathrm{t}}=\sum_{i=1}^{W} N_i^{\mathrm{t}} w_i^{\mathrm{t}} \\ \boldsymbol{x}^{\mathrm{t}}=\sum_{i=1}^{W} N_i^{\mathrm{t}} x_i^{\mathrm{t}}, \quad \boldsymbol{y}^{\mathrm{t}}=\sum_{i=1}^{W} N_i^{\mathrm{t}} y_i^{\mathrm{t}}, \quad \boldsymbol{z}^{\mathrm{t}}=\sum_{i=1}^{W} N_i^{\mathrm{t}} z_i^{\mathrm{t}} \end{gathered} \tag{4.5}$$

where N_i denotes the shape function for node i and W is the number of nodes on one side of the interface. The displacements and coordinates of the bottom nodes of interface elements are denoted in the same way by replacing superscript “t” with “b”.

The nodal displacements of an interface element are defined according to its local coordinates system, on the other hand the relative displacements and tractions at integration points are defined in normal and tangential directions of the interface element. It should be taken into account that if the elements do not transmit a rotational stiffness, only the relative displacements in the local coordinate system are used to compute the relative displacement [Midas IT, 2020]:

$$\Delta \boldsymbol{u}=\boldsymbol{u}^{\mathrm{t}}-\boldsymbol{u}^{\mathrm{b}} \tag{4.6}$$

where:

$$\boldsymbol{u}^{\mathbf{t}}=\left[u_n^{\mathrm{t}} \;\; u_s^{\mathrm{t}} \;\; u_t^{\mathrm{t}}\right]^T, \quad \boldsymbol{u}^{\mathbf{b}}=\left[u_n^{\mathrm{b}} \;\; u_s^{\mathrm{b}} \;\; u_t^{\mathrm{b}}\right]^T \tag{4.7}$$

4.2 Point interface element

The definition of a point interface element which is identical with a spring element is given by top and bottom nodes and the element axes at the boundary surface. In Fig. 4.1 a point interface element is shown with two nodes separately to clarify its definition. Actually, the top and bottom nodes can lie at the same position which should be carefully taken into account when assigning the interface element to both sides of the material joint.

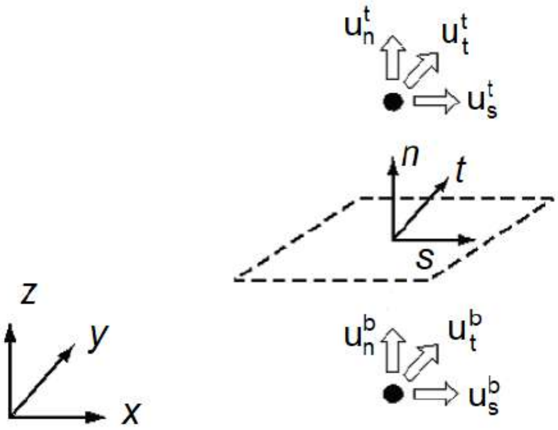

Fig. 4.1: Point interface element [Midas IT, 2020]

The global coordinates of a point in an element are defined using the shape functions given below:

$$\boldsymbol{x}^{\mathrm{b}} = N_1^{\mathrm{b}} \cdot x_1^{\mathrm{b}}, \quad \boldsymbol{x}^{\mathrm{t}} = N_2^{\mathrm{t}} \cdot x_2^{\mathrm{t}} \tag{4.8}$$

The total displacements at nodes t and b are defined using isoparametric shape functions:

$$\boldsymbol{u}^{\mathrm{b}} = N_1^{b} \cdot u_1^{\mathrm{b}}, \quad \boldsymbol{u}^{\mathrm{t}} = N_2^{t} \cdot u_2^{\mathrm{t}} \tag{4.9}$$

The shape function for a point interface element is formally given by:

$$N_1^{\mathrm{b}} = N_2^{\mathrm{t}} = 1 \tag{4.10}$$

The relative displacement matrix for a point interface element can be expressed as:

$$\boldsymbol{B} = \begin{bmatrix} -N_1^{\mathrm{b}} & 0 & 0 & N_2^{t} & 0 & 0 \end{bmatrix} \tag{4.11}$$

4.3 Line interface element

The next class of interface elements are line elements (Fig. 4.2) which are numerically integrated. This kind of elements finds application in plane-stress, plain-strain, axisymmetric and bond slip simulations [Schellekens, 1990]. Line interface elements can be formulated with different orders of interpolation functions [Midas IT, 2020] (linear, quadratic or cubic).

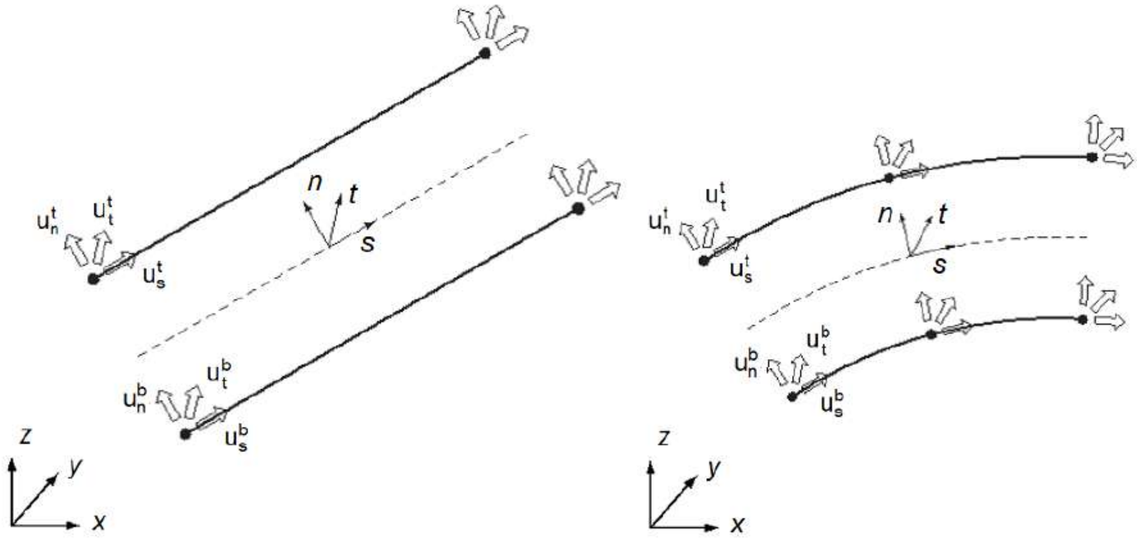

Fig. 4.2: Line interface elements [Midas IT, 2020]

The stiffness matrix for a line interface element is identical with point element matrix. The global coordinate of a point in a line interface element is defined by shape functions given below:

$$\begin{aligned} \mathrm{x}^{\mathrm{b}} &= N_1^{\mathrm{b}} \cdot x_1^{\mathrm{b}} + N_2^{\mathrm{b}} \cdot x_2^{\mathrm{b}} (+N_5^{\mathrm{b}} \cdot x_5^{\mathrm{b}}) \\ \mathrm{x}^{\mathrm{t}} &= N_3^{\mathrm{t}} \cdot x_3^{\mathrm{t}} + N_4^{\mathrm{t}} \cdot x_4^{\mathrm{t}} (+N_6^{\mathrm{t}} \cdot x_6^{\mathrm{t}}) \\ \mathrm{y}^{\mathrm{b}} &= N_1^{\mathrm{b}} \cdot y_1^{\mathrm{b}} + N_2^{\mathrm{b}} \cdot y_2^{\mathrm{b}} (+N_5^{\mathrm{b}} \cdot y_5^{\mathrm{b}}) \\ \mathrm{y}^{\mathrm{t}} &= N_3^{\mathrm{t}} \cdot y_3^{\mathrm{t}} + N_4^{\mathrm{t}} \cdot y_4^{\mathrm{t}} (+N_6^{\mathrm{t}} \cdot y_6^{\mathrm{t}}) \end{aligned} \tag{4.12}$$

The terms in parentheses are for a quadratic element.

The total displacement at a point is given by:

$$
\begin{aligned}
\mathrm{u}^{\mathrm{b}} &= N_1^{\mathrm{b}} \cdot u_1^{\mathrm{b}} + N_2^{\mathrm{b}} \cdot u_2^{\mathrm{b}} (+ N_5^{\mathrm{b}} \cdot u_5^{\mathrm{b}}) \\
\mathrm{u}^{\mathrm{t}} &= N_3^{\mathrm{t}} \cdot u_3^{\mathrm{t}} + N_4^{\mathrm{t}} \cdot u_4^{\mathrm{t}} (+ N_6^{\mathrm{t}} \cdot u_6^{\mathrm{t}}) \\
\mathrm{v}^{\mathrm{b}} &= N_1^{\mathrm{b}} \cdot v_1^{\mathrm{b}} + N_2^{\mathrm{b}} \cdot v_2^{\mathrm{b}} (+ N_5^{\mathrm{b}} \cdot v_5^{\mathrm{b}}) \\
\mathrm{v}^{\mathrm{t}} &= N_3^{\mathrm{t}} \cdot v_3^{\mathrm{t}} + N_4^{\mathrm{t}} \cdot v_4^{\mathrm{t}} (+ N_6^{\mathrm{t}} \cdot v_6^{\mathrm{t}})
\end{aligned}
\tag{4.13}
$$

where nodes 5 and 6 are relevant for higher order elements.

The shape functions for a lower order line interface element are defined by:

$$
\begin{aligned}
N_1^{\mathrm{b}}(\xi) &= N_3^{\mathrm{t}}(\xi) = \tfrac{1}{2}(1-\xi) \\
N_2^{\mathrm{b}}(\xi) &= N_4^{\mathrm{t}}(\xi) = \tfrac{1}{2}(1+\xi)
\end{aligned}
\tag{4.14}
$$

where $\xi \in [-1, 1]$ is the coordinate in a parent element according to isoparametric mapping. The shape functions for the quadratic line interface element are defined by:

$$
\begin{aligned}
N_1^{\mathrm{b}}(\xi) &= N_3^{\mathrm{t}}(\xi) = -\tfrac{1}{2}(1-\xi)\,\xi \\
N_2^{\mathrm{b}}(\xi) &= N_4^{\mathrm{t}}(\xi) = \tfrac{1}{2}(1+\xi)\,\xi \\
N_5^{\mathrm{b}}(\xi) &= N_6^{\mathrm{t}}(\xi) = (1-\xi^2)
\end{aligned}
\tag{4.15}
$$

4.4 Surface interface element

The most sophisticated interface elements are surface elements (plate, shell). These elements are used in combination with solids (solid-solid interaction) and shells (shell-solid interaction), [Schellekens, 1990, Midas IT, 2020]. Surface elements are divided into triangular and quadrilateral ones (lower or higher order), see Fig. 4.3.

The total displacements of an arbitrary point in a quadrilateral element are defined by isoparametric shape functions as specified in Appendix B [Midas IT, 2020].

4.5 FEM equations for interface elements

According to Eq. (4.1) the tractions in the local coordinate system are derived from relative displacements in the local coordinate system of the interface element and the stiffness matrix. There are two ways in which the stiffness matrix of line and plane interface elements can be computed, by Gaussian or by lumped integration. In the former case of numerically integrated interface elements the traction-relative displacement relation is calculated from the interpolated displacement field at the integration

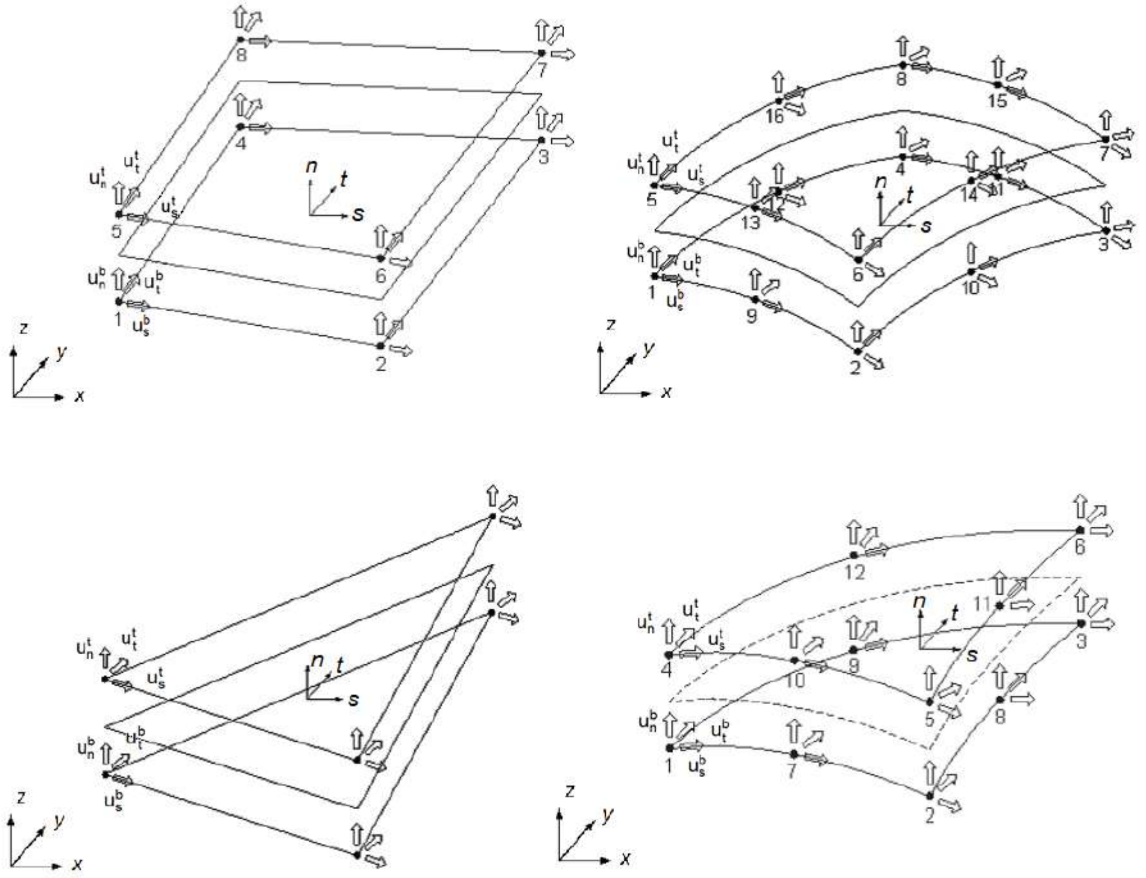

Fig. 4.3: Surface interface elements [Midas IT, 2020]

points. The evaluation of the relation for node pairs is needed for lumped integrated interface elements [Schellekens, 1992, Schellekens, 1990, Schipperen, 2001].

With normal direction (n) and directions tangential to the interface surface (s and t) this leads to continuous displacement field with indication for t (*“t”*) and bottom (*“b”*) side of the interface element:

$$\boldsymbol{u} = \left({u_n}^{\mathrm{b}}, {u_n}^{\mathrm{t}}, {u_s}^{\mathrm{b}}, {u_s}^{\mathrm{t}}, {u_t}^{\mathrm{b}}, {u_t}^{\mathrm{t}}\right)^T \tag{4.16}$$

When considering multi-node line or surface interface element, each node has three translational degrees of freedom in a 3D configuration. It is possible to build the element nodal displacement vector

$$\underline{\boldsymbol{a}} = (a^{\mathrm{b}}_{n1}, a^{\mathrm{b}}_{n2}, ..., a^{\mathrm{b}}_{nW}, a^{\mathrm{b}}_{s1}, a^{\mathrm{b}}_{s2}, ..., a^{\mathrm{b}}_{sW}, a^{\mathrm{b}}_{t1}, a^{\mathrm{b}}_{t2}, ..., a^{\mathrm{b}}_{tW}; \tag{4.17}$$

$$a^{\mathrm{t}}_{n1}, a^{\mathrm{t}}_{n2}, ..., a^{\mathrm{t}}_{nW}, a^{\mathrm{t}}_{s1}, a^{\mathrm{t}}_{s2}, ..., a^{\mathrm{t}}_{sW}, a^{\mathrm{t}}_{t1}, a^{\mathrm{t}}_{t2}, ..., a^{\mathrm{t}}_{tW})^T \tag{4.18}$$

where W denotes the number of node pairs *“b”* and *“t”*.

Using matrix $\boldsymbol{H}$ containing interpolation polynomials:

$$\boldsymbol{H} = \begin{bmatrix} \boldsymbol{h} & \mathbf{0} & \mathbf{0} & \mathbf{0} & \mathbf{0} & \mathbf{0} \\ \mathbf{0} & \boldsymbol{h} & \mathbf{0} & \mathbf{0} & \mathbf{0} & \mathbf{0} \\ \mathbf{0} & \mathbf{0} & \boldsymbol{h} & \mathbf{0} & \mathbf{0} & \mathbf{0} \\ \mathbf{0} & \mathbf{0} & \mathbf{0} & \boldsymbol{h} & \mathbf{0} & \mathbf{0} \\ \mathbf{0} & \mathbf{0} & \mathbf{0} & \mathbf{0} & \boldsymbol{h} & \mathbf{0} \\ \mathbf{0} & \mathbf{0} & \mathbf{0} & \mathbf{0} & \mathbf{0} & \boldsymbol{h} \end{bmatrix} \tag{4.19}$$

where $\boldsymbol{h}$ is a matrix with size 1xW, the continuous displacement field $\boldsymbol{u}$ is connected with nodal displacement vector $\boldsymbol{a}$ as follows:

$$\boldsymbol{u} = \boldsymbol{Ha} \tag{4.20}$$

It is necessary to introduce the operator matrix:

$$\boldsymbol{L} = \begin{bmatrix} -1 & +1 & 0 & 0 & 0 & 0 \\ 0 & 0 & -1 & +1 & 0 & 0 \\ 0 & 0 & 0 & 0 & -1 & +1 \end{bmatrix} \tag{4.21}$$

to build a relation between the continuous displacement field and relative displacement vector $\boldsymbol{\Delta u}$ as follows:

$$\boldsymbol{\Delta u} = \boldsymbol{Lu} \tag{4.22}$$

The relation between the nodal displacements and the relative displacement is derived as:

$$\boldsymbol{\Delta u} = \boldsymbol{LHa} = \boldsymbol{B_I a} \tag{4.23}$$

Matrix $\mathbf{B}_I$ represents the relationship between the relative displacement and the nodal displacement vector:

$$\boldsymbol{B}_I = \begin{bmatrix} -\boldsymbol{h} & \boldsymbol{h} & \mathbf{0} & \mathbf{0} & \mathbf{0} & \mathbf{0} \\ \mathbf{0} & \mathbf{0} & -\boldsymbol{h} & \boldsymbol{h} & \mathbf{0} & \mathbf{0} \\ \mathbf{0} & \mathbf{0} & \mathbf{0} & \mathbf{0} & -\boldsymbol{h} & \boldsymbol{h} \end{bmatrix} \tag{4.24}$$

For an element which has the local coordinate system defined at the integration points that coincides with the global coordinate system, the transformation is not necessary. In any other case the interface element matrix $\boldsymbol{B}_I$ should be transformed to the local tangential coordinate system [Schellekens, 1992, Schellekens, 1990, Schipperen, 2001].

We recall the equation which describes traction-relative displacement relation:

$$\boldsymbol{t} = \boldsymbol{D}_I \boldsymbol{\Delta u} \tag{4.25}$$

According to the interface element formulation tractions and relative displacements are determined between top and bottom interface sides or surfaces. The orientation of the element sides is a key factor to determine the components of traction and relative displacement vectors. The virtual internal energy is given by:

$$\delta W = \int_{S_0} \delta \boldsymbol{\Delta u}^T \boldsymbol{t} \; \mathrm{d}S_0 \tag{4.26}$$

with S_0 as an initial element surface.

When considering non-linear phenomena in the interface behaviour, the traction vector in the j-th iteration is expressed as:

$$\boldsymbol{t}_j = \boldsymbol{t}_{j-1} + \boldsymbol{D}_I \mathrm{d}\boldsymbol{\Delta u}_j \tag{4.27}$$

In the above equation $\mathrm{d}\boldsymbol{\Delta u}_j$ is the change in the relative displacement vector. Introducing the variation of the internal energy and we obtain

$$\delta(\mathrm{d}\boldsymbol{a}_j)^T \int_{S_0} \boldsymbol{B}_I^T \boldsymbol{D}_I \boldsymbol{B}_I \; \mathrm{d}S_0 \; \mathrm{d}\boldsymbol{a}_j = -\delta(\mathrm{d}\boldsymbol{a}_j)^T \int_{S_0} \boldsymbol{B}_I^T \boldsymbol{t}_{j-1} \; \mathrm{d}S_0 \tag{4.28}$$

Based on the internal strain energy, the stiffness matrix for the interface elements is thus obtained as [Midas IT, 2020]:

$$\boldsymbol{K} = \int_{S_0} \boldsymbol{B}_I{}^T \boldsymbol{D}_I \boldsymbol{B}_I \; \mathrm{d}S_0 \tag{4.29}$$

The internal force vector is given by:

$$\boldsymbol{f}_{j-1} = -\int_{S_0} \boldsymbol{B}_I^T \boldsymbol{t}_{j-1} \; \mathrm{d}S_0 \tag{4.30}$$

After expanding the stiffness matrix into a numerical integration expression and introducing integration over isoparametric coordinates, Eq. (4.29) becomes:

$$\boldsymbol{K} = \int_{\xi=-1}^{\xi=+1} \int_{\eta=-1}^{\eta=+1} \boldsymbol{B}_I{}^{\boldsymbol{T}} \boldsymbol{D}_I \boldsymbol{B}_I \;\; \det \boldsymbol{J} \; \mathrm{d}\xi \; \mathrm{d}\eta \tag{4.31}$$

In the expression above $\det \boldsymbol{J}$ is the determinant of the Jacobian matrix.

Numerical integration gives:

$$\boldsymbol{K} = \sum_{i=1}^{n_i} w_i \det \boldsymbol{J}_i \boldsymbol{B}_{Ii}{}^T \boldsymbol{D}_{Ii} \boldsymbol{B}_{Ii} \tag{4.32}$$

When using 2x2 Gauss quadrature scheme for integration of the element stiffness matrix of a linear 8-noded plane interface with surface S, the stiffness matrix is expressed as:

$$\boldsymbol{K}=\frac{1}{36}S\begin{bmatrix}\boldsymbol{K}_n & \mathbf{0} & \mathbf{0}\\ \mathbf{0} & \boldsymbol{K}_s & \mathbf{0}\\ \mathbf{0} & \mathbf{0} & \boldsymbol{K}_t\end{bmatrix} \tag{4.33}$$

where each of the 8x8 sub-matrices has the form:

$$\boldsymbol{K}_k=\begin{bmatrix}4d_k & 2d_k & d_k & 2d_k & -4d_k & -2d_k & -d_k & -2d_k\\ 2d_k & 4d_k & 2d_k & d_k & -2d_k & -4d_k & -2d_k & -d_k\\ d_k & 2d_k & 4d_k & 2d_k & -d_k & -2d_k & -4d_k & -2d_k\\ 2d_k & d_k & 2d_k & 4d_k & -2d_k & -d_k & -2d_k & -4d_k\\ -4d_k & -2d_k & -d_k & -2d_k & 4d_k & 2d_k & d_k & 2d_k\\ -2d_k & -4d_k & -2d_k & -d_k & 2d_k & 4d_k & 2d_k & d_k\\ -d_k & -2d_k & -4d_k & -2d_k & d_k & 2d_k & 4d_k & 2d_k\\ -2d_k & -d_k & -2d_k & -4d_k & 2d_k & d_k & 2d_k & 4d_k\end{bmatrix} \tag{4.34}$$

for $k = n$, s, and t.

The other option are lumped integrated interface elements, where relative displacements are sampled at W node pairs. Matrix $\boldsymbol{B}_I$ then represents the relative displacement - nodal displacement relation for a node pair.

The summation over element node pairs has the form

$$\boldsymbol{K} = \sum_{i=1}^{W} \boldsymbol{B}_{Ii}^T \boldsymbol{D}_{Ii} \boldsymbol{B}_{Ii} S_i \tag{4.35}$$

where W is a number of node pairs, S_i is the surface contribution of node pair i. Matrix $\boldsymbol{B}_{Ii}$ is then as follows:

$$\boldsymbol{B}_{Ii}=\begin{bmatrix}-1 & +1 & 0 & 0 & 0 & 0\\ 0 & 0 & -1 & +1 & 0 & 0\\ 0 & 0 & 0 & 0 & -1 & +1\end{bmatrix} \tag{4.36}$$

5 Interface behaviour – benchmark and calibration

The results of the numerical analysis of the considered interface behaviour strongly depend on input parameters [Jarno and Pamin, 2017]. The interface models require from the user carefully chosen input data. To avoid over- and under-estimation of the properties of the composite beam, benchmark tests on a very simple geometry are performed. To check and calibrate the interface constitutive description two boxes (solid elements) with plane interface elements between them are modelled. The box dimensions are 30×30×30 cm (Fig. 5.1), the lower box is supported on the whole bottom surface and the upper box is loaded with a pressure load on the front face, the intensity of the load is 1.0 MPa (the load factor will be denoted by p). Different types of interface constitutive models are applied for the interface elements, the input parameters are calibrated and discussed for each case. The material model for the lower and upper boxes is isotropic linear elasticity with the modulus of elasticity equal to 36.9 GPa and 24.4 GPa, respectively, and the Poisson ratio equal to 0.3 for both the boxes.

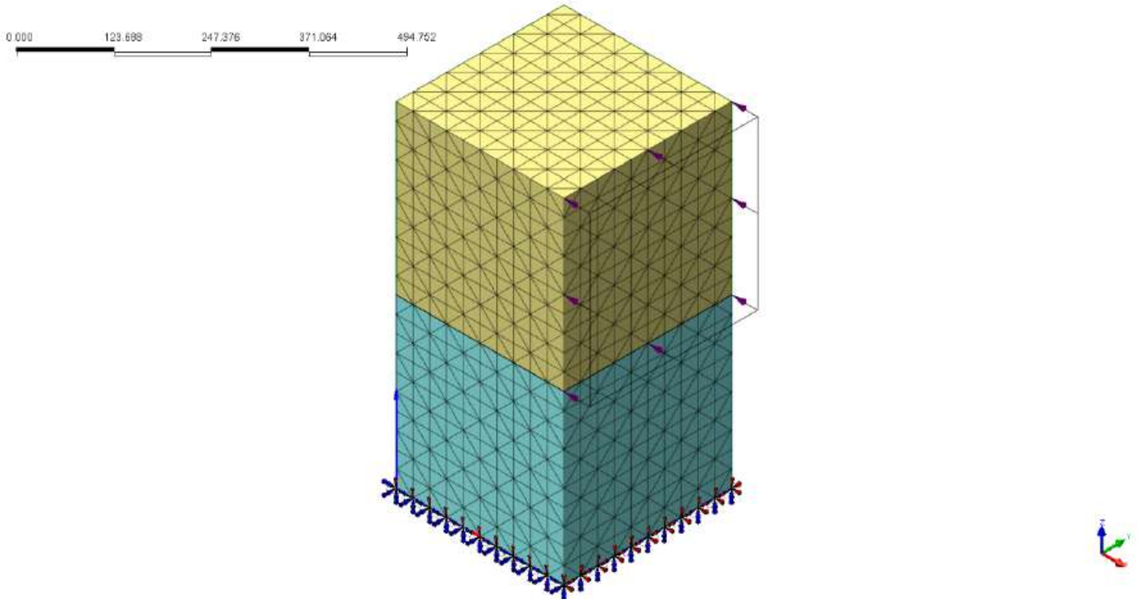

Fig. 5.1: Geometry, boundary conditions, load of benchmark sample

5.1 Coulomb friction model

The interface between two parts of a structure is governed in most cases by a frictional behaviour. This kind of behaviour can be simulated with the Coulomb friction model, which is derived from Mohr-Coulomb plasticity theory for continuum elements. The Coulomb friction behaviour with a tensile cut-off is shown in Fig. 5.2. The model is defined by the yield surface f and the plastic potential surface g:

$$\begin{cases} f = \sqrt{{t_t}^2} + t_n \tan\phi(\kappa) - \bar{c}(\kappa) = 0 \\ g = \sqrt{{t_t}^2} + t_n \tan\psi \end{cases} \tag{5.1}$$

where $\phi(\kappa)$ is the friction angle and $\bar{c}(\kappa)$ is the adhesion, both can be functions of an internal parameter κ. The direction of the irreversible displacements is given by the plastic potential function g where the uplift is determined by the dilatancy angle ψ. When the friction angle is not equal to the dilatancy angle (non-associated flow rule) the tangent stiffness matrix becomes non-symmetric. It is recommended to keep the difference between ϕ and ψ not higher than 20 degrees, otherwise the analysis may fail to converge. The gap value is the tensile strength f_t. The default value corresponds to the apex of the Coulomb friction criterion. The Midas FEA software assumes that a gap arises if the tensile traction t_n normal to the interface exceeds a certain value. After gap formation, t_n is reduced to zero immediately (brittle cracking).

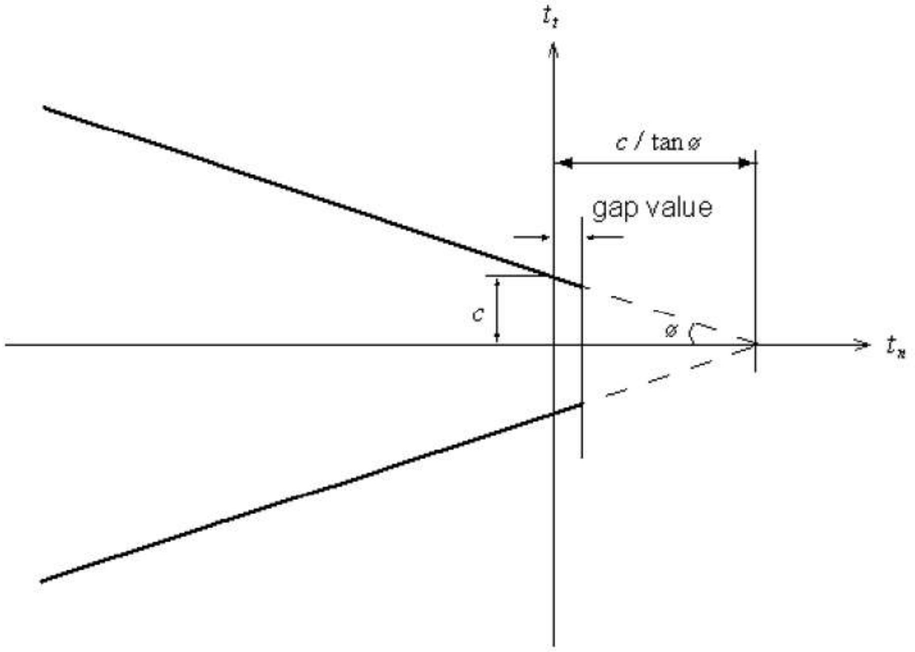

Fig. 5.2: Coulomb friction model [Midas IT, 2020]

For the benchmark test the input parameters for the Coulomb friction model are: normal stiffness modulus k_n = 40000 N/mm^3, shear stiffness modulus k_t = 40000

N/mm^3, adhesion $c = 4$ N/mm^2, internal friction angle $\phi = 30$ degrees, dilatancy angle $\psi = 0$ degrees.

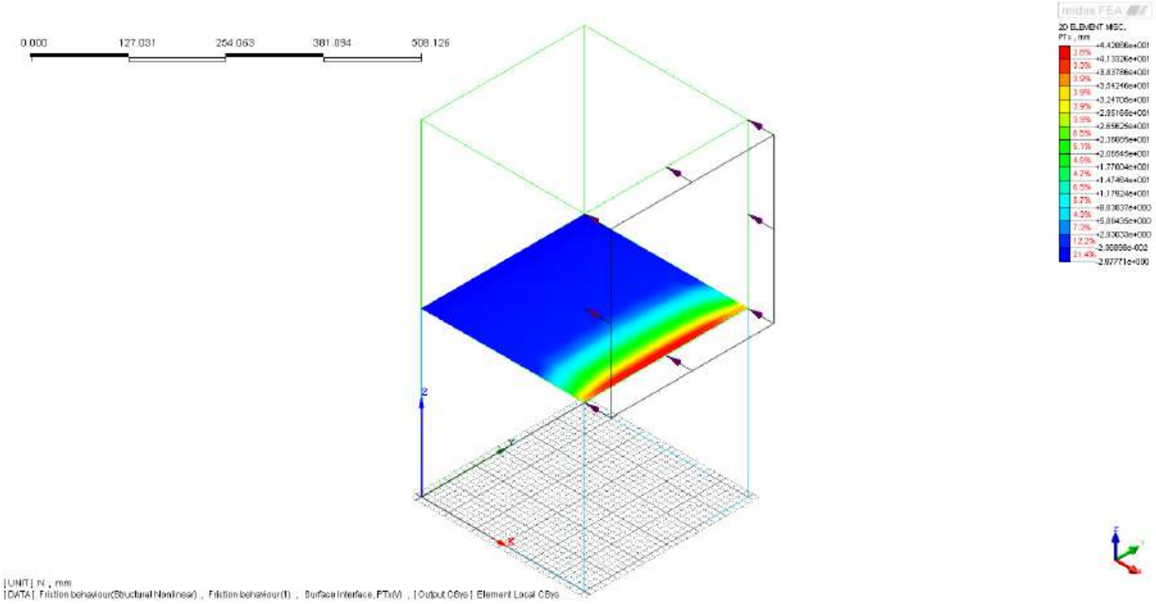

Fig. 5.3: Normal relative displacement Δu_x

In Fig. 5.3 the relative normal displacement plot is shown. Due to very high adhesion between elements there is no non-linear behaviour obtained for the load applied. The interface on the loaded side opens with the normal relative displacement of 4.42 cm. This non-realistic behaviour is the results of adhesion value and the bending character of the deformation which is also shown by very high values of the normal interface stress (Fig. 5.4) as well as the von Mises stress in the solid elements (Fig. 5.5).

The tests performed lead to the conclusion that changing the parameter of adhesion in the Coulomb friction model one could achieve results much closer to those obtained in the laboratory tests. For the composite beam the Coulomb model will be calibrated to calculate the whole structure with realistic results.

Based on the initial calculation, the parameters for a non-linear calculation with the Newton-Raphson method were chosen (load steps scheme, number of increments and iterations). Fig. 5.6 shows total displacement D_{xyz} for the load level equal to 0.592, for which non-linear behaviour occurs just before the slip of surfaces of the interface elements.

Fig. 5.7 shows normal relative displacement for the load level. The next increment of the applied load causes slip behaviour of the interface elements, which is shown in Figures 5.8 and 5.9.

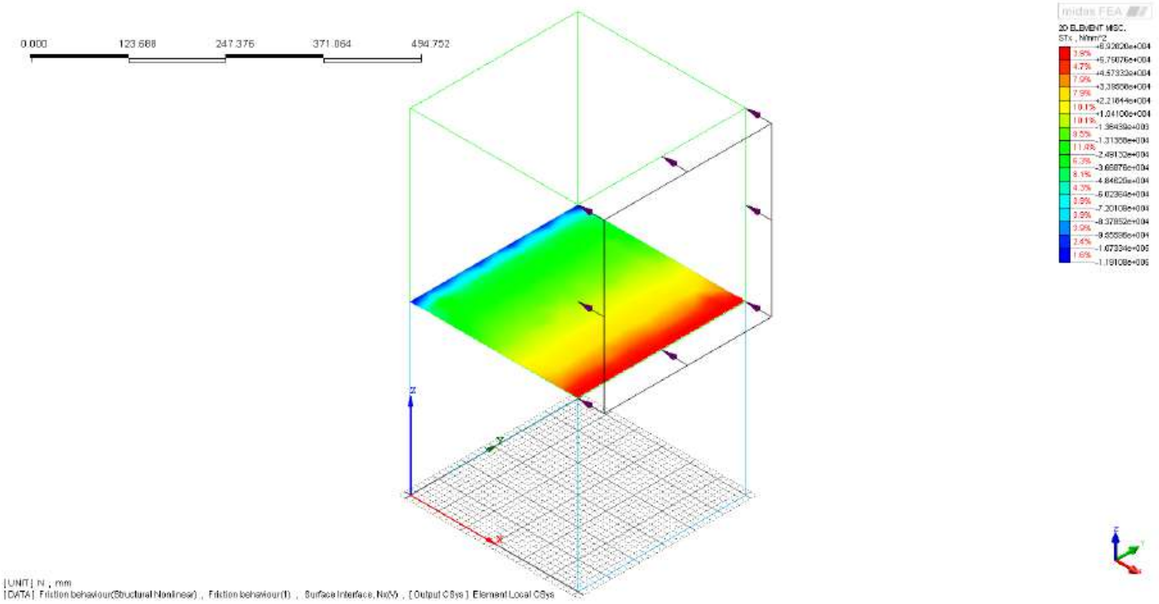

Fig. 5.4: Normal stress t_x in interface elements

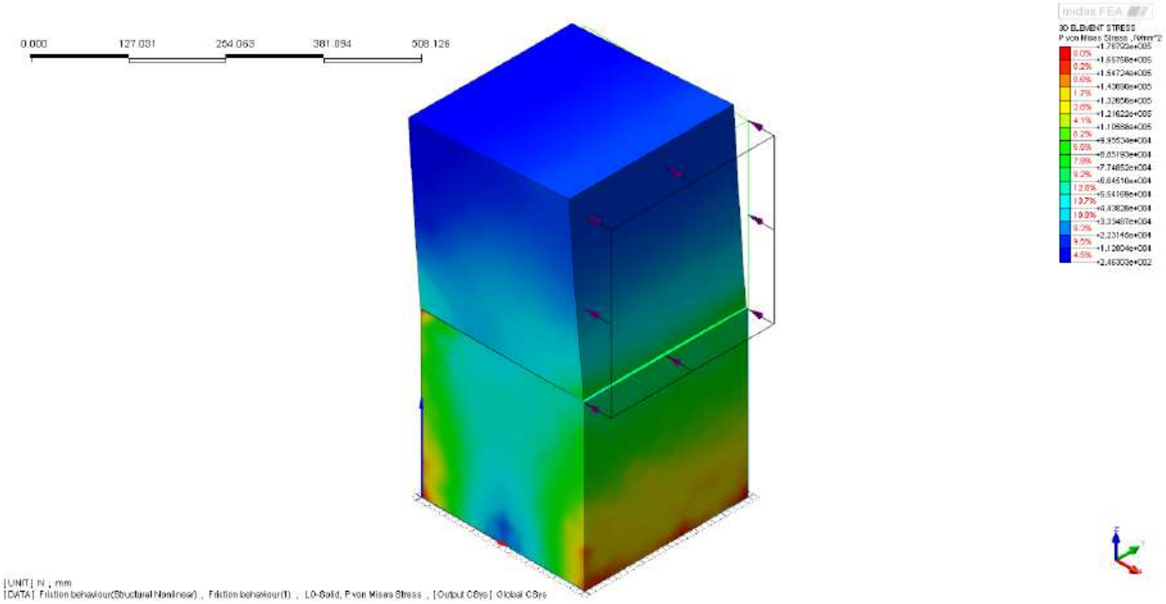

Fig. 5.5: 3D element von Mises stress

Figures 5.10 and 5.11 show the diagrams of load factor p versus the displacement of the node located in the middle of the bottom side of the upper box respectively in x and z directions according to the global coordinate system. The linear behaviour occurs for load factor from 0 to 0.4, from 0.41 to 0.592 non-linear behaviour of the interface elements can be noticed. The range of the load from 0.593 to 0.641 results in a lack of resistance of the interface model which results in the slip behaviour since there are no more bond forces between the boxes.

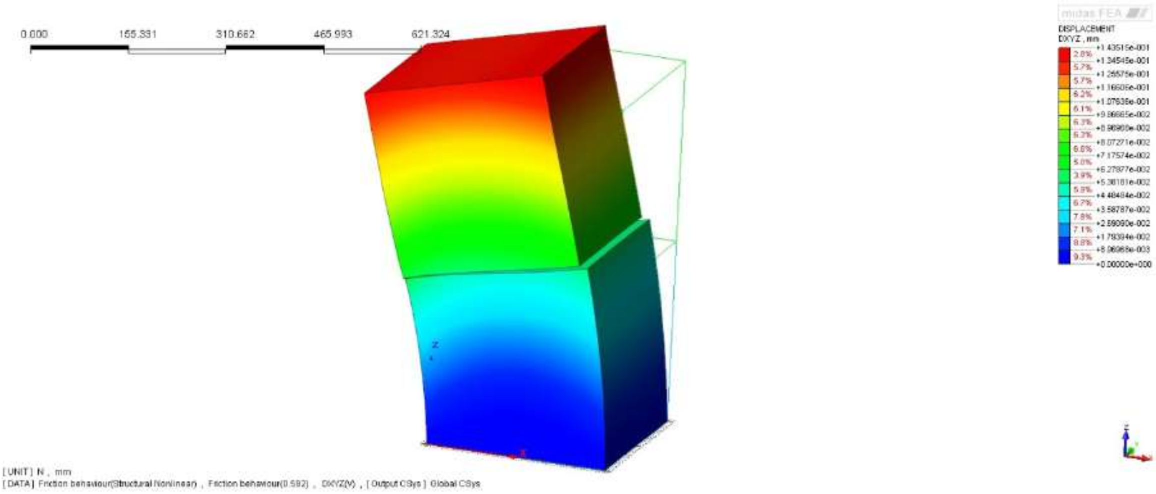

Fig. 5.6: Total displacement D_{xyz}

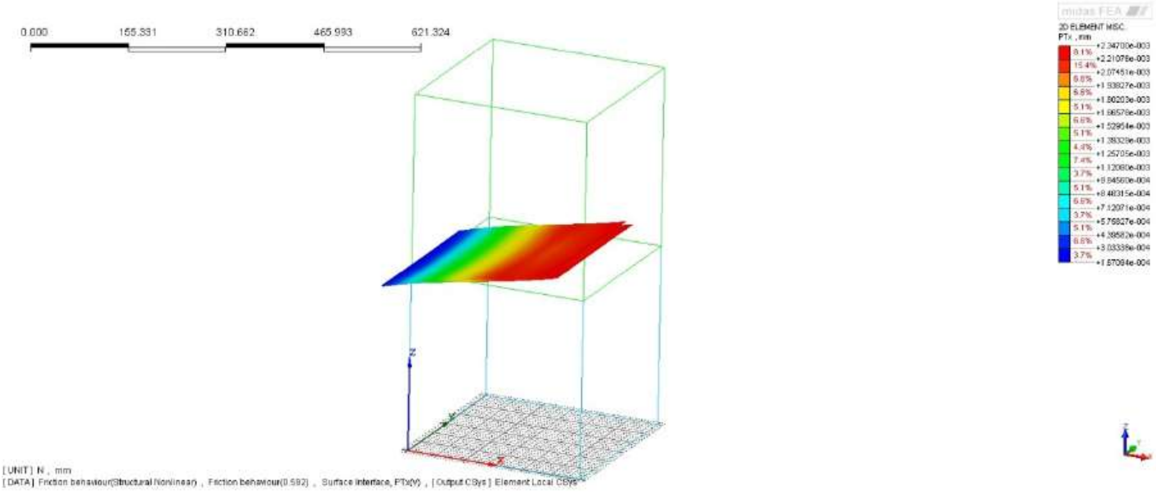

Fig. 5.7: Normal relative displacement Δu_x

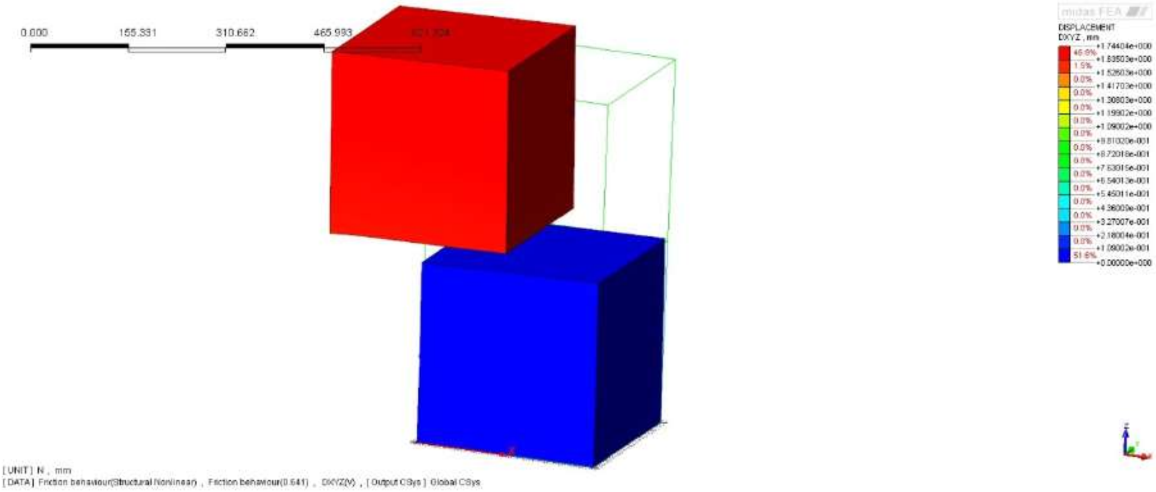

Fig. 5.8: Total displacement D_{xyz}

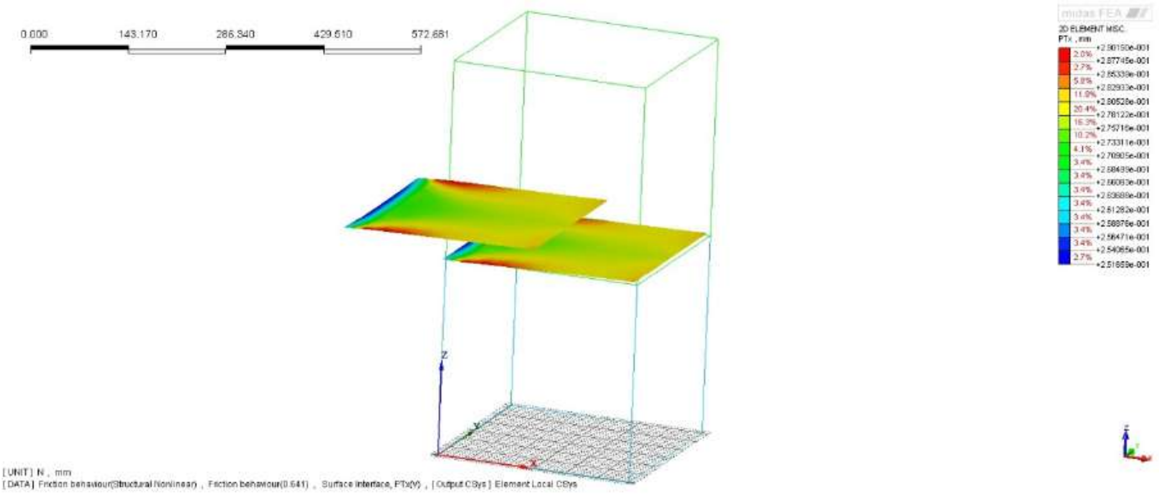

Fig. 5.9: Normal relative displacement Δu_x

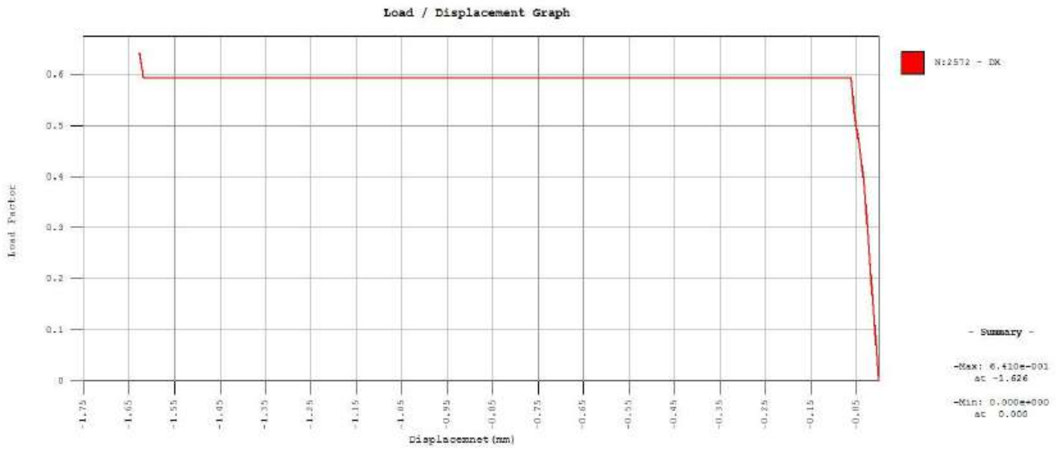

Fig. 5.10: Load vs displacement graph $p(D_x)$

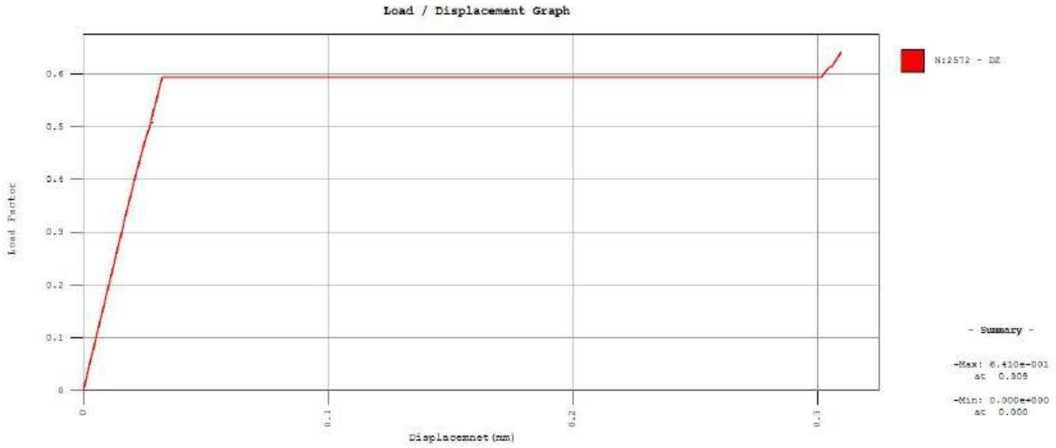

Fig. 5.11: Load vs displacement graph $p(D_z)$

5.2 Aggregate interlock model

A general practice for composite structures is to properly prepare the connected surfaces, for example by using sanding methods. The purpose of this treatment is to reveal coarse aggregate to achieve stronger connection between the two parts. When a shear force is applied to the composite member, adhesion is strengthened by aggregate used in the concrete mixture. This phenomenon is called *aggregate interlock* and it is numerically described for instance by a two-phase Walraven model [Midas IT, 2020]. The Walraven model is based on the assumptions given below:

- concrete is treated as a two-phase material, with plastic matrix and perfectly stiff spherical inclusions,
- the grading of the aggregate corresponds to Fuller's curve [Midas IT, 2020],
- the active contact areas between the inclusions and the matrix are related to interface displacements, while the stochastic character of aggregate distribution is taken into consideration,
- the compressive contact strength of the matrix grows with the concrete strength while the shear contact strength is related to the compressive one by a constant friction coefficient.

The Walraven model is developed for pure aggregate (surfaces not intersected by reinforcing bars). The response diagram is shown in Fig. 5.12. The shear stress and normal stress are obtained when given tangential and normal crack displacements occur.

The model is given by the following relations:

$$\begin{aligned} f_t &= \sigma_{mu}\left(A_n + \mu A_t\right) \\ f_n &= -\sigma_{mu}\left(A_t - \mu A_n\right) \end{aligned} \tag{5.2}$$

where A_n and A_t are the average contact areas in directions n and t between the inclusions and the matrix, σ_{mu} is the compressive strength of the matrix, μ is the friction coefficient between the inclusion and the matrix. The tangential stiffness terms are functions of the tangential crack displacement Δu_t, the normal crack displacement Δu_n and the distribution of the aggregate.

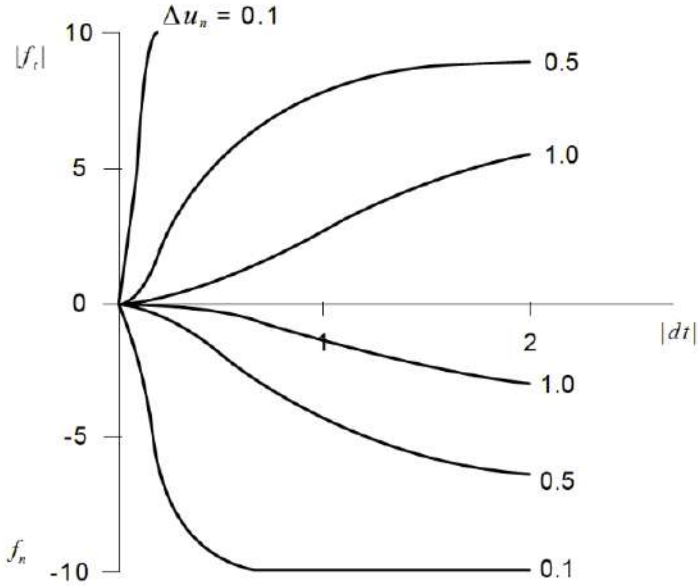

Fig. 5.12: Two-phase Walraven model [Midas IT, 2020] (Δu_t is denoted by dt)

The input parameters for the aggregate interlock model are: normal stiffness modulus k_n= 8000 kN/mm^3, shear stiffness modulus k_t = 4000 kN/mm^3, adhesion c = 4 kN/mm^2, internal friction angle ϕ = 30 degrees, dilatancy angle ψ = 0 degrees, tension cut-off (tensile strength) σ_t = 4 MPa, shear contact strength (compressive strength) σ_c = 40 MPa.

In this case a non-linear static analysis is performed. The results for load factor p=0.1 and p=1 of the applied load are presented. Fig. 5.13 shows the normal relative displacement in the 2D interface elements. The interface opening is 1.43m due to bending and very low value of the normal stiffness of the interface, stress t_n (Fig. 5.14) is too high as well. Figures 5.15 and 5.16 present the normal relative displacement and the normal traction for 100% of the applied load.

Figures 5.17 and 5.18 show the diagrams of load factor p versus the displacement of the node located in the middle of the edge of the upper box respectively in x and z directions according to the global coordinate system for the aggregate interlock interface behaviour. At first the aggregate interlock allows for displacement only in the x direction. When the load factor increases to 1.8, the interface starts to open and the displacement in the z direction occurs as well as the non-linear behaviour of the interface. However, the benchmark test calibration seems to show unrealistic results, hence the aggregate interlock model is not used for the composite beam analysis.

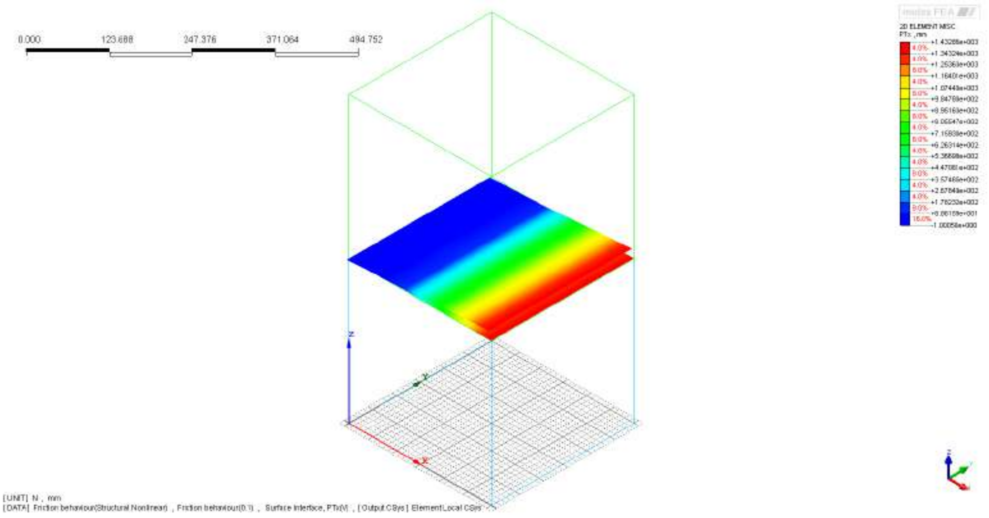

Fig. 5.13: Normal relative displacement Δu_x for load factor p=0.1 of applied load

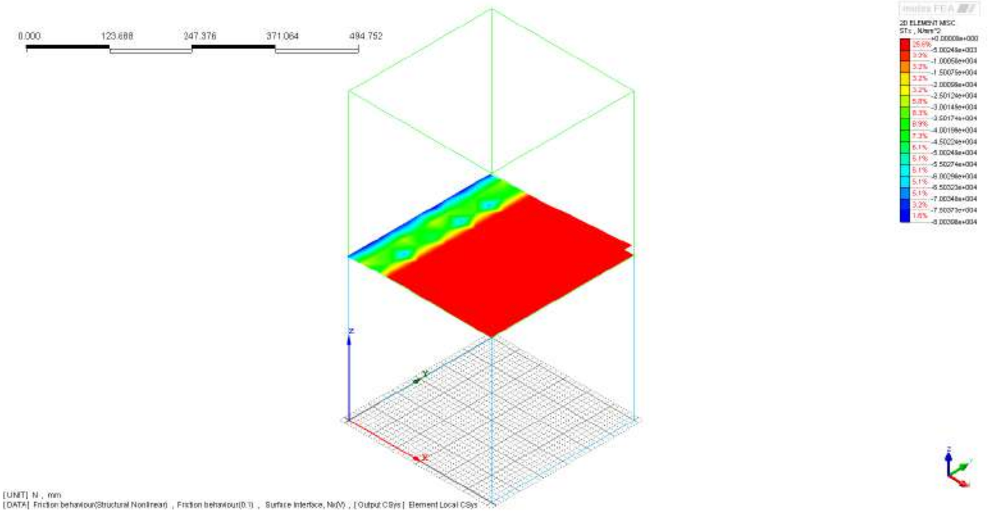

Fig. 5.14: Normal interface traction t_n for load factor p=0.1

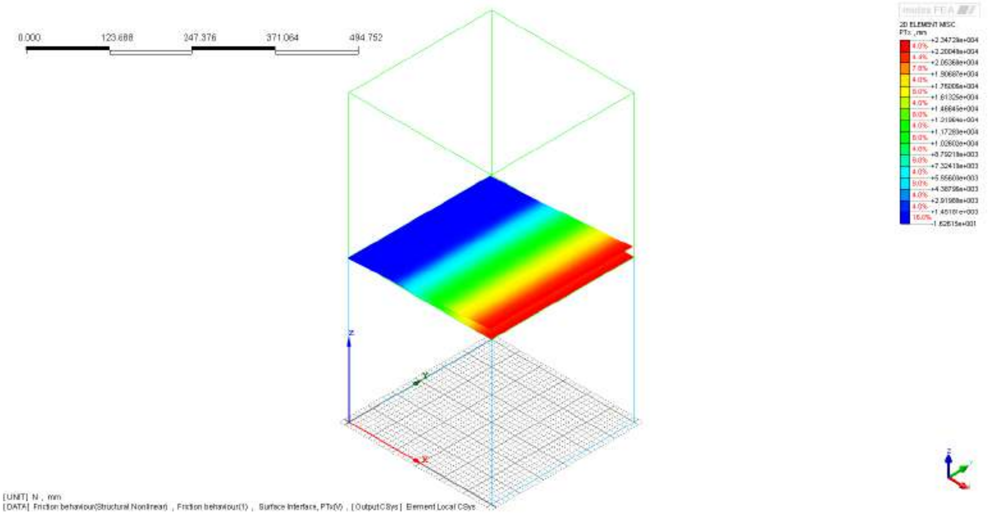

Fig. 5.15: Normal relative displacement Δu_x for load factor p=0.1

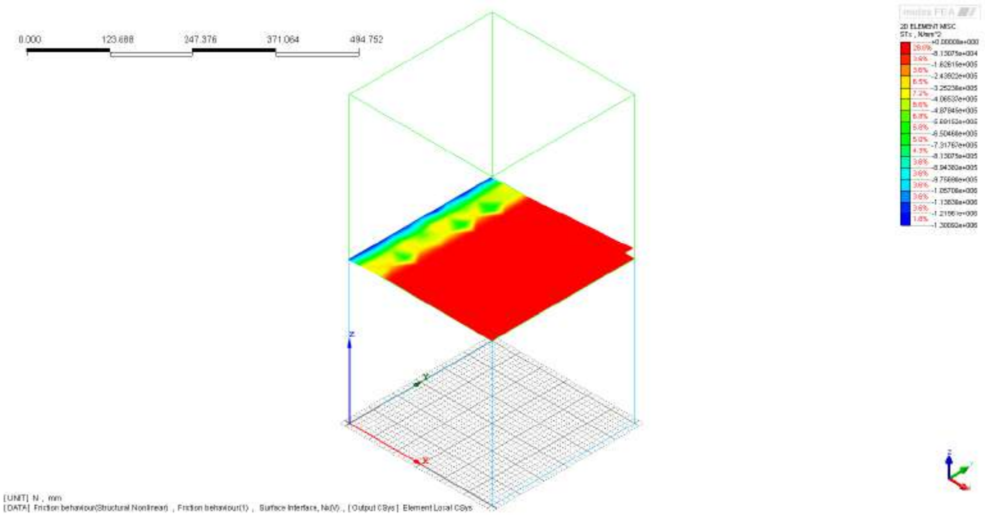

Fig. 5.16: Normal interface traction stress t_n for load factor p=0.1

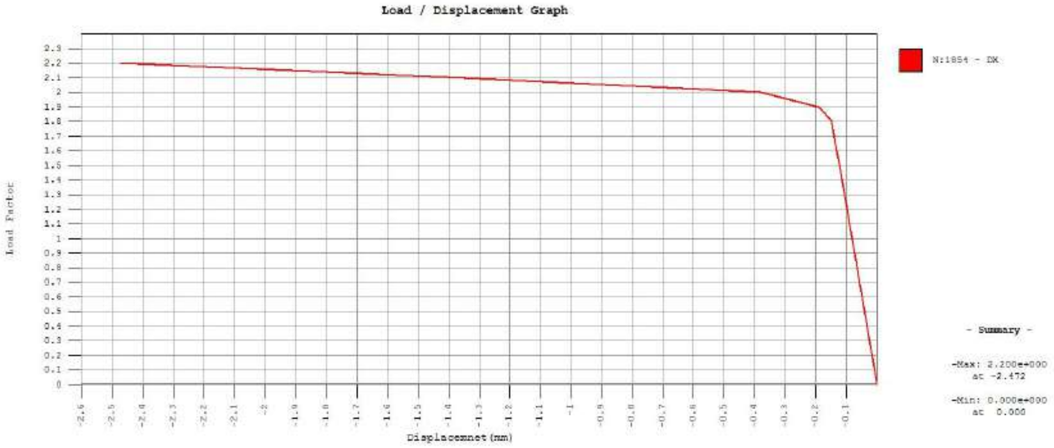

Fig. 5.17: Load factor p versus displacement D_x

Fig. 5.18: Load factor p versus displacement D_y

5.3 Indented connection

The indented connection as a form of contact zone in composite structures was described in Chapter 3. In the benchmark test the geometry of an indented connection is modelled (Fig. 5.19). The connection surface is discretized with plane interface elements, in which the Coulomb friction model is applied. The width and depth of the lock in the bottom box is 10 cm (1/3 of the box width).

The parameters of the Coulomb model are: normal stiffness modulus $k_n = 36900$ N/mm^3, shear stiffness modulus $k_t = 15375$ N/mm^3, adhesion $c = 4$ N/mm^2, internal friction angle $\phi = 15$ degrees, dilatancy angle $\psi = 0$ degrees.

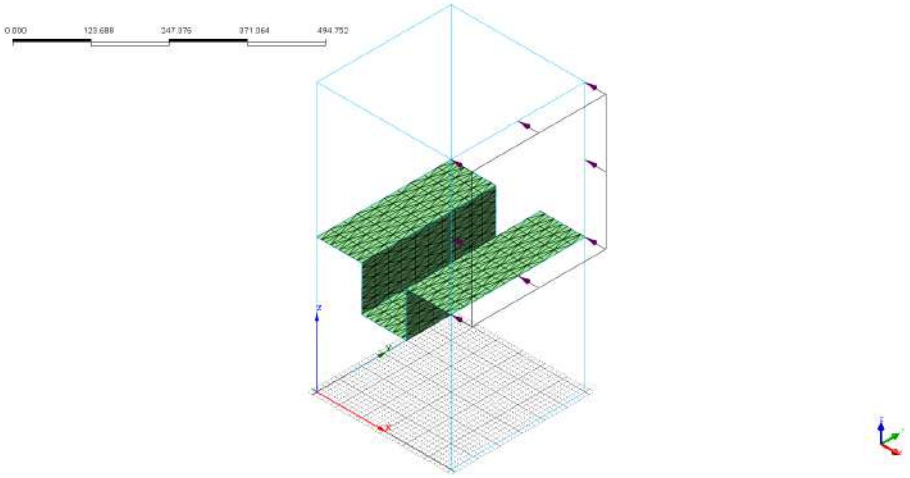

Fig. 5.19: Geometry and mesh of indented connection

The applied load influences the interface elements in normal and tangential directions simultaneously (parts of the interface resist either shear or compression/tension).

Fig. 5.20 shows normal relative displacement Δu_x and the maximum opening in the normal direction is $2.7 \cdot 10^{-5}$ mm on the edge where the load is applied. The values of the displacement, normal interface traction t_n (Fig. 5.21) and 3D element von Mises stress (Fig. 5.22) are quite realistic and they match each other.

Fig. 5.23 shows normal relative displacement of the interface elements for load factor $p = 1.86$, it is a moment in the behaviour just before the slip of the interface surfaces occurs and the interface opens. Figures 5.24 and 5.25 show displacements of the node located in the middle of the lower edge of the upper box in global x and z directions, respectively, for the indented type of the composite connection zone. The range of the load factor from 0 to 0.5 is the linear part of the graphs and then non-linear

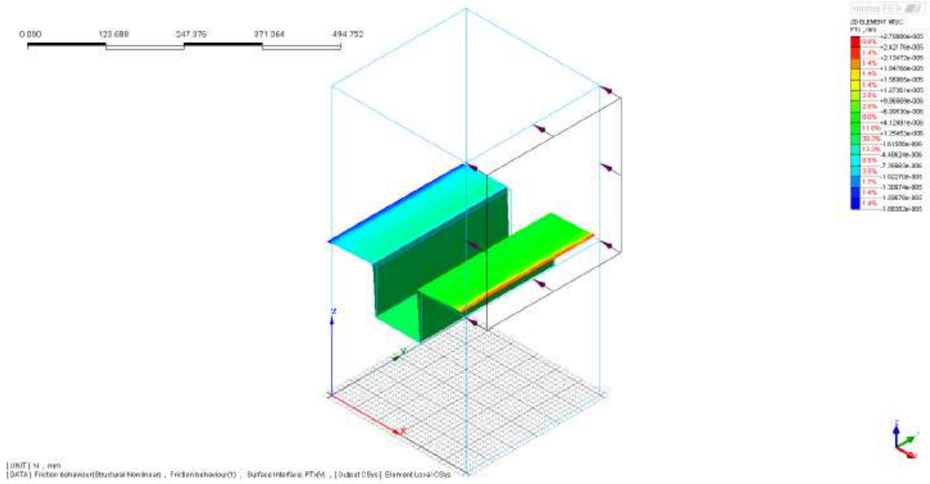

Fig. 5.20: Normal relative displacement Δu_x for load factor p=0.1

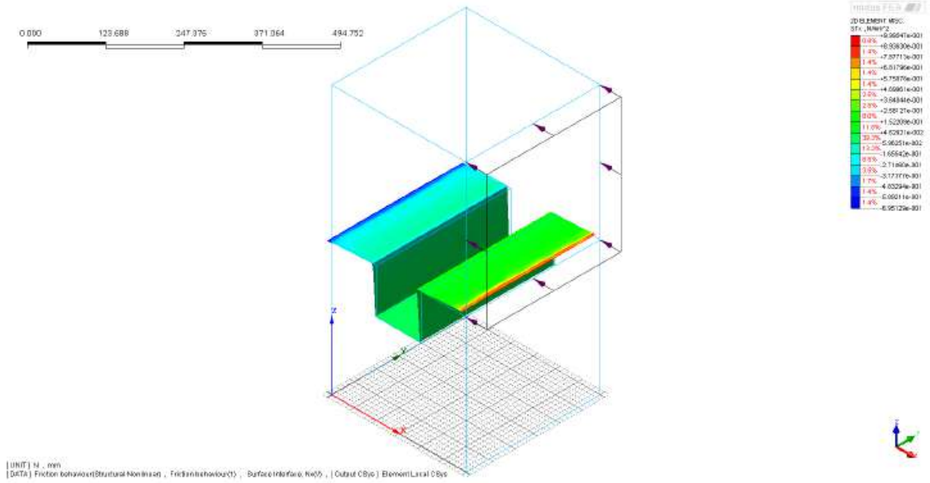

Fig. 5.21: Normal stress t_n in interface elements for load factor p=0.1

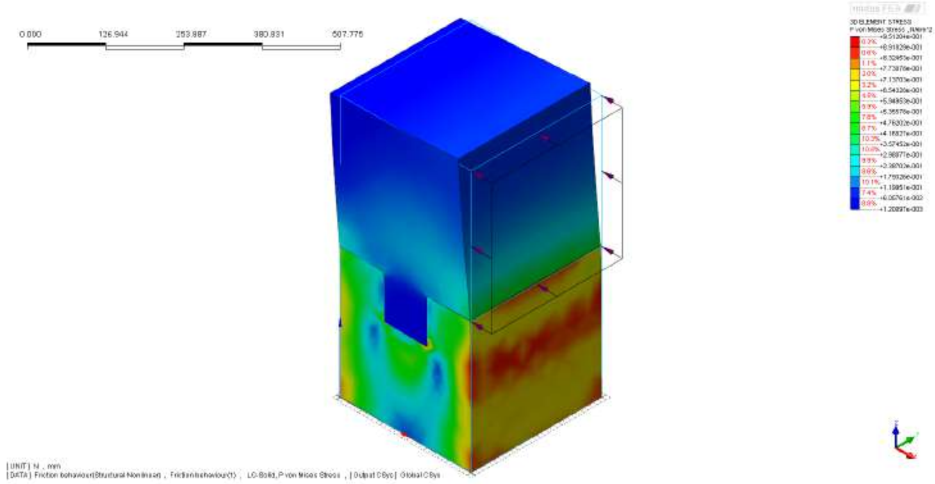

Fig. 5.22: Von Mises stress in 3D elements for load factor p=0.1

behaviour occurs. For the load factor $p = 1.9$ we observe a disturbance in the diagram of displacement D_z related to slip of the vertical surfaces of the indented connection.

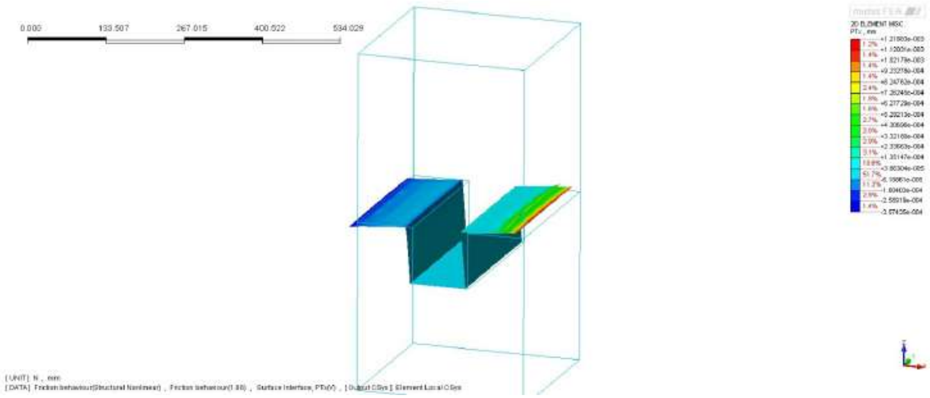

Fig. 5.23: Normal relative displacement Δu_x for p=1.86

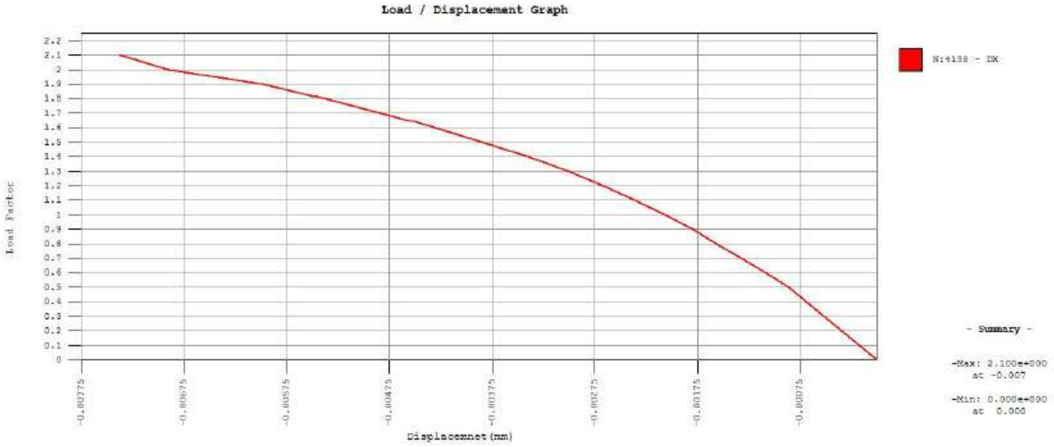

Fig. 5.24: Load factor versus displacement graph $p(D_x)$

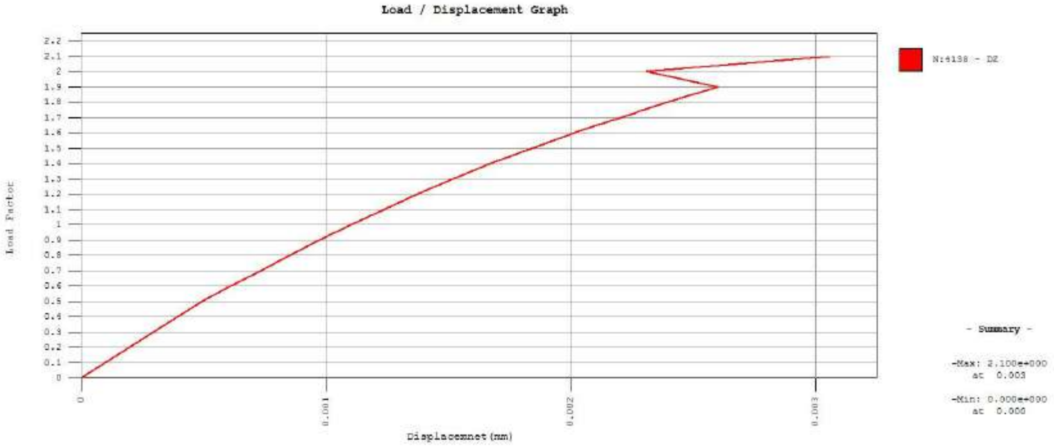

Fig. 5.25: Load factor versus displacement $p(D_z)$

5.4 Stitching reinforcement

5.4.1 Stitching reinforcement – 3D modelling

The stitching reinforcement is the most popular method of constructing the connection zone in the composite bridge girders. It seems that reinforcement starter bars embedded in the girder and connecting the cast deck are the most efficient in terms of the capacity of the composition zone. In the numerical simulations the reinforcement can be represented in several ways. The first option is to model a discrete bar with solid geometry, which is surrounded by another solid geometry which represents concrete. In Fig. 5.26 the test geometry is shown with a transparent mesh, dimensions are the same as in the previous benchmark tests, in the middle of the boxes a steel bar with 8 mm diameter is placed and connected to the boxes. The material of the bar is isotropic elastic steel with the modulus of elasticity equal to 200 GPa and the Poisson ratio equal to 0.3.

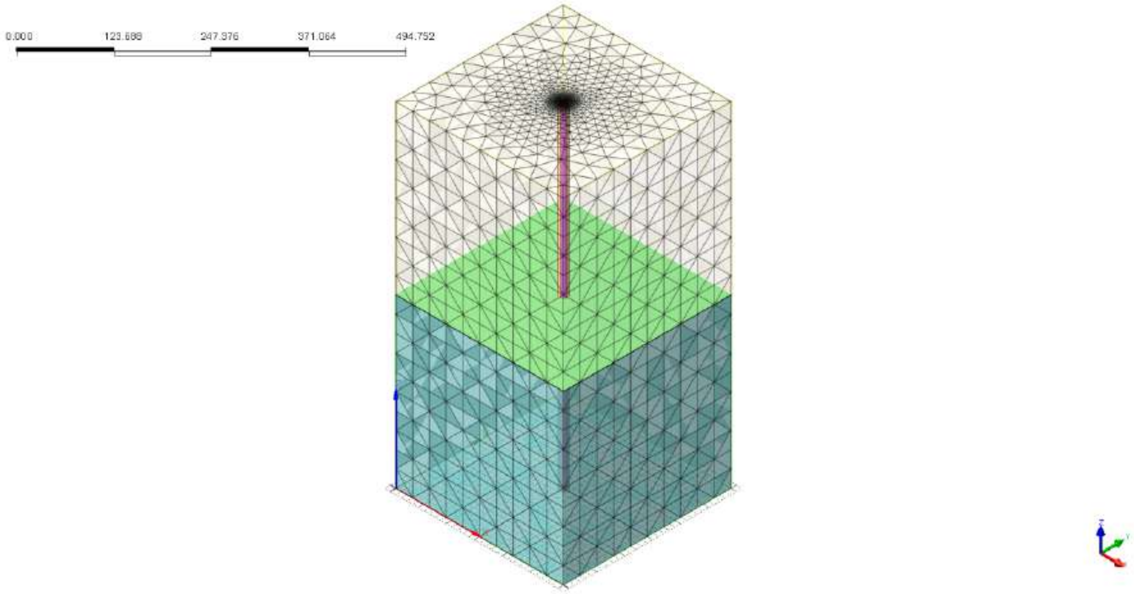

Fig. 5.26: Geometry and mesh for stitching reinforcement case

Between the bar and the concrete boxes a rigid nodal connection is assumed. Between the boxes plane interface elements are applied with exception of the geometrical opening for placing the bar. The interface is governed by Coulomb friction model with the following parameters: normal stiffness modulus k_n = 36900 N/mm^3, shear stiffness modulus k_t = 15375 N/mm^3, adhesion c = 4 N/mm^3, internal friction angle ϕ = 30 degrees, dilatancy angle ψ = 0 degrees.

The non-linear static analysis is performed and the load is divided into steps from load factor p equal 2.5 (first increment of the load which causes nonlinear behaviour) to 5. In the thesis only selected states are presented. The normal relative displacement Δu_x of the interface element is shown in Fig. 5.27 for p=2.5. It can be observed that there is only a small concentration (red colour) in the area where the reinforcing bar pushes concrete. The maximum value of the normal displacement is 7.91e-4 mm.

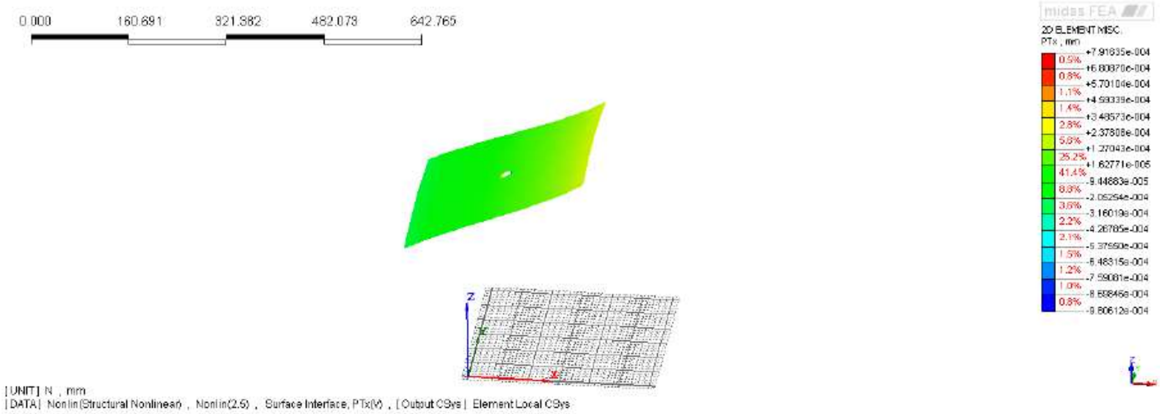

Fig. 5.27: Normal relative displacement Δu_x for load factor p=2.5

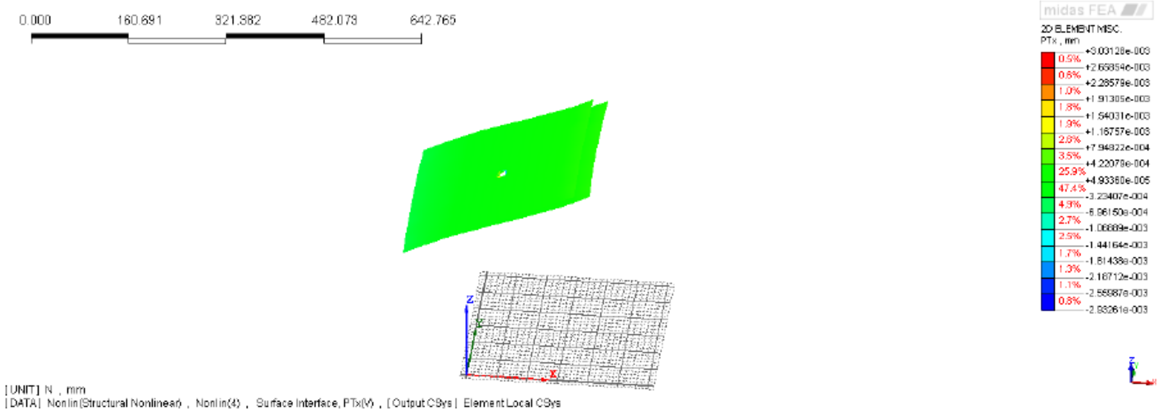

Fig. 5.28: Normal relative displacement Δu_x for load factor p=4

Fig. 5.28 shows the response of the benchmark sample for p=4. The interface has opened with the value of normal relative displacement of 3.03e-3 mm and still the concentration in the area of reinforcing bar. When the load is increased to p=5 (Fig. 5.29), the maximum value of Δu_x goes up to 8.80e-3 mm. The two sides of the interface are now separated and the contour plot surrounding the bar shows the expected influence of the stitching reinforcement. The interface opening increases and the results show the reinforcement resisting the horizontal shear force.

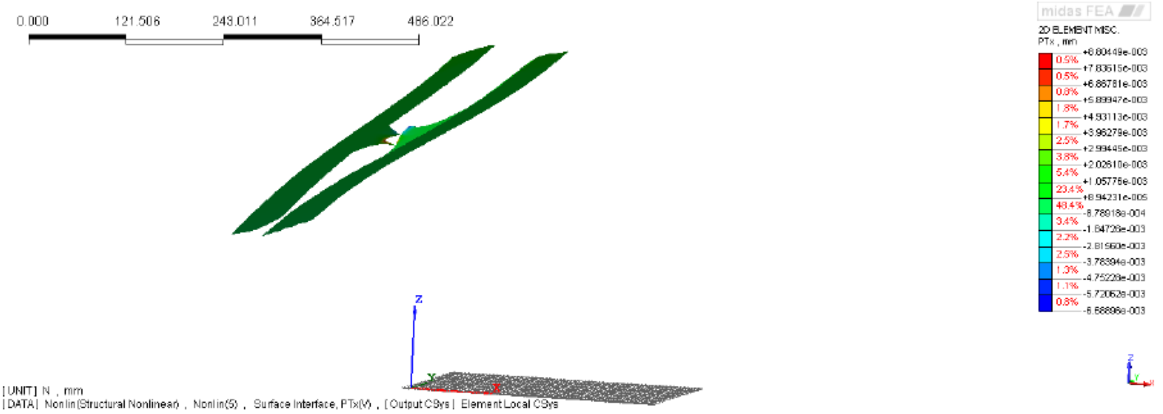

Fig. 5.29: Normal relative displacement Δu_x for load factor p=5

In Fig. 5.30 the von Mises stress in 3D elements of the bar is presented for p=2.5. The stress corresponding to the relative displacement in Fig. 5.27 is 19.5 MPa and the bar shows a bending behaviour at this stage.

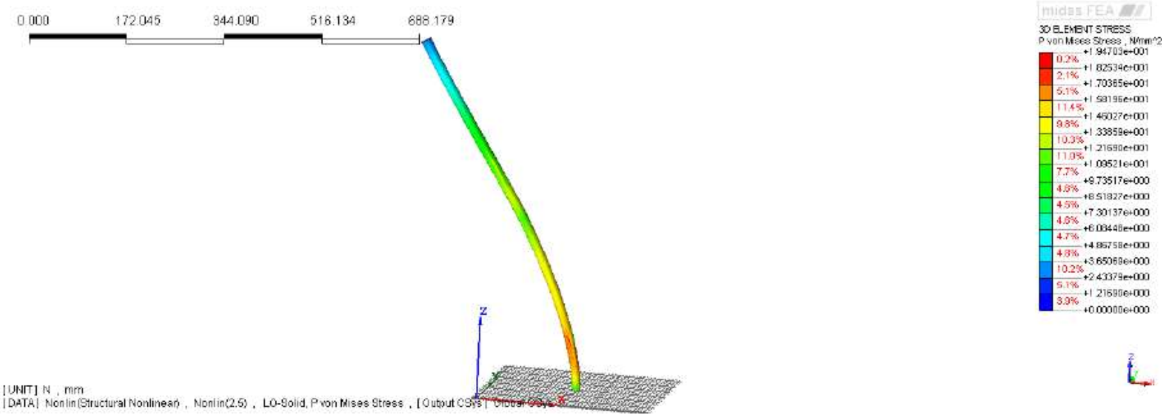

Fig. 5.30: Von Mises stress in reinforcement bar for load factor p=2.5

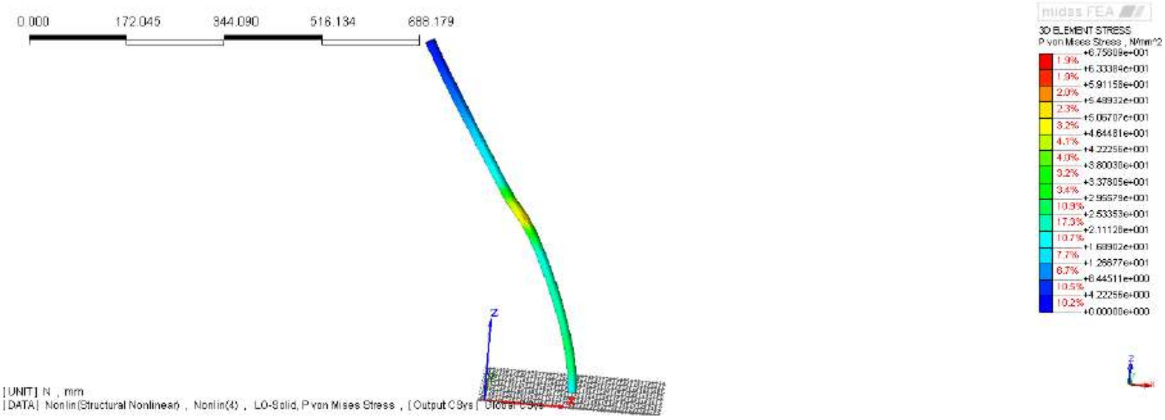

Fig. 5.31: Von Mises stress in reinforcement bar for load factor p=4

Figures 5.31 and 5.32 show the evolution of the stress in the bar and deformation

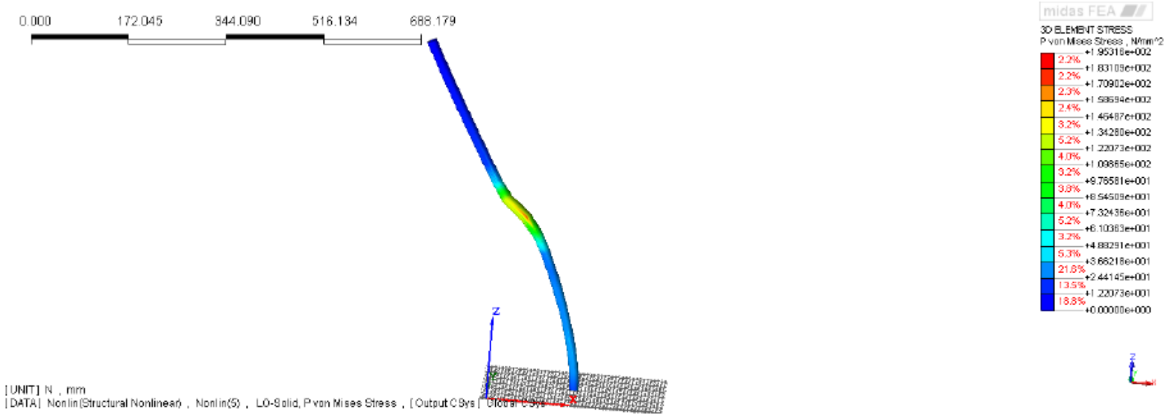

Fig. 5.32: Von Mises stress in reinforcement bar for load factor p=5

specific for the dowel action. The concentration of stress is expected in the middle of the bar due to the shear force in the contact zone, which is also represented quite well in the numerical simulation. The maximum stress for p=5 is 195 MPa.

Next, the influence of change of the dilatancy angle to 15 degrees is examined.

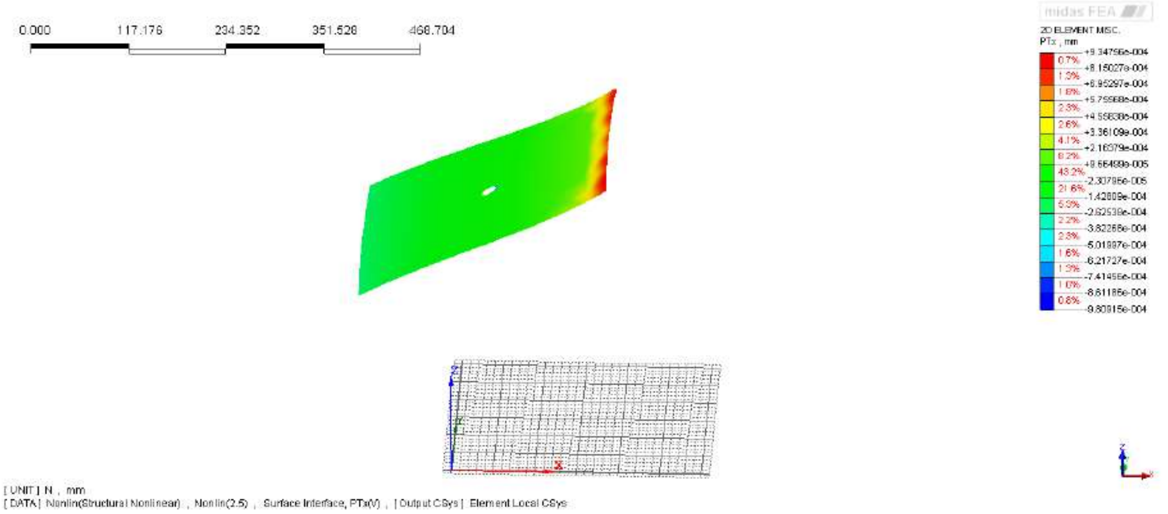

Fig. 5.33: Normal relative displacement Δu_x for load factor p=2.5 ($\psi = 15$)

Figures 5.33–5.35 show the increasing values of the normal relative displacement. For p=2.5 a concentration is visible at the edge of the hole in the interface from the side where the load is applied (the maximum value of he normal relative displacement is 9.34e-4 mm).

As the applied load increases, differences in comparison to the previous results can be observed. When p=2.8, the interface begins to open and the maximum value of the normal relative displacement is 2e-3 mm. For p=2.9 the interface is fully open and the two parts separate (see Fig. 5.35).

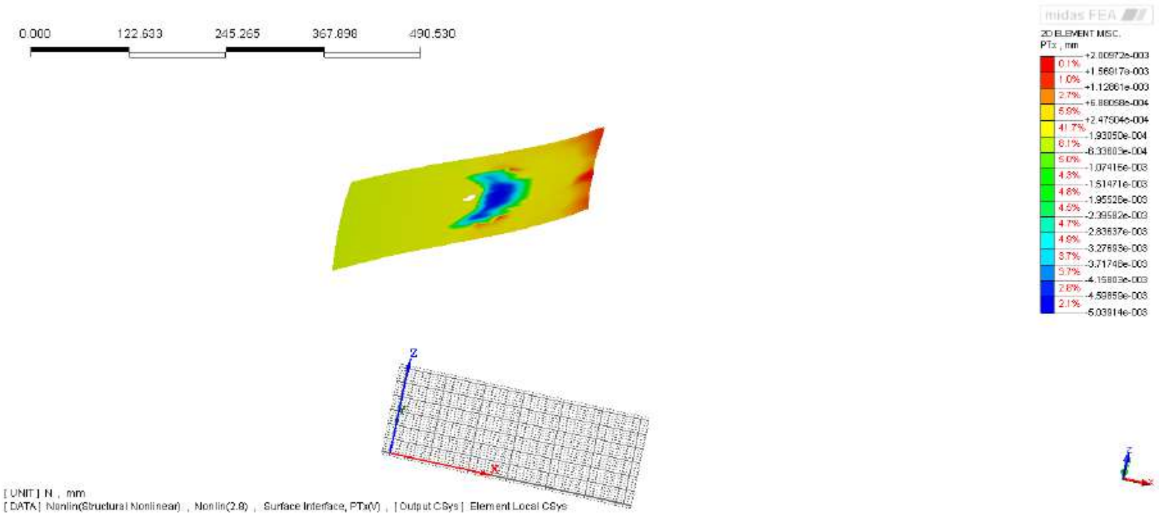

Fig. 5.34: Normal relative displacement Δu_x for load factor p=2.8 ($\psi = 15$)

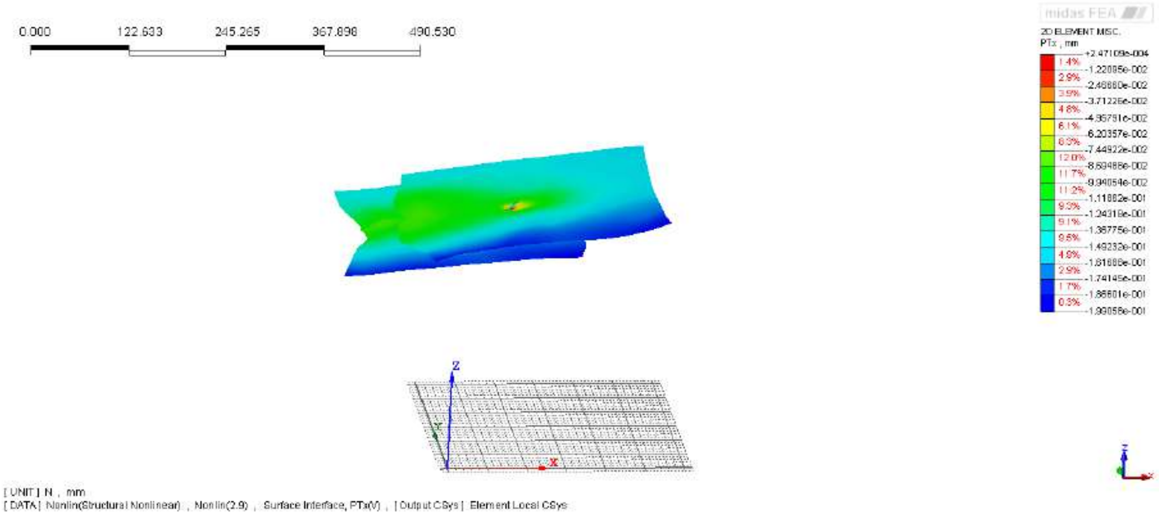

Fig. 5.35: Normal relative displacement Δu_x for load factor p=2.9 ($\psi = 15$)

Fig. 5.36 shows the von Mises stress in the steel bar. The stress concentration at the bottom of the bar is observed, which is a result of stiff boundary conditions and bending. The maximum value of the stress is 19.4 MPa. The load increase is adopted in the way allowing for the observation of the dowel action.

For p=2.9 the concentration of the stress moves from the bottom to the middle of the steel bar, because due to the slip of the interface the bar is under shear forces with the proper form of the dowel action shown in Figures 5.37–5.38.

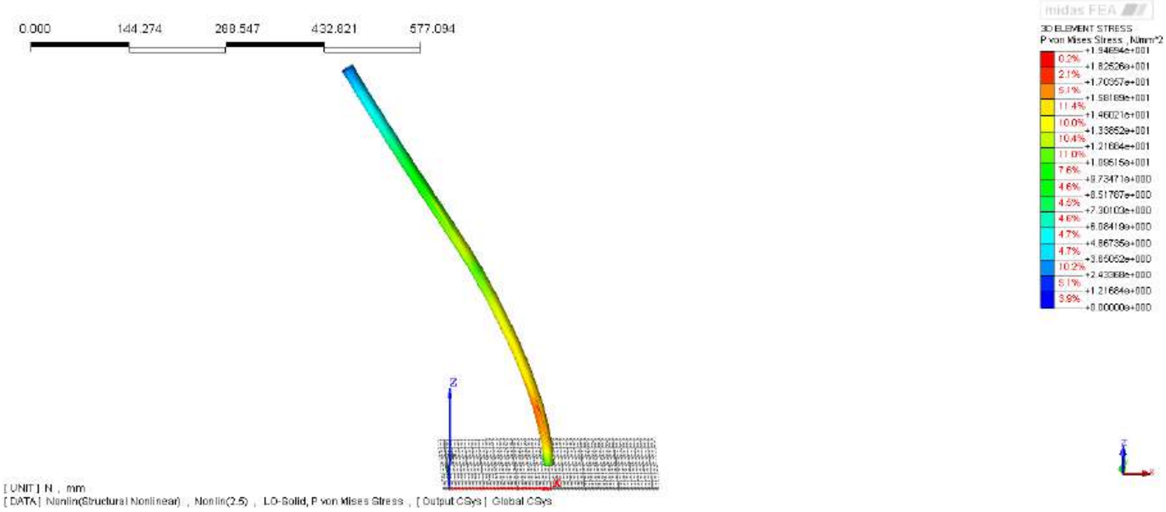

Fig. 5.36: Von Mises stress in reinforcement bar for load factor p=2.5 ($\psi = 15$)

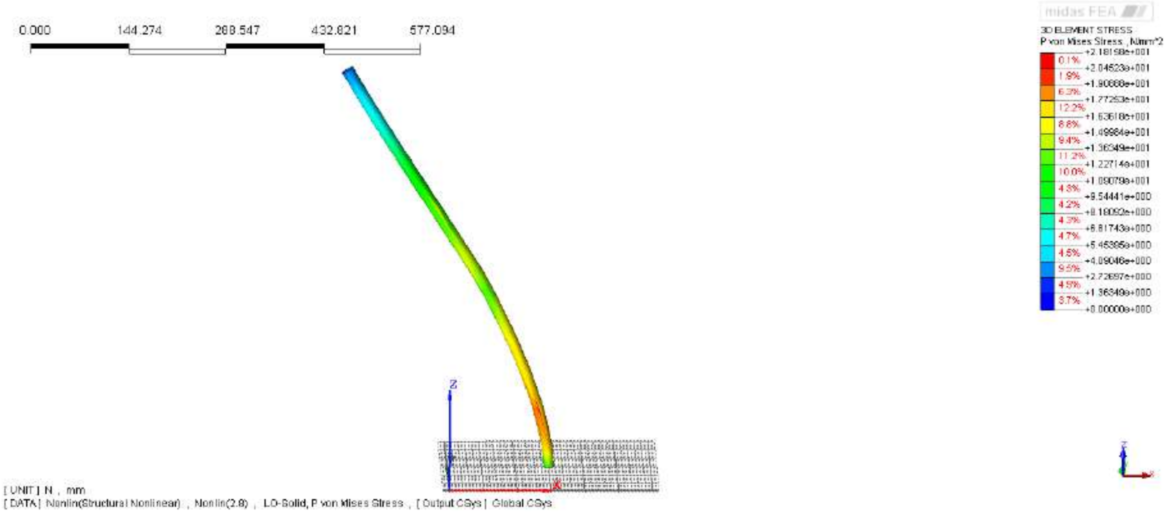

Fig. 5.37: Von Mises stress in reinforcement bar for load factor p=2.8 ($\psi = 15$)

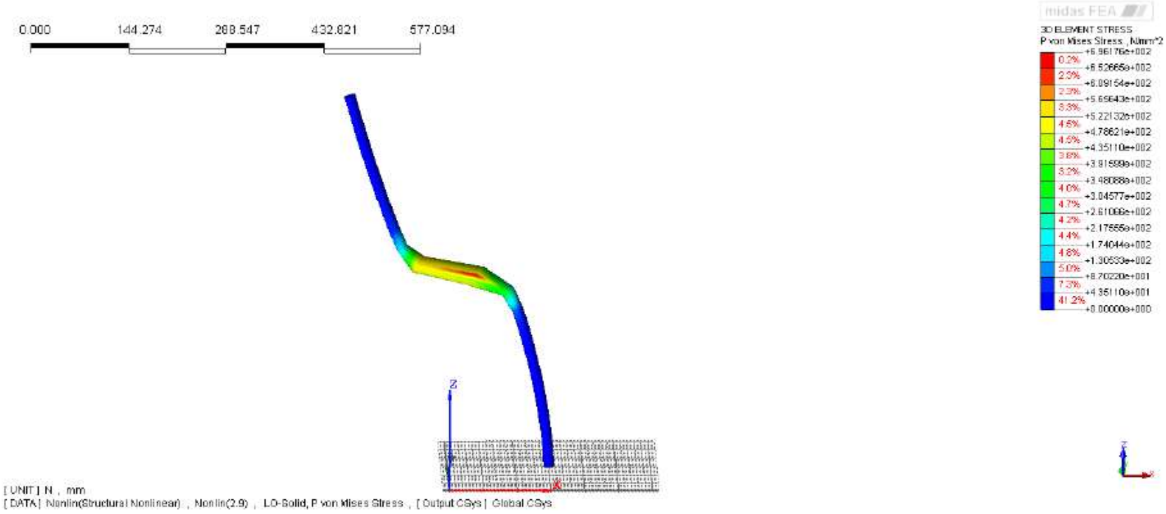

Fig. 5.38: Von Mises stress in reinforcement bar for load factor p=2.9 ($\psi = 15$)

5.4.2 Stitching reinforcement – bar in solid

A different method of modelling the stitching reinforcement is to use so-called *bar-in-solid* elements.

The reinforcement bar is modelled as reinforcement elements embedded in a solid. It is possible to see the differences with respect to the geometrical modelling presented in the previous sections. The geometry, mesh and the bar in solid are presented in Fig. 5.39.

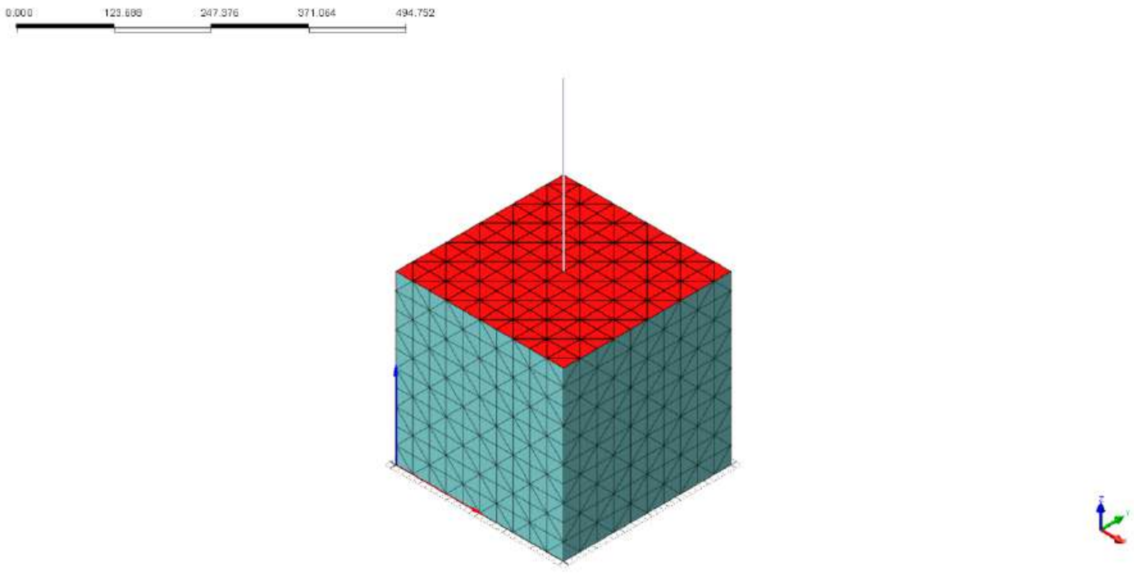

Fig. 5.39: Geometry of lower box with bar embedded in solid

As shown in Fig. 5.40, for p=4.6 the normal relative displacement of 2D interface elements exhibits the maximum value of 4.03e-4 mm, but unfortunately the software used for the calculation (Midas FEA) does not show in this figure any effect resulting from the presence of the reinforcement bar.

Fig. 5.41 shows the longitudinal stress distribution along the reinforcing bar (for this type of reinforcement the longitudinal stress S_{xx} can be monitored and not the von Mises stress). The values have a similar range to the geometrically modelled reinforcement and the shape resulting from the dowel action is represented correctly. Since the bar-in-solid option of reinforcement modelling is easier to use and computationally more efficient, it will further be employed in the simulations of the pre-stressed composite beam.

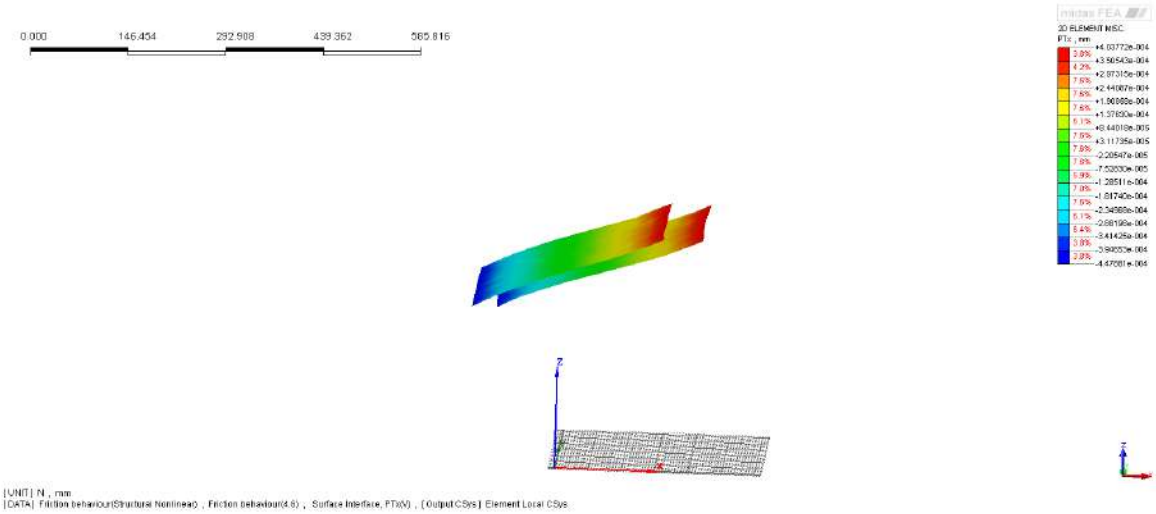

Fig. 5.40: Normal relative displacement in interface elements

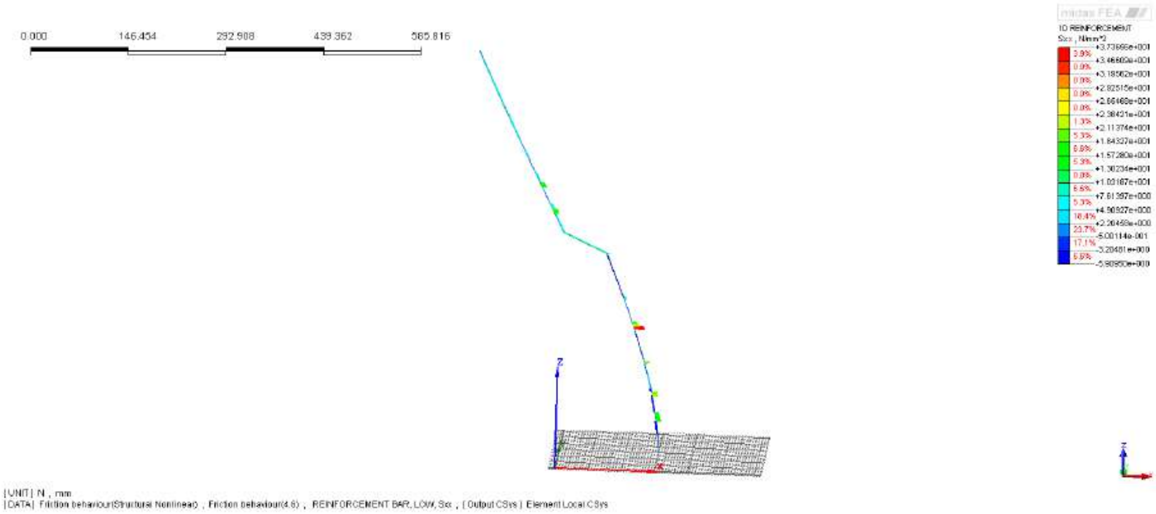

Fig. 5.41: Longitudinal stress S_{xx} in 1D reinforcement element

6 Generalized Maxwell model for creep

6.1 Introduction to linear visco-elasticity

Visco-elasticity is the property of materials that exhibit both viscous and elastic characteristics when undergoing deformation [Ottosen and Ristinmaa, 2005, de Borst et al., 2012, Marques and Creus, 2012]. Viscous materials resist shear flow and strain in a nonlinear manner in time when stress is applied. Elastic materials deform instantaneously when they are stressed and immediately return to their original shape when the stress is removed. Visco-elastic materials have both of these properties and exhibit time-dependent strain. Whereas elasticity is the result of bond stretching along crystallographic planes in an ordered solid, viscosity is usually a result of the diffusion of atoms or molecules inside an amorphous material.

The following phenomena are observed in visco-elastic materials:

a) if the stress is held constant, the strain increases with time (creep),

b) if the strain is held constant, the stress decreases with time (relaxation),

c) the effective stiffness depends on the rate of load application,

d) if cyclic loading is applied, hysteresis (phase lag) occurs, leading to the dissipation of mechanical energy.

All materials exhibit some visco-elastic response [Gwoździewicz et al., 2015]. In common metals such as steel or aluminium, as well as in quartz, at room temperature and at small strain, the behaviour does not deviate much from linear elasticity. Synthetic polymers, wood, and human tissue as well as metals at high temperature display significant visco-elastic effects. In some applications even a small visco-elastic response can be significant. To be complete, an analysis or design in such cases must incorporate the visco-elastic behaviour. The knowledge of the visco-elastic response of a material is based on measurements.

In uni-axial state of stress and strain, when the loading is constant in time (see Fig. 6.1a), the response of the material can be expressed as:

$$r\left(t\right) = f\left(t_0, t\right) a(t_0) \tag{6.1}$$

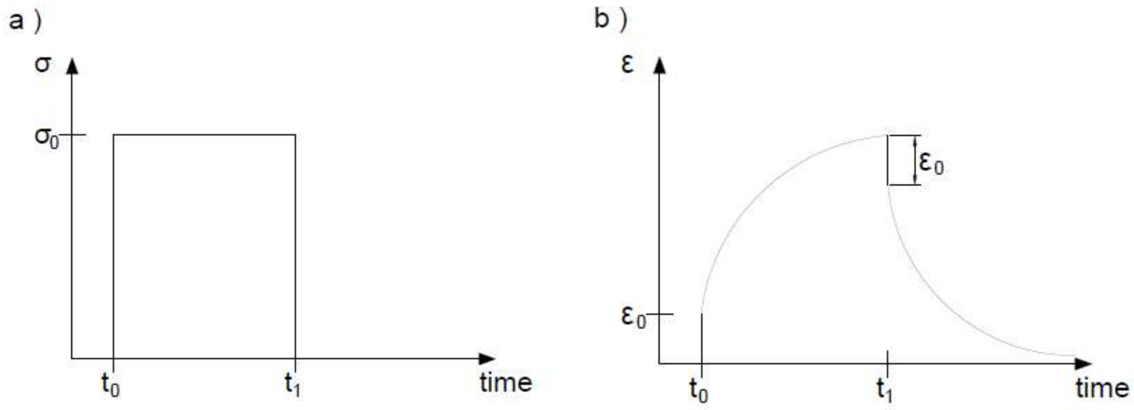

Fig. 6.1: Applied stress a) and visco-elastic strain as a function of time b)

where $f\left(t_0, t\right)$ is a characteristic function of the material. In the case presented in Fig. 6.1 this function is denoted by $J\left(t_0, t\right)$ and it is called creep function, $r(t)$ and $a(t)$ are respectively the response and action at the point considered. Using strain and stress as the response and action, and the creep function as a characteristic, equation (6.1) can be rewritten as:

$$\varepsilon(t) = J\left(t_0, t\right) \sigma(t_0) \tag{6.2}$$

At time $\mathrm{t_0}$, when the loading is applied, elastic strain $\varepsilon(\mathrm{t_0})$ occurs, which can be written as follows:

$$\varepsilon\left(t_0\right) = J\left(t_0, t_0\right) \sigma(t_0) \tag{6.3}$$

Then according to Hooke's law for elasticity:

$$\varepsilon\left(t_0\right) = \frac{\sigma(t_0)}{E(t_0)} \tag{6.4}$$

we can write:

$$J\left(t_0, t_0\right) = \frac{1}{E(t_0)} \tag{6.5}$$

In general, we finally have:

$$J\left(t, t\right) = \frac{1}{E(t)} \tag{6.6}$$

Formula (6.6) is a relationship between the creep function and modulus of elasticity at any point in time, but only for ageing materials like concrete.

There is another way to write equation (6.1). When long-term constant strain is applied to a visco-elastic member, there is a response as stress function changing in time.

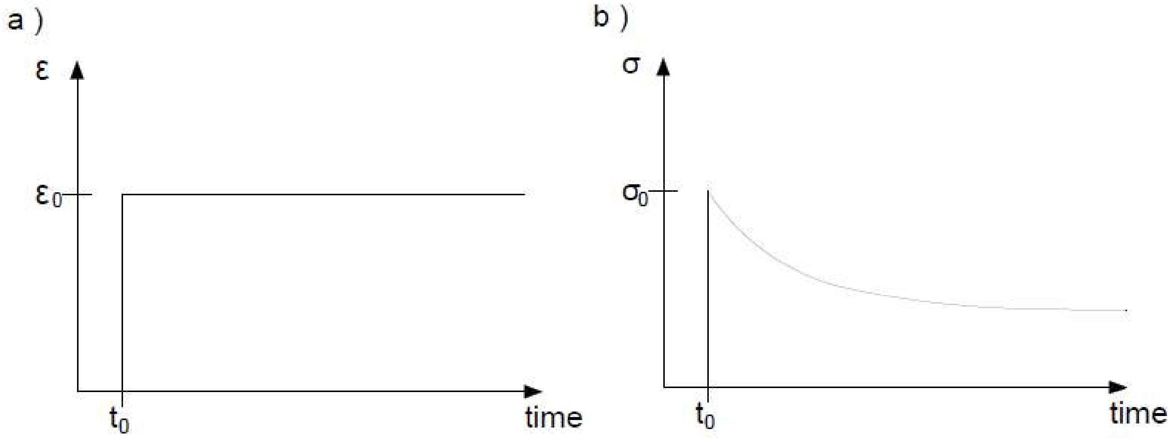

Fig. 6.2: Applied stress a) and stress as a function of time b)

The diagram of this time change of stress (Fig. 6.2) is described by the following equation:

$$\sigma\left(t\right) = R\left(t_0, t\right)\varepsilon(t_0) \tag{6.7}$$

where $R(t_0, t)$ is so-called relaxation function. There is a relation between the creep function and the relaxation function:

$$R\left(t_0, t\right) = E\left(t\right) = \frac{1}{J(t_0, t)} \tag{6.8}$$

This visco-elastic theory is linear because according to the Boltzmann superposition principle the stress and strain in time are additive [Gwoździewicz, 1999].

6.2 Visco-elastic behaviour under continuous loading

The visco-elastic theory describes well the behavior of concrete under long–term loading. Since expression (6.1) is valid only for constant loading (applied stress or strain), it is necessary to find a solution in the case of continuous and changeable process of loading. Based on fundamental laws of visco-elasticity it is difficult to find this solution, because of the number of variables in the loading history. However, an incremental form of the constitutive law for a material can be built. In the theory based on Boltzmann principle and linearity it is proposed to divide the finite period of time into infinitely small intervals, and write the response function as an integral form of the superposition principle

$$r\left(t\right) = \int_0^t f(s,t)\frac{\partial a}{\partial s}\mathrm{d}s \tag{6.9}$$

with $f(s,t)$ as a characteristic function representing material properties. There is a more general form of this equation including the value of the age at loading time t_0 :

$$r\left(t\right)=f\left(t_0,t\right)a\left(t_0\right)+\int_{t_0}^{t} f(s,t)\frac{\partial a(s)}{\partial s}\mathrm{d}s \tag{6.10}$$

The action $a(t)$ and response $r\left(t\right)$ express either the local strain or the local stress. They depend on the formulation of the equation. A characteristic function in the kernel of the integral describes the relation between the stress and strain and can be used either as a creep function in the creep equation or as a relaxation function in the relaxation equation.

The creep equation reads:

$$\varepsilon\left(t\right)=J\left(t_0,t\right)\sigma\left(t_0\right)+\int_{t_0}^{t} J(s,t)\frac{\partial \sigma(s)}{\partial s}\mathrm{d}s \tag{6.11}$$

In turn, the relaxation equation reads:

$$\sigma\left(t\right)=R\left(t_0,t\right)\varepsilon\left(t_0\right)+\int_{t_0}^{t} R(s,t)\frac{\partial \varepsilon(s)}{\partial s}\mathrm{d}s \tag{6.12}$$

There is also another formulation of these equations called Volterra equations [Gwoździewicz, 1999, Destrebecq et al., 1999], however, it is not considered here.

6.3 Visco-elastic Maxwell models

6.3.1 Simple spring-dashpot model

The elastic and viscous properties can be represented using the Maxwell model. The model is composed of an elastic spring with the modulus of elasticity E and a viscous part idealized by a dashpot with viscosity coefficient η. It is presented in Fig. 6.3.

Fig. 6.3: Maxwell spring – dashpot model

As previously mentioned, the elastic component can be represented by Hooke's law:

$$\sigma=E\varepsilon \tag{6.13}$$

The viscous part is modeled by stress-strain rate relationship attributed to Newton and given by:

$$\sigma = \eta \frac{\mathrm{d}\varepsilon}{\mathrm{d}t} \tag{6.14}$$

We define the ratio of viscosity coefficient and modulus of elasticity called relaxation time

$$\tau = \frac{\eta}{E} \tag{6.15}$$

It will be seen that this ratio is a useful measure of the time of visco-elastic response.

The stress-strain constitutive equation corresponding to the Maxwell model is:

$$\frac{\mathrm{d}\varepsilon}{\mathrm{d}t} = \frac{\sigma}{\eta} + \frac{1}{E}\frac{\mathrm{d}\sigma}{\mathrm{d}t} \tag{6.16}$$

This differential equation can be integrated assuming $\varepsilon(t) = \sigma(t) = 0$ for $t < t_0$ and either the strain or stress as the controlled variable [Marques and Creus, 2012]. We will limit consideration to the case of no aging and strain-driven loading history to obtain an integral form of the Maxwell model:

$$\sigma(t) = E \int_{t_0}^{t} \exp(-\frac{t-s}{\tau}) \frac{\partial \varepsilon}{\partial s} \mathrm{d}s \tag{6.17}$$

Then the relaxation function is expressed as:

$$R(t - t_0) = E \exp(-\frac{t - t_0}{\tau}) \tag{6.18}$$

6.3.2 Generalized Maxwell model

This model takes into account the fact that relaxation does not occur at a single time, but at a set of time moments. The Maxwell-Wiechert model (see Fig. 6.4) takes this into account by having as many spring-dashpot Maxwell elements as are necessary to accurately represent the distribution [Roylance, 2001].

The model is composed of n Maxwell chains and a spring. Since the components are connected in parallel the following relations hold:

$$\varepsilon = \varepsilon_0 = \varepsilon_1 = \cdots = \varepsilon_n, \quad \sigma = \sigma_0 + \sigma_1 + \cdots + \sigma_n \tag{6.19}$$

For each of Maxwell constituents the differential equation (6.16) holds.

The total stress can be computed from the symbolic equation [Marques and Creus, 2012]:

$$\sigma(t) = E_0 \varepsilon(t) + \sum_{i=1}^{n} \frac{\partial/\partial t}{\frac{\partial/\partial t}{E_i} + \frac{1}{\eta_i}} \varepsilon(t) \tag{6.20}$$

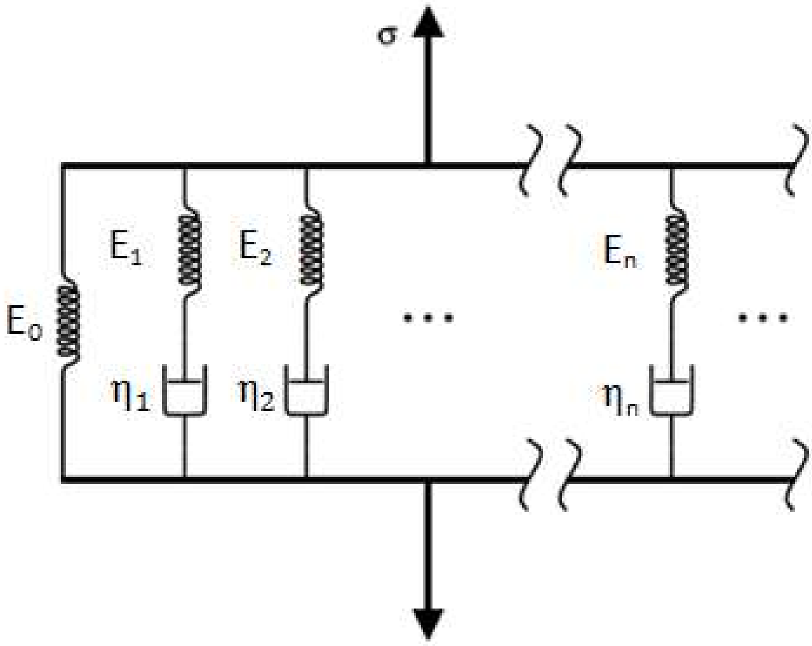

Fig. 6.4: Maxwell–Wiechert model [Roylance, 2001]

The relaxation function for a generic time s is written as:

$$R\left(t-s\right)=E_0+\sum_{i=1}^{n}E_i\,\exp\left(-\frac{t-s}{\tau_i}\right) \tag{6.21}$$

where $\tau_i=\frac{\eta_i}{E_i}$, i=1,...,n.

To find the creep function equation (6.20) must be solved, see [Marques and Creus, 2012] for the example of the Zener model ($n=1$).

Alternatively, to determine the stress function an internal variable approach can be used, introducing n integral functions q_i as follows:

$$q_i(t)=\int_{t_0}^{t}\exp\left(-\frac{t-s}{\tau_i}\right)\frac{\partial\varepsilon}{\partial s}\mathrm{d}s \tag{6.22}$$

which have the interpretation of strains in the springs. The derivative of this equation with respect to t gives the set of n differential equations for q_i:

$$\dot{q}_i\left(t\right)+\frac{1}{\tau_i}q_i(t)=\dot{\varepsilon}(t) \tag{6.23}$$

with initial conditions $q_i=0$ for $t=t_0$, while the stress can be expressed as:

$$\sigma(t)=E_0\varepsilon\left(t\right)+\sum_{i=1}^{n}E_iq_i\left(t\right) \tag{6.24}$$

To trace the response of the general Maxwell model in time it is necessary to compute the internal variable for a sequence of time increments $[t,t+\Delta t]$. Writing (6.22) for time $t + \Delta t$

$$q_i^{t+\Delta t} = \int_{t_0}^{t} \exp\left(-\frac{t+\Delta t - s}{\tau_i}\right)\frac{\partial \varepsilon}{\partial s}\,\mathrm{d}s + \int_{t}^{t+\Delta t} \exp\left(-\frac{t+\Delta t - s}{\tau_i}\right)\frac{\partial \varepsilon}{\partial s}\,\mathrm{d}s \tag{6.25}$$

and assuming that $\frac{\partial \varepsilon}{\partial s}$ is constant over time interval Δt one can further compute the two integrals as:

$$q_i^{t+\varDelta t} = \exp\left(-\frac{\varDelta t}{\tau_i}\right) q_i^t + \tau_i \left[1 - \exp\left(-\frac{\varDelta t}{\tau_i}\right)\right]\frac{\varDelta \varepsilon}{\varDelta t} \tag{6.26}$$

The increment of q can be computed as follows:

$$\varDelta q = \ q_i^{t+\varDelta t} - q_i^t \ = \left[1 - \exp\left(-\frac{\varDelta t}{\tau_i}\right)\right]\left(\frac{\tau_i}{\varDelta t}\Delta\varepsilon - q_i^t\right) \tag{6.27}$$

More information about creep and shrinkage of concrete can be found in [Al-Omaishi et al., 2009, Ngab et al., 1981a, Puchalska and Kuczma, 2017a, Puchalska and Kuczma, 2017b, Bazant, 1975, Bazant and Prasannan, 1989].

6.4 Implementation of Generalized Maxwell model in 3D

The implementation of the Generalized Maxwell model as a user-supplied subroutine in Midas FEA is based on integral expressions defining the stress at time moments t and $t + \Delta t$. It is assumed that the strain rate is constant within the time interval. In general material aging could be taken into account [DIANA FEA, 2020], but this aspect is neglected here.

In three-dimensional version of the model it is assumed that all tangent components of the stiffness (or compliance) tensor evolve in time in the same way, so the expansion of the model from 1D to 3D is performed using the following matrix:

$$\bar{\boldsymbol{D}} = \frac{1}{E_0}\boldsymbol{D}^e \tag{6.28}$$

where obviously $\boldsymbol{D}^e$ is Hooke's tensor. Hence $\bar{\boldsymbol{D}}$ can be written as:

$$\bar{\boldsymbol{D}} = \frac{1}{(1+\nu)(1-2\nu)}\begin{bmatrix} 1-\nu & \nu & \nu & 0 & 0 & 0 \\ \nu & 1-\nu & \nu & 0 & 0 & 0 \\ \nu & \nu & 1-\nu & 0 & 0 & 0 \\ 0 & 0 & 0 & \frac{1-2\nu}{2} & 0 & 0 \\ 0 & 0 & 0 & 0 & \frac{1-2\nu}{2} & 0 \\ 0 & 0 & 0 & 0 & 0 & \frac{1-2\nu}{2} \end{bmatrix} \tag{6.29}$$

with Poisson ratio ν.

According to [DIANA FEA, 2020] one can write the stress at time t in each Maxwell chain as:

$$\boldsymbol{\sigma}_i^t = \bar{\boldsymbol{D}} \int_{t_0}^{t} E_i \exp\left(-\frac{t-s}{\tau_i}\right) \frac{\partial \boldsymbol{\varepsilon}}{\partial s} \mathrm{d}s \tag{6.30}$$

and at time $t + \Delta t$ in a similar way to obtain the increments:

$$\Delta \boldsymbol{\sigma}_i = \left[1 - \exp\left(-\frac{\Delta t}{\tau_i}\right)\right] \left(E_i \frac{\tau_i}{\Delta t} \Delta \boldsymbol{\varepsilon} - \boldsymbol{\sigma}_i^t\right) \tag{6.31}$$

which means the computation of new stress at $t + \Delta t$ is based only on the previous stress at t and the incremental quantities. The total stress increment is equal to:

$$\Delta \boldsymbol{\sigma} = E_0 \bar{\boldsymbol{D}} \Delta \boldsymbol{\varepsilon} + \sum_{i=1}^{n} \Delta \boldsymbol{\sigma}_i \tag{6.32}$$

The algorithm of stress update and computation of tangent operator $\boldsymbol{D}_{tang}$ is now presented for the applied strain-driven finite element procedure. For each time step, at each integration point we have given $\boldsymbol{\varepsilon}^t$, $\Delta\boldsymbol{\varepsilon}$, $\boldsymbol{\sigma}_i^t$,$\boldsymbol{\sigma}^t$, where $\boldsymbol{\sigma}_i^t$ is an internal variable vector. One should find $\boldsymbol{\varepsilon}^{t+\Delta t}$, $\boldsymbol{\sigma}^{t+\Delta t}$, $\boldsymbol{\sigma}_i^{t+\Delta t}$ and $\boldsymbol{D}_{tang}$.

First the strain is updated

$$\boldsymbol{\varepsilon}^{t+\Delta t} = \boldsymbol{\varepsilon}^t + \Delta \boldsymbol{\varepsilon} \tag{6.33}$$

Now the stress tensor in each Maxwell chain can be updated using (6.31)

$$\boldsymbol{\sigma}_i^{t+\Delta t} = \boldsymbol{\sigma}_i^t + \ \Delta \boldsymbol{\sigma}_i \tag{6.34}$$

and the stress is updated using (6.32)

$$\boldsymbol{\sigma}^{t+\Delta t} = \boldsymbol{\sigma}^t + \Delta \boldsymbol{\sigma} \tag{6.35}$$

Finally, the consistent tangent necessary to obtain quadratic convergence of the iterative Newton algorithm can be computed as:

$$\bar{\boldsymbol{D}}_{tang} \overset{def}{=} \frac{\partial \boldsymbol{\sigma}^{t+\Delta t}}{\partial \boldsymbol{\varepsilon}^{t+\Delta t}} = E_0 \ \bar{\boldsymbol{D}} + \sum_{i=1}^{n} E_i \frac{\tau_i}{\Delta t} \left[1 - \exp\left(-\frac{\Delta t}{\tau_i}\right)\right] \bar{\boldsymbol{D}} \tag{6.36}$$

6.5 Tests of Generalized Maxwell model

6.5.1 1D benchmark

To validate and calibrate the newly implemented 3D Generalized Maxwell model, a 1D benchmark test is carried out. The 1D model with 5 Maxwell branches is considered. A reference relaxation function is used to compare the results of the model. As both curves give approximately the same results, see Figures 6.5 and 6.6, the model is treated as successfully validated and gives direction for further development in three-dimensional space.

Table 6.1: Data used in 1D visco-elastic benchmark

i	τ_i [days]	E_i [MPa]
0	-	8000
1	1	4000
2	10	6000
3	100	4000
4	1000	6000

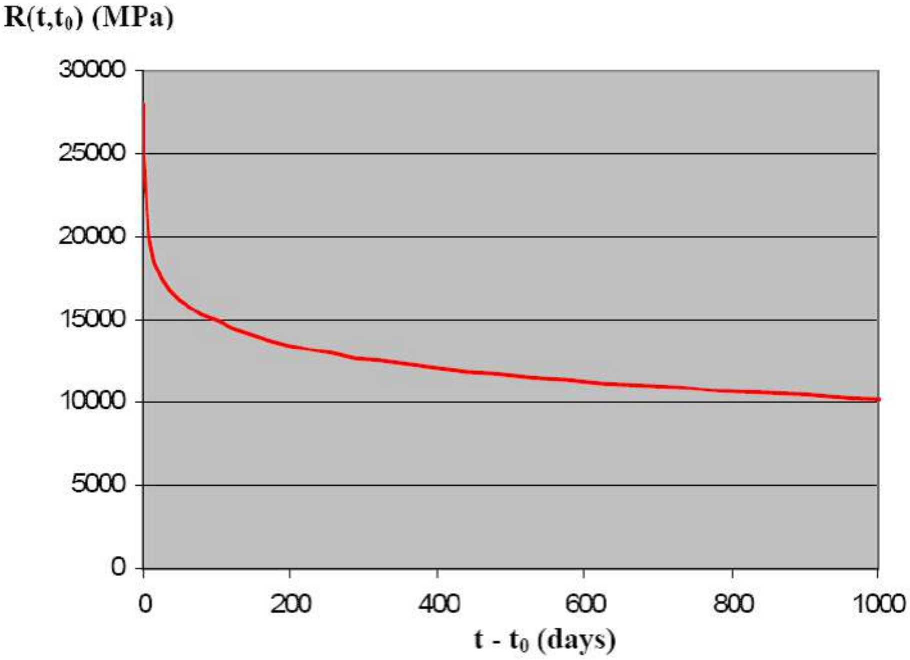

Fig. 6.5: Reference relaxation function

6.5.2 3D test

To validate the three-dimensional rheological model a concrete cube configuration is analyzed using finite elements. The cube with dimensions of 30x30x30cm is discretized using 3D solid elements. Elastic material model is adopted for concrete with the modulus of elasticity equal to 25GPa and Poisson's ratio equal to 0.2. Two variants

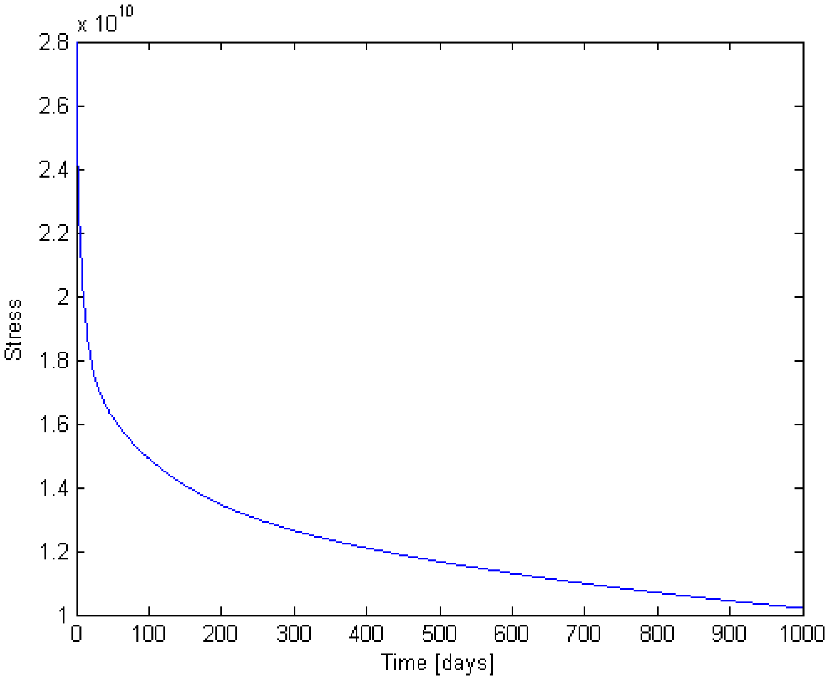

Fig. 6.6: Relaxation function calculated with implemented model

of rheological properties are tested: according to Eurocode and the implemented 3D Generalized Maxwell model. The Eurocode creep model is introduced with the properties as follows: characteristic compressive strength 20MPa, 70% of relative humidity, notional size as 30cm, normal cement. Regarding the Maxwell model, the input data are the same as described in Subsection 6.5.1. First a static analysis is performed – the box is fixed on the bottom face and loaded on the top face with pressure 10 MPa.

The vertical displacements (DZ) and vertical strains (EZZ) are checked. Fig. 6.7 shows the maximum vertical displacement as 9.92×10^{-2} mm and Fig. 6.8 shows the maximum absolute value of compressive strain EZZ equal to 4.42×10^{-4}.

Next, the construction stage analysis is performed with the two creep models. There are two stages, the first identical to the previous linear statics and the second with the duration 10000 days (no modification of the model comparing to stage one is made). The results of the analysis with the Eurocode model are shown in Figures 6.9 and 6.10. The maximum vertical displacement after 10000 days is 3.71×10^{-1} mm and the maximum vertical strain is 1.65×10^{-3}.

Next, the same analysis is performed with the Generalized Maxwell model. The results of the analysis are shown in Figures 6.11 and 6.12. The maximum vertical displacement is 3.46×10^{-1} mm and maximum vertical strain is 1.54×10^{-3}.

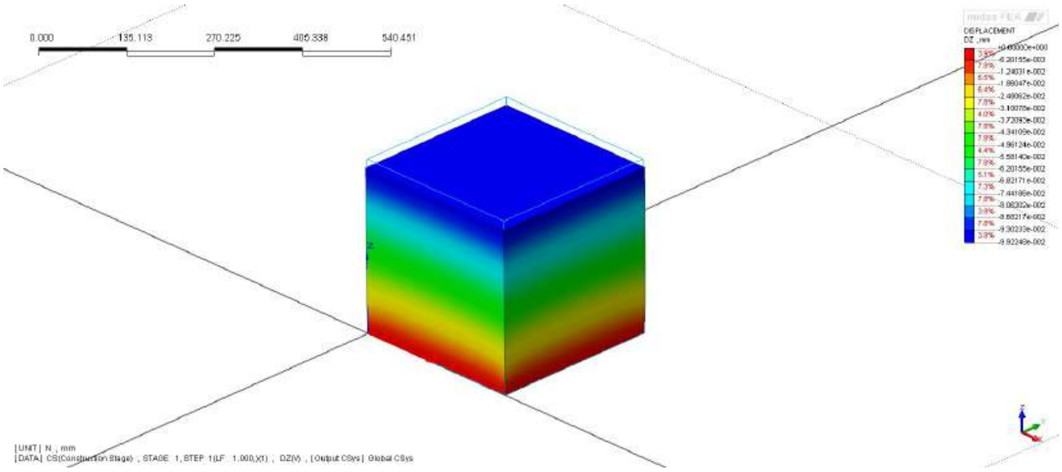

Fig. 6.7: Vertical displacement (DZ) – linear static analysis

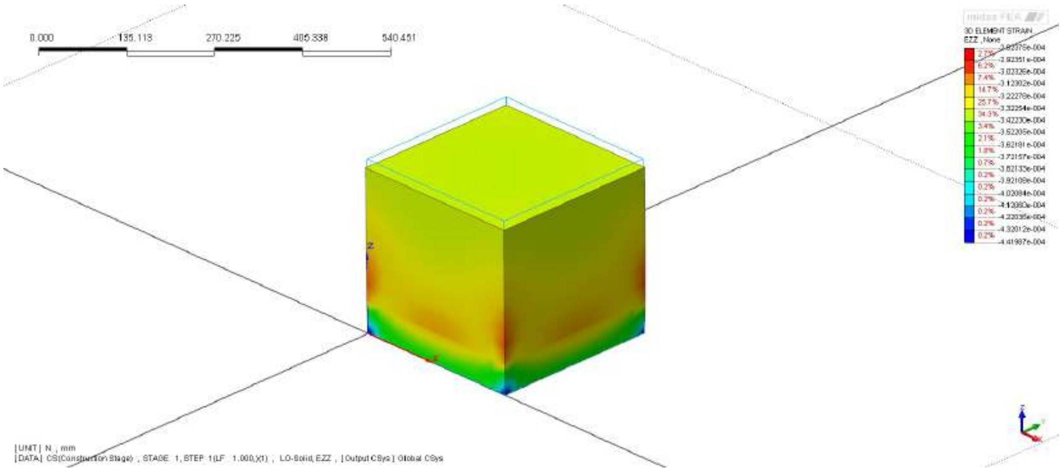

Fig. 6.8: Vertical strain (EZZ) – linear static analysis

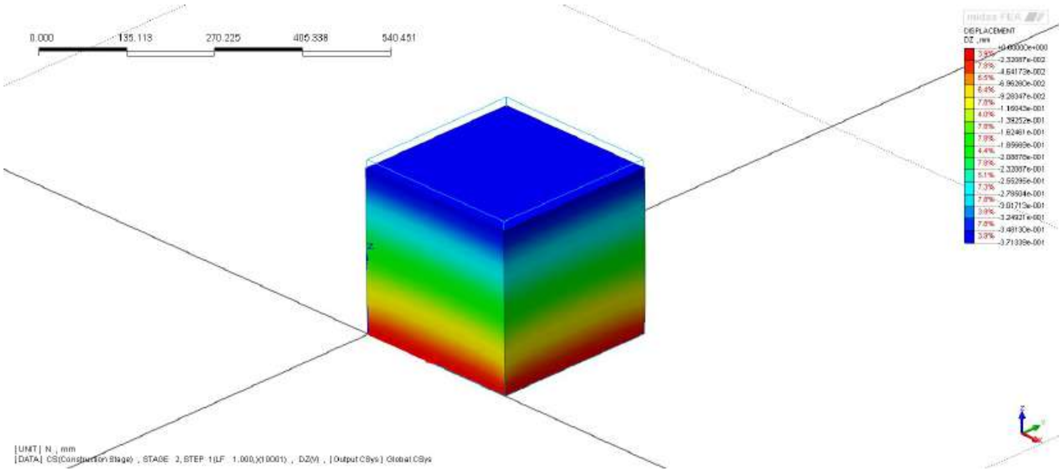

Fig. 6.9: Vertical displacement (DZ) – 10000 days – Eurocode model

The calibration tests show that the more complex Generalized Maxwell model gives lower values of the results like displacements and strains, which leads to the initial

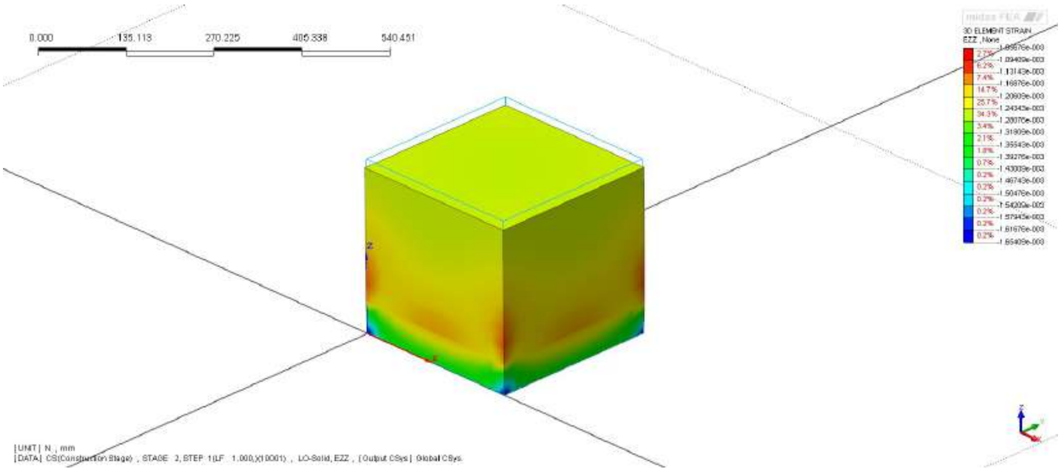

Fig. 6.10: Vertical strain (EZZ) – 10000 days – Eurocode model

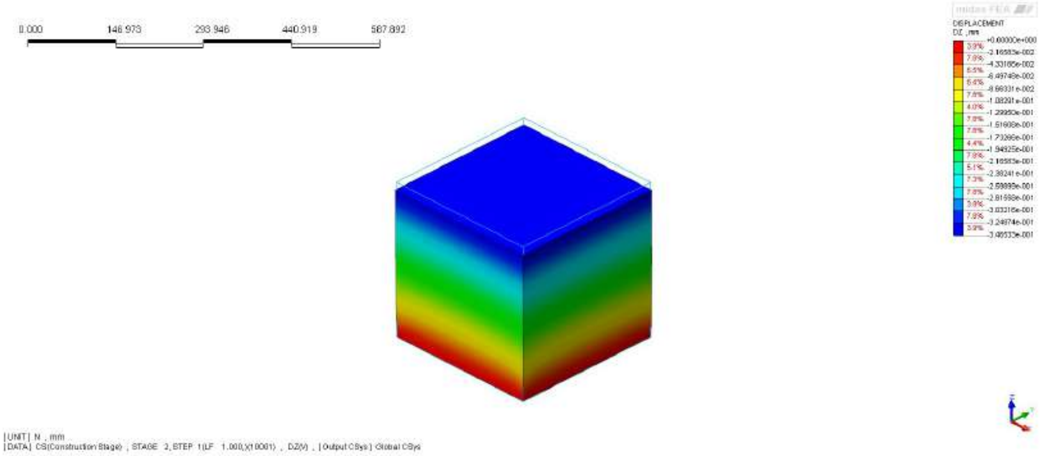

Fig. 6.11: Vertical displacement (DZ) – 10000 days – Generalized Maxwell model

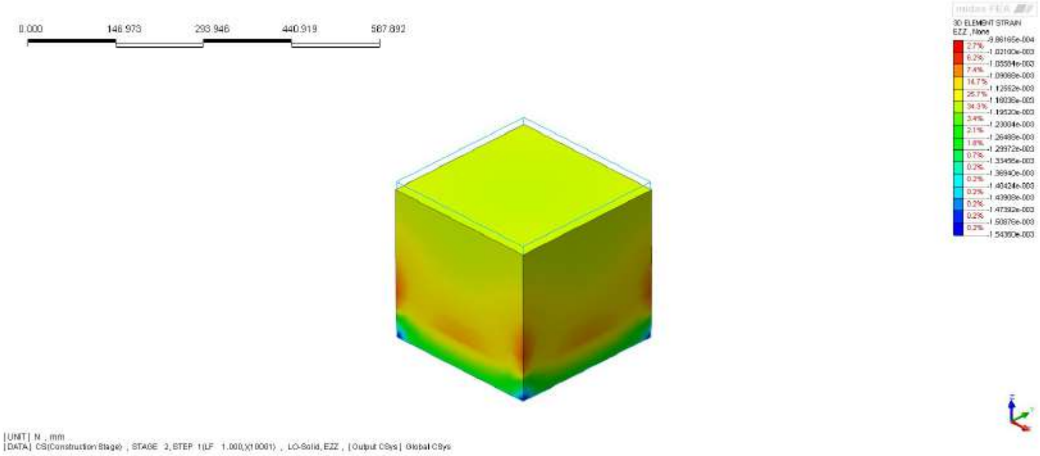

Fig. 6.12: Vertical stress (SPZZ) – 10000 days – Generalized Maxwell model

conclusion that code-based models are safer in terms of structural design and, on the other hand, more accurate calculations including more sophisticated material models could lead to more economic and effective design.

7 Numerical model and cracking analysis

7.1 Geometry, material and mesh

The concrete-concrete girder with 1.5 meter broad deck (Fig. 7.1) is chosen for initial tests and for the model calibration for further analysis. The specimen is made of the concrete with lowest compressive strength of 69 MPa from the experiments of Choi [Choi, 2006]. The composite deck is made of concrete with compressive strength 28 MPa. The girder is modelled using 8-node hexahedron solid elements with linear shape functions.

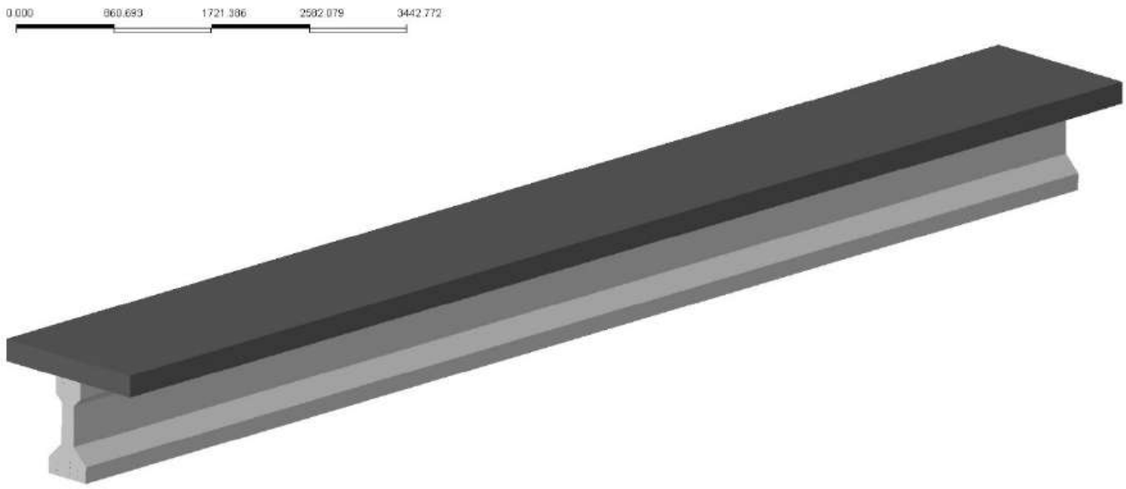

Fig. 7.1: Geometry of the model

The girder with total length of 12.5 meters and the distance between supports (span) of 12.2 meters is connected at the final stage to the slab with 152.4 cm width and 20.32 cm thickness. The connection of these two parts of the composite girder is assumed as rigid in preliminary tests. The modelled girder has an I shape cross-section with 91.44 cm height, 45.72 cm width of the bottom flange and 30.48 cm width of the top flange (Fig. 7.2). Fig. 7.3 presents the finite element discretization of the model. The mesh is relatively coarse to be able to perform complex nonlinear simulations in reasonable time.

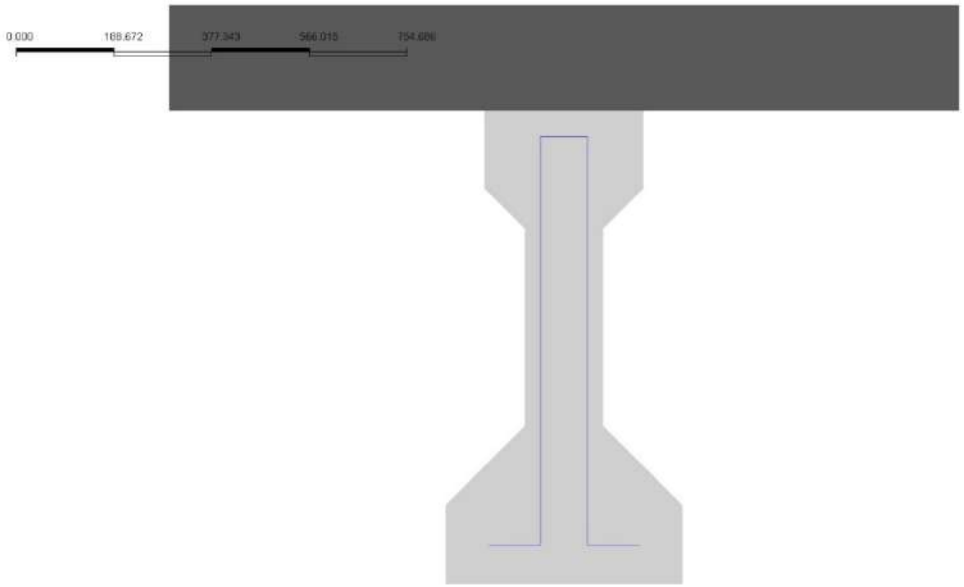

Fig. 7.2: Cross-section of the modelled girder

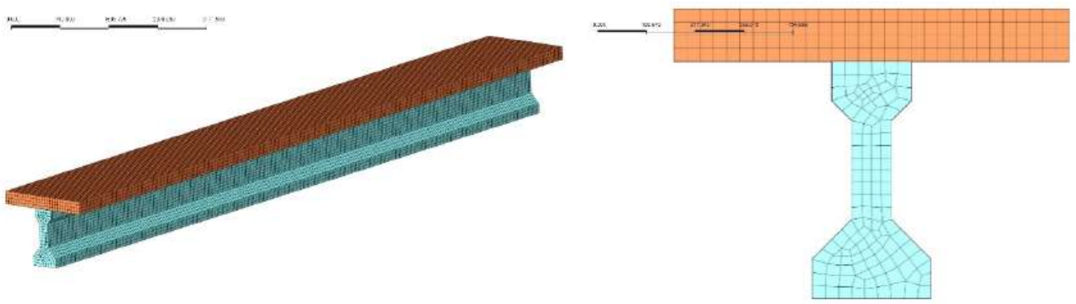

Fig. 7.3: Mesh sets

7.2 Reinforcement

Each tested girder contains stirrups with Φ=4 mm and the spacing of 7.62 cm near the end blocks and 15.24 cm along the entire length of the girder. The longitudinal reinforcement is neglected due to its negligible influence on the behaviour of the structure in the presence of pre-stressing strands and because of the lack of relevant data in the references. The stirrups are modelled as discrete bars embedded in solid elements (Fig. 7.4). Each stirrup is defined as a separate bar element (Fig. 7.5).

7.3 Pre-stressing

The modelled girder was pre-stressed with 16 straight strands with Φ=12.7 mm (1860 MPa low relaxation pre-stressing steel was used). Each strand was tested and the average ultimate breaking strength 194.6 kN was measured. 14 strands were placed

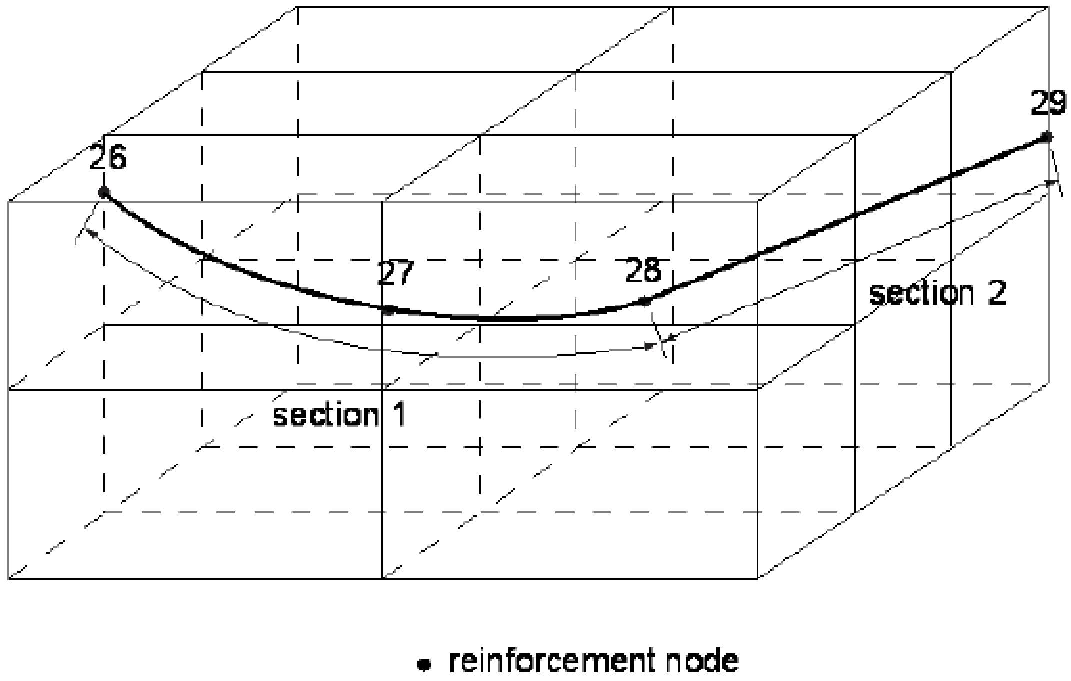

Fig. 7.4: Bar in solid reinforcement element [Midas IT, 2020]

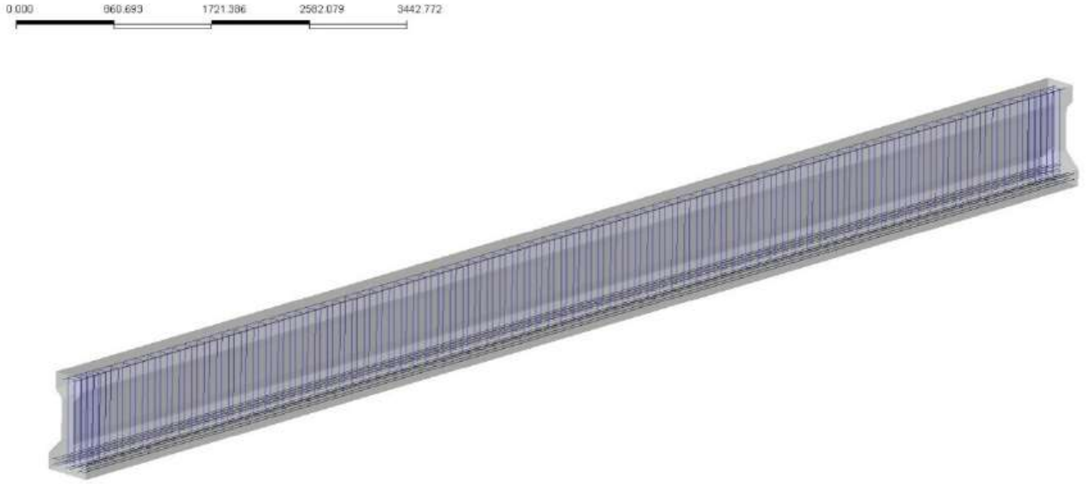

Fig. 7.5: Reinforcement of the girder

at the bottom flange and 2 at the top. Each strand was tensioned up to 75% of its ultimate strength. Each particular strand is modelled separately using the bar-in-solid discrete reinforcement elements and a uniform pre-stressing force is applied (Fig. 7.6)

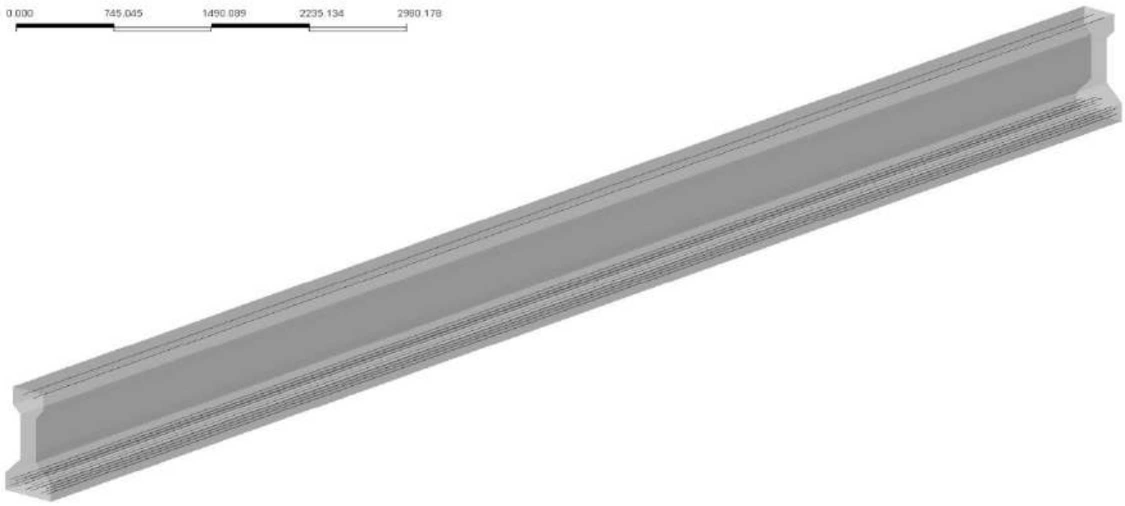

Fig. 7.6: Configuration of the pre-stressing strands

7.4 Boundary conditions and loads

The girder analyzed experimentally by Choi was a simply supported beam (Fig. 7.7). The supports with 12.2 meters spacing were made of a steel plate above a neoprene pad. In the numerical approach the supports are defined as rigid in vertical direction, which can have influence on the results as the model is stiffer than the real specimen.

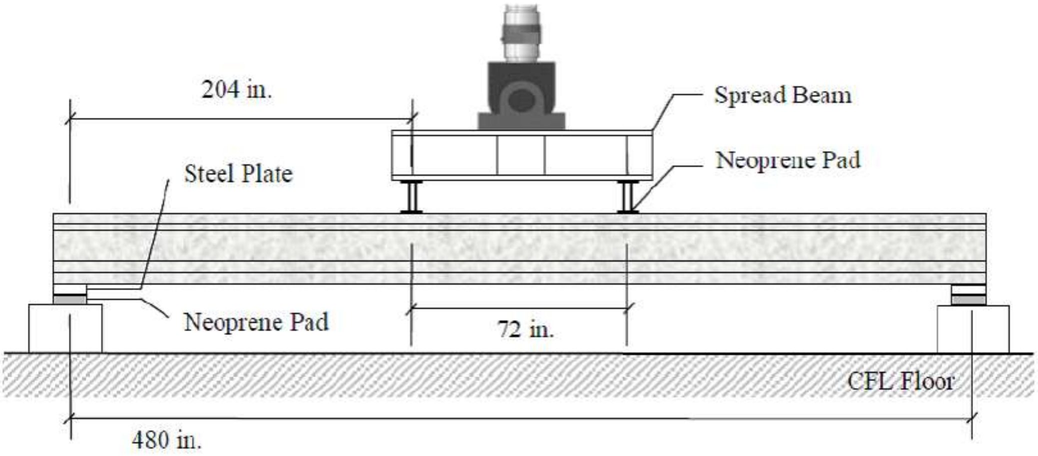

Fig. 7.7: Test set-up [Choi, 2006]

The load was applied to the girder with MTS closed-loop actuator. The girder was loaded up to the yielding of the pre-stressing strands. To examine the accuracy of the model, the cracking load obtained from experimental results is applied to the model as a pressure load according to the test set-up shown in Fig. 7.8. The total value of the load is 573.82 kN. In the nonlinear simulations the load is applied in increments and the load increase factor is denoted by p, so the cracking load given above is specified by $p = 1$.

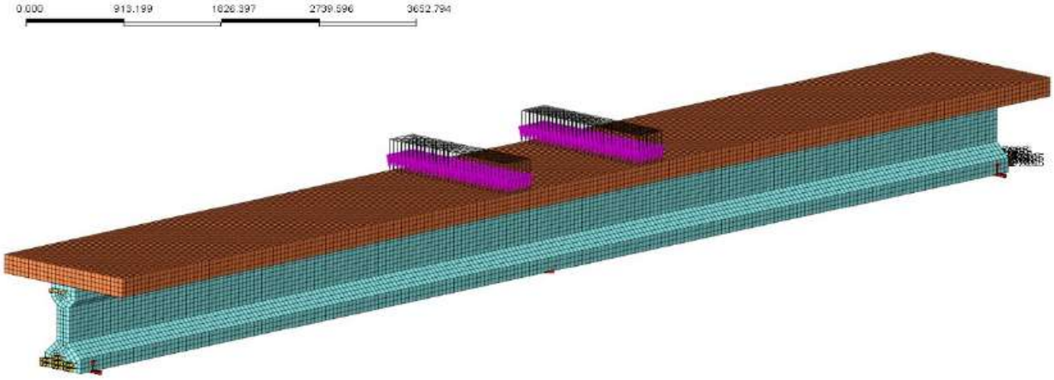

Fig. 7.8: Boundary conditions and load definition in the numerical model

7.5 Analysis cases

For preliminary tests and calibration of the model three types of analysis are performed.

Linear static analysis - this type of fundamental analysis is performed to check the overall correctness of the model, geometry, loads, boundary conditions etc.

Cracking analysis - this analysis is used for prediction of cracks distribution and of the failure mode. Smeared type of cracking model, in particular the Total Strain Crack model described in Appendix A, was used for the analysis to check if the results of the numerical analysis are similar to the ones obtained from the experimental research [Choi, 2006].

Construction stage analysis – the building process is divided into five stages: girder with reinforcement, pre-stressing of the girder, wet concrete load, composite girder with the slab, external load. The staging analysis is performed without any duration in time for a particular stage (stage duration time equals zero), which means that no time-dependent effects are taken into account. This kind of analysis allows one to evaluate the influence of the building process divided into stages in terms of changing geometry and deformed shape from one stage to another.

More advanced computations are then performed to examine the importance of rheological aspects of the analysis (in particular creep) and the influence of the interface model for the girder-slab concrete-concrete connection.

Construction stage analysis with time-dependent effects – this analysis is performed to simulate the influence of concrete creep. The shrinkage phenomenon and compressive strength evolution in time are neglected to isolate pure creep behaviour. Two different creep functions based on the CEB-FIP code recommendations [fib, 2010] are introduced for HSC (Fig. 7.9) and NSC (Fig. 7.10). Next, the Generalized Maxwell model is used instead of the CEB-FIP creep model and the results are compared. It is assumed that each construction stage has a seven days duration and an additional sixth stage is introduced to reach 10000 days duration time of the whole process and show long term behaviour.

Construction stage analysis with interface elements – the final analysis is performed to simulate the behaviour of the composite girder with cthe onnection zone modeled in different ways, taking into account construction stages as in the previous analysis case. Two different load setups were taken into account: first to simulate the bending behaviour as before and second to represent longitudinal shear. For the first load the interface model chosen for the analysis is the Coulomb friction model and for the second one the Coulomb friction is combined with stitching reinforcement to enhance the interface behaviour. Initially, in the process of calibration tests indented connection was also considered, but for the analysis of the whole girder the indented interface geometry turned out to be quite complex to be modelled so this option has not been examined. The stage composition was identical as in the previous analysis

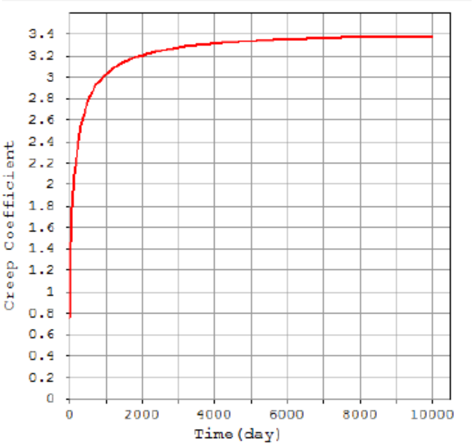

Fig. 7.9: HSC creep function

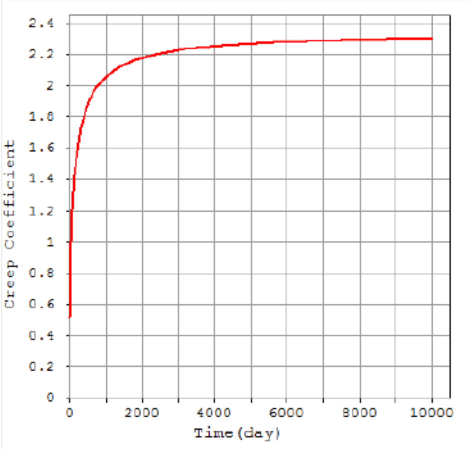

Fig. 7.10: NSC creep function

case.

7.6 Cracking behaviour analysis – Total Strain Crack model

For the analysis of progressive cracking of the girder due to bending under increasing load the Total Strain Crack (TSC) model is employed (see Appendix A). A fixed crack model is used with the secant stiffness option in the Newton-Raphson procedure, see Fig. 7.11. Thermal and dynamic effects are neglected. The lateral crack effect and the concrete confinement are not considered. The elasticity parameters are: Young's modulus for HSC 36900 N/mm^2 and for NSC 24400 N/mm^2, Poisson's ratio for both concretes 0.18. Moreover, the input data for the TSC model are specified below. For HSC the Hordijk model is adopted for tension with uniaxial tensile strength f_t = 4.4 MPa, fracture energy G_f = 0.114 N/mm, notional element size h= 320mm, while in compression and shear HSC is assumed to be elastic. For NSC the Thorenfeldt model is used for compression with the uniaxial compressive strength f_c = 28 MPa, while in tension and shear NSC is assumed to be elastic. The properties of the pre-stressing steel, assumed to remain in elastic state, are: Young's modulus 197200 N/mm^2, Poisson's ratio 0.3.

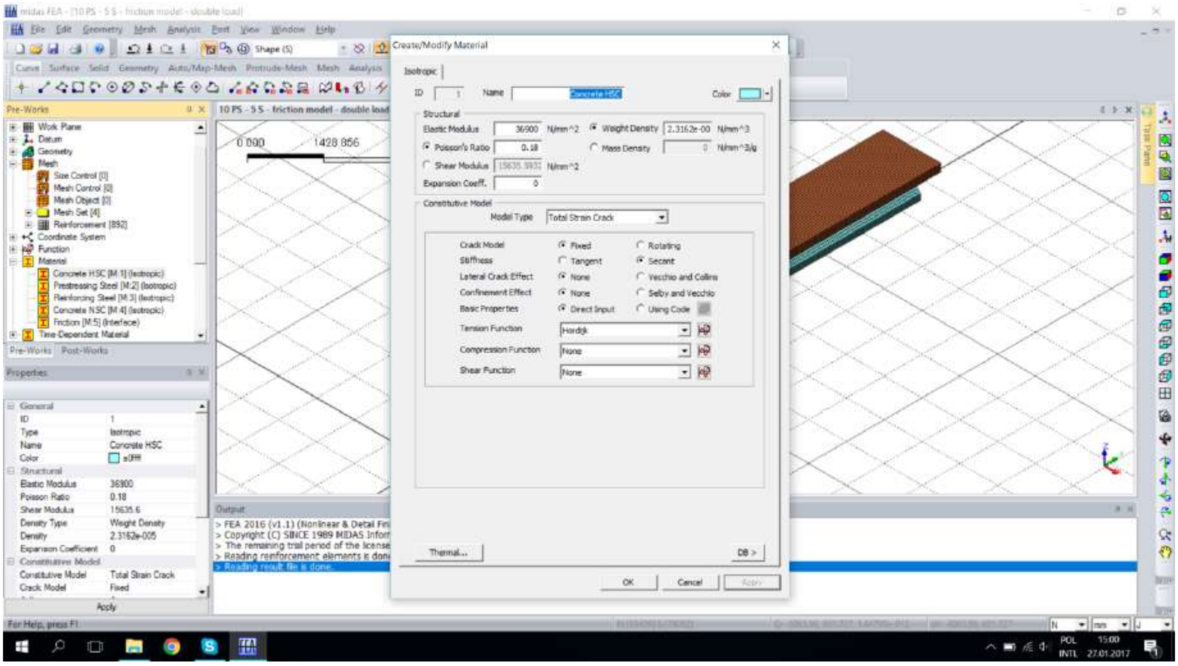

Create/Modify Material

Isotropic

ID 1 Name Concrete HSC Color

Structural

Elastic Modulus 36900 N/mm^2 ● Weight Density 2.3162e-00 N/mm^3

● Poisson's Ratio 0.18 ○ Mass Density 0 N/mm^3/g

○ Shear Modulus 15635.5932 N/mm^2

Expansion Coeff. 0

Constitutive Model

Model Type Total Strain Crack

Crack Model ● Fixed ○ Rotating

Stiffness ○ Tangent ● Secant

Lateral Crack Effect ● None ○ Vecchio and Collins

Confinement Effect ● None ○ Selby and Vecchio

Basic Properties ● Direct Input ○ Using Code

Tension Function Hordijk

Compression Function None

Shear Function None

Properties

General	
ID	1
Type	Isotropic
Name	Concrete HSC
Color	a0ffff
Structural	
Elastic Modulus	36900
Poisson Ratio	0.18
Shear Modulus	15635.6
Density Type	Weight Density
Density	2.3162e-005
Expansion Coefficient	0
Constitutive Model	
Constitutive Model	Total Strain Crack
Crack Model	Fixed

Output

```
> FEA 2016 (v1.1) (Nonlinear & Detail Fin
> Copyright (C) SINCE 1989 MIDAS Infor
> The remaining trial period of the license
> Reading reinforcement elements is done
> Reading result file is done.
```

Fig. 7.11: Example input data for TSC model

The load is incrementally applied to the model and successive stages of crack development are shown in Figures 7.12-7.14. After applying the load of 685 kN the first cracks are noticed. When the load increases further, we can observe a 3D crack pattern forming in the middle part of the beam. Fig. 7.15 shows how cracks propagate to the sides of the beam. After reaching the ultimate load of 1230 kN the model predicts failure due to reaching the yield stress of the strands after extensive softening of concrete.

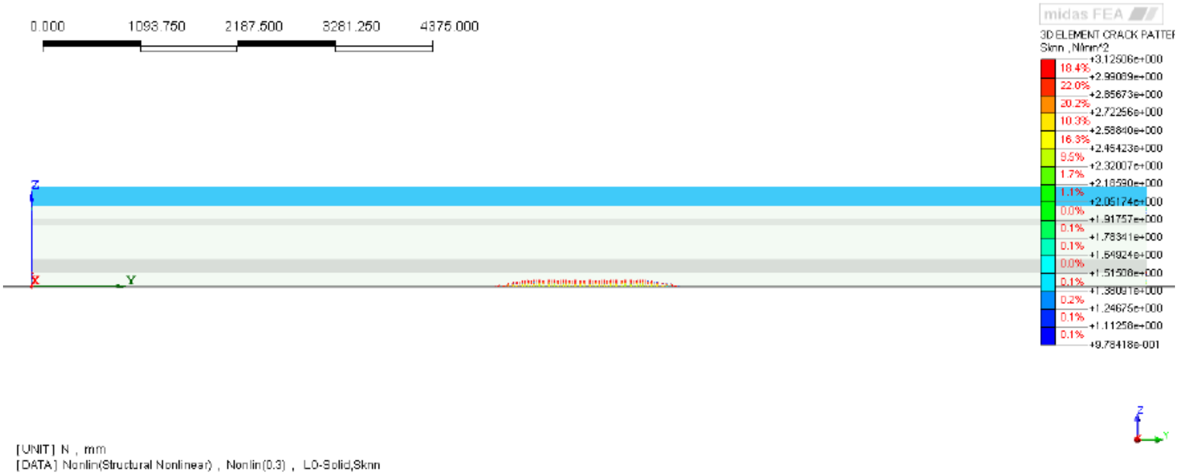

Fig. 7.12: Crack pattern after reaching the load of 685kN

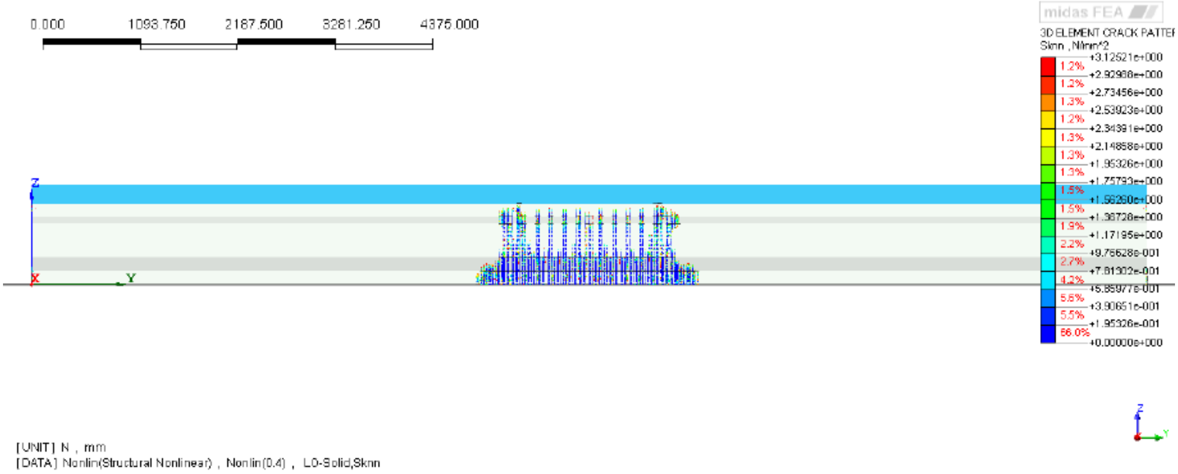

Fig. 7.13: Development of cracks after increasing the load

Fig. 7.16 shows the anchorage zone area of the pre-stressed element. In this work the anchorage zone is not checked, therefore no special protection for this zone has been applied. However, the shear reinforcement spacing was reduced here to protect the anchorage zone against splitting forces.

From the diagram of the load versus the displacement of node 18832 (which is situated at the bottom in the middle of the beam), shown in Fig. 7.17, we can observe that the linear behaviour finishes for the deflection of 2 mm.

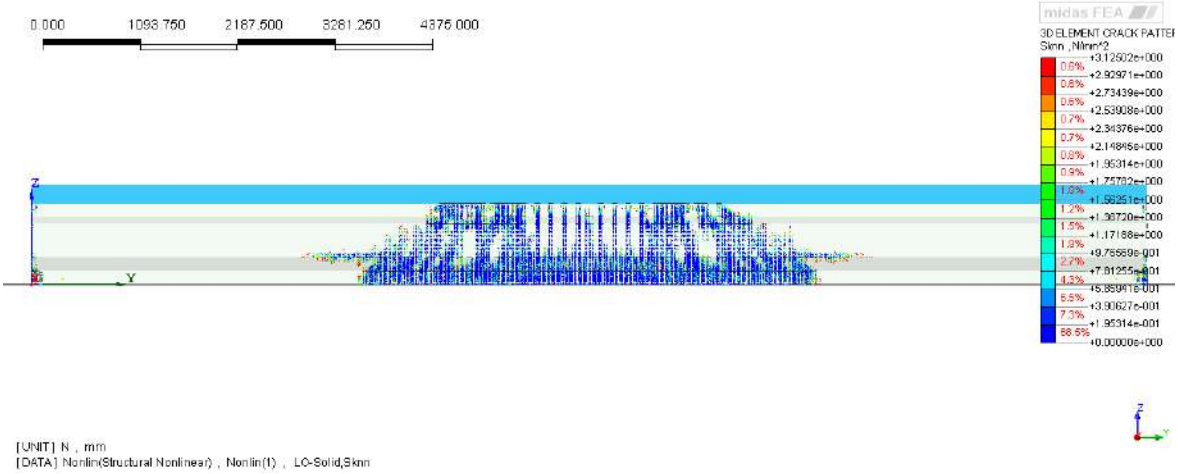

Fig. 7.14: Development of cracks before failure

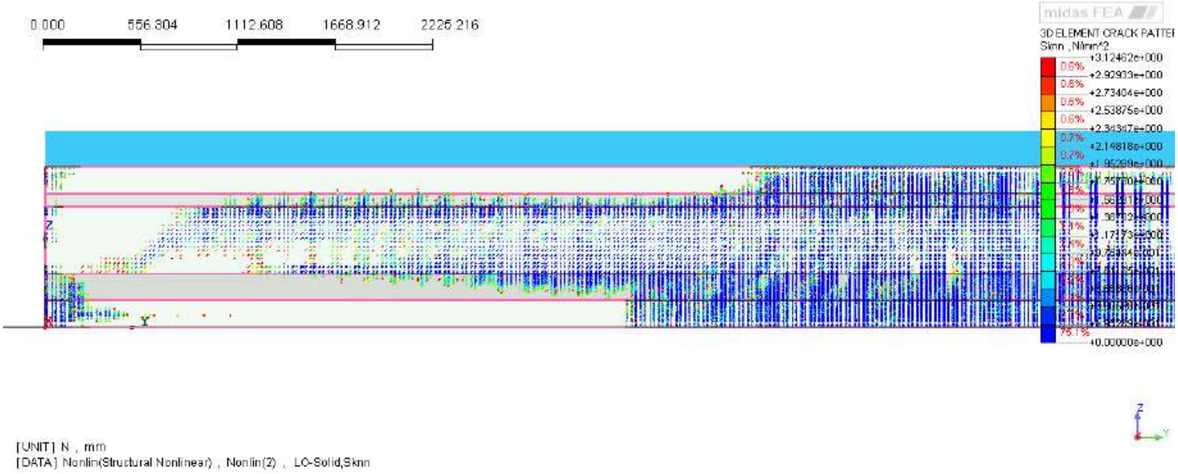

Fig. 7.15: Crack pattern at failure after reaching the load of 1230 kN

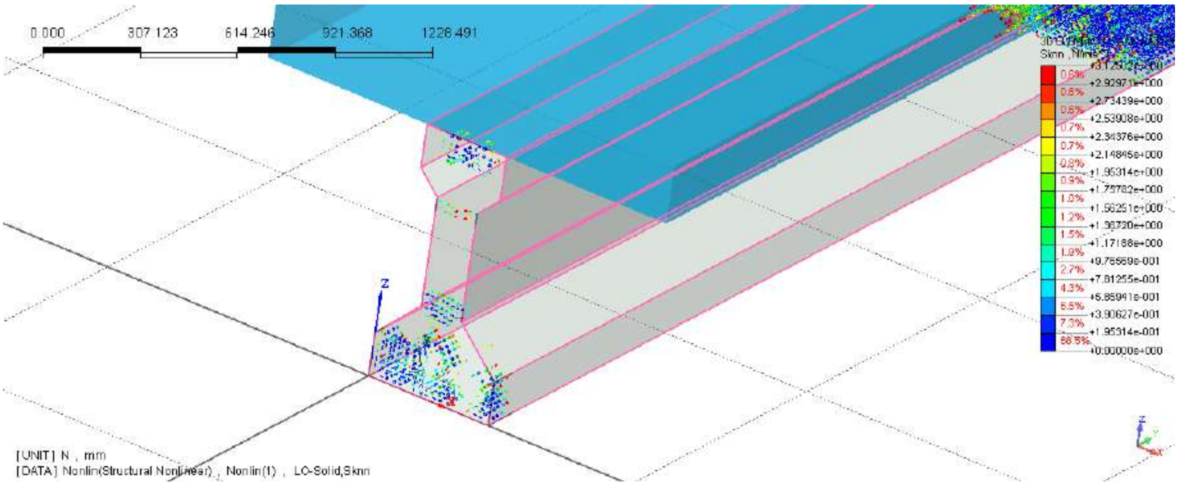

Fig. 7.16: Anchorage zone

Assessing the test results, the focus is on the flexural response. Analysing the load-deflection diagrams for all three types of the girder, it is noticed that the presence and

Fig. 7.17: Load vs displacement graph

the width of the composite slab has a significant influence on the cracking load, load-bearing capacity at the ultimate limit state and on the failure mode for the flexural response. For the 1.5-meter-wide slab we observe a linear initial stiffness and then the cracking of concrete occurs. The load-displacement relation becomes non-linear and a significant deflection at mid-span is observed before failure.

8 Construction stage analysis results

The structure is completed in a number of construction stages (CS). The configuration of the structure, loading, boundary conditions, physical properties of structural members can change during the construction stages, especially when composite and additionally pre-stressed structures are considered [Adanur et al., 2012, Dolinajová and Moravčík, 2013, Adanur et al., 2012, Altunisik et al., 2010, Somja and de Ville de Goyet, 2008, Karakaplan et al., 2009, Taejun and Tae, 2008, Mari, 2000]. If the structural system changes as the construction progresses, the real behaviour of the structure in the final stage may be different from that analyzed without considering the staging. The elastic CS analysis of the model described in Chapter 7 is divided into 5 construction stages. Then the results of the analysis which neglects the staging effects are presented.

8.1 First stage – concrete girder with reinforcement

In the modelling procedure it is impossible to reproduce the actual flow of events during the production of a prestensioned element. Instead, the first stage of constructing the girder model is treated as a *virtual stage* to see the behaviour before pre-stressing. In reality the strands are tensioned on the stressing-bed and then concrete is cast, in the numerical simulation it is not possible to model the strands first, but in the case of linear analysis the Boltzmann superposition principle holds. In the first stage only the self-weight load of the girder and steel stirrups is active. Fig. 8.1 shows the deflection of the girder with maximum mid-span value of 2.5 mm.

In this stage the maximum tensile stress in the direction defined by the longitudinal axis of the girder is calculated as 2.38 MPa and the maximum compressive stress is 3.03 MPa (Fig. 8.2).

8.2 Second stage – pre-stressing of the girder

In the second stage the strands are embedded into the girder and pre-stressing force is applied. As a result, camber is observed. In Fig. 8.3 the camber is shown with maximum negative deflection of almost 8 mm.

In Fig. 8.4 the local concentration of longitudinal tensile stresses close to the anchorage zone can be observed, this part of the model is zoomed in and shown in Fig. 8.5.

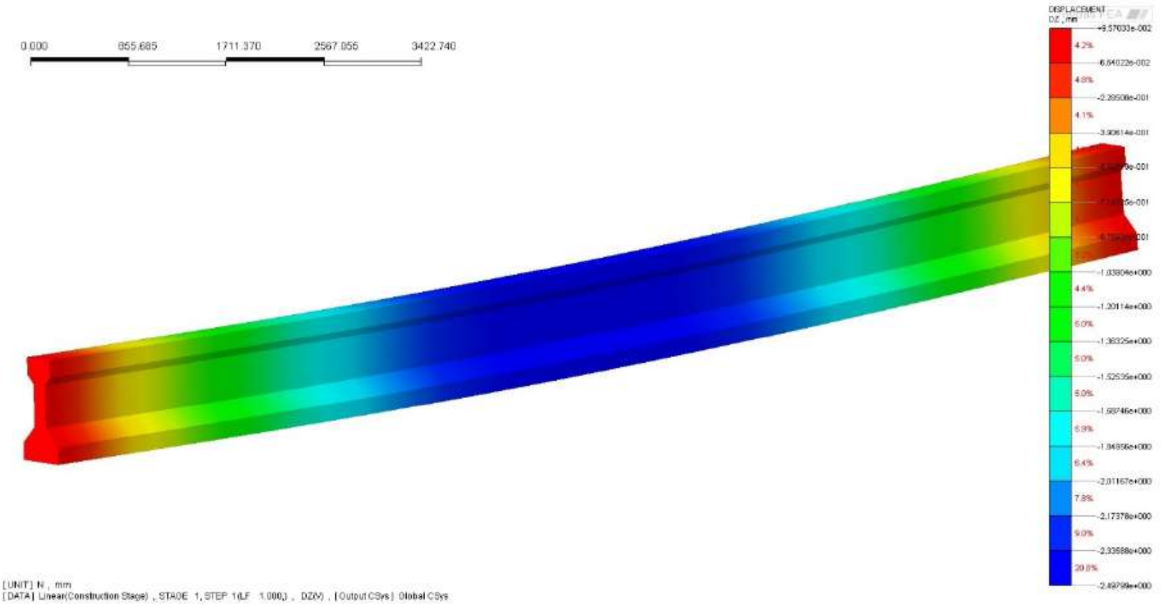

Fig. 8.1: Deflection of the girder after stage 1

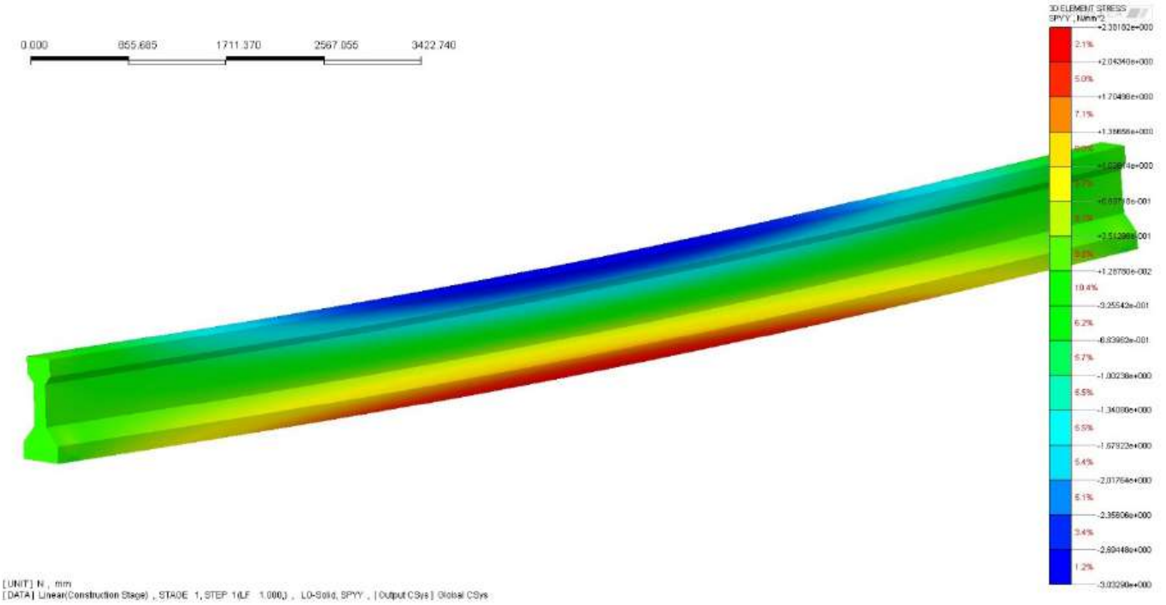

Fig. 8.2: Longitudinal stress distribution after stage 1

In this figure the stress distribution over the cross-section is examined. The average compressive stress along the girder is about 30 MPa, while in the anchorage zone the maximum compressive stress is about 57 MPa. In Fig. 8.6 the longitudinal stress distribution along pre-stressing strands is shown with a maximum value of about 1400 MPa.

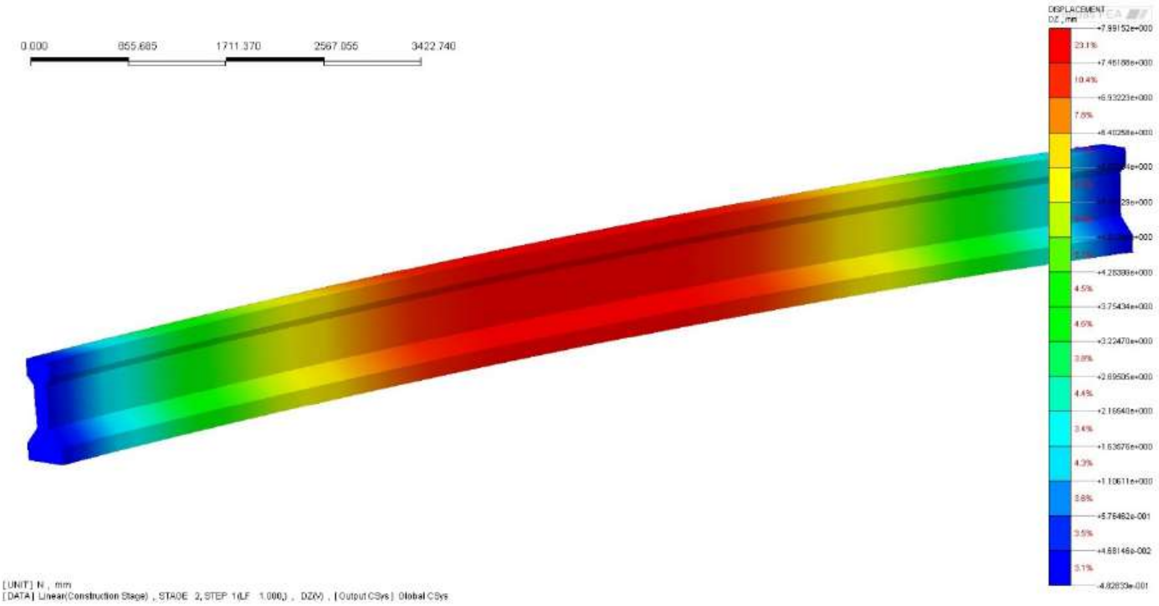

Fig. 8.3: Displacements due to self-weight and pre-stressing

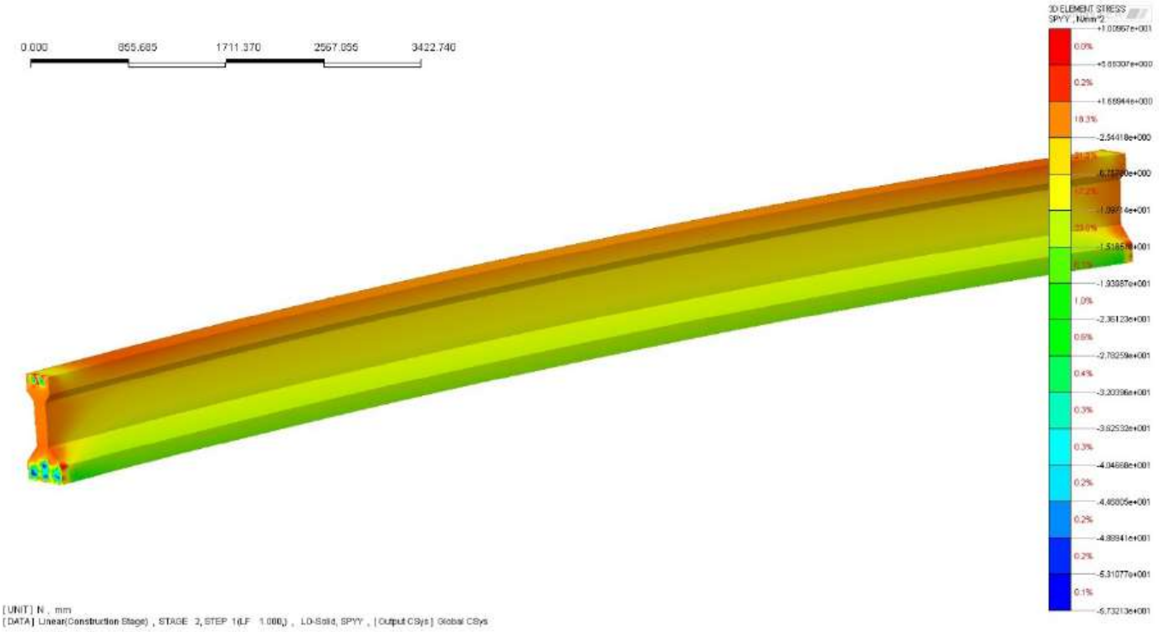

Fig. 8.4: Longitudinal stress $\sigma_y y$ due to self-weight and pre-stressing

8.3 Third stage – slab casting – wet concrete load

In the third stage casting of the normal-strength concrete deck is simulated. To represent wet concrete with density $\rho = 2316$ kg/m^3 an equivalent uniform pressure load is applied to the top surface of the girder (Fig. 8.7).

In this stage the wet-concrete load reduces the maximum camber reached in the second stage (after pre-stressing forces were applied) from 7.99 mm to 5.48 mm (Fig. 8.8).

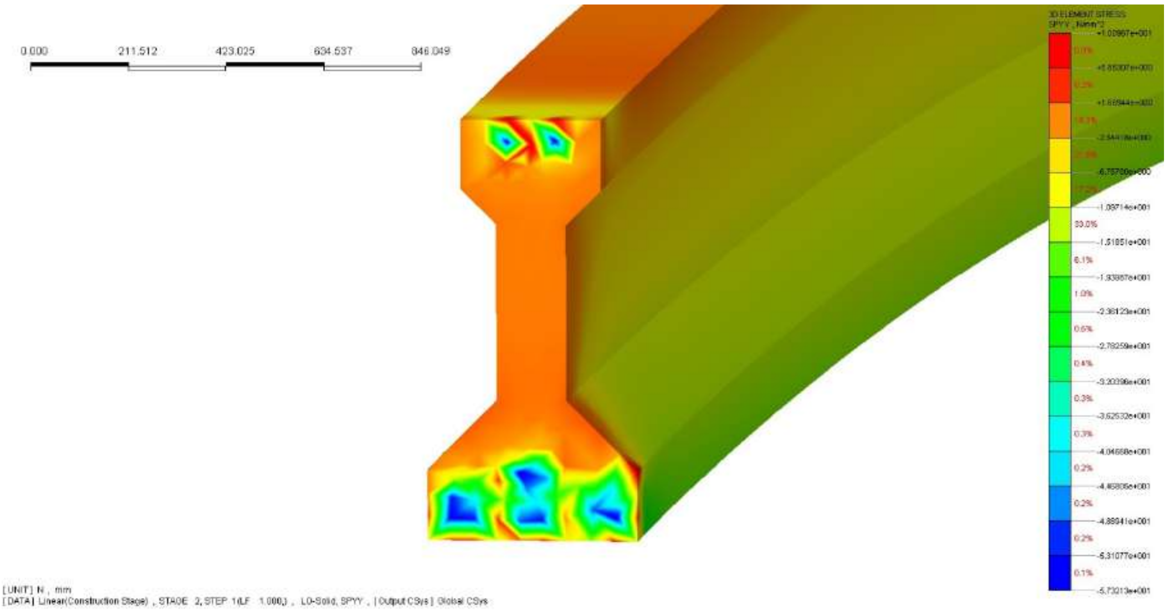

Fig. 8.5: Longitudinal stress distribution in anchorage zone

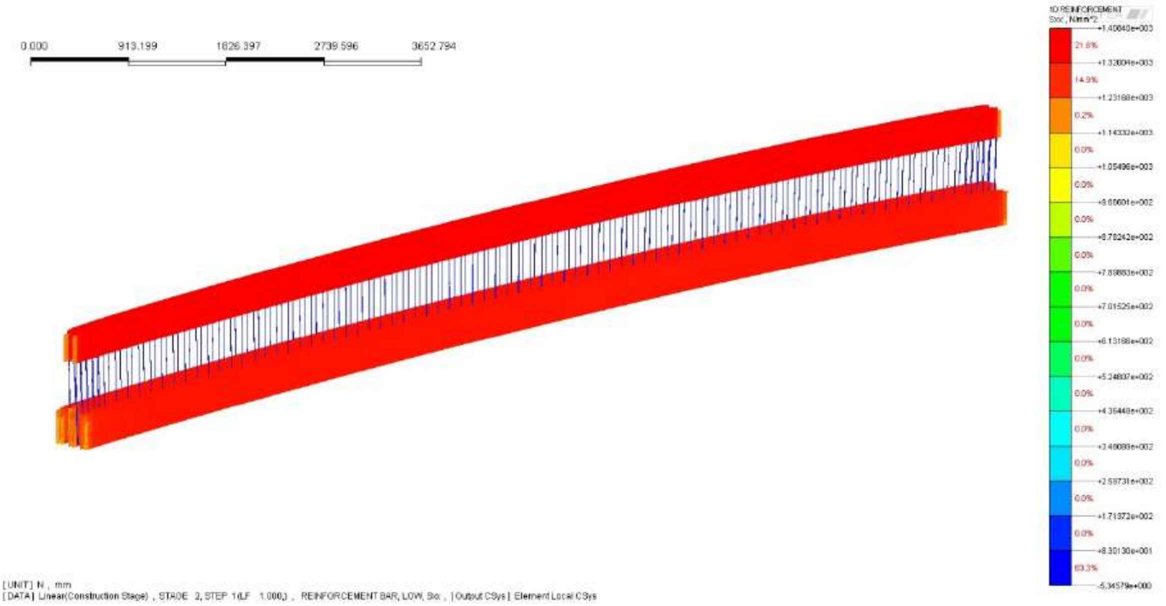

Fig. 8.6: Stress in pre-stressing strands

8.4 Fourth stage – composite girder

In the fourth stage the cross-section of the girder becomes composite, the substitute wet-concrete load is deactivated in this stage and the slab stiffness becomes active. The cross-section of the girder now consists of two parts: the girder and the slab with rigid connection between them. The changes of the slab weight due to evaporation of water during the hardening of concrete have been neglected. Comparing the results of stage 3 and 4 no significant differences are expected. This is shown in Figures 8.9 and 8.10.

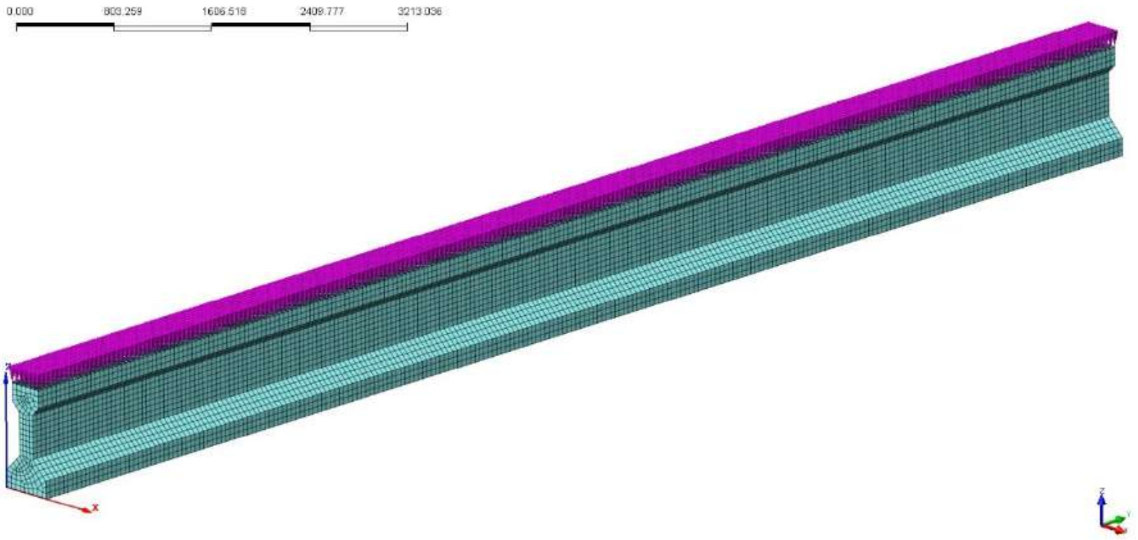

Fig. 8.7: Wet-concrete load

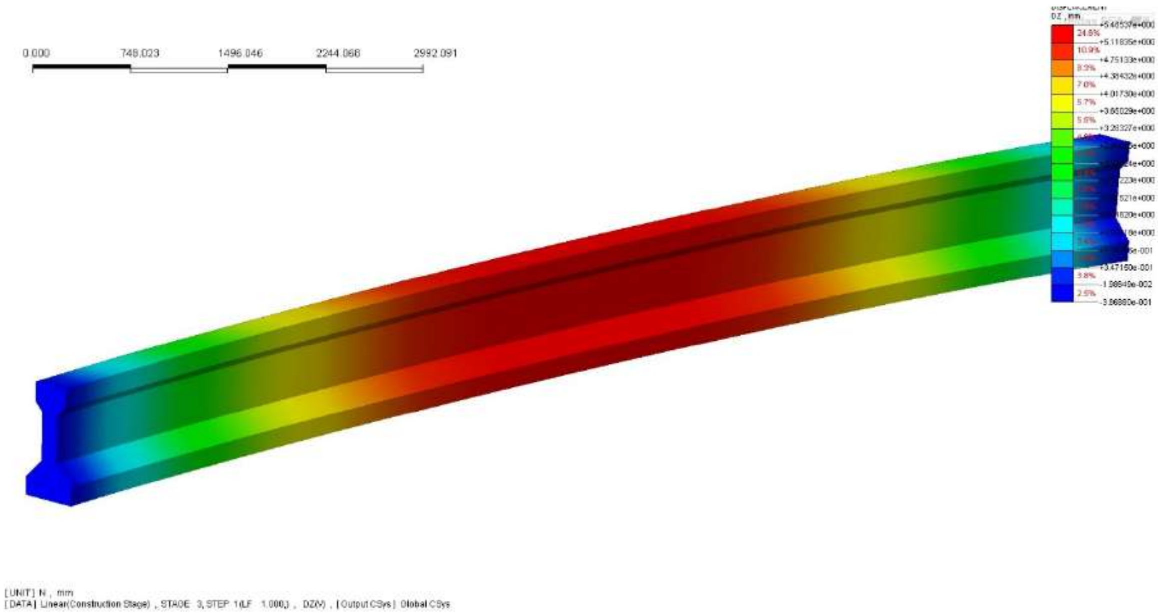

Fig. 8.8: Displacement after applying wet-concrete load

The maximum vertical displacement of the composite girder at the mid-span is 5.46 mm, so it is almost the same as in stage 3.

8.5 Fifth stage – external load

In the last stage the external load is applied as shown in Fig. 7.17. The value of the load is adopted according to the experimental results as described in Section 7.4. The maximum displacement caused by the cracking load is 4.6 mm with $L/250$ condition

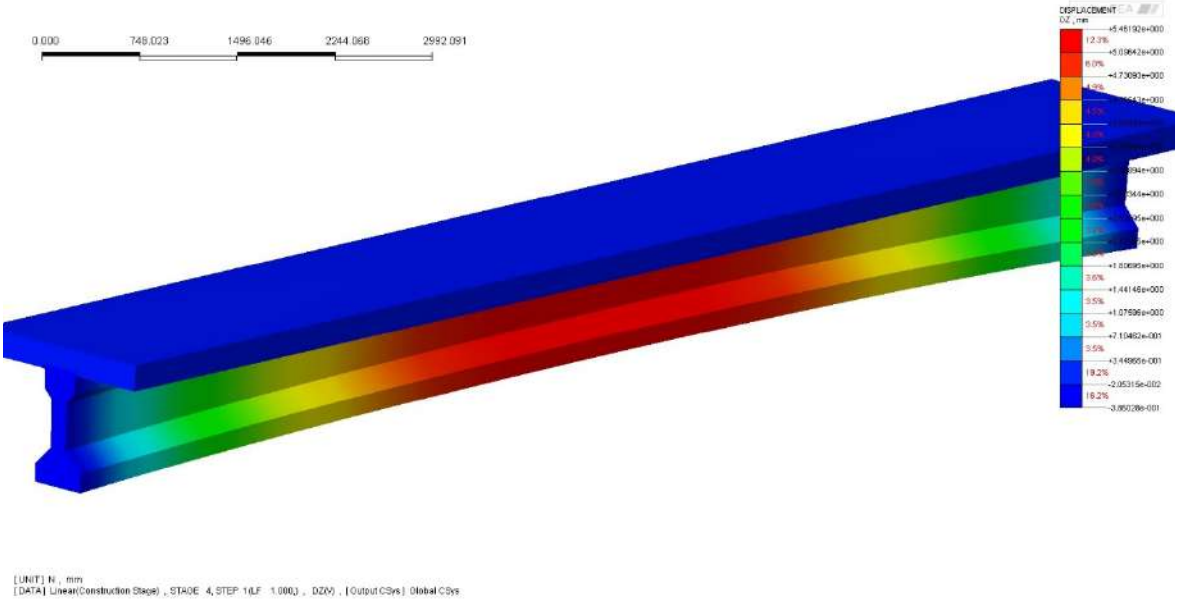

Fig. 8.9: Displacement of composite girder (due to graphics malfunction proper deck curvature is not represented)

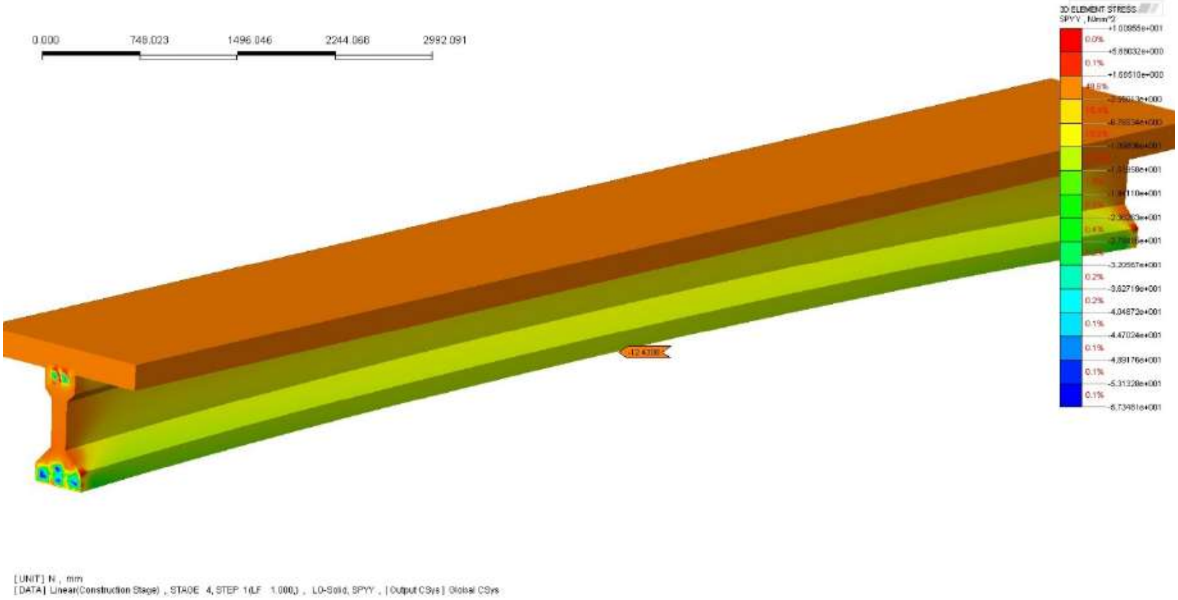

Fig. 8.10: Longitudinal stress in composite girder after stage 4 (due to graphics malfunction proper deck curvature is not represented)

of 5 mm (Fig. 8.11). The maximum tensile stress at the mid-span of the girder is calculated as 3.7 MPa (Fig. 8.12), which compares well to the tension strength f_t = 4.58 MPa of concrete with approximately the same grade as the one assumed.

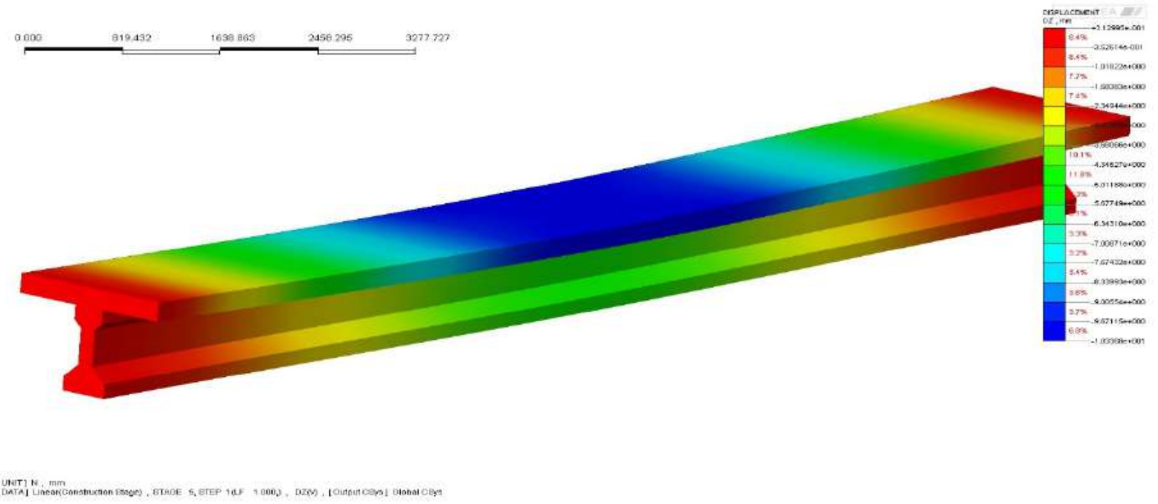

Fig. 8.11: Displacement due to external cracking load

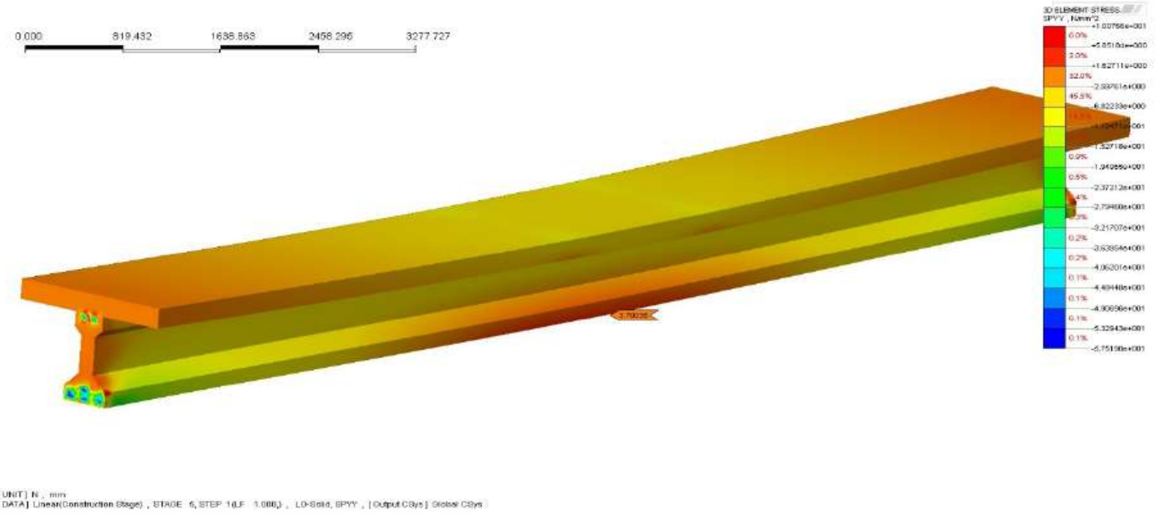

Fig. 8.12: Longitudinal stress after stage 5

8.6 Final results without construction stage analysis

To check the influence of the construction stage analysis even for the structure which is modelled using FEM without taking into account time-dependent behaviour, an analysis without staging is performed. The deflection and stress show that there is a significant difference between the analysis with or without construction staging. The current research allows one to expect even bigger differences when taking into account other phenomena like creep and shrinkage of concrete, evolution of compressive strength of concrete in time etc.

Fig. 8.13 shows that the maximum deflection at the mid-span of the composite girder is calculated as 3.8 mm. When compared with 4.6 mm obtained from the construction stage analysis it is 21% underestimated.

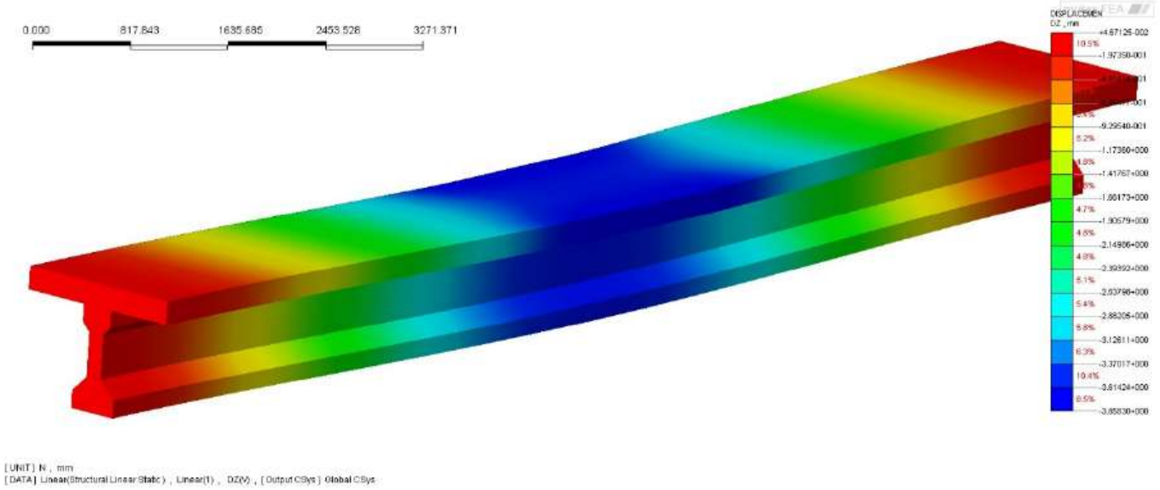

Fig. 8.13: Maximum displacement of composite girder without CS analysis

Much more dangerous from the safety point of view is the difference in stress distribution. Fig. 8.12 shows that the maximum tension stress at the mid-span is 2.81 MPa. The stress obtained from construction stage analysis at the final stage is 3.7 MPa, it is 31% larger.

According to Eurocode 2 for concrete grade higher than $C50/60$ the following formula is valid: $f_{ctm} = 2.12 \cdot (\ln{(1 + 0.1 \cdot f_{cm})})$. Hence, the mean value of tensile strength f_{ctm} for the concrete with compressive strength $f_{cm} = 69$ MPa is equal to 4.58 MPa, and the computed tensile stress is lower than the safety limit.

9 Construction stage analysis with time-dependent effects

9.1 Third stage – casting the slab – wet concrete load

In this chapter the evolution of concrete stiffness due to creep is taken into account and the creep model according to Eurocode is first employed, see Figures 7.9 and 7.10. Then, the construction stage analysis with creep is repeated using the implemented Maxwell rheological model.

The first and the second stages are not presented because there is no creep influence on the deformations and the stress distribution then. The results from the construction stage analysis with or without taking into account the creep phenomenon are also the same for these two stages. In the third stage, after the pre-stressing is applied and the wet concrete load as well, the model predicts the mid-span deflection (camber) of 12.7 mm (Fig. 9.1), comparing with 5.48 mm when creep is not taken into account. This difference occurs due to creep behaviour in 14 days after pre-stressing of the girder.

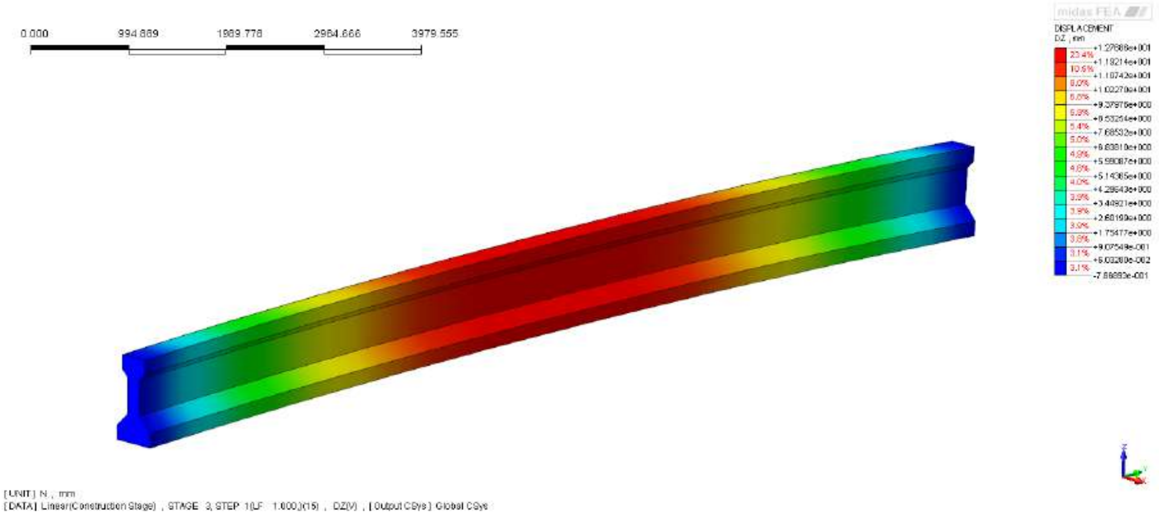

Fig. 9.1: Displacement after application of wet-concrete load when creep is considered

9.2 Fourth stage – composite girder

In this stage, after forming the composite section, the mid-span deflection increases slightly from 12.7 mm to 13.2 mm (Fig. 9.2). The small increment of the deformation is due to creep of concrete which is limited by a self-weight load of the slab. The stresses in the girder in this stage (Fig. 9.3) are lower comparing with the third stage (the difference is about 1.0 MPa) and this is because of creep which causes a decrease in pre-stressing force (Fig. 9.4).

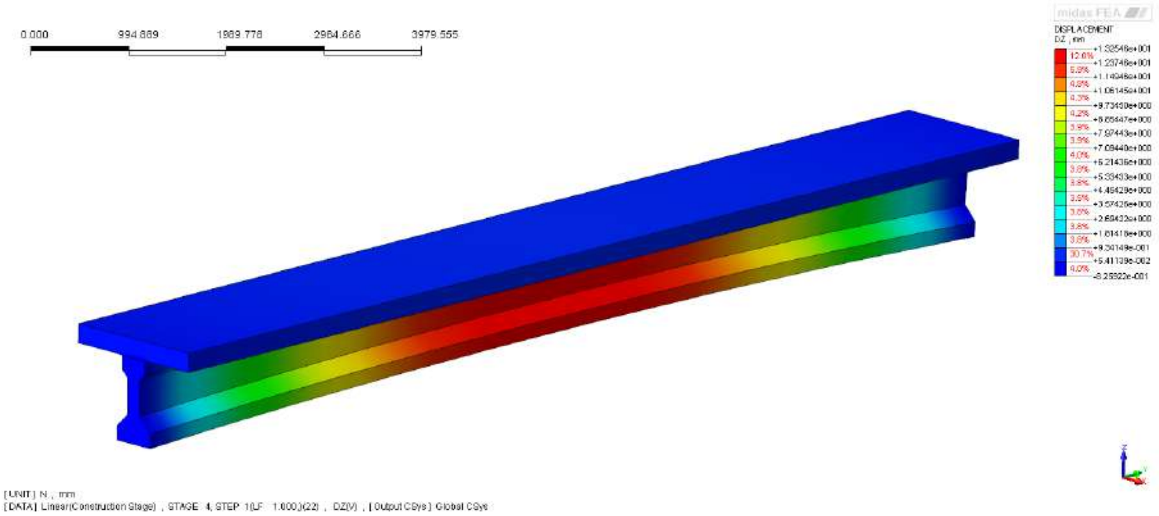

Fig. 9.2: Displacement of composite girder with creep considered (due to graphics malfunction the curvature of the deck is not represented)

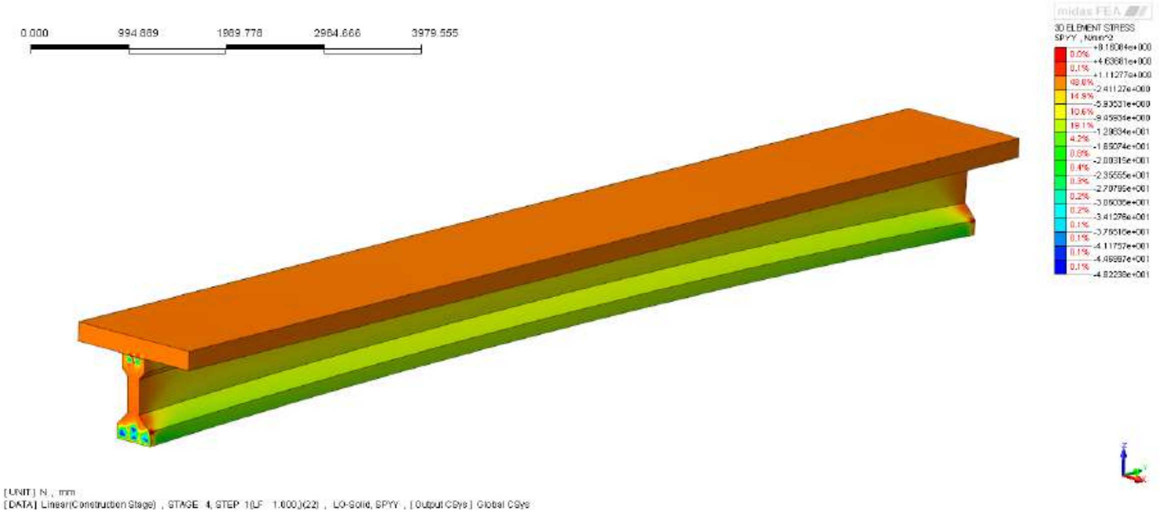

Fig. 9.3: Longitudinal stress in composite girder with creep considered

9.3 Fifth stage – external load

After the cracking load is applied one can observe the change in the girder deflection (camber) from 13.2 mm to 3.42 mm and deflection of the slab becomes 9.6 mm (Fig. 9.5). The deflection of the slab is approximately the same as the deflection in CS analysis without time-dependent behaviour in the fifth stage. This is because the creep

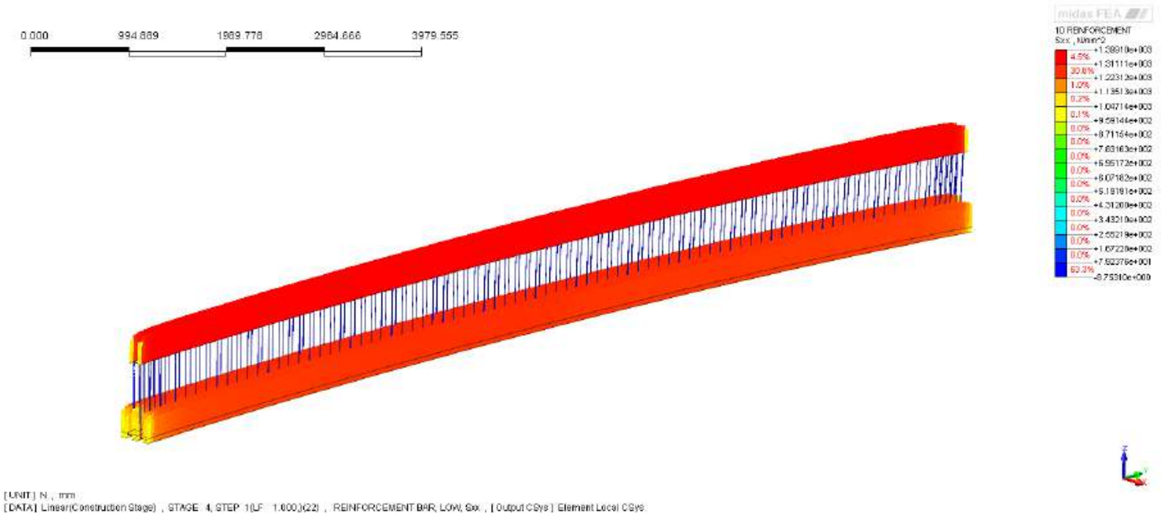

Fig. 9.4: Stress distribution along pre-stressing strands

phenomenon for NSC (slab) starts in this stage when the external load is applied on the slab. In the short time period creep has a positive influence on the girder deflection which is smaller and but still negative. The maximum tensile stress at the mid-span on the bottom surface is now 4.28 MPa (Fig. 9.6) comparing with 3.7 MPa when creep is not taken into account.

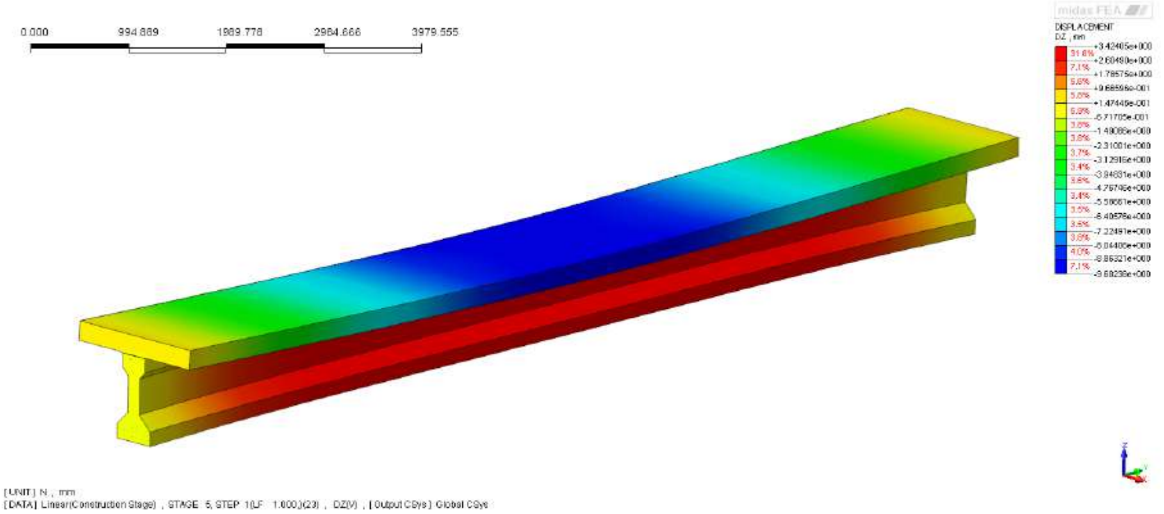

Fig. 9.5: Deflection of composite girder after loading

9.4 Sixth stage – long term behaviour (10000 days)

The sixth stage is an additional stage which represents long-time behaviour of concrete and it is finished after 10000 days. The deflection of the girder increases from negative 3.42 mm to positive 8.0 mm and from 9.6 mm to 21 mm for the slab (Fig. 9.7). The

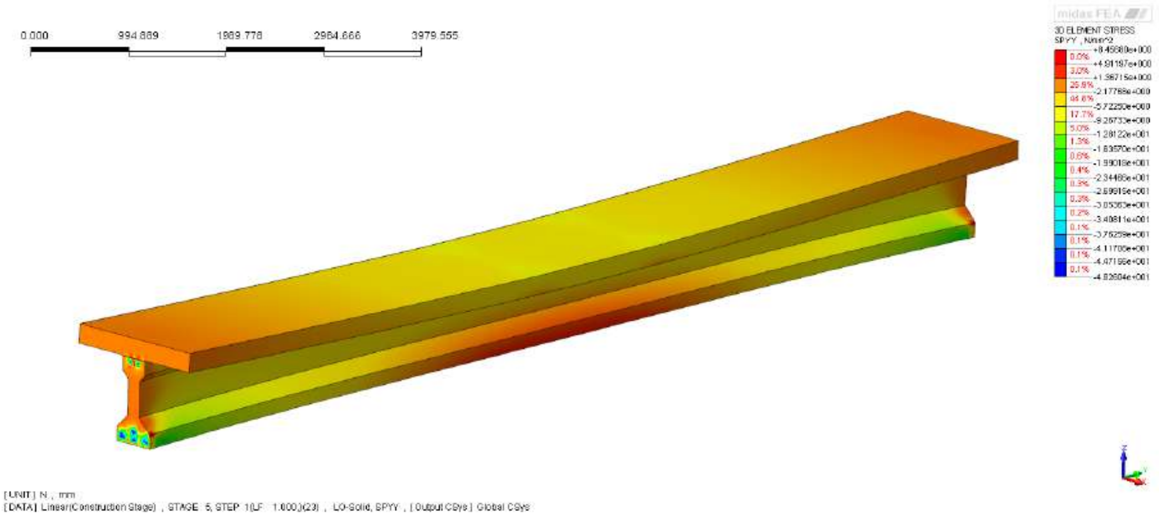

Fig. 9.6: Longitudinal stress distribution after loading

increase of the maximum tensile stress at the mid-span on the bottom surface of the girder due to the creep is observed with the value of 7.68 MPa which exceeds the tensile strength of concrete (Fig. 9.8).

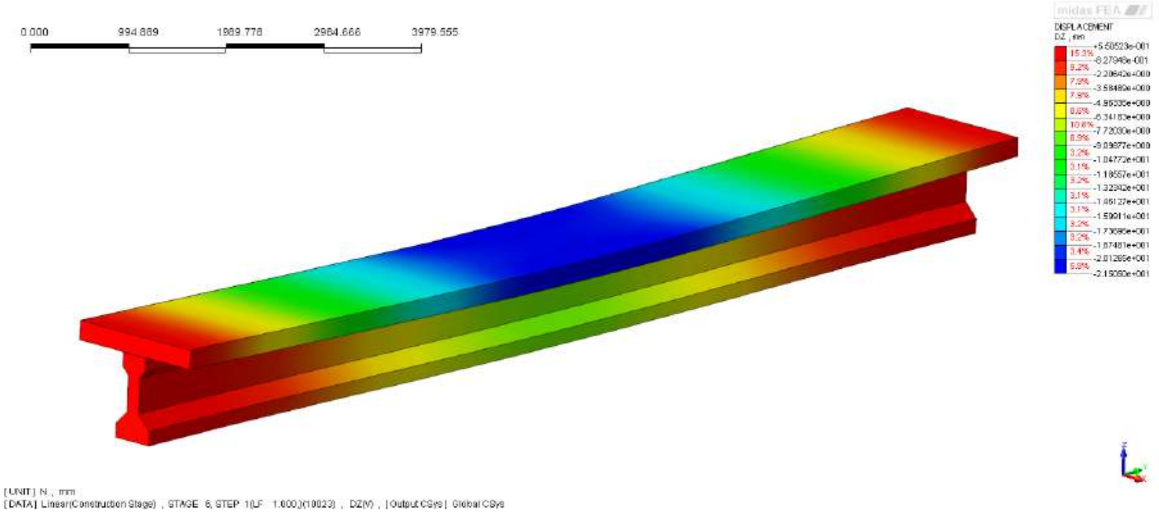

Fig. 9.7: Deflection of composite girder for long time behaviour (after 10000 days)

The longitudinal stress distribution along the pre-stressing strands after 10000 days is shown in Fig. 9.9. The maximum stress in strands is 1316 MPa and long-term loss of the pre-stressing force due to creep is observed (7% loss).

9.5 Input data for Generalized Maxwell model

In this section the three-dimensional Generalized Maxwell model is used, which has been implemented into the software as user-supplied subroutine of a material model. In

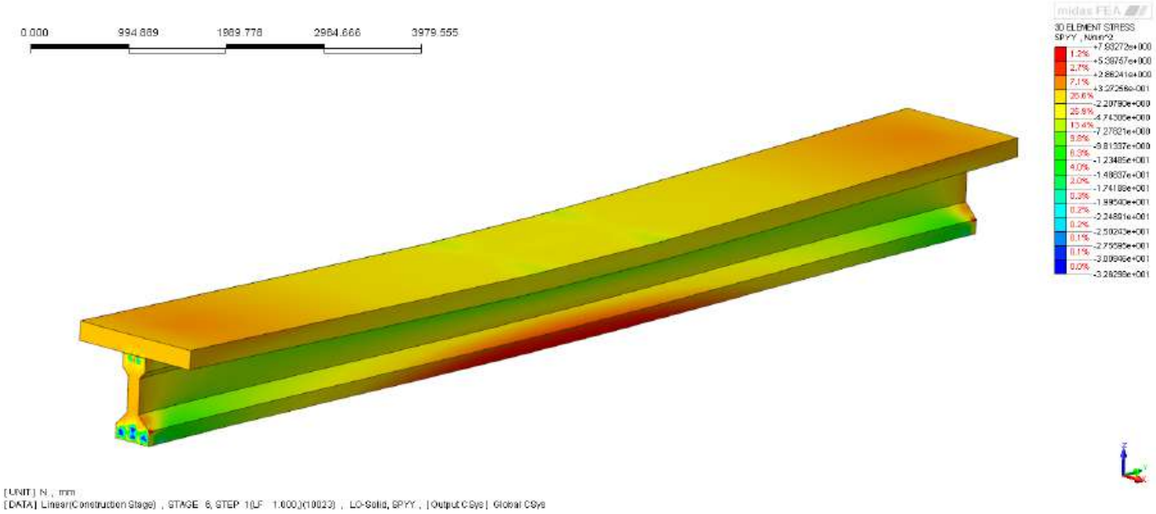

Fig. 9.8: Longitudinal stress distribution after 10000 days

Fig. 9.9: Stress distribution along the pre-stressing strands after 10000 days

this routine the parameters, internal state variables and integer indicator are defined. Fig. 9.10 presents the dialog window with the basic input data for the high-strength concrete. Table 9.1 contains the input data for the assumed five Maxwell chains $i = 0 \dots 4$. The source code of the model can be found in Appendix C at the end of this thesis. The results of calculations with the implemented model are presented in the next sections.

9.6 Third stage – casting the slab (Maxwell model)

As at the beginning of this chapter, the first and second stages are omitted in the study description. The influence of wet concrete appears in the third stage. Also in this stage

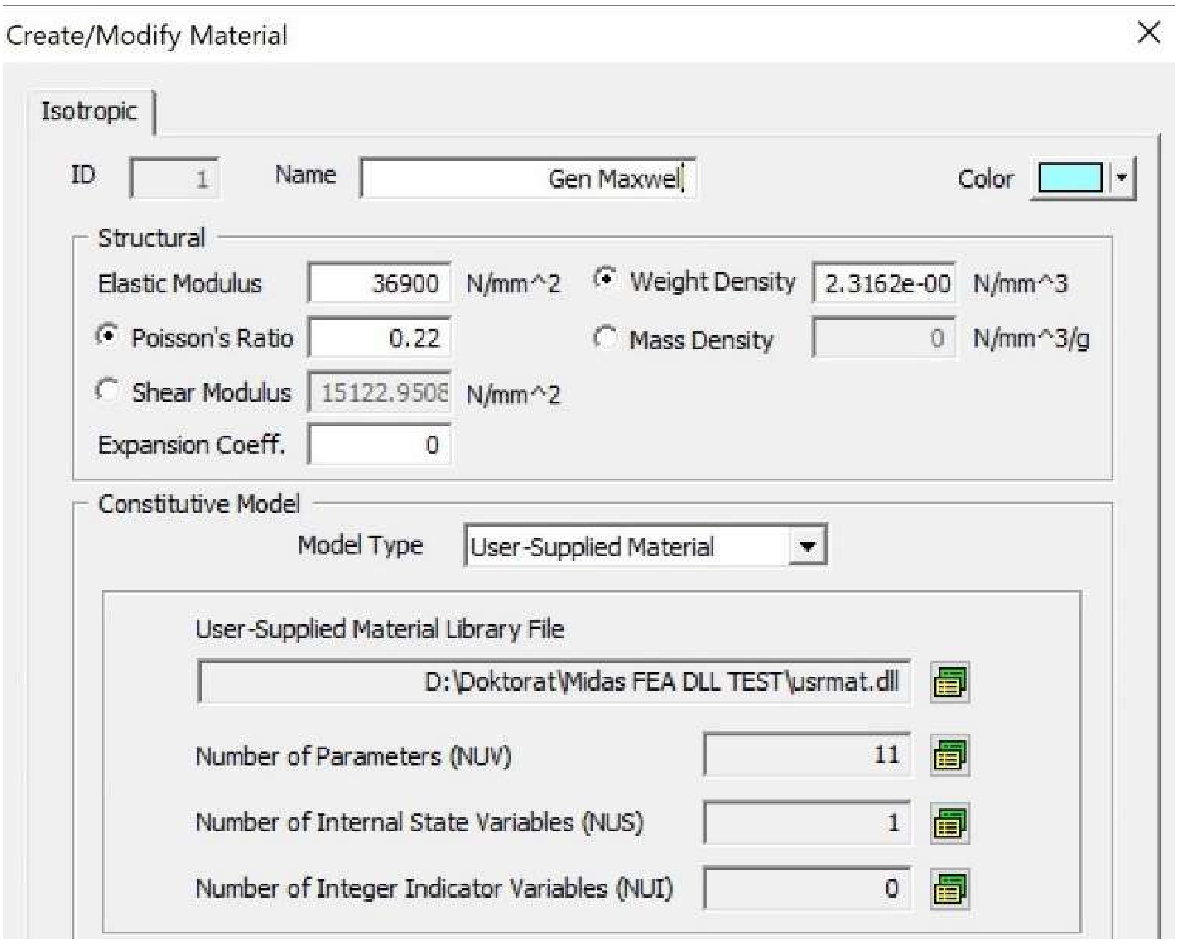

ID 1
Name Gen Maxwel
Color

Elastic Modulus 36900 N/mm^2

● Weight Density 2.3162e-00 N/mm^3

● Poisson's Ratio 0.22

○ Mass Density 0 N/mm^3/g

○ Shear Modulus 15122.9508 N/mm^2

Expansion Coeff. 0

Model Type User-Supplied Material

User-Supplied Material Library File D:\Doktorat\Midas FEA DLL TEST\usrmat.dll

Number of Parameters (NUV) 11

Number of Internal State Variables (NUS) 1

Number of Integer Indicator Variables (NUI) 0

Fig. 9.10: User supplied material definition

Table 9.1: Data used in computations with Maxwell model

i	E_i [Pa]	η_i [Pa·days]
0	6.9d9	0
1	9.0d9	9.0d9
2	6.0d9	6.0d10
3	9.0d9	9.0d11
4	6.0d9	6.0d12

the pre-stressing is applied, which causes a mid-span deflection of 10.2 mm (Fig. 9.11). This can be compared to 12.7 mm when using the Eurocode model of creep.

9.7 Fourth stage – composite girder (Maxwell model)

In the next stage the slab is added at the top of the girder, which influences the increment of the deformation. The mid-span deflection increases to 10.7 mm (Fig. 9.12).

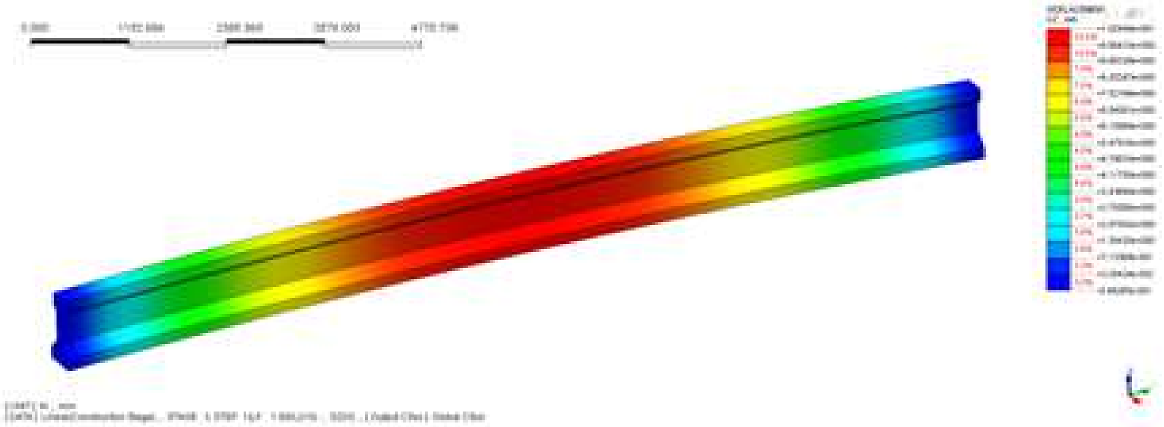

Fig. 9.11: Displacement due to wet-concrete load for Maxwell creep model

The stresses in the girder in this stage reach the value of 2.32 MPa (Fig. 9.13), which corresponds with the values obtained previously for the Eurocode model at the same stage, the difference is 0.5 MPa. Fig. 9.14 shows the stress distribution along prestressing strands.

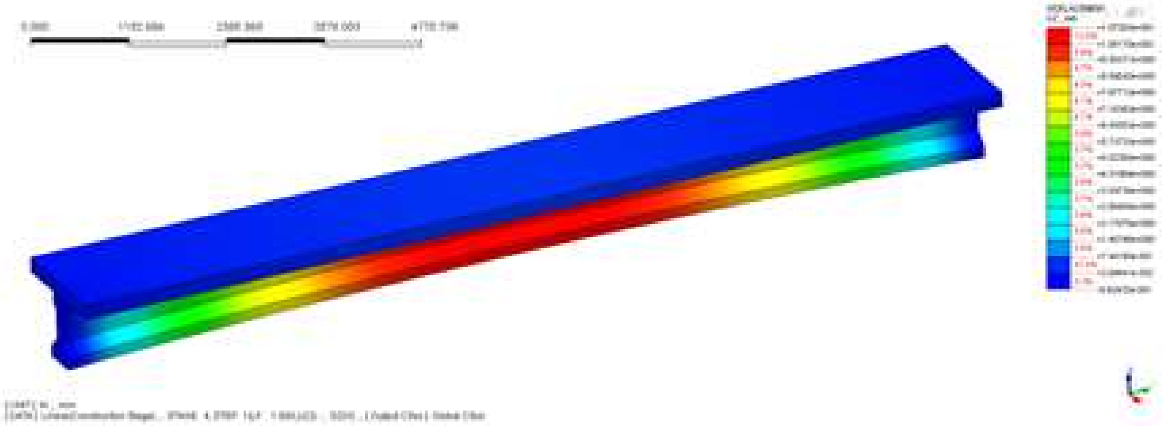

Fig. 9.12: Displacement of composite girder for Maxwell creep model (due to graphics malfunction the curvature of the deck is not represented)

9.8 Fifth stage – external load (Maxwell model)

In the fifth stage the influence of creep on the slab occurs after applying the external load. It is noticed that the deflection of the slab in the fifth stage of the CS analysis without time-dependent behaviour and the values obtained with time-dependent effects according to the Eurocode creep model are quite similar with the values observed with the Maxwell rheological model. In this last case the girder deflection decreases from 12.7 mm to 2.91 mm (Fig. 9.15). The maximum tensile stress at the mid-span on

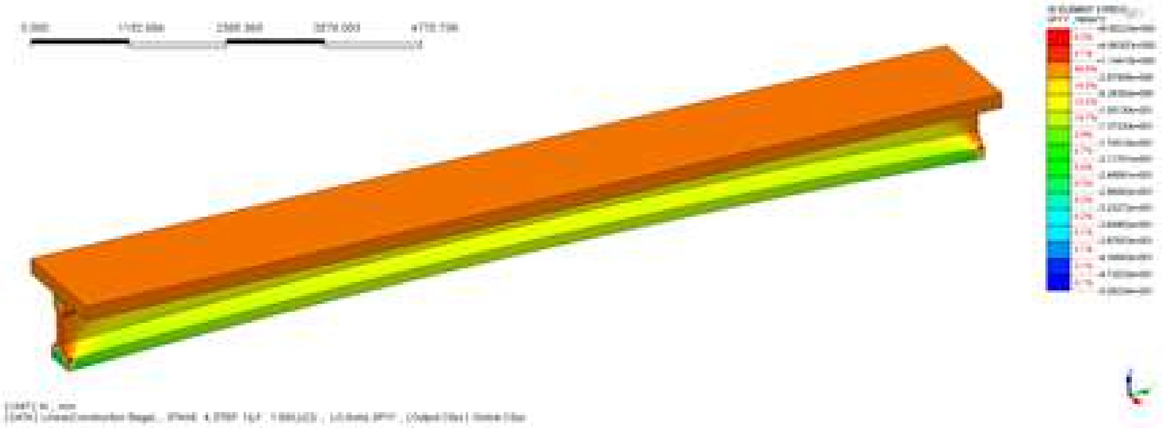

Fig. 9.13: Longitudinal stress in composite girder for Maxwell creep model

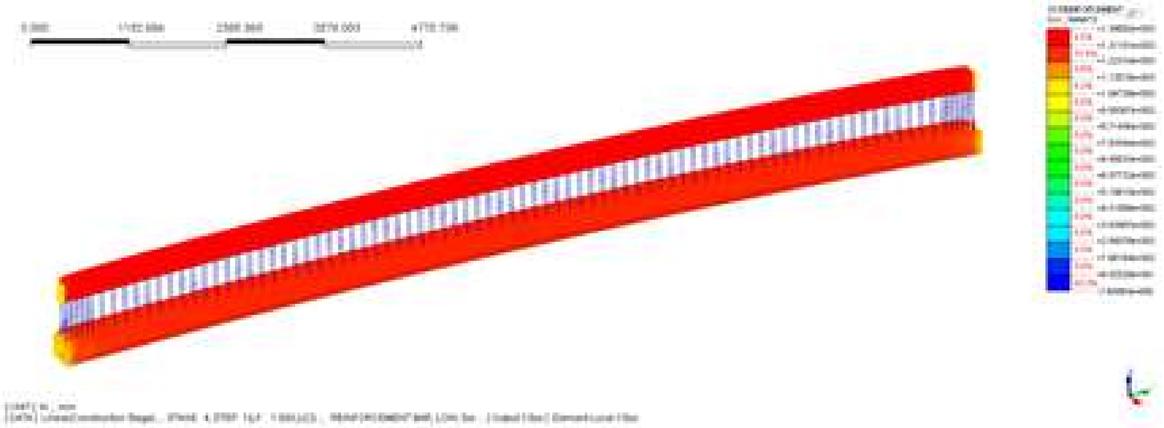

Fig. 9.14: Stress distribution along pre-stressing strands for Maxwell creep model

the bottom surface is now 3.90 MPa (Fig. 9.16). After reviewing the values from the previously investigated model without creep phenomenon, it is noticed that in that case the stress reached 3.70 MPa.

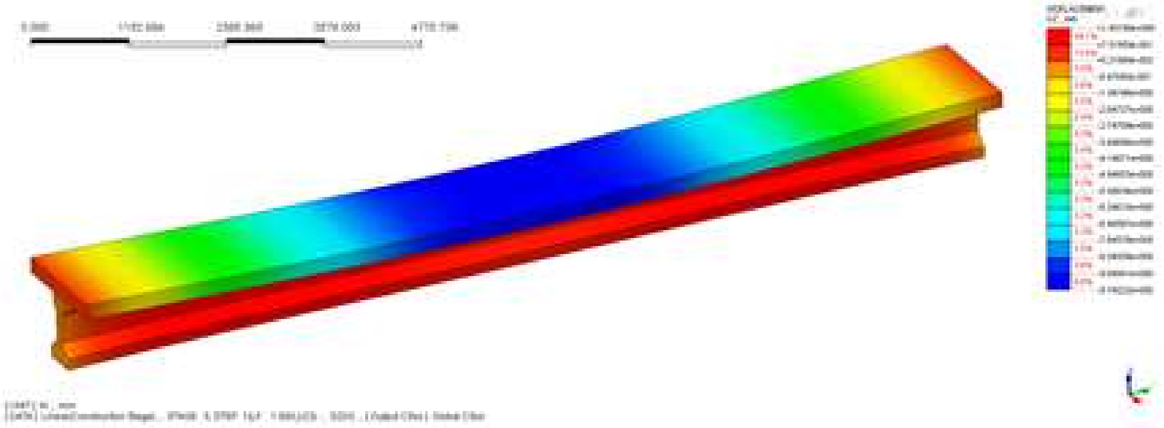

Fig. 9.15: Deflection of the composite girder for Maxwell creep model

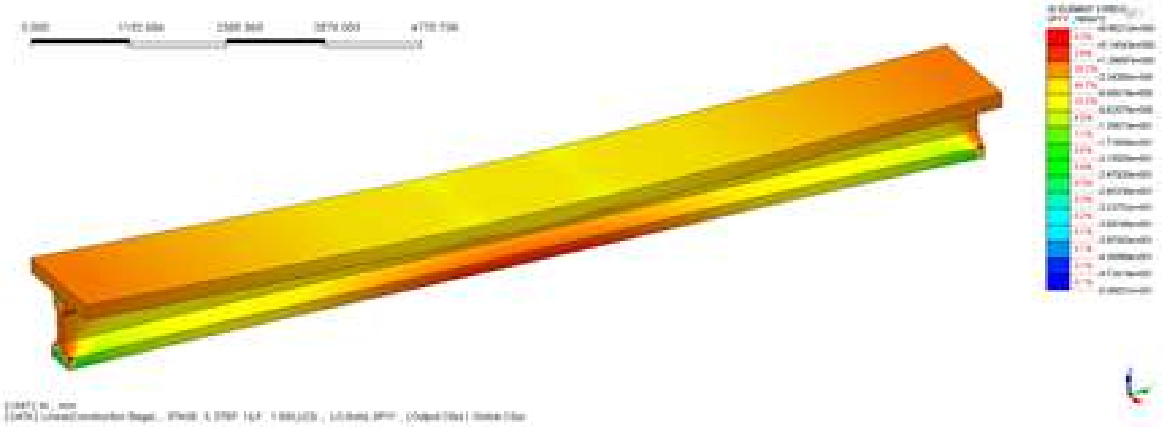

Fig. 9.16: Longitudinal stress distribution

9.9 Sixth stage – long term behaviour (Maxwell model)

To assess the long term behaviour with the Maxwell rheological model, the stage which is finished after 10 000 days is also simulated. It is checked that the girder deflection changes from 2.91 mm to negative -7.1 mm. This result is compared with the value from the Eurocode model analysis, which is -8.0 mm. The deflection of the slab reaches 16 mm (Fig. 9.17). Attention is also paid to the increase in the tensile stress at the mid-span on the bottom surface of the girder, which reaches the value of 5.24 MPa (Fig. 9.18). The longitudinal stress distribution along the pre-stressing strands in the sixth stage is shown in Fig. 9.19. The maximum stress in the strands is 1347 MPa and the long-term loss of pre-stressing force due to creep is observed (7 % loss). It can be observed that the application of the more complex and presumably accurate description for creep, i.e. the Generalized Maxwell model, instead of the Eurocode

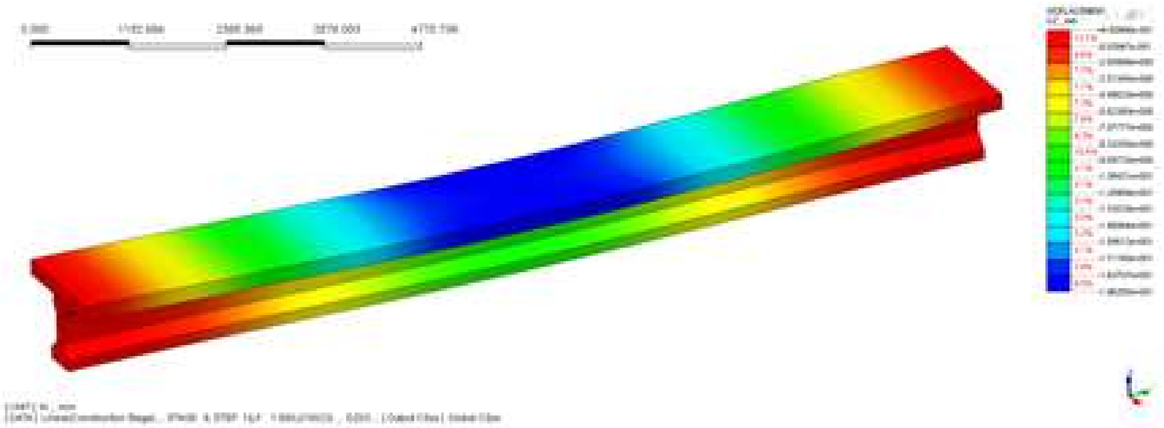

Fig. 9.17: Deflection of composite girder after 10000 days (Maxwell creep model)

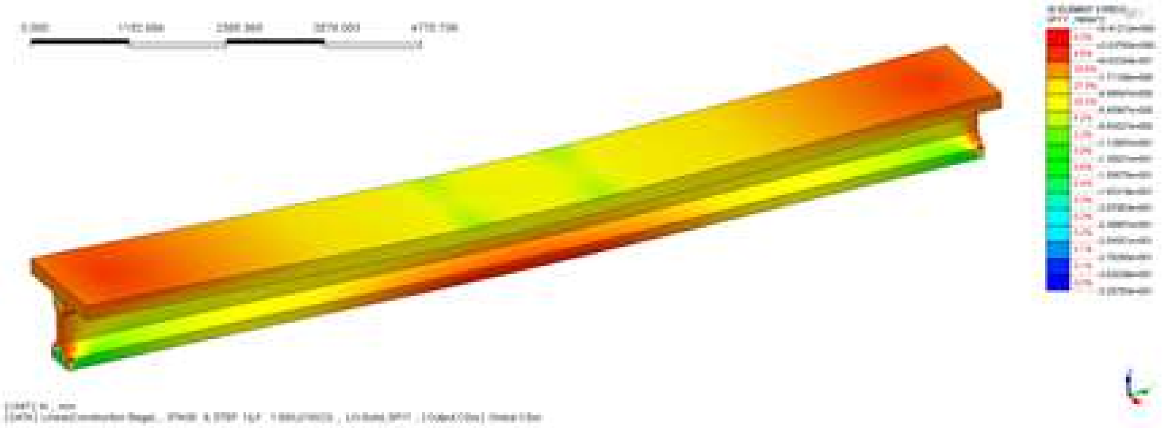

Fig. 9.18: Longitudinal stress distribution after 10000 days

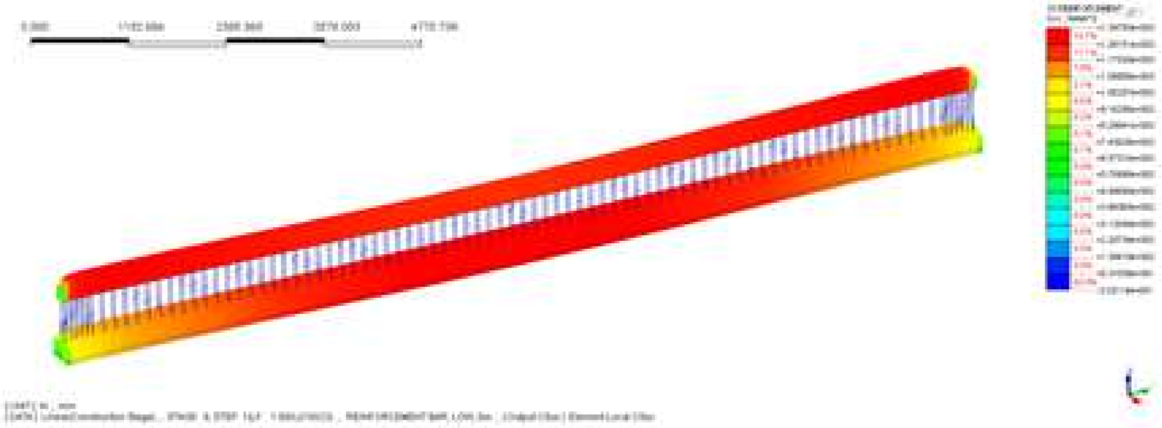

Fig. 9.19: Stress distribution along pre-stressing strands after 10000 days

recommendations leads to lower values of deflection and stress. The conclusion from these calculations could be that the code based models are safer in terms of design of the structure, but on the other hand using more complex models could lead to more effective design and could be economically justified.

10 Construction stage analysis with interface elements

10.1 Bending behaviour for frictional interface

10.1.1 Model data

The geometry of the model and the test set-up are described in Chapter 7, however the connection type in the composite zone is changed from rigid links to interface elements. The interface parameters are chosen based on the calibration tests described in Chapter 6 and the material data for the con crete used for the girder. The interface is governed by the Coulomb friction model with the following parameters: normal stiffness modulus $k_n = 36900$ N/mm^3, shear stiffness modulus $k_t = 15375$ N/mm^3, adhesion $c = 4$ N/mm^2, internal friction angle $\Phi = 30$ degrees, dilatancy angle $\psi = 30$ degrees. The interface stiffness moduli are respectively derived from the Young and Kirchhoff moduli of concrete, the adhesion is assumed to be approximately 90% of the tensile stiffness and the angle values are adopted according to literature recommendations for concrete models [Wosatko et al., 2019].

The non-linear static analysis is performed separately for each stage. For stages 1 to 4 the load step is adjusted automatically and for step 5 manual load control is applied. The load is divided into 20 steps with load factor increment $\Delta p = 0.1$, i.e. the load factor for the cracking load grows to $p = 2$. Only selected states are presented below. Fig. 10.1 shows the deflection of the girder at the end of stage 1 with maximum mid-span value of 2.5 mm.

In the second stage pre-stressing is applied to the girder and a camber is observed. In Fig. 10.2 the camber is shown with maximum negative deflection of almost 8 mm.

In the third stage, applying the wet-concrete load to represent casting the slab (uniform pressure load on the top surface of the girder) reduces the maximum camber reached in stage 2 (when the pre-stressing forces were applied) from 7.99 mm to 5.48 mm, see Fig. 10.3.

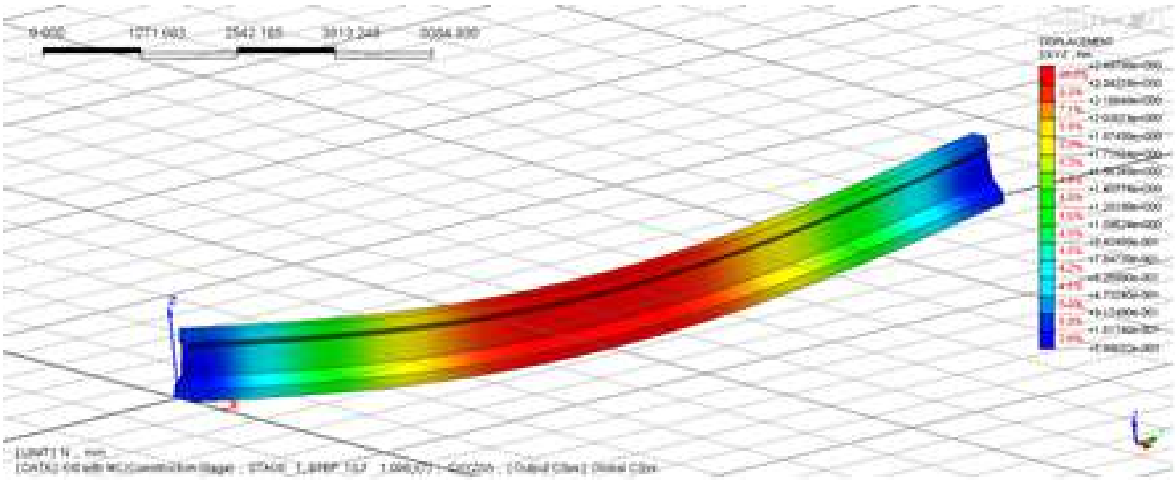

Fig. 10.1: Deflection of the girder in stage 1

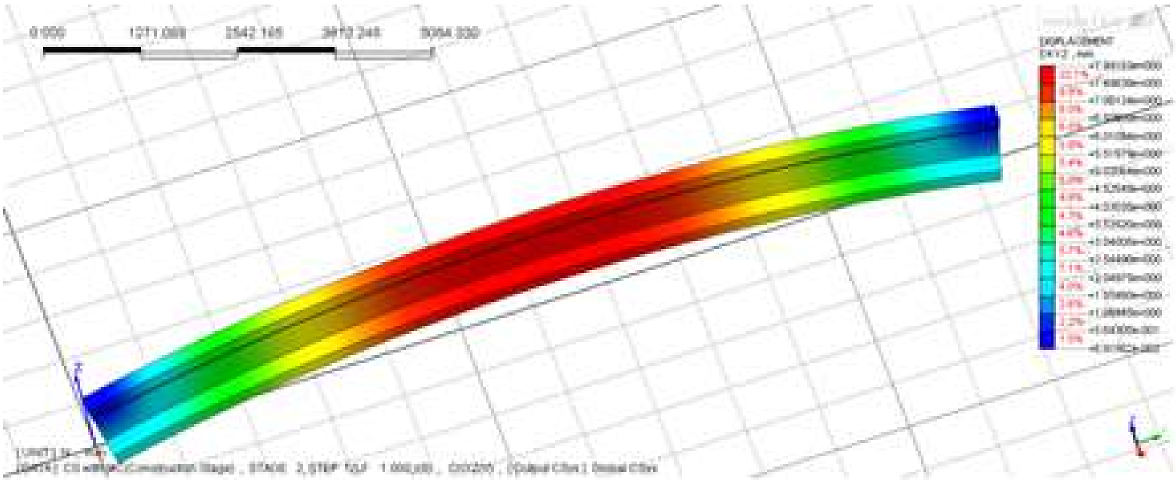

Fig. 10.2: Displacements due to pre-stressing

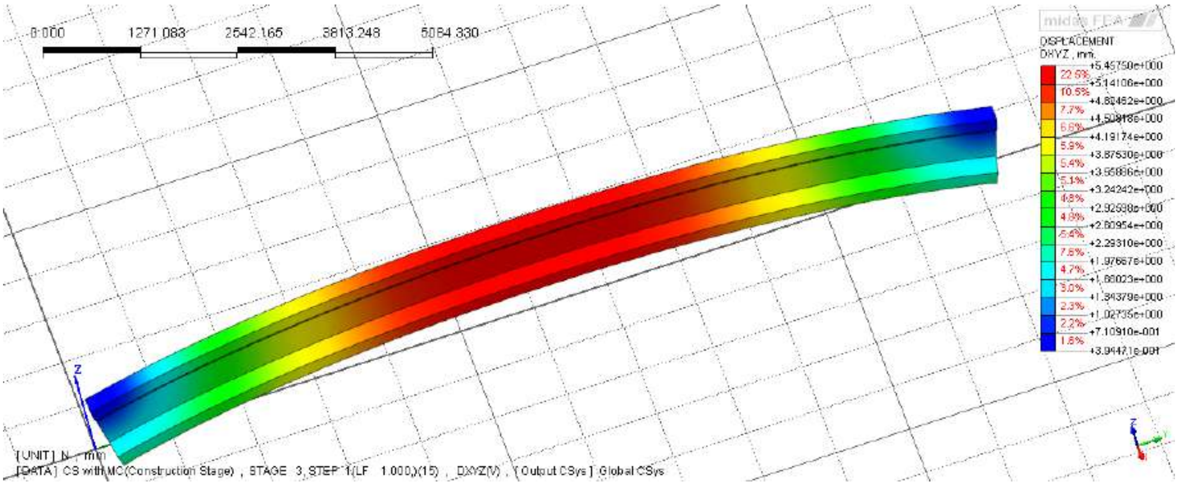

Fig. 10.3: Displacement after application of wet-concrete load

10.1.2 Fourth stage – composite girder

In the fourth stage the cross-section of the girder becomes composite, the wet-concrete load is deactivated, the slab member and the interface become active. The cross-section of the beam consists of two parts: the girder and the slab with interface elements in between. Comparing the results from stage 3 and 4, the deflection decreases from 5.48 mm to 3.51 mm. This is shown in Fig. 10.4.

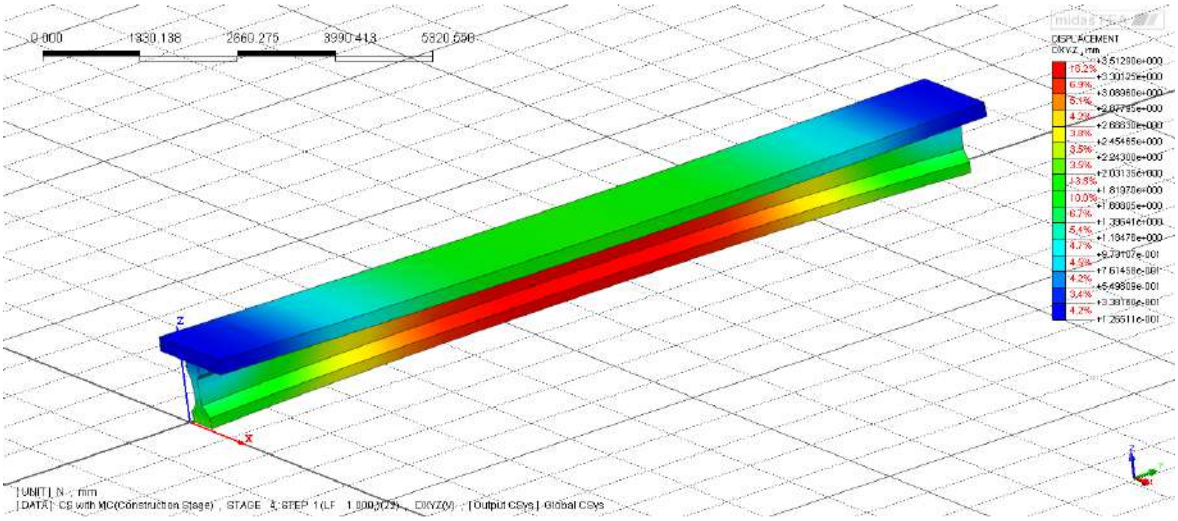

Fig. 10.4: Displacement of composite girder after stage 4 (due to graphics malfunction the curvature of the deck is not represented properly)

Figures 10.5 and 10.6 show respectively the normal relative displacement and the normal traction in the interface elements with values close to zero. This is the results of bending character of the loading which causes almost no horizontal movements between interface sides.

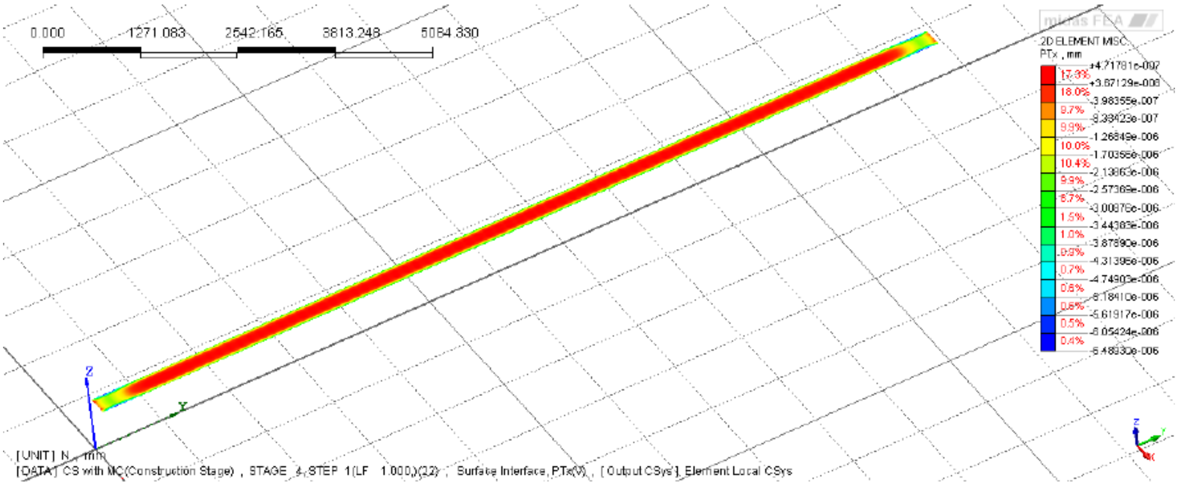

Fig. 10.5: Normal relative displacement of interface elements after stage 4

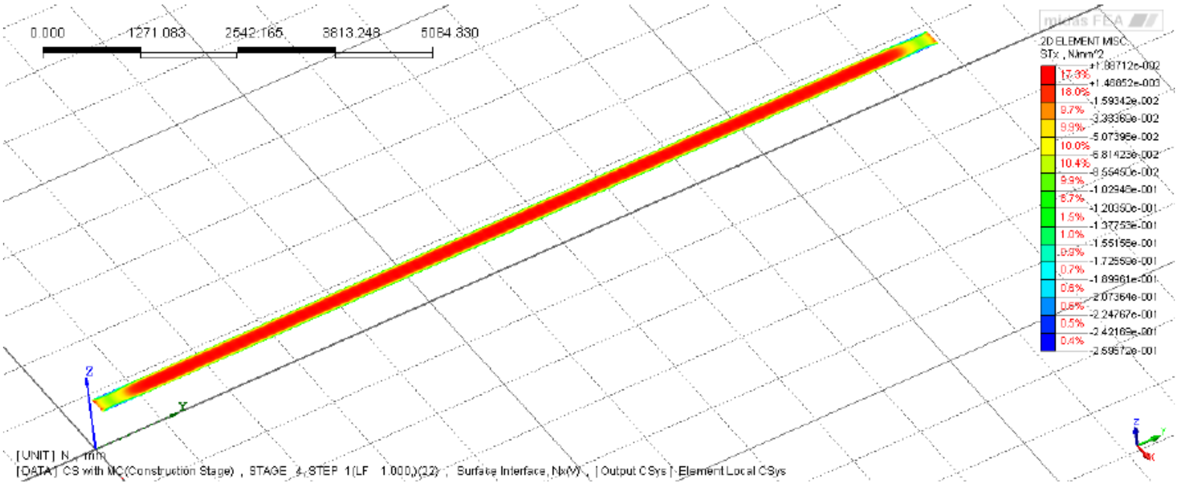

Fig. 10.6: Normal stress in interface elements after stage 4

10.1.3 Fifth stage – external load

In the last stage the external load is applied as shown in Chapter 7. The value of the load adopted according to the experimental results is given in Section 6.4. The maximum displacement caused by the cracking load is 43.8 mm with $L/250$ condition of 5 mm (Fig. 10.7). The reason of such increment of the deflection is that the interface friction connection is obviously much weaker than the rigid one, for which the deflection at this stage is 4.6 mm.

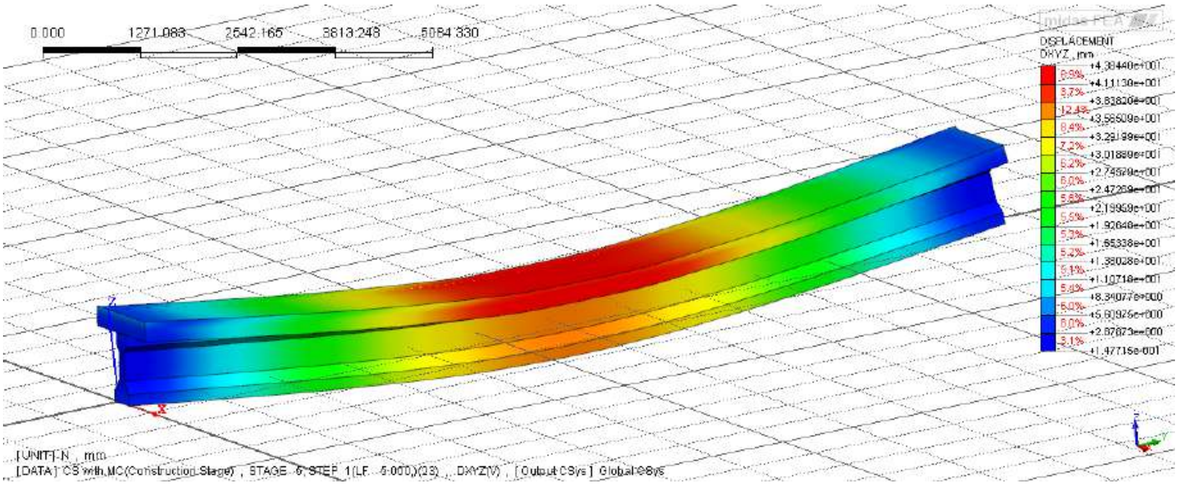

Fig. 10.7: Displacement due to external cracking load after stage 5

Fig. 10.8 shows the normal relative displacement of the interface elements and Fig. 10.9 shows the normal traction. Strong concentration of the stress is visible on the edges of the upper surface of the girder under the applied load. This is due to rotation of the wide deck around the girder axis y. However, considering the bending

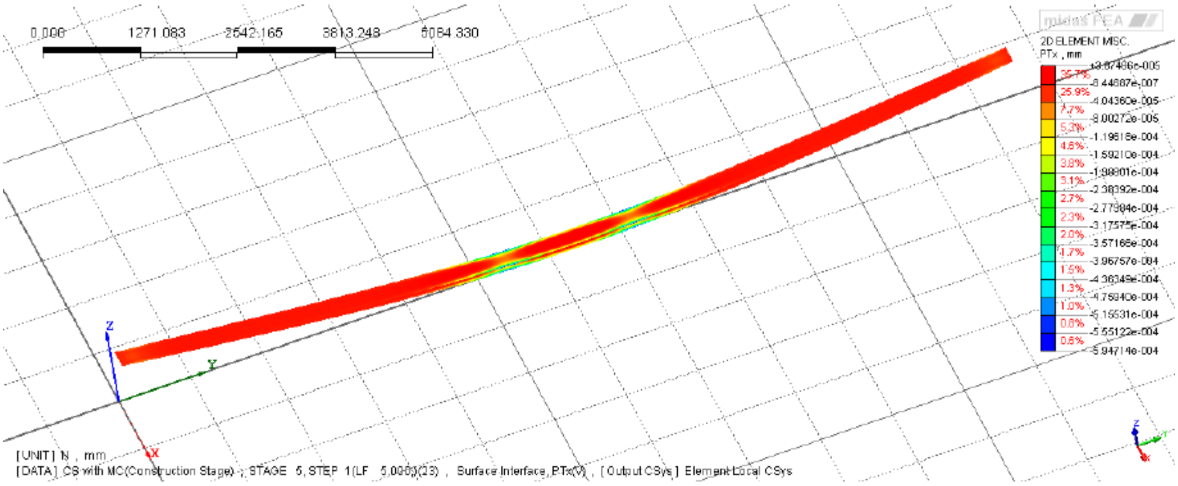

Fig. 10.8: Normal relative displacement of interface elements after stage 5

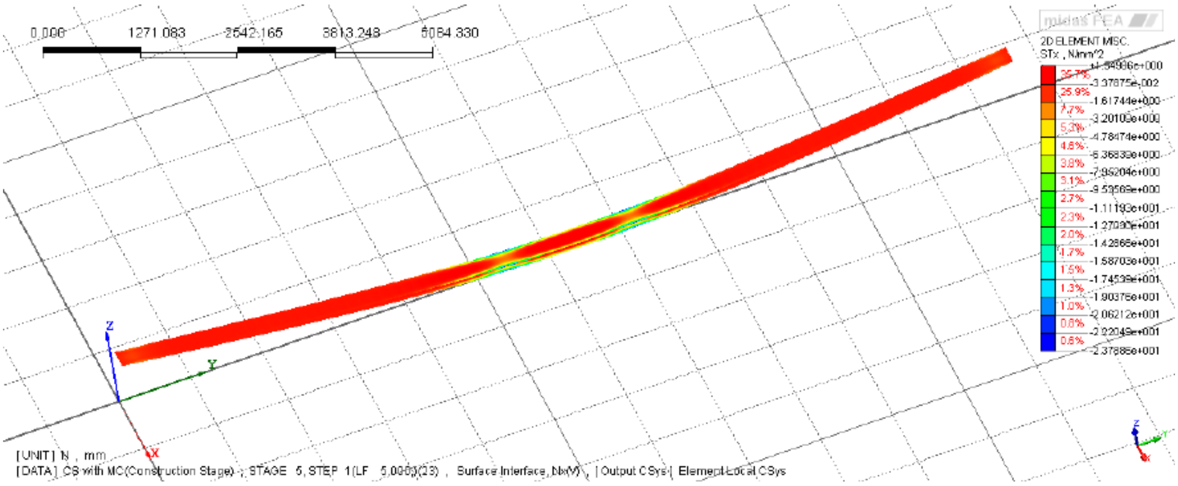

Fig. 10.9: Normal traction in interface elements after stage 5

behaviour and a realistic configuration of the interface constitutive model, the level of the load which causes non-linear (slip) behaviour of the interface results in non-realistic deformations (deflection at the mid-span approx. 8 meters). Considering this phenomenon and the benchmark test presented in Chapter 5, the longitudinal shear behaviour is analyzed in the next chapter.

10.2 Longitudinal shear behaviour for frictional interface

In this section the construction stage analysis of the longitudinal shear behaviour is provided. The final external load is applied in stage 5 and has no influence on the previous stages, so the results from this stage are only presented. The test set-up and material model parameters remain the same as before and the external load of pressure type with the value of 10 MPa is shown in Fig. 10.10. The only nonlinear effect in this analysis is the Coulomb-Mohr plastic response of the interface. The longitudinal shear behaviour is crucial in terms of designing composite girders as the shear force is carried by the connection zone.

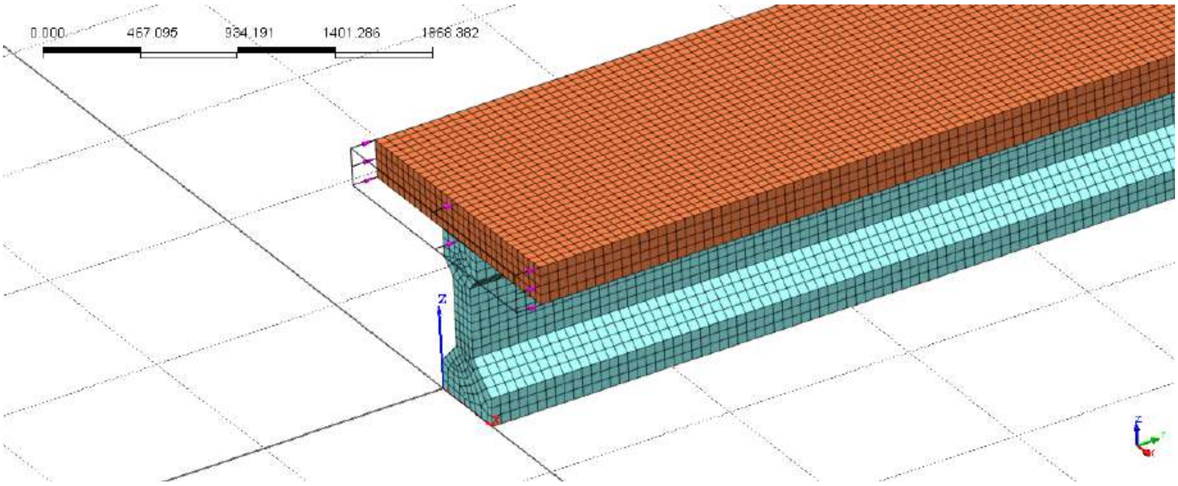

Fig. 10.10: External load applied to composite girder

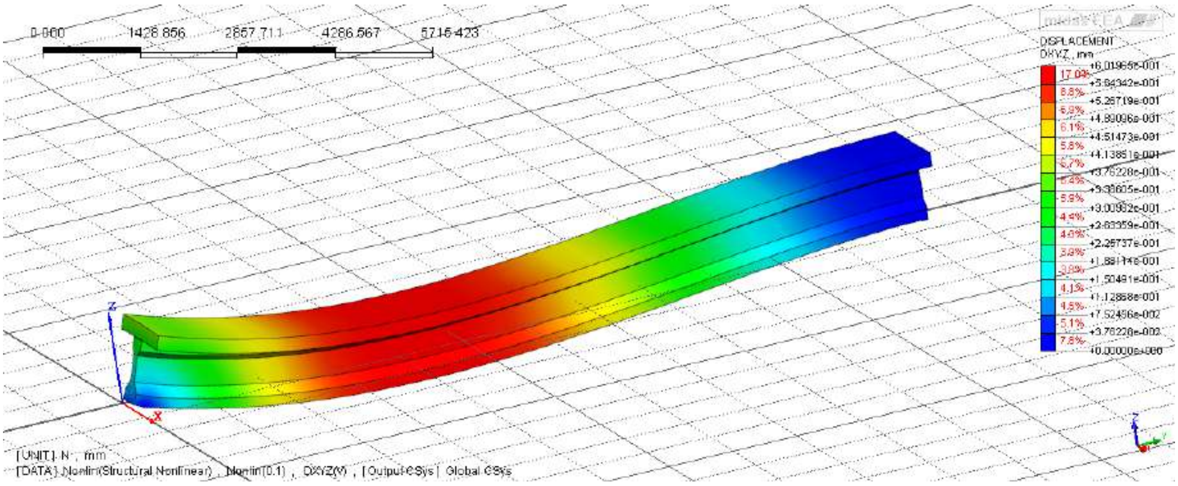

Fig. 10.11: Total displacement in stage 5 for 10% of assumed pressure ($p = 0.1$)

The interface configuration is chosen as in the previous chapter. The displacement of the girder for 10% of the load ($p = 0.1$) is shown in Fig. 10.11 and maximum longitudinal deformation 0.6mm is noted. The bending character of the deformation is due to curvature from pre-stressing in the previous stages. The true deformations are scaled 100:1 for the visualisation purpose.

Figures 10.12 and 10.13, respectively, show the normal and tangent (in longitudinal direction) relative displacement in the interface elements. For $p = 0.1$ it can be observed that very small displacement occurs only at the ends of the beam. For the assumed load $p = 1$ the response is still linear, so the loading is incrementally increased to $p = 2$.

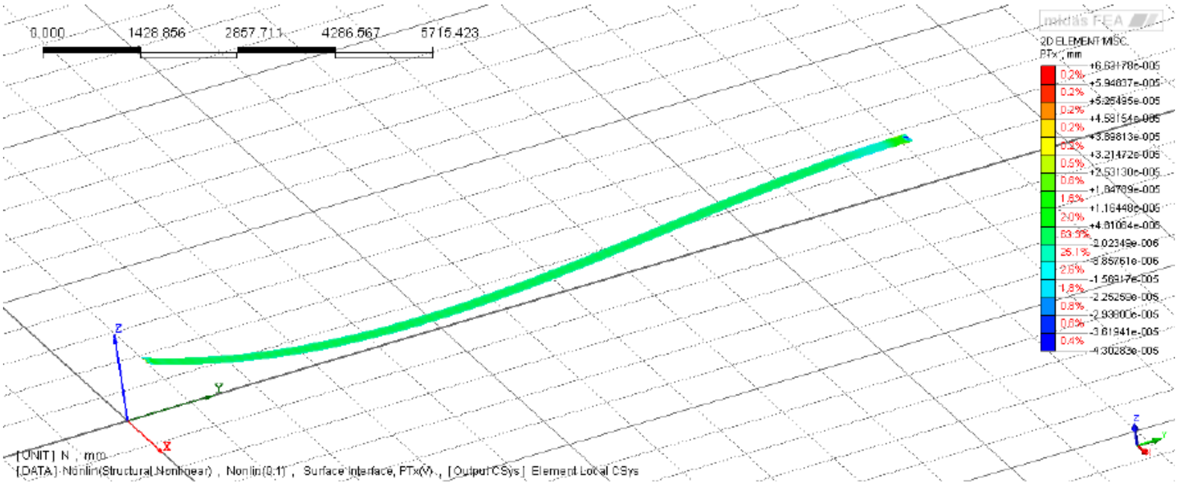

Fig. 10.12: Normal relative displacement of interface elements ($p = 0.1$)

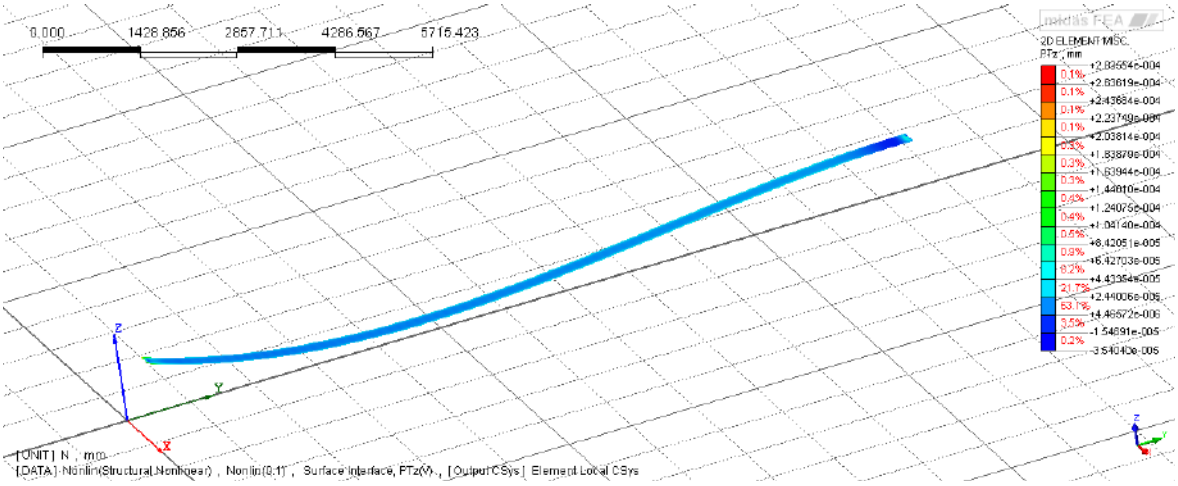

Fig. 10.13: Tangent relative displacement of interface elements

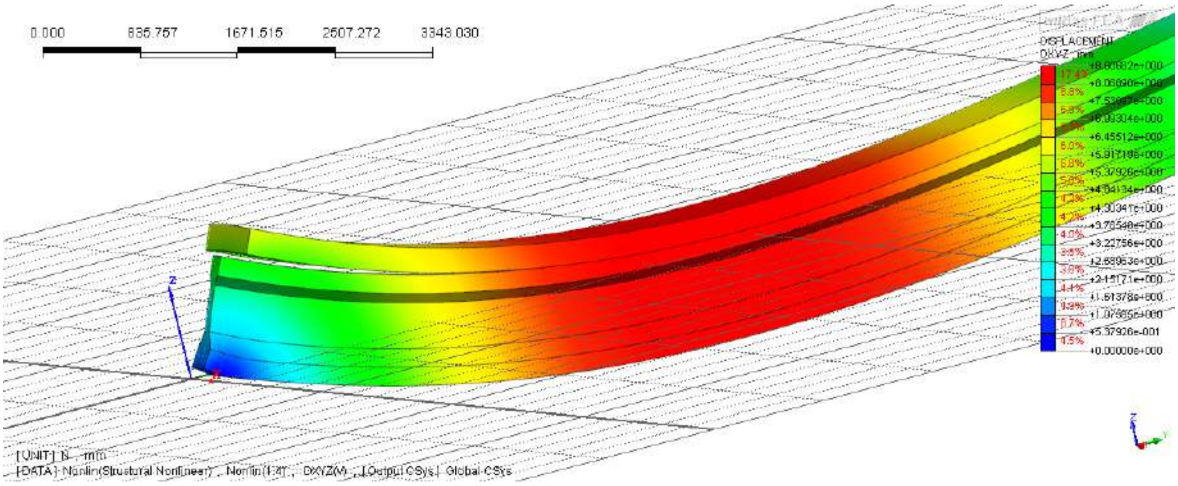

Fig. 10.14: Displacement of the girder for $p = 1.4$

In Fig. 10.14 one can observe the displacement of the girder for $p = 1.4$. At this level the interface starts to open at the left end of the girder and the maximum longitudinal deflection is 8.6 mm. Figures 10.15 and 10.16 show the normal and tangent relative displacement of the interface for the load level. Interface opening at the left end can be observed and it develops along the beam.

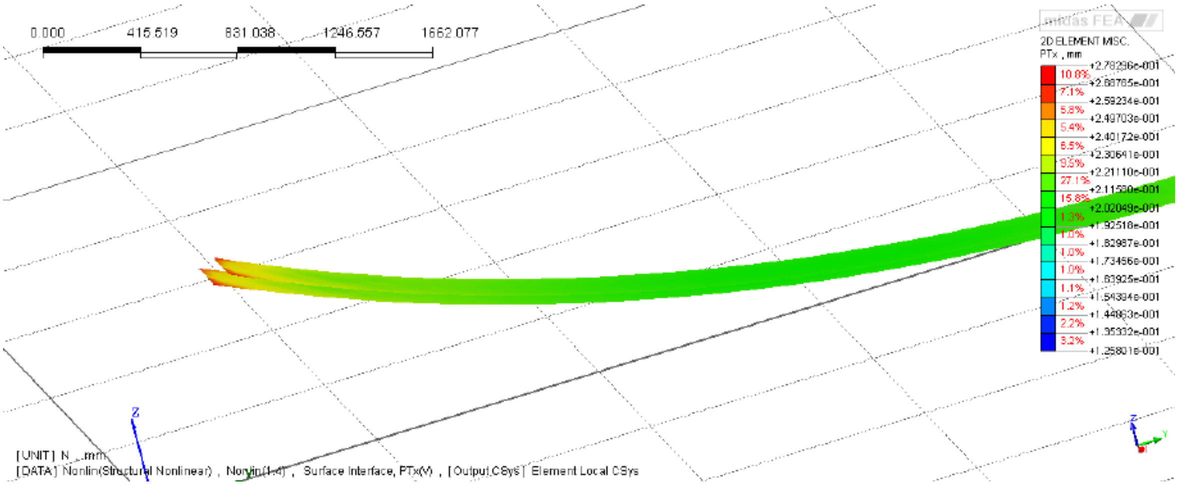

Fig. 10.15: Normal relative displacement of interface elements ($p = 1.4$)

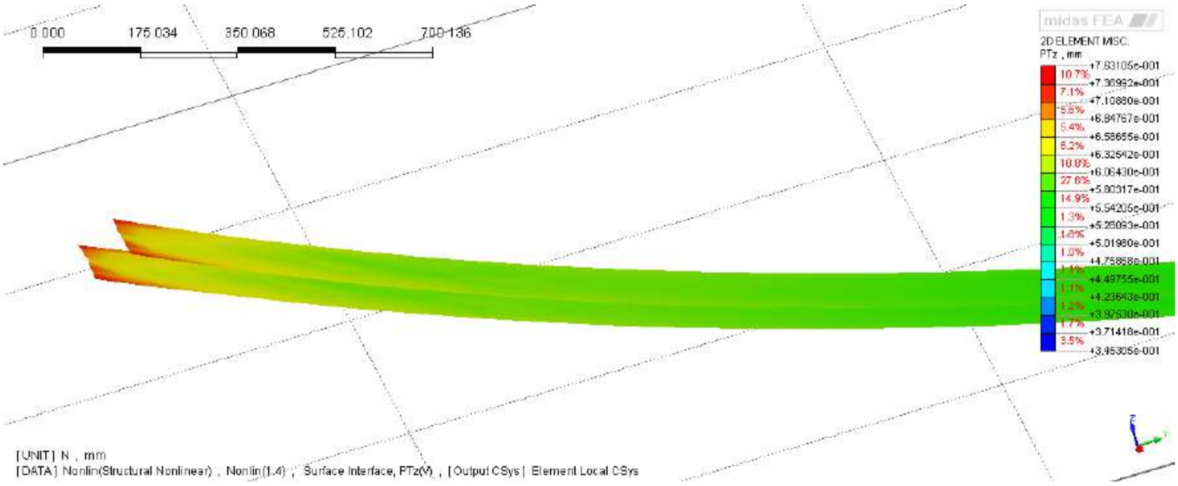

Fig. 10.16: Tangent relative displacement of interface elements ($p = 1.4$)

Fig. 10.17 shows the displacement of the girder for $p = 2$. The interface opening at the left end propagates more and the interface at the right end of the girder is open as well. The maximum longitudinal displacement is 12.3 mm.

Figures 10.18 and 10.19 show the normal and tangent relative displacement of the interface for $p = 2$. The deck moves along the girder with openings at both ends. The red colour is the strongest place of the connection zone, which is the result of curvature due to pre-stressing and of friction in the interface.

Fig. 10.20 shows the node which is chosen to present the displacement vs load diagrams.

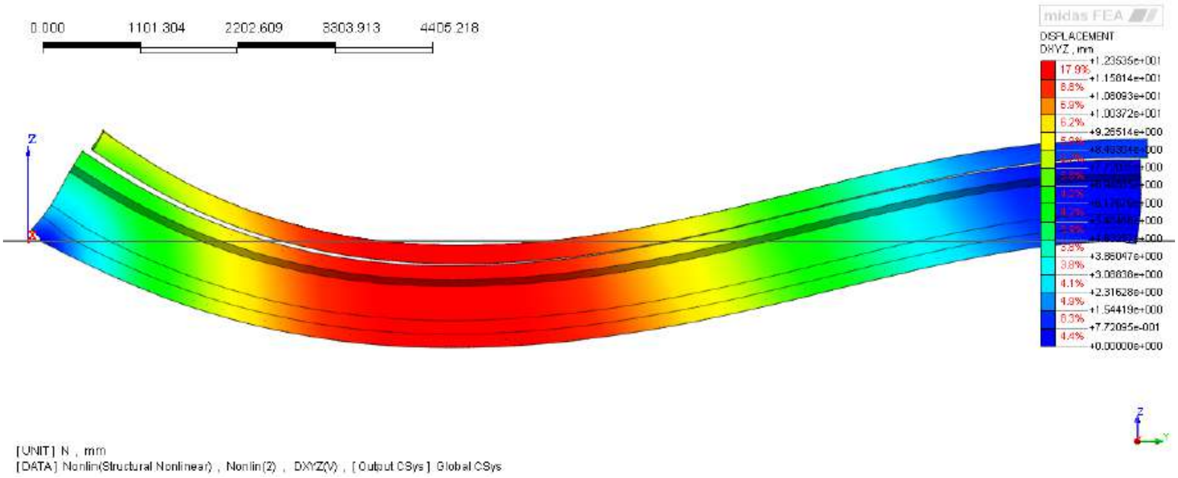

Fig. 10.17: Displacement of the girder for $p = 2$

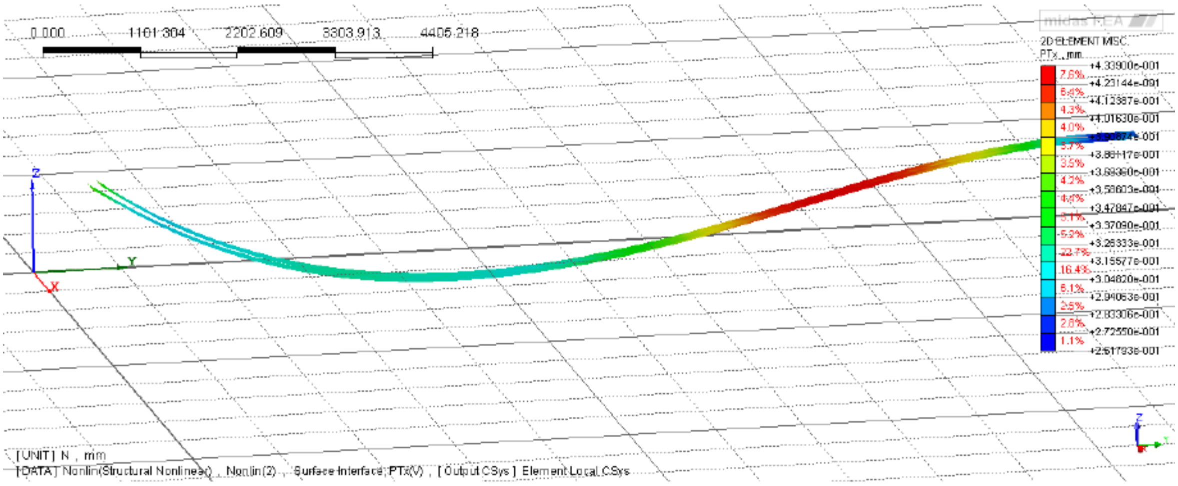

Fig. 10.18: Normal relative displacement of interface elements ($p = 2$)

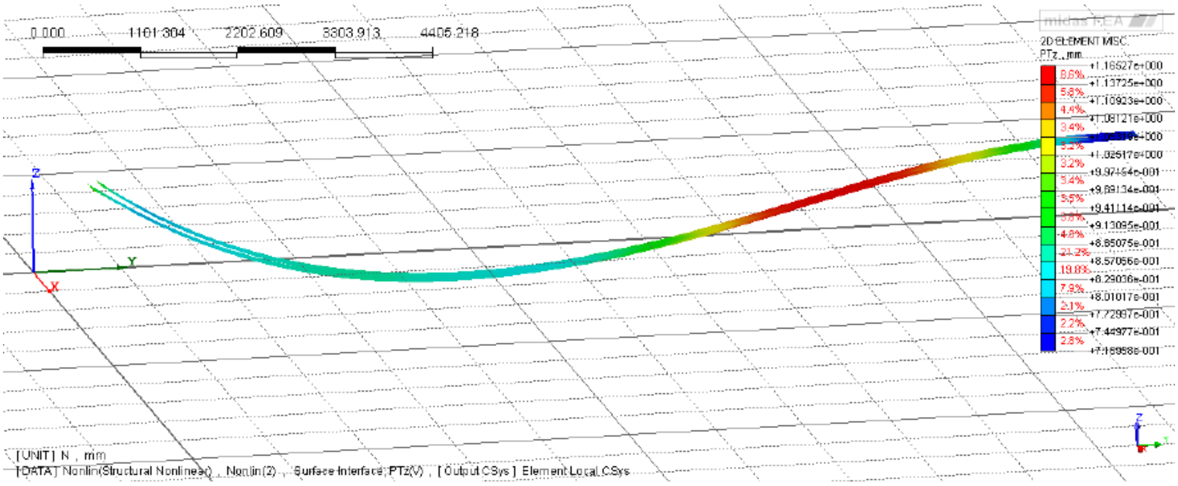

Fig. 10.19: Tangent relative displacement of interface elements ($p = 2$)

Figures 10.21 and 10.22 show the diagrams of displacements D_y and D_z, respectively, versus the load factor. When the pressure with load factor $p = 1.1$ is applied,

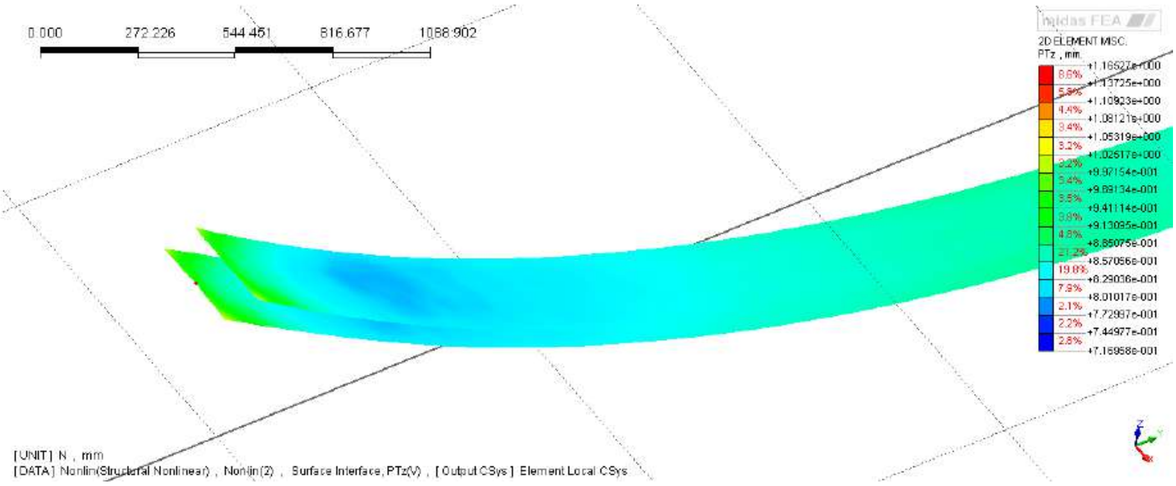

Fig. 10.20: Tangent relative displacement of interface elements ($p = 2$)

the linear elastic behaviour of the interface is finished. The strong change of inclination of the diagrams from load factor 1.3 to 1.4 is due to a slip between interface surfaces, which is the source of the non-linear behaviour. After the slip occurs, a hardening part is noticed due to the return of the friction traction forces.

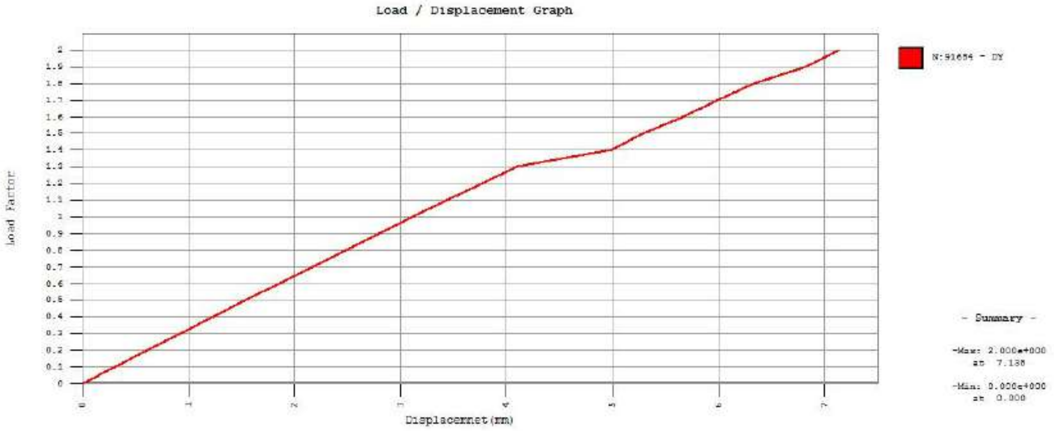

Fig. 10.21: Displacement D_y vs load factor (initial stage of loading)

The analysis is performed until the load factor $p = 4$. Fig. 10.23 shows the displacement of the girder with the maximum value of 26 mm. Figures 10.24 and 10.25 show the normal and tangent relative displacement of the interface for $p = 4$. The maximum normal (opening) relative displacement of the interface at this level of the load is 4.72 mm and for the tangent relative displacement in longitudinal direction it is 11.3 mm.

The non-linear character of the behaviour of the interface is shown in Fig. 10.26 for displacement D_y and in Fig. 10.27 for displacement D_z. Each decrease of the secant

Fig. 10.22: Displacement D_z vs load factor (initial stage of loading)

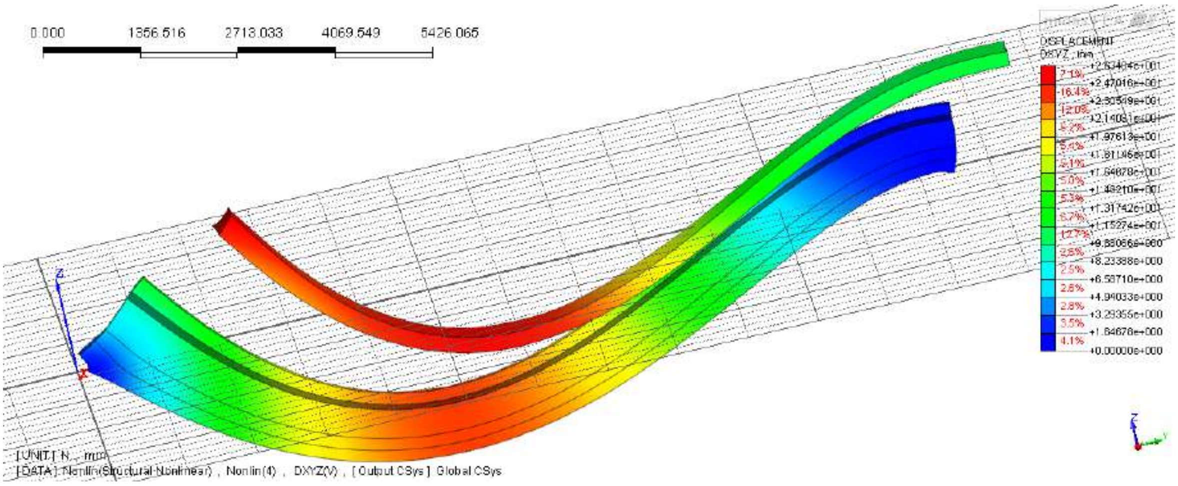

Fig. 10.23: Displacement of the girder for $p = 4$

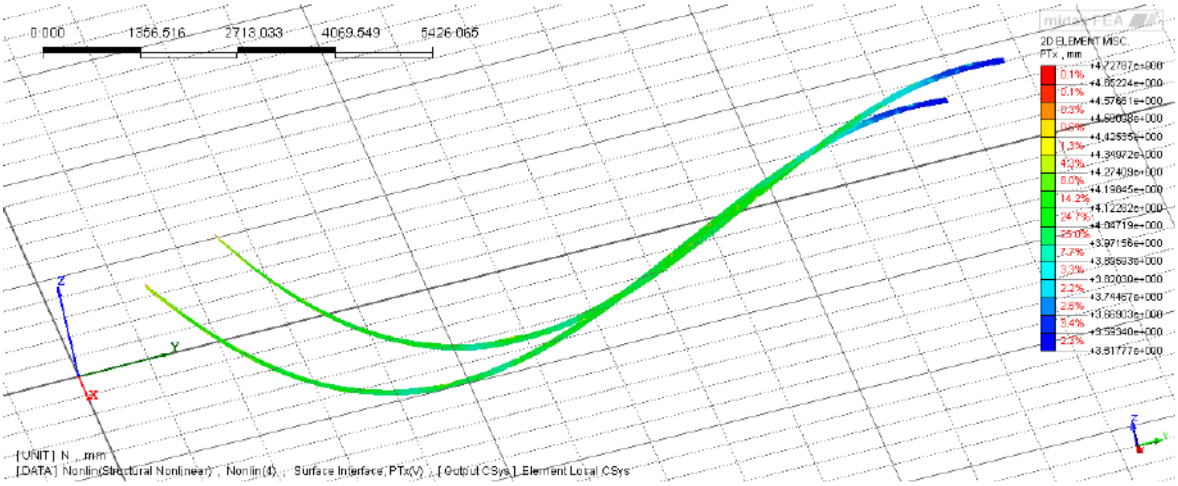

Fig. 10.24: Normal relative displacement of interface elements ($p = 4$)

stiffness is caused by a slip in the interface, after which hardening due to friction forces takes place.

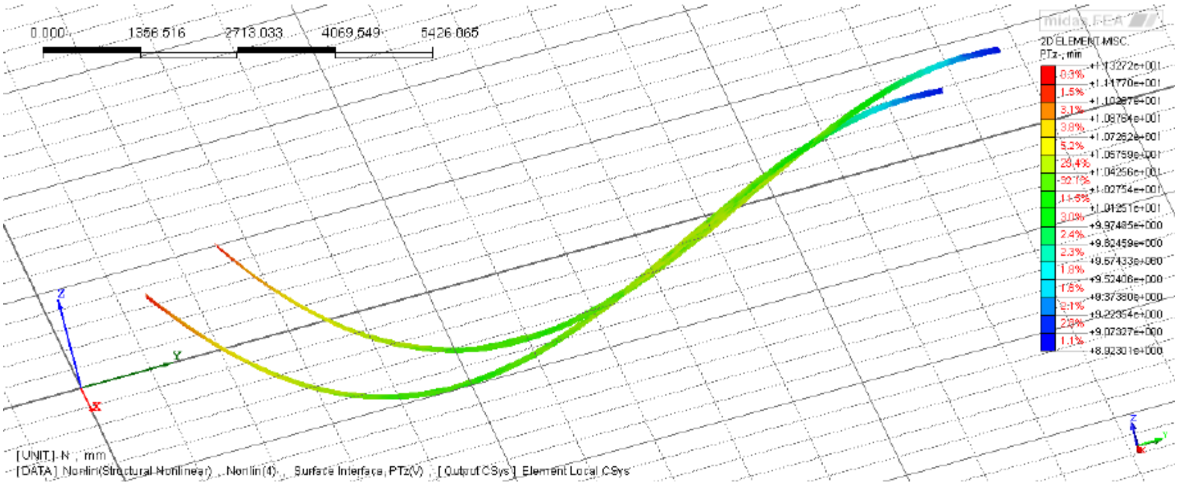

Fig. 10.25: Tangent relative displacement of interface elements ($p = 4$)

Fig. 10.26: Displacement D_y vs load factor

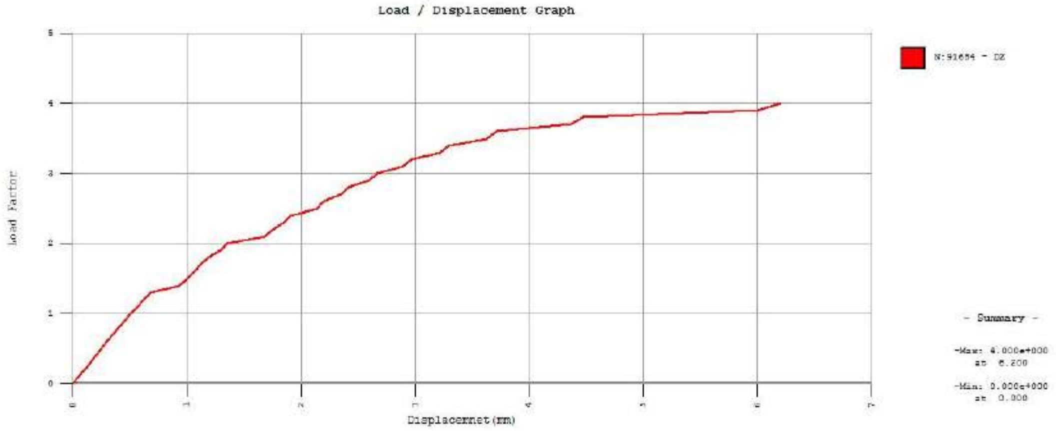

Fig. 10.27: Displacement D_z vs load factor

10.3 Stitching reinforcement in connection zone

In the previous section the friction connection of the composite zone was analyzed. Another commonly used type of connection, which is discussed in this section, is the use of stitching reinforcement. The stitching reinforcement is modelled by elongation of the already existing stirrups and can be seen in Fig. 10.28.

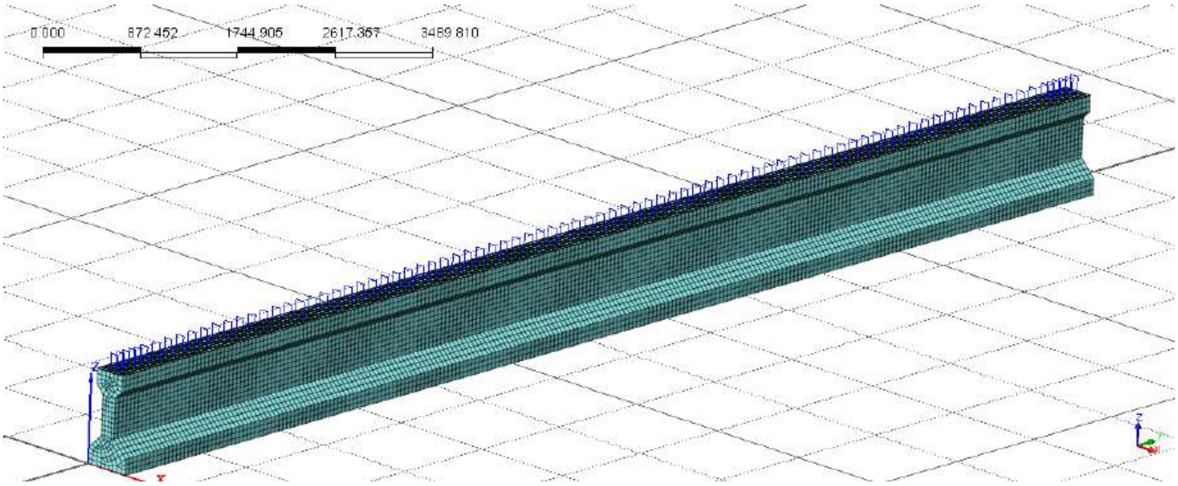

Fig. 10.28: Stitching reinforcement geometry

As in the previous section a full construction stage analysis is performed, but only the fifth stage with external load and stitching reinforcement is presented. The set-up, geometry and boundary conditions remain the same to obtain a clear comparison. In Fig. 10.29 the displacement of the girder at 10% of the applied load is shown, the maximum value is 0.6 mm.

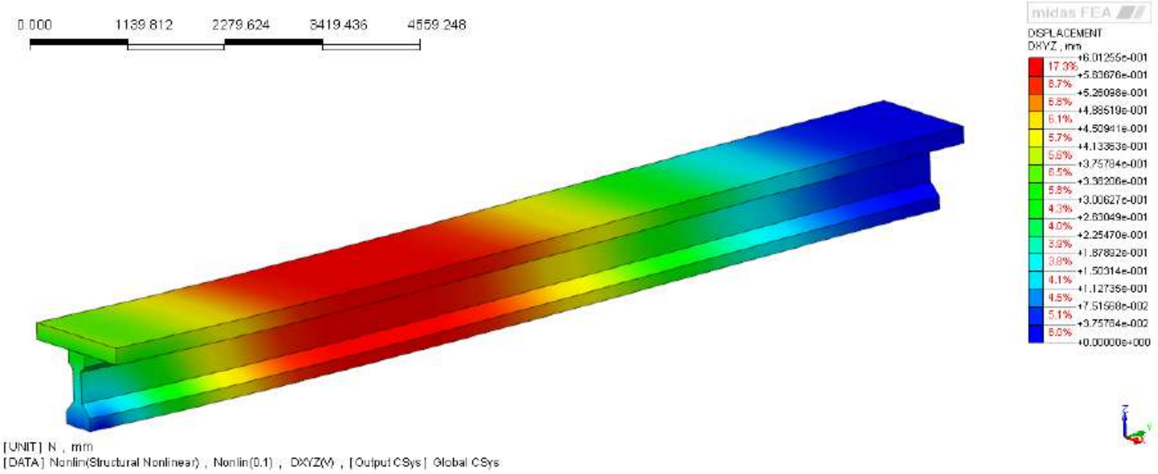

Fig. 10.29: Displacement of the girder for $p = 0.1$

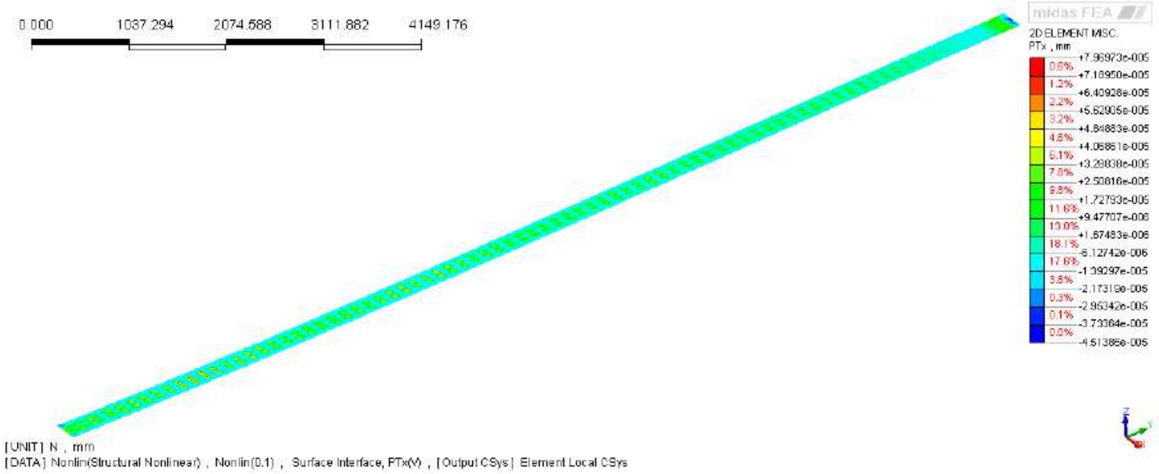

Fig. 10.30: Normal relative displacement in interface elements for $p = 0.1$

In Fig. 10.30 the normal relative displacement in interface elements is shown with almost zero value along the girder, however the influence of the stitching reinforcement on the interface can be noticed as is zoomed and presented in Fig. 10.31.

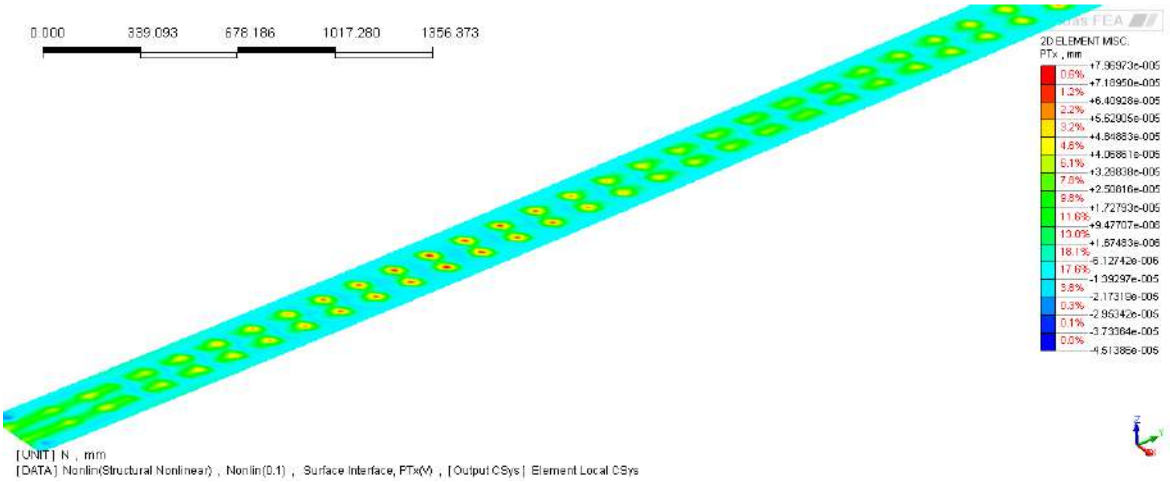

Fig. 10.31: Normal relative displacement in interface elements for $p = 0.1$

In Fig. 10.32 the displacement of the girder for $p = 1.4$ is shown. First opening of the interface at the left end of the girder is noticed, as well as the dowel action of the stitching reinforcement bars. The maximum longitudinal displacement is 3.7 mm.

Figures 10.33 and 10.34, respectively, show the normal and tangent relative interface displacement for $p = 1.4$. Small opening at the left end can be noticed and the values of the displacements are close to zero along the girder.

Fig. 10.35 shows strain E_{xx} in the reinforcement bars. The maximum values of the strain and stress in the reinforcement elements are recorded in pre-stressing strands, however, considering the longitudinal shear behaviour the expected response represents

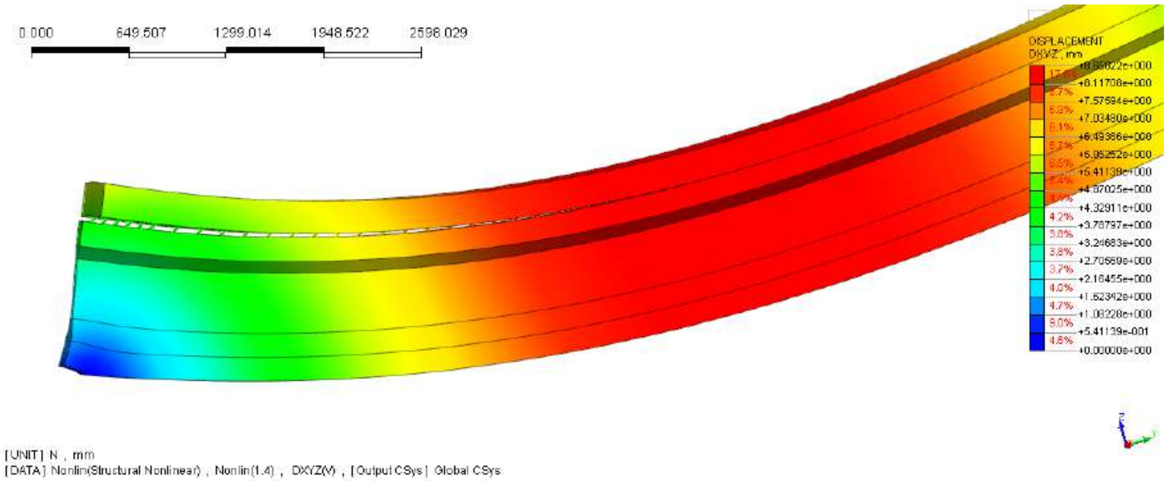

Fig. 10.32: Displacement of the girder for $p = 1.4$

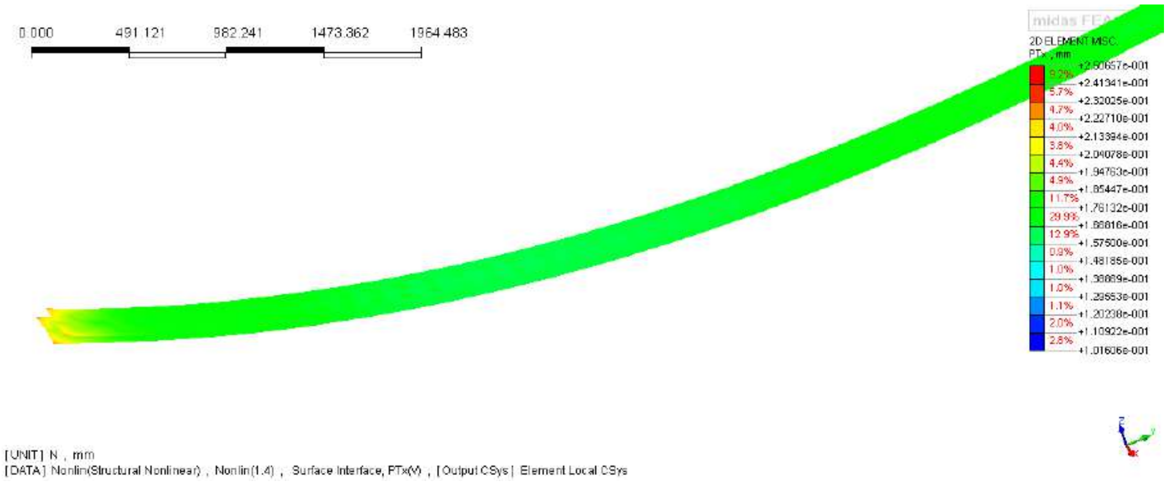

Fig. 10.33: Normal relative displacement in interface elements for $p = 1.4$

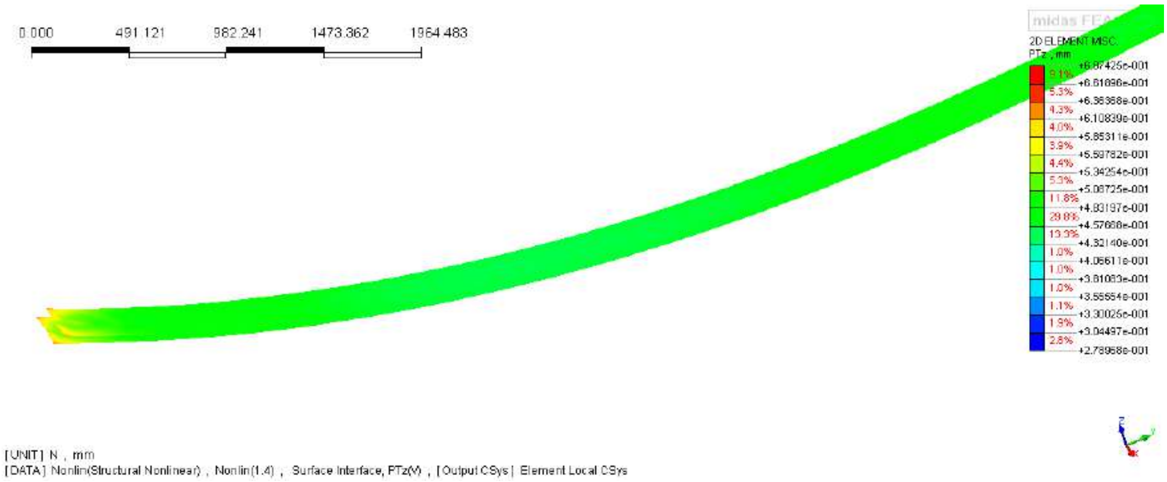

Fig. 10.34: Tangent relative displacement of the interface elements for $p = 1.4$

the dowel action and the deformation of the bars shows exactly this phenomenon.

Fig. 10.36 shows the displacement of the girder for $p = 2$. The opening of the

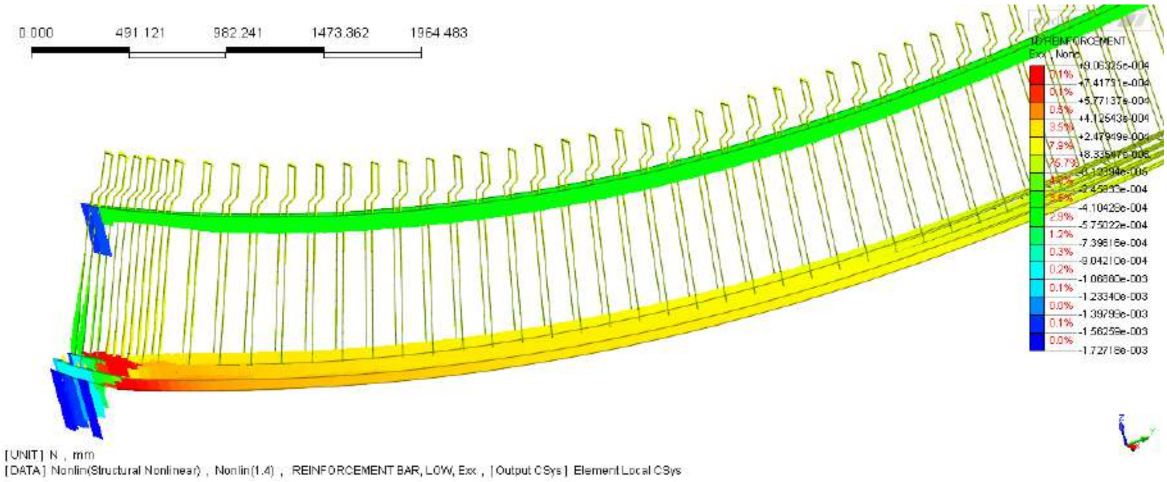

Fig. 10.35: Strain E_{xx} in reinforcement bars

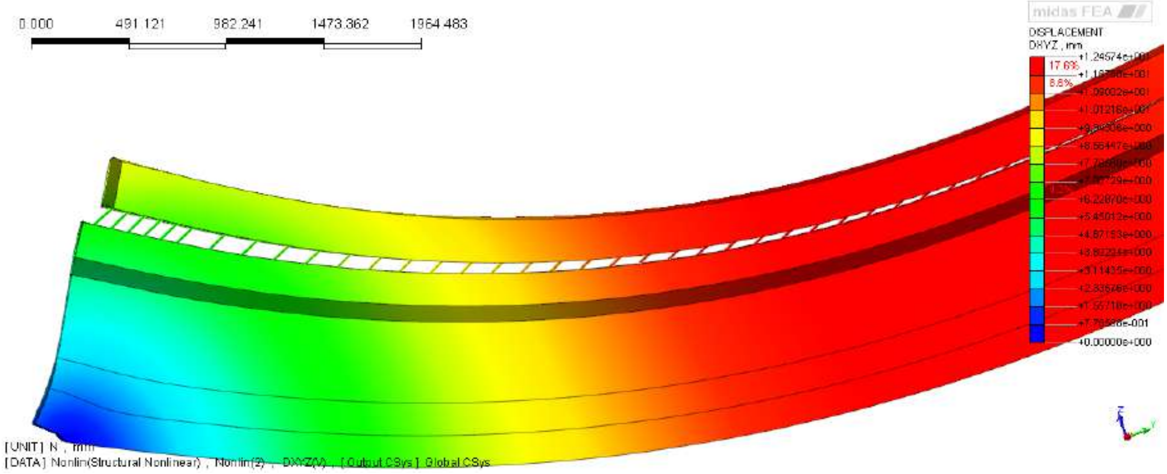

Fig. 10.36: Displacement of the girder for $p = 2$

interface between the girder and the slab is bigger, but the values of the displacement are quite similar to the case without stitching reinforcement. The dowel action can be observed, the interface behaviour is shown in Figures 10.37 and 10.38 with the maximum values of 0.48 mm for the normal and 1.35 mm for the tangent relative displacement.

Fig. 10.39 shows the strain distribution in the reinforcement elements for 200% of the applied load ($p = 2$). It can be noticed that the values of the strains in the stitching reinforcement are about 10 times higher than in the previously presented load step (Fig. 10.35) and proper dowel action can be observed as well.

The displacement vs load factor diagrams are prepared for the same node as it was shown in the previous section. Non-linear character can be observed from the same level of load as in the case without the stitching reinforcement bars.

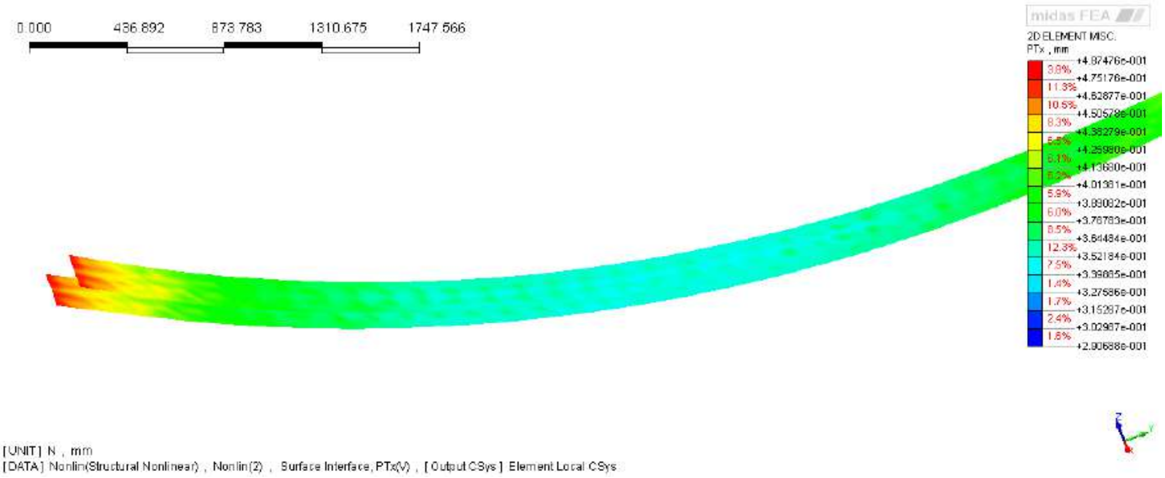

Fig. 10.37: Normal relative displacement in interface elements

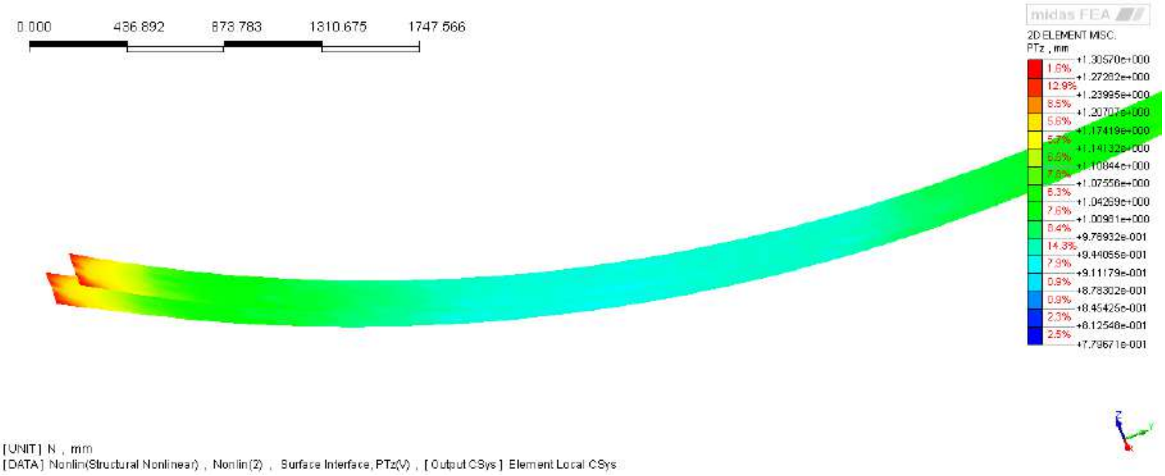

Fig. 10.38: Tangent relative displacement in interface elements

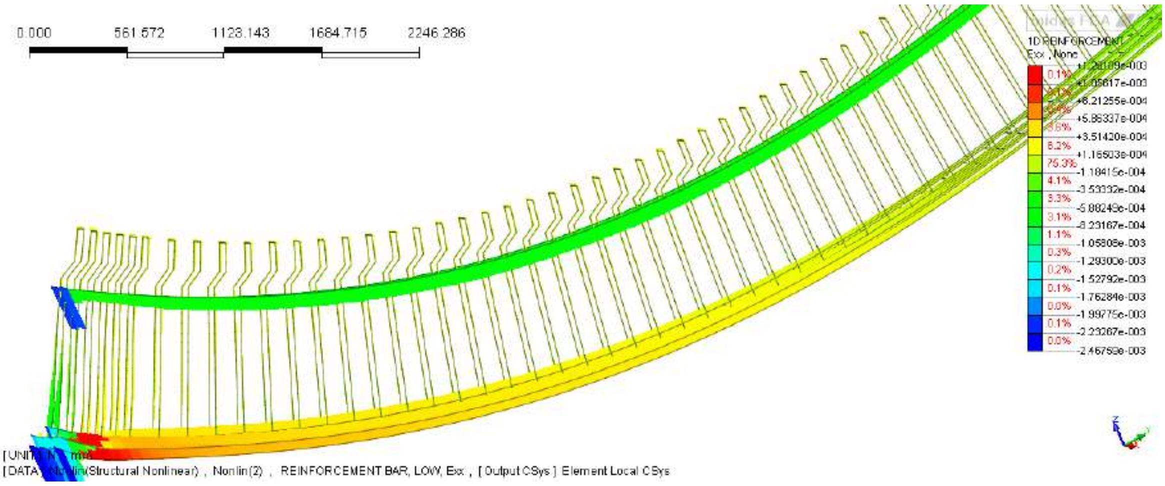

Fig. 10.39: Strain E_{xx} in reinforcement bars

Figures 10.40 and 10.41 show the displacements in directions Y and Z, respectively. The non-linear behaviour is strongly visible, the slips and hardening phases as well,

Fig. 10.40: Displacement D_y vs load factor

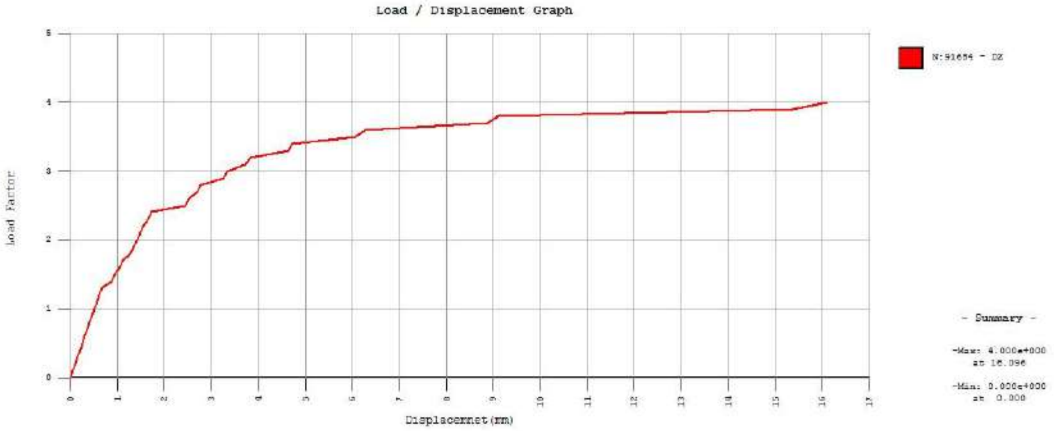

Fig. 10.41: Displacement D_z vs load factor

however the displacement for the same load factor is much larger than in the case without the stitching reinforcement.

11 Summary and conclusions

The topic of this doctoral project has been the numerical modelling of pre-stressed bridge girder made of HSC composite with bridge deck made of NSC. The girder is precast and the deck slab is cast on site. The contact zone in the concrete-concrete composite structure is the major issue requiring analysis. This is a key factor of load-bearing capacity of such composite girders.

The experimental research performed by W. Choi at State University of North Carolina, Raleigh was a motivation and provided the research object for the assessment of such composite girder. The experimental study aimed at the evaluation of the flexural behaviour of pre-stressed composite girders combining high and normal-strength concrete. In that study three types of girders with 1.5m-wide or 0.3m-wide cast deck or without the deck were tested. In this thesis a simulation study of the beam with the wider deck is performed, taking into account construction stages and two nonlinear effects: creep or interface between the girder and the deck. Moreover, the experimental cracking response is reproduced.

The analysis starts by discussing the main properties of a composite cross-section and phenomena that occur in the HSC-NSC interface. The first contact mechanism is adhesion. A phenomenon associated with it is the aggregate interlock between new and old concrete. Several theories describing friction are analyzed. The importance of the shear friction phenomenon makes it the basis of most models describing composite elements.

We can treat a composite member as a member with homogeneous cross-section if the contact zone is properly formed and the conditions for longitudinal shear strength are met. When adhesion and friction forces are exhausted, stitching reinforcement is a crucial factor of load-carrying capacity. To confirm this, some tests with reinforcement bars acting against longitudinal shear slip in the contact zone are analyzed. Moreover, design code recommendations for the concrete-concrete connection, including the option of indented geometry, are reviewed.

Further, the properties of interface elements used to model composite structures are discussed. The interface elements are introduced into the finite element model to represent a relationship between the relative displacement vector and the contact traction vector. Choosing the right type of interface element is important for the reproduction of the concrete-concrete interaction. In order to select an appropriate method of modelling the contact, a simple calculation model is created consisting of two solid boxes with plane interface elements between them. Different types of interface constitutive relations are applied in the interface elements to simulate sliding and opening.

First, the Coulomb friction model which is derived from Mohr-Coulomb plasticity for continuum elements is considered. An aggregate interlock model of Walraven is the next contact model analyzed in the benchmark. Next, an indented connection is examined, which consists of 2D interface elements with friction. Due to the connection geometry, one part of the interface resists shear and the other compression or tension. It is noticed that the computed values of displacements, normal interface stress and von Mises stress in the 3D element are quite realistic. Nevertheless, due to the complexity of geometrical representation of the indented connection, it has not been employed in the main computations of the composite girder.

The last model used is the stitching reinforcement. A steel bar is placed in the middle of the boxes connecting them in addition to adhesion and Coulomb friction. The results allow us to see that the stitching bar adequately reflects the behaviour of the reinforcement resisting the horizontal shear force.

Another important issue that has been discussed is a rheological response of the materials under long-term loading. The interest is limited to creep. To properly characterize it, the following material models have been analyzed: the analytical model from code guidelines and the Generalized Maxwell model based on visco-elasticity. In the model, a relaxation function is used as a characteristic, since the result of the solution is stress. In a one-dimensional benchmark the relaxation function calculated with the model is exactly the same as the experimental one. Further, the proper performance of the model is checked using a 3D test of compressed box.

As said before, the main object of the research has been the composite girder with the geometry based on Choi's experiments. Four types of analysis have been carried out. First, the girder is analyzed using the Total Strain Crack model to simulate the experimental cracking response and the results are satisfactory. Then, the influence of the building process is evaluated by the construction stage analysis. To analyze the creep of concrete the CS analysis with time-dependent effects is performed. Finally, the analysis is repeated neglecting the creep representation, but taking into account the nonlinear interface response of the girder-slab connection.

Table 11.1 contains a comparison of deflections obtained in all construction stages for the three variants of numerical analysis: short-term, long-term (both performed with full bond between the girder and the plate) and with interfaces (i.e. with interface slip and opening).

In the analysis of time-dependent effects the beam is connected to the slab with a rigid connection. Each construction stage is seven days long, but there is also an additional stage with duration of 10 000 days, in which long term behaviour is considered. The first stage is prepared to see the behaviour before pre-stressing. In the second stage pre-stressing is applied to the girder, which results in negative deflection (camber). At this stage the local concentration of tensile stresses close to the anchorage zone can be observed. In the third stage casting the slab with the effect of wet concrete is simulated. In this stage the creep influences the girder response and increases the camber due to pre-stressing. On the other hand, the wet-concrete load reduces the camber. The maximum deflections of the girder observed in the simulations are listed in the second column of Table 11.1 and compared there to the results of the CS analysis without creep (first column).

Stage	Short-term	Creep (Eurocode)	Creep (Maxwell)	Interfaces
1	2.50	2.50	2.50	2.50
2	-7.99	-7.99	-7.99	-7.99
3	-5.48	-12.70	-10.20	-5.48
4	-5.46	-13.20	-12.70	-3.51
5	4.60	-3.42	-2.91	43.80
6	–	8.00	7.10	–

Table 11.1: Comparison of deflections in millimeters obtained at the ends of construction stages for all types of numerical analysis (short-term, long-term, with interfaces), camber understood as negative deflection

In the fourth stage the cross-section of the girder becomes composite, the wet-concrete load is deactivated and the slab stiffness becomes active. Comparing the results from stages 3 and 4 it is shown that the differences are not significant. The stress in the girder in stage 4 is lower comparing with the third stage because of creep.

In the fifth stage the load causing four-point bending is applied with the value equal to the cracking load from the experiment. The maximum displacement caused by the cracking load is still negative (camber) and the maximum tension stress at the mid-span is 3.7 MPa (without creep the deflection at this stage is already 4.6 mm downwards).

In the sixth stage which represents long-time behaviour of concrete, a change in girder displacement from the camber of 3.42 mm to the deflection of 8.00 mm is observed. The maximum tensile stress is affected by creep and its maximum value is 7.68 MPa. The maximum stress in strands is 1316 MPa. The long-term loss of the pre-stressing force due to creep is also noticed.

The next analyzed case is the time-dependent analysis with the creep model developed and programmed on the basis of the visco-elasticity theory, in particular the Generalized Maxwell model, including a spectral form of the characteristic relaxation function, instead of the Eurocode model used in the previous case. The influence of the model appears from the third stage, when at the beginning of the girder life-cycle an increase of deflection is observed. In the fourth stage the mid-span deflection increases slightly and in the fifth stage the results immediately after the application of the load are almost the same as for the Eurocode creep model (see Table 11.1).

In the sixth stage, when the long-time behaviour is analyzed, it can be noticed that the values of deflection and stress are lower for the implemented Maxwell model, which leads to the conclusion that advanced creep models taking into account the whole history of the member and including multi-parameter concrete descriptions are economically more efficient and on the other hand the Eurocode models are safer in terms of the load bearing capacity.

Finally, the CS analysis with interface elements is carried out. The creep and long-term loading (sixth stage) are not included in the analysis, because the Midas software employed in the research does not permit the combination of non-linear effects. The static computations are performed, whereby the results of the first three stages (the girder without the plate) are obviously as before. In the fourth stage the cross-section of the girder becomes composite. The interface allows for frictional slip and opening, since its behaviour is governed by Mohr-Coulomb plasticity. It is noticed that the camber caused by pre-stressing in the previous stage decreases to 3.51 mm. In the fifth (last) stage the external load is applied. Due to the weaker concrete-concrete connection, a significant increment of the deflection to about 44 mm is observed.

The application of the interface elements between the composite parts to simulate properly the behaviour of the connection zone leads to higher values of the deflection and stress, and hence to a safer design comparing to a rigid interface.

Longitudinal shear behaviour of the composite beam is the next phenomenon studied. The pressure load of 10 MPa is applied to the frontal face of the slab. At 140% of the load the interface starts to open and the predicted longitudinal displacement is 8.6 mm. At the maximum load the deck slides along the girder with the interface opening at both ends of the girder and the maximum longitudinal displacement is 12.3 mm.

Then the connection with stitching reinforcement is analyzed. For 10% of the load almost the same displacement is obtained as in the previous analysis of girder shear. At 200% of the assumed load the displacement is quite similar to the case without stitching reinforcement, although the dowel action of the reinforcement is simulated. This result is surprising and suggests the need for a further analysis of the complex model.

In the thesis the following statements have been discussed:

Statement 1 – The consideration of construction stages in the FEM analysis has a significant influence on the analysis results of pre-stressed concrete-concrete composite beams.

The research carried out proved Statement 1: it has been shown in Chapter 8 that the results of one-step static computations of the girder under consideration differ strongly from the results of the construction stage analysis. In fact, for all pre-stressed structures it is necessary to use construction stage analysis rather than one step static analysis because every pre-stressed structure is built in several subsequent steps, each step should be treated as a separate analysis stage and the history of the previous steps has a significant impact on the following steps.

Statement 2 – The load bearing capacity of composite (HSC-NSC) bridge girders depends strongly on the type of contact zone construction.

The research proved Statement 2: the calculations performed in Chapter 10 have shown that there is a significant difference between the load bearing capacity of two different types of the connection zone, i.e. the use of additional stitching reinforcement in a frictional interface strongly influences the behaviour of the composite girder.

Statement 3 – To accurately examine the behaviour of the pre-stressed concrete composite of two different types of concrete it is advisable to implement an advanced rheological constitutive model (for instance, Generalized Maxwell model based on viscoelasticity theory) rather than use a simple function for creep, based on standards.

The research provided arguments in favour of Statement 3: the application of more complex (multi-parameter) rheological models of concrete allows for a better use of the load-carrying capacity of a considered structural element. The standards and creep models they contain lead to more conservative design which results in a higher level of safety, but reduced economic efficiency. When advanced rheological models are employed, the designer can exploit the material strength in a better way. Such creep models also allow one to reproduce the whole history of variable load acting on the element and this is not possible when simple code models based on the creep coefficient are used.

The research has shown that it is possible to combine many different effects occurring in an advanced structural solution (e.g. composite pre-stressed girder) using numerical simulation, but the results obtained depend on many factors and are sometimes difficult to interpret. Moreover, the software itself can have limitations, for example not all important effects can be combined in one analysis case. Therefore, it is reasonable to validate calculations by proper experimental studies.

Based on the research to date and the analyses carried out here, a conclusion is drawn about the work needed in the future. A detailed parametric analysis is required to verify the employed models in more detail. In order to describe the behavior of the structure examined in this thesis in the aspect of long-term behavior, it is advisable to carry out rheological analyses taking into account concrete shrinkage and strength evolution over time. An important element is the integration of individual nonlinear phenomena in the same computational case - interface analysis, rheology and concrete cracking should be combined. Finally, more composite zone types should be analyzed, in particular the indented connection (much more difficult to produce in practice and not considered in the current numerical analysis of the composite girder).

References

[ACI Committee 318, 1995] ACI Committee 318 (1995). Building code requirements for structural concrete (ACI 318-95). Technical report, American Concrete Institute, Farmington Hills.

[ACI Committee 318, 2008] ACI Committee 318 (2008). Building code requirements for structural concrete (ACI 318-08). Technical report, American Concrete Institute, Farmington Hills.

[ACI Committee 363, 1997] ACI Committee 363 (1997). State of art report on high-strength concrete. Technical report, American Concrete Institute.

[ACI Committee 363, 2007] ACI Committee 363 (2007). Guide to quality control and testing of high strength concrete. Technical report, American Concrete Institute.

[Adanur et al., 2012] Adanur, S., Günaydin, M., A., A., and Sevim, B. (2012). Construction stage analysis of Humber Suspension Bridge. *Applied Mathematical Modelling*, 36(11):5492–5505.

[Al-Omaishi et al., 2009] Al-Omaishi, N., Tadros, M., and Seguirant, S. (2009). Elasticity modulus, shrinkage and creep of high strength concrete as adopted by AASHTO. *PCI Journal*, 54(3):44–63.

[Altunisik et al., 2010] Altunisik, A., Bayraktar, A., Sevim, B., Adanur, S., and Domanic, A. (2010). Construction stage analysis of Kömürhan Highway Bridge using time dependent material properties. *Structural Engineering and Mechanics*, 36(2):207–223.

[American Association of State Highway and Transportation Officials, 2017] American Association of State Highway and Transportation Officials (2017). AASHTO LRFD bridge design specification. Washington DC.

[Ates, 2011] Ates, S. (2011). Numerical modelling of continuous concrete box girder bridges considering construction stages. *Applied Mathematical Modelling*, 35(8):3809–3820.

[Bass et al., 1989] Bass, R., Carrasquillo, R., and Jirsa, J. (1989). Shear transfer across new and existing concrete interfaces. *ACI Structural Journal*, 86(4):383–39.

[Bazant, 1975] Bazant, Z. P. (1975). Theory of creep and shrinkage in concrete structures: A précis of recent developments. *Mechanics Today*, 2:1–93.

[Bazant and Prasannan, 1989] Bazant, Z. P. and Prasannan, S. (1989). Solidification theory for concrete creep: I. Formulation, and II. Verification and application. *Journal of Engineering Mechanics ASCE*, 115:1691–1725.

[Benaim, 2008] Benaim, R. (2008). *The Design of Prestressed Concrete Bridges: Concepts and Principles.* Taylor&Francis, New York, 1st edition.

[Bfer, 1985] Bfer, G. (1985). An isoparametric joint/interface element for finite element analysis. *International Journal for Numerical Methods in Engineering*, 21(4):585–600.

[Bilal et al., 1990] Bilal, A., Young, S., and Hamid, S. (1990). Prestressed composite girders under positive moment. *Journal of Structural Engineering ASCE*, 116(11).

[Biliszczuk and Rajski, 2002] Biliszczuk, J. and Rajski, O. (2002). Zastosowanie betonów wysokich klas w mostownictwie. Konferencja Dni Betonu - Tradycja i Nowoczesność, Szczyrk.

[Bradford and Gilbert, 1992] Bradford, M. A. and Gilbert, R. I. (1992). Composite beams with partial interaction under sustained loads. *Journal of Structural Engineering*, 118(7):1871–1883.

[Bruyneel et al., 2009] Bruyneel, M., Delsemme, J.-P., and Jetteur, P. (2009). Modeling inter-laminar failure in composite structures: illustration on an industrial case study. *Applied Composite Materials*, 16(3):149–162.

[Bryson and Carpenter, 1970] Bryson, J. O. and Carpenter, E. F. (1970). *Flexural Behaviour of Prestressed Concrete Tee-Beams.* U.S. Government Printing Office, Washington D. C.

[Building and Construction Authority, 2008] Building and Construction Authority (2008). Design Guide of High Strength Concrete to Singapore Standard CP 65. Technical report, Building and Construction Authority, Singapore.

[Carrasquillo et al., 1981a] Carrasquillo, R., Nilson, A., and Slate, F. (1981a). Properties of high strength concrete subject to short-term loads. *ACI Journal*, 78(3):171–178.

[Carrasquillo et al., 1981b] Carrasquillo, R., Slate, F., and Nilson, A. (1981b). Microcracking and behavior of high strength concrete subject to short-term loading. *ACI Journal*, 78(3):179–186.

[Chin et al., 1997] Chin, M., Mansur, M., and Wee, T. (1997). Effects of shape, size and casting direction of specimens on stress-strain curves of high strength concrete. *ACI Materials Journal*, 94(3):209–219.

[Choi, 2006] Choi, W. (2006). *Flexural behavior of prestressed girder with high strength concrete*. Ph.D. dissertation, A&T State University, Raleigh, North Carolina.

[Choi et al., 2008] Choi, W., Rizkalla, S., Zia, P., and Mirmiran, A. (2008). Behavior and design of high-strength prestressed concrete girders. *PCI Journal*, 53(5):54–69.

[Cholewicki, 2001] Cholewicki, A. (2001). *Konstrukcje zespolone z prefabrykatów*. Prace Naukowe ITB, Warszawa.

[de Borst, 2018] de Borst, R. (2018). *Computational Methods for Fracture in Porous Media. Chapter 4 - Interface Elements*. Elsevier.

[de Borst et al., 2012] de Borst, R., Crisfield, A., Remmers, J., and Verhoosel, V. (2012). *Nonlinear Finite Element Analysis of Solids and Structures*. Wiley, 2nd edition.

[Destrebecq et al., 1999] Destrebecq, J.-F., Gwoździewicz, P., and Jurkiewicz, B. (1999). Time analysis of prestressed concrete members subjected to axial plus shear loads. Wroclaw, Poland.

[DIANA FEA, 2020] DIANA FEA (2020). Diana user's maual. Delft, The Netherlands.

[Dolinajová and Moravčík, 2013] Dolinajová, K. and Moravčík, M. (2013). Monitoring and numerical analysis of construction stages on the bridge realized by the free cantilever method. *Procedia Engineering*, 65:321–326.

[Ducret and Lebet, 1999] Ducret, J.-M. and Lebet, J.-P. (1999). Behaviour of composite bridges during construction. *Structural Engineering International*, 9(3):212–218.

[European Committee for Standardization, 2004] European Committee for Standardization (2004). Design of Concrete Structures. Part 1-1: General Rules and Rules for Buildings. Brussels.

[Evans and Parker, 1955] Evans, R. H. and Parker, A. S. (1955). Behavior of prestressed concrete composite beams. *Journal Proceedings*, 51(5):861–878.

[fib, 2010] fib (2010). Model code 2010. Technical report, International Federation for Structural Concrete (fib), Lausanne.

[Fowler et al., 1999a] Fowler, D., Choi, D.-U., and Jirsa, J. (1999a). Shear transfer across interface between new and existing concretes using large powder-driven nails. *ACI Structural Journal*, 96(2):183–192.

[Fowler et al., 1999b] Fowler, D., Jirsa, J., and Choi, D.-U. (1999b). Interface shear strength of concrete at early ages. *ACI Structural Journal*, 96(3):343–347.

[French and Mokhtarzadeh, 1993] French, C. and Mokhtarzadeh, A. (1993). High strength concrete: Effects of materials, curing and test procedures on short-term compressive strength. *PCI Journal*, 38(3):76–87.

[Furtak, 2006] Furtak, K. (2006). Ocena możliwości powstania rys skurczowych w płycie żelbetowej belek zespolonych typu beton-beton. *Inżynieria i Budownictwo*, 2006/5:248–250.

[Gens et al., 1989] Gens, A., Carol, I., and Alonso, E. E. (1989). An interface element formulation for the analysis of soil-reinforcement interaction. *Computers and Geotechnics*, 7(1):133–151.

[Gromysz and Starosolski, 2003] Gromysz, K. and Starosolski, W. (2003). Badanie zespolonego stropu deskowego w skali naturalnej. *Inżynieria i Budownictwo*, 2003/9:522–525.

[Gupta et al., 2009] Gupta, S., Sehgal, V., and Kaushik, S. (2009). Shrinkage of high strength concrete. *World Academy of Science, Engineering and Technology*, 50:264–267.

[Gwoździewicz et al., 2015] Gwoździewicz, P., Jarno, Ł., and Pamin, J. (2015). Accounting for time-dependent effects in the construction stage fem analysis of composite pre-stressed bridge girders. *Czasopismo Techniczne. Budownictwo*, 112:77–88.

[Gwoździewicz, 1999] Gwoździewicz, P. (1999). Time analysis of prestressed concrete structures with accounting for bending and shear effects. Clermont-Ferrand.

[Halicka, 2001] Halicka, A. (2001). O skuteczności zespolenia dwóch betonów. *Inżynieria i Budownictwo*, 2001/3:144–146.

[Halicka, 2007] Halicka, A. (2007). *Studium stanu naprężeń i odkształceń w płaszczyźnie styku i strefie przypodporowej elementów zespolonych z udziałem betonów skurczowych i ekspansywnych.* Wydawnictwo Politechniki Lubelskiej, Lublin.

[Halicka and Franczak, 2009] Halicka, A. and Franczak, D. (2009). Rozwój przyczepności między dwoma betonami w czasie twardnienia betonu. *Budownictwo i Architektura*, 5(2):5–16.

[Halicka and Franczak, 2012] Halicka, A. and Franczak, D. (2012). Wpływ wieku betonu na nośność styku w elementach zespolonych typu beton-beton. *Przegląd budowlany*, 2012/1:46–51.

[Hambly, 1990] Hambly, E. C. (1990). *Bridge Deck Behaviour.* CRC Press, 2nd edition.

[Hamid et al., 1989] Hamid, S., Pedro, A., and Bilal, A. (1989). Analytical study of prestressed composite beams. *Journal of Structural Engineering ASCE*, 115(9).

[Hanswille et al., 1998] Hanswille, G., Jost, K., Schmitt, C., and R., T. (1998). Experimentelle untersuchungen zur tragfähigkeit von kopfbolzendübeln mit großen schaftdurchmessern. *Stahlbau*, 67(7).

[Hewson, 2012] Hewson, N. (2012). *Prestressed Concrete Bridges: Design and Construction.* CE Publishing, London, 2nd edition.

[Hou et al., 2016] Hou, H., Liu, X., Qu, B., Ma, T., Liu, H., Feng, M., and Zhang, B. (2016). Experimental evaluation of flexural behavior of composite beams with cast-in-place concrete slabs on precast prestressed concrete decks. *Engineering Structures*, 126:405–416.

[Hueste et al., 2004] Hueste, M. B., Chompreda, P., Trejo, D., Cline, D., and Keating, P. (2004). Mechanical properties of high strength concrete for prestressed members. *ACI Structural Journal*, 101(4):457–465.

[Iravani, 1996] Iravani, S. (1996). Mechanical properties of high – performance concrete. *ACI Materials Journal*, 93(5):416–426.

[Issa et al., 2003] Issa, M., Patton, T., Abdalla, H., and Yousif, A. (2003). Composite behavior of shear connections in full-depth precast concrete bridge deck panels on steel stringers. *PCI Journal*, 48(5):76–89.

[Jarek, 2004] Jarek, B. (2004). *Zarysowanie płyty żelbetowej w belkach zespolonych typu stal-beton*. Ph.D. dissertation, Politechnika Krakowska, Kraków.

[Jarno, 2012a] Jarno, Ł. (2012a). High strength prestressed concrete girders combined with normal strength concrete slab. In *Proc. of the 14th International Conference of PhD Students - Juniorstav 2012*, Brno.

[Jarno, 2012b] Jarno, Ł. (2012b). Sprężone zespolone dźwigary mostowe z betonu wysokiej wytrzymałości. Analiza doświadczalna i teoretyczna. In *Materiały konferencyjne Konferencja Młodych Naukowców – II edycja, Wpływ młodych naukowców na osiągnięcia polskiej nauki*, Gdańsk.

[Jarno, 2013a] Jarno, Ł. (2013a). Contact zone bearing capacity of concrete-concrete composite structures. In *JUNIORSTAV 2013: 15th International Conference of PhD Students. Proceedings of annotations*, Brno. Vysoké učení technické v Brně. Fakulta stavebn.

[Jarno, 2013b] Jarno, Ł. (2013b). High strength concrete – mechanical and rheological properties. In *Materiały konferencyjne: Wpływ młodych naukowców na osiągnięcia polskiej nauki*, Gdańsk.

[Jarno and Dyba, 2013a] Jarno, Ł. and Dyba, M. (2013a). Connection zone in composite bridge girders made of high performance concrete. In *Materiały konferencyjne: Dokonania Naukowe Doktorantów I Edycja*, Kraków.

[Jarno and Dyba, 2013b] Jarno, Ł. and Dyba, M. (2013b). Stress state analysis during pretensioning of precast high performance concrete panel. In *Materiały konferencyjne Dokonania Naukowe Doktorantów I Edycja*, Kraków.

[Jarno et al., 2014] Jarno, Ł., Dyba, M., and Ślaga, Ł. (2014). Connection zone forming methods in composite prestressed bridge girders made of high strength concrete. In *Proc. of the 16th International Conference of PhD Students „JUNIORSTAV 2014*, page 133, Brno.

[Jarno and Pamin, 2017] Jarno, Ł. and Pamin, J. (2017). FEM modeling of concrete-concrete contact zone in construction stage analysis of composite bridge girders. In Salamak, M., editor, *Proc. of the VIII Polish Conference of Bridge Engineers infraMOST*, pages 107–114, Wisła.

[Kamiński and Kmiecik, 2010] Kamiński, M. and Kmiecik, P. (2010). Analysis of the horizontal shear load capacity of concrete composite structures. The 10th International Conference in Vilnius- Modern Building Materials, Structures and Techniques.

[Kamiński and Kmiecik, 2011a] Kamiński, M. and Kmiecik, P. (2011a). Analytical models of load capacity of shear reinforcement in composite concrete structures. fib Symposium 2011- Concrete engineering for excellence and efficiency.

[Kamiński and Kmiecik, 2011b] Kamiński, M. and Kmiecik, P. (2011b). Obliczanie połączenia prefabrykatów żelbetowych z nadbetonem konstrukcyjnym – przegląd wytycznych normowych. *Przegląd budowlany*, 2011/6:69–73.

[Karakaplan et al., 2009] Karakaplan, A., Caner, A., Kurc, O., Domantc, A., and Lulec, A. (2009). A new era in structural analysis: Construction staging. *Teknik Dergi*, 20(10):4905–4917.

[Khan et al., 1995] Khan, A., Cook, W., and Mitchell, D. (1995). Early age compressive stress-strain properties of low, medium and high strength concretes. *ACI Materials Journal*, 92(6):617–624.

[Khan et al., 1996] Khan, A., Cook, W., and Mitchell, D. (1996). Tensile strength of low, medium and high strength concretes at early ages. *ACI Materials Journal*, 93(5):487–493.

[Kim et al., 2018] Kim, C., Park, H., Hong, G., Lee, H., and Suh, J. (2018). Shear strength of reinforced concrete-composite beams with prestressed concrete and non-prestressed concrete. *Structural Journal*, 115(4):917–930.

[Kim et al., 2011] Kim, K., Lee, D., Cho, S., Choi, Y., and Jung, S. (2011). Flexural behavior of prestressed composite beams with corrugated web: Part I. Development and analysis. *Composites Part B: Engineering*, 42:1603 – 1616.

[Król and Tur, 2001] Król, M. and Tur, M. (2001). O obliczaniu przekrojów zespolonych z nadbetonem z betonu ekspansywnego. *Inżynieria i Budownictwo*, 2001/3:137–139.

[Król et al., 2001] Król, M., Tur, W., Szałobyta, T., and Halicka, A. (2001). Obliczanie styków elementów zespolonych z betonu zwykłego i ekspansywnego z uwzględnieniem analizy nieliniowej. *Inżynieria i Budownictwo*, 2001/3:140–143.

[Kuś et al., 1999] Kuś, S., Wilczyński, R., and Zieliński, J. (1999). Konstrukcje zespolone w tradycji oraz normach polskich i europejskich. *Inżynieria i Budownictwo*, 1999/6:319–324.

[Lindig, 2007] Lindig, V. (2007). Empfehlungen zur Mindestbewehrung von schubbeanspruchten Fugen. *Beton und Stahlbetonbau*, 102(3):168–181.

[Logan et al., 2009] Logan, A., Choi, W., Mirmiran, A., Rizkalla, S., and Zia, P. (2009). Short-term mechanical properties of high-strength concrete. *ACI Materials Journal*, 106(5):413–418.

[Lorenc and Kubica, 2016] Lorenc, W. and Kubica, E. (2016). Behavior of composite beams prestressed with external tendons: Experimental study. *Journal of Constructional Steel Research*, 62:1353–1366.

[Lorenc and Kubica, 2020] Lorenc, W. and Kubica, E. (2020). Nonlinear modelling of composite beams prestressed with external tendon. *Journal of Structural Engineering*, 4(1):83–94.

[Lou and Karavasilis, 2019] Lou, T. and Karavasilis, T. (2019). Numerical assessment of the nonlinear behavior of continuous prestressed steel-concrete composite beams. *Engineering Structures*, 190:116–127.

[Magureanu et al., 2012] Magureanu, C., Sosa, I., Negrutiu, C., and Heghes, B. (2012). Mechanical properties and durability of ultra-high-performance concrete. *ACI Materials Journal*, 109(2):177–183.

[Malm and Sundquist, 2020] Malm, R. and Sundquist, H. (2020). Time-dependent analyses of segmentally constructed balanced cantilever bridges. *Engineering Structures*, 32(4):1038–1045.

[Mari, 2000] Mari, R. A. (2000). Numerical simulation of the segmental construction of three dimensional concrete frames. *Engineering Structures*, 22(6):585–596.

[Marques and Creus, 2012] Marques, S. and Creus, G. (2012). *Computational Viscoelasticity.* Springer, Heidelberg.

[Menkulasi and Roberts-Wollmann, 2005] Menkulasi, F. and Roberts-Wollmann, C. (2005). Behavior of horizontal shear connections for full-depth precast concrete bridge decks on prestressed I-girders. *PCI Journal*, 50(3):60–73.

[Menn, 2011] Menn, C. (2011). *Prestressed Concrete Bridges.* Springer.

[Midas IT, 2020] Midas IT (2020). Midas FEA analysis reference. Seoul, South Korea.

[Mokhtarzadeh and French, 2000] Mokhtarzadeh, A. and French, C. (2000). Mechanical properties of high-strength concrete with consideration for precast applications. *ACI Materials Journal*, 97(2):136–147.

[Mokhtarzadeh and French, 2004] Mokhtarzadeh, A. and French, C. (2004). Bibliography on high strength concrete. *PCI Journal*, 38:130–137.

[Ngab et al., 1981a] Ngab, A., Nilson, A., and Slate, F. (1981a). Shrinkage and creep of high strength concrete. *ACI Journal*, 78(4):255–261.

[Ngab et al., 1981b] Ngab, A., Slate, F., and Nilson, A. (1981b). Microcracking and time-dependent strains in high strength concrete. *ACI Journal*, 78(4):262–268.

[Ottosen and Ristinmaa, 2005] Ottosen, N. and Ristinmaa, M. (2005). *The Mechanics of Constitutive Modeling.* Elsevier.

[Ozbakkaloglu and Saatcioglu, 2004] Ozbakkaloglu, T. and Saatcioglu, M. (2004). Rectangular stress block for high strength concrete. *ACI Structural Journal*, 101(4):475–483.

[Pantano and Averill, 2007] Pantano, A. and Averill, R. (2007). A penalty-based interface technology for coupling independently modeled 3D finite element meshes. *Finite Elements in Analysis and Design*, 43:271–286.

[Pipinato and De Miranda, 2016] Pipinato, A. and De Miranda, M. (2016). *Innovative Bridge Design Handbook. Chapter 10 - Steel and composite bridges.* Butterworth-Heinemann, Boston.

[Polski Komitet Normalizacyjny, 2002] Polski Komitet Normalizacyjny (2002). PN-B-03264, Konstrukcje betonowe, żelbetowe i sprężone. Obliczenia statyczne i projektowanie.

[Portland Cement Association, 1994] Portland Cement Association (1994). High strength concrete. concrete technology today. *Concrete Technology Today*, 15(1).

[Puchalska and Kuczma, 2017a] Puchalska, D. and Kuczma, M. (2017a). Skurcz i pełzanie betonu w ujęciach norm PN-B 03264:2002, PN-EN 1992-1-1: część 1. *Builder*, 2017/1:69–71.

[Puchalska and Kuczma, 2017b] Puchalska, D. and Kuczma, M. (2017b). Skurcz i pełzanie betonu w ujęciach norm: pre-norma konstrukcji betonowych: część 2. *Builder*, 2017/2:54–56.

[Rakowski and Kacprzyk, 2016] Rakowski, G. and Kacprzyk, Z. (2016). *Metoda elementów skończonych w mechanice konstrukcji.* Oficyna Wydawnicza Politechniki Warszawskiej, Warszawa.

[Randl et al., 2008] Randl, N., Zilch, K., and Muller, A. (2008). Bemessing nachtraglich erganzter Betonbauteile mit langsschubbeanspruchter Fuge. *Beton und Stahlbetonbau*, 103(7):482–496.

[Ranzi and Bradford, 2006] Ranzi, G. and Bradford, M. (2006). Analytical solutions for the time-dependent behaviour of composite beams with partial interaction. *International Journal of Solids and Structures*, 43(13):3770–3793.

[Roberts, 1985] Roberts, T. M. (1985). Finite difference analysis of composite beams with partial interaction. *Computers & Structures*, 21(3):469–473.

[Roller et al., 1993] Roller, J., Martin, B., Russel, H., and Bruce, R. (1993). Performance of prestressed high strength concrete bridge girders. *PCI Journal*, 38(3):34–45.

[Rots, 1988] Rots, J. (1988). *Computational modeling of concrete fracture.* Ph.D. dissertation, Delft University of Technology, Delft.

[Roylance, 2001] Roylance, D. (2001). Engineering viscoelasticity. Massachusetts Institute of Technology.

[Saadatmanesh et al., 1989] Saadatmanesh, H., Albrecht, P., and Ayyub, B. M. (1989). Experimental study of prestressed composite beams. *Journal of Structural Engineering*, 115(9).

[Schellekens, 1990] Schellekens, J. (1990). Interface elements in finite element analysis. TNO Institute for Building Materials and Structures, Delft.

[Schellekens, 1992] Schellekens, J. (1992). *Computational strategies for composite structures.* Ph.D. dissertation, Delft University of Technology, Delft.

[Schellekens and de Borst, 1993] Schellekens, J. C. J. and de Borst, R. (1993). On the numerical integration of interface elements. *International Journal for Numerical Methods in Engineering*, 36:43–46.

[Schipperen, 2001] Schipperen, J. (2001). *Computational modelling of failure in fibre reinforced plastic.* Ph.D. dissertation, Delft University of Technology, Delft.

[Seeber, 2004] Seeber, K. e. a. (2004). *Precast and Prestressed Concrete.* PCI Designed Handbook, 6th edition.

[Sengul et al., 2002] Sengul, O., Tasdemir, C., and Tasdemir, M. (2002). Influence of aggregate type on mechanical behavior of normal and high strength concrete. *ACI Materials Journal*, 99(6):528–533.

[Shah and Ahmad, 1985] Shah, S. and Ahmad, S. (1985). Structural properties of high strength concrete and its implications for precast prestressed concrete. *PCI Journal*, 30(6):92–119.

[Shiming and Ping, 2005] Shiming, C. and Ping, G. (2005). Load carrying capacity of composite beams prestressed with external tendons under positive moment. *Journal of Constructional Steel Research*, 61:515–530.

[Smarzewski, 2009] Smarzewski, P. (2009). Analiza numeryczna niesprężystych belek żelbetowych z betonu wysokiej wytrzymałości o niskim stopniu zbrojenia. *Budownictwo i Architektura*, 4(1):5–30.

[Somja and de Ville de Goyet, 2008] Somja, H. and de Ville de Goyet, V. (2008). A new strategy for analysis of erection stages including an efficient method for creep analysis. *Engineering Structures*, 30(10):2871–2883.

[Sououshian et al., 1987] Sououshian, P., Obaseki, K., Rojas, M., and Najm, H. (1987). Behavior of bars in dowel action against concrete cover. *ACI Journal*, 84(2):170–176.

[Stallings et al., 2003] Stallings, J., Barnes, R., and Eskildsen, S. (2003). Camber and prestress losses in Alabama HPC bridge girders. *PCI Journal*, 48(5):90–104.

[Stewart and Rosowsky, 1998] Stewart, M. G. and Rosowsky, D. V. (1998). Structural safety and serviceability of concrete bridges subject to corrosion. *Journal of Infrastructure Systems*, 4(4):146–155.

[Taejun and Tae, 2008] Taejun, C. and Tae, S. K. (2008). Probabilistic risk assessment for the construction phases of a bridge construction based on finite element analysis. *Finite Elements in Analysis and Design*, 44(6):383–400.

[Tan et al., 1999] Tan, K., Guan, L., Lu, X., and Lim, T. (1999). Horizontal shear strength of indirectly loaded composite concrete beams. *ACI Structural Journal*, 96(4):533–538.

[Tanner, 2008] Tanner, J. (2008). Calculating shear friction using an effective coefficient of friction. *PCI Journal*, 53(3):114–119.

[Troitsky et al., 1989] Troitsky, M., Zielinski, Z., and Nouraeyan, A. (1989). Pretensioned and posttensioned composite girders. *Journal of Structural Engineering ASCE*, 115(12).

[Valluvan et al., 1999] Valluvan, R., Kreger, M., and Jirsa, J. (1999). Evaluation of shear-friction provisions. *ACI Structural Journal*, 96(4):473–481.

[Wang et al., 2011] Wang, W., Dai, J., Li, G., and Huang, C. (2011). Long-term behavior of prestressed old-new concrete composite beams. *Journal of Bridge Engineering*, 16(2):275–285.

[Wang et al., 2020a] Wang, X., Wang, H., Sun, Y., Mao, X., and Tang, S. (2020a). Process-independent construction stage analysis of self-anchored suspension bridges. *Automation in Construction*, 117:103227.

[Wang et al., 2020b] Wang, Y., Yu, J., Liu, J., Zhou, B., and Y., C. (2020b). Experimental study on assembled monolithic steel-prestressed concrete composite beam in negative moment. *Journal of Constructional Steel Research*, 167:105667.

[Weiss, 2000] Weiss, J. (2000). High performance concrete: strength, permeability and shrinkage cracking. Proceedings of the PCI/FHWA International Symposium on High Performance Concrete, Orlando Florida.

[Wiegrink et al., 1996] Wiegrink, K., Marikunte, S., and Shah, S. (1996). Shrinkage cracking of high-strength concrete. *ACI Materials Journal*, 93(5):409–415.

[Wilczyński, 2003] Wilczyński, R. (2003). Komentarz naukowy do PN-B-03264:2002 – Konstrukcje zespolone. Technical report, Instytut Techniki Budowlanej, Warszawa.

[Wisnom, 2010] Wisnom, M. (2010). Modelling discrete failures in composites with interface elements. *Composites Part A: Applied Science and Manufacturing*, 41(7):795–805.

[Wollmann et al., 2003] Wollmann, G., Anderson, R., and Wollmann, C. (2003). Creep and shrinkage effects in spliced prestressed concrete girder bridges. *PCI Journal*, 48(6):92–105.

[Wosatko et al., 2019] Wosatko, A., Winnicki, A., Polak, M. A., and Pamin, J. (2019). Role of dilatancy angle in plasticity-based models of concrete. *Arch. Civ. Mech. Eng.*, 19(4):1268–1283.

[Zhou et al., 2018] Zhou, H., Li, S., Chen, L., and Zhang, C. (2018). Fire tests on composite steel-concrete beams prestressed with external tendons. *Journal of Constructional Steel Research*, 143:62–71.

[Zienkiewicz et al., 2000] Zienkiewicz, O., Chan, A., Pastor, M., Schrefler, B., and Shiomi, T. (2000). *Computational Geomechanics*. John Wiley & Sons, Chichester.

[Zienkiewicz et al., 2005] Zienkiewicz, O., Taylor, R., and Zhu, J. (2005). *The Finite Element Method*. Elsevier Butterworth-Heinemann, Oxford, sixth edition.

Appendix A

A.1 Total Strain Crack model

In concrete cracking analysis a discrete crack model (discontinuous model) or a smeared crack model (continuous model) can be used (see Fig. A.1).

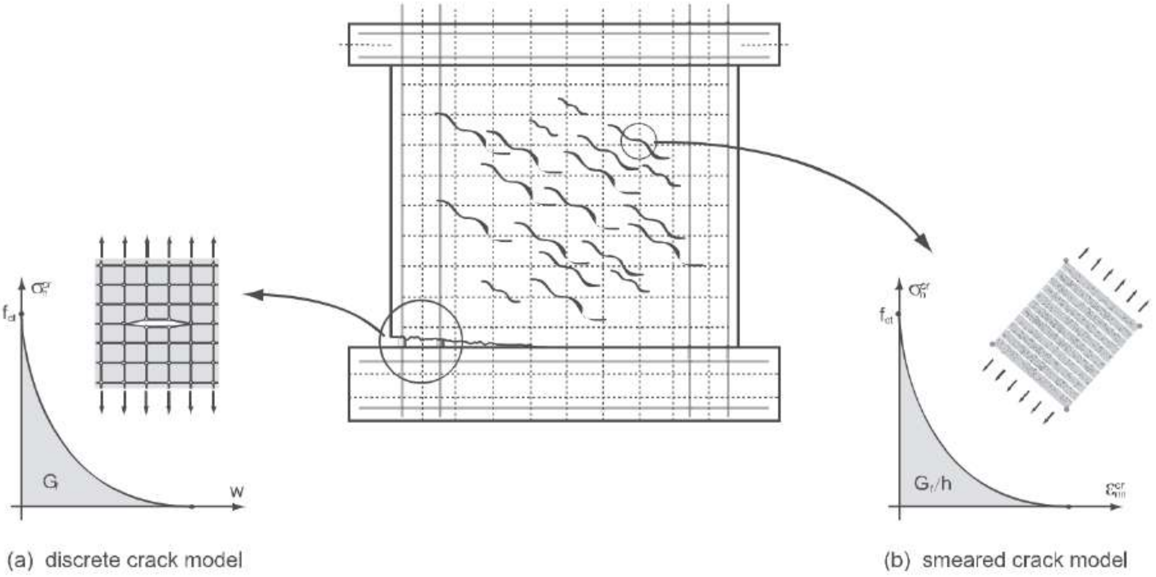

(a) discrete crack model

(b) smeared crack model

Figure 13-(1) Concrete crack models

Fig. A.1: Concrete crack models [Midas IT, 2020]

The discrete crack model simulates the occurrence of physical discontinuities related to concrete cracking, failure and bond slip of reinforcing bars. The smeared crack model is based on the assumption that cracks are evenly scattered over a certain area.

The smeared crack models can be classified into orthogonal and non-orthogonal models, depending on the assumption concerning the direction of second crack. In the strain decomposition model the total strain is calculated as the sum of material strain and crack strain. The material strain can include elastic strain, plastic strain, creep strain, thermal strain, etc. The crack strain can include a number of crack strains at different angles. In this type of model the selection of material properties is difficult, so convergence may become an issue. The simple total strain crack algorithm uses one stress-strain relation to represent the tensile behaviour, including cracks and shear retention after cracking, and another one for the compressive behaviour.

Before performing an analysis with the Total Strain Crack (TSC) model the following parameters need to be set: crack model type, concrete properties, definition of tensile, shear and compressive behaviour, specification of lateral influences. In MIDAS programs the TSC model contains the smeared fixed crack model and smeared rotating crack model. Usually both represent the cracking response of general reinforced concrete structures quite well.

A.2 Concrete properties

MIDAS programs have two options to determine the required material properties. It can either be done manually by the user or chosen automatically by the program after setting a correct code. The properties which can be selected be the user are: Young's modulus, Poisson's ratio, tensile strength, compressive strength and fracture energy.

When a user wants to set the values on the basis of a code of practice, the material properties are calculated according to CEB-FIP 1990 and applied in the analysis. In order to select material properties the user needs to set the concrete grade (f$_{ck}$)and the maximum aggregate size (D$_{max}$). The concrete grade and aggregate size are used to calculate the Young's modulus. The compressive strength is represented by:

$$f_{cm} = f_{ck} + \Delta f \tag{A.1}$$

where $\Delta f = 8$ MPa. The Young's modulus is expressed using compressive strength:

$$E_c = E_{c0}\left(\frac{f_{cm}}{f_{cm0}}\right)^{\frac{1}{3}} \tag{A.2}$$

where $E_{c0} = 2.15 \times 10^4$ N/mm^2, and $f_{cm0} = 10$ N/mm^2. The tensile strength is:

$$f_{ct,m} = f_{ctk0,m}\left(\frac{f_{ck}}{f_{ck0}}\right)^{\frac{2}{3}} \tag{A.3}$$

where: $f_{ctk0,m} = 1.4$ N/mm^2 and $f_{ck0} = 10$ N/mm^2. The fracture energy is computed according to the following equation:

$$G_f = G_{f0}\left(\frac{f_{cm}}{f_{cm0}}\right)^{0.7} \tag{A.4}$$

where Table A.1 shows the values of G_{f0}.

D$_{max}$(mm)	**G**$_{f0}$(J/m^2)
8	25
16	30
32	58

Table A.1: Values of G_{f0} corresponding to D_{max}

A.3 Crack strain transformation

In the TSC model the stress is defined as a function of the total strain. Loading and unloading follow different paths, unloading follows the secant slope.

The stress-strain relationship is determined depending on the directions of principal strains. The rotating crack model is mainly used to predict the behaviour of reinforced concrete structures. The fixed crack model defines the stress-strain relationships of all subsequent steps based on fixed coordinate axes of the incipient crack direction. The orthogonal crack model is widely used for crack analysis.

The strains in the element coordinate system (x,y,z) are updated by considering the incremental strain $\Delta\varepsilon_{xyz}$, namely

$$\boldsymbol{\varepsilon}_{xyz}^{t+\Delta t} = \boldsymbol{\varepsilon}_{xyz}^{t} + \Delta\boldsymbol{\varepsilon}_{xyz}^{t+\Delta t} \tag{A.5}$$

A transformation matrix is used to obtain the strains in a crack coordinate system, (u, s, t)

$$\boldsymbol{\varepsilon}_{nst} = \mathbf{T}\boldsymbol{\varepsilon}_{xyz}^{t+\Delta t} \tag{A.6}$$

The strain tensor is expressed in its general form

$$\boldsymbol{\varepsilon} = \begin{bmatrix} \varepsilon_{xx} & \varepsilon_{xy} & \varepsilon_{xz} \\ \varepsilon_{yx} & \varepsilon_{yy} & \varepsilon_{yz} \\ \varepsilon_{zx} & \varepsilon_{zy} & \varepsilon_{zz} \end{bmatrix} \tag{A.7}$$

and its eigenvectors are saved in a rotation matrix:

$$R = \begin{bmatrix} c_{xn} & c_{xs} & c_{xt} \\ c_{yn} & c_{ys} & c_{yt} \\ c_{zn} & c_{zs} & c_{zt} \end{bmatrix} \tag{A.8}$$

where $c_{i,j}$ are directional cosines of versors of crack coordinate system in element coordinate set.

The transformation matrix $\mathbf{T}$ is then calculated as

$$\mathbf{T} = \begin{bmatrix} c_{xn}^2 & c_{yn}^2 & c_{zn}^2 & c_{xn}c_{yn} & c_{yn}c_{zn} & c_{zn}c_{xn} \\ c_{xs}^2 & c_{ys}^2 & c_{zs}^2 & c_{xs}c_{ys} & c_{ys}c_{zs} & c_{zs}c_{xs} \\ c_{xt}^2 & c_{yt}^2 & c_{zt}^2 & c_{xt}c_{yt} & c_{yt}c_{zt} & c_{zt}c_{xt} \\ 2c_{xn}c_{xs} & 2c_{yn}c_{ys} & 2c_{zn}c_{zs} & c_{xn}c_{ys} + c_{yn}c_{xs} & c_{yn}c_{zs} + c_{zn}c_{ys} & c_{zn}c_{xs} + c_{xn}c_{zs} \\ 2c_{xs}c_{xt} & 2c_{ys}c_{yt} & 2c_{zs}c_{zt} & c_{xs}c_{yt} + c_{ys}c_{xt} & c_{ys}c_{zt} + c_{zs}c_{yt} & c_{zs}c_{xt} + c_{xs}c_{zt} \\ 2c_{xt}c_{xn} & 2c_{yt}c_{yn} & 2c_{yt}c_{yn} & c_{xt}c_{yn} + c_{yt}c_{xn} & c_{yt}c_{zn} + c_{zt}c_{yn} & c_{zt}c_{xn} + c_{xt}c_{zn} \end{bmatrix} \tag{A.9}$$

in a general three-dimensional stress situation. The constitutive model is then formulated in the crack coordinate system

$$\boldsymbol{\sigma}_{nst}^{t+\Delta t} = \boldsymbol{\sigma}\left(\boldsymbol{\varepsilon}_{nst}^{t+\Delta t}\right) \tag{A.10}$$

The stress in the crack coordinate systems is transformed to the element coordinate systems

$$\boldsymbol{\sigma}_{xyz}^{t+\Delta t} = \mathbf{T}^{T}\boldsymbol{\sigma}_{nst}^{t+\Delta t} \tag{A.11}$$

The transformation matrix $\mathbf{T}$ is a function of the current strain $\mathbf{T}\left(\boldsymbol{\varepsilon}_{xyz}^{t+\Delta t}\right)$ in the rotating crack model, and in the fixed crack model it is constant.

A.4 Stiffness matrix

For concrete crack analysis we use an incremental iterative scheme. Balance between external and internal force vectors is approached by implementing the Newton-Raphson method. The constitutive model needs to be defined by a proper stiffness matrix. In MIDAS programs the secant and tangent stiffness approaches are available. The secant stiffness approach provides stable solutions in analyses of reinforced concrete structures, where many cracks occurs and the tangent stiffness approach is suitable for analyses of local cracking or crack propagation.

A.5 Tangent stiffness matrix

The tangent stiffness matrix is given by

$$\mathbf{D} = \mathbf{T}^{\mathrm{T}}\mathbf{D}_{tangent}\mathbf{T} \tag{A.12}$$

where $\mathbf{T}$ - strain transformation matrix, and $\mathbf{D}_{tangent}$ - tangent stiffness matrix in the crack coordinate system.

The tangent stiffness matrix can be decomposed into four sub-matrices

$$\mathbf{D}_{tangent} = \begin{bmatrix} \mathbf{D}_{nn} & \mathbf{D}_{ns} \\ \mathbf{D}_{sn} & \mathbf{D}_{ss} \end{bmatrix} \tag{A.13}$$

where: $\mathbf{D}_{nn}$ - tangent stiffness sub-matrix for the normal components of the local strain, $\mathbf{D}_{ss}$ - tangent stiffness sub-matrix for the shear components of the local strain, and $\mathbf{D}_{ns}$ and $\mathbf{D}_{sn}$ - tangent stiffness sub-matrices representing the coupling terms between the normal and shear strain.

A.6 Tension models

The tensile response model can be idealized by the following options:

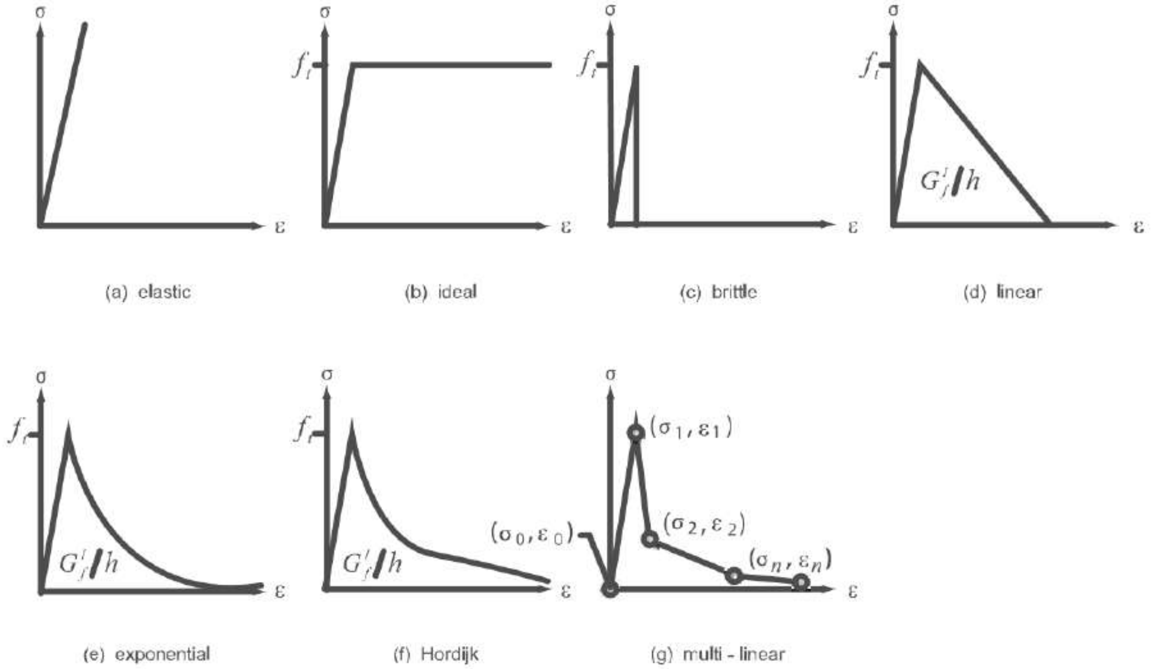

(a) elastic (b) ideal (c) brittle (d) linear

(e) exponential (f) Hordijk (g) multi - linear

Fig. A.2: Tension models [Midas IT, 2020]

- elastic behaviour,
- ideal plastic behaviour,
- brittle behaviour,
- linear softening,
- exponential softening,
- Hordijk softening,
- multi-linear behaviour,
- user defined behaviour.

The models of linear, exponential and non-linear softening are based on the fracture energy considerations. In the smeared crack models the so-called crack bandwidth must be assumed. The ideal-plastic, multi-linear and brittle behaviours are not directly related to the fracture energy. The MIDAS programs also allow the user to provide a user-defined subroutine for the tensile behaviour.

A.7 Compression models

A pressure-dependent behaviour is characteristic for concrete which is exposed to compressive stresses. The compressive stress-strain relationship can be modified in order to include the effects of the increased isotropic stress. The compressive behaviour is assumed to be influenced by lateral cracking.

The base function in compression can be modelled with one of many different curves, selected by user. Fig. A.3 shows the available hardening-softening curves in compression.

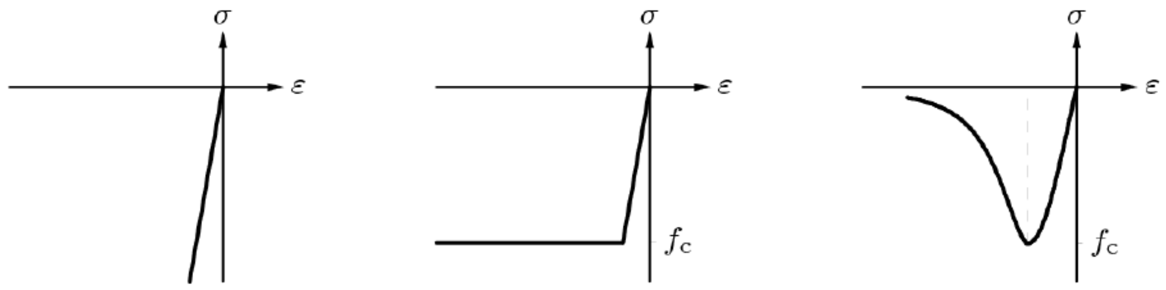

(a) elastic (b) ideal (c) Thorenfeldt

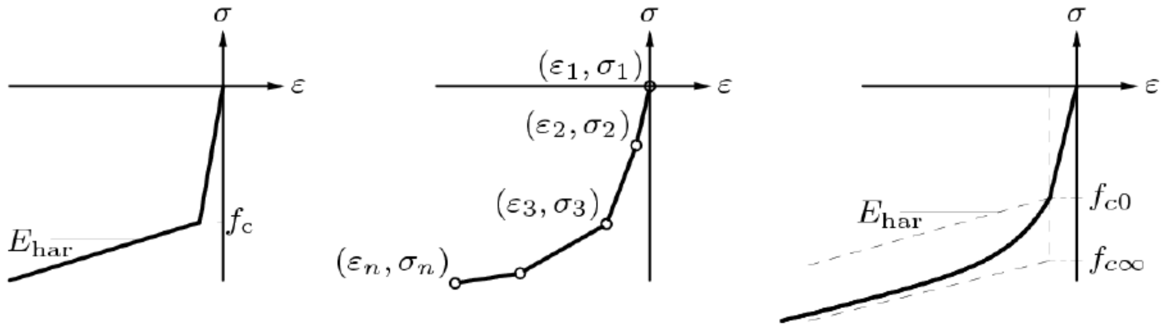

(d) linear (e) multi-linear (f) saturation type

Fig. A.3: Compression models [Midas IT, 2020]

A.8 Shear models

In the fixed crack concept where the shear stiffness is usually reduced after cracking it is necessary to model the shear behaviour. In MIDAS, only a constant shear stiffness reduction is modelled, i.e.

$$G^{cr} = \beta G \tag{A.14}$$

where $0 \leqslant \beta \leqslant 1$. For the rotating crack concept, β can be assumed equal to one.

Appendix B

B.1 Isoparametric shape functions for surface interface element

Shape functions of 8-node interface element:

$$\begin{aligned}
N_1^b(\xi,\eta) &= N_5^t(\xi,\eta) = \tfrac{1}{4}(1-\xi)(1-\eta) \\
N_2^b(\xi,\eta) &= N_6^t(\xi,\eta) = \tfrac{1}{4}(1+\xi)(1-\eta) \\
N_3^b(\xi,\eta) &= N_7^t(\xi,\eta) = \tfrac{1}{4}(1+\xi)(1+\eta) \\
N_4^b(\xi,\eta) &= N_8^t(\xi,\eta) = \tfrac{1}{4}(1-\xi)(1+\eta)
\end{aligned} \tag{B.15}$$

Shape functions of 16-node interface element:

$$\begin{aligned}
N_1^b(\xi,\eta) &= N_5^t(\xi,\eta) = \tfrac{1}{4}(1-\xi)(1-\eta)(-\xi-\eta-1) \\
N_2^b(\xi,\eta) &= N_6^t(\xi,\eta) = \tfrac{1}{4}(1+\xi)(1-\eta)(\xi-\eta-1) \\
N_3^b(\xi,\eta) &= N_7^t(\xi,\eta) = \tfrac{1}{4}(1+\xi)(1+\eta)(\xi+\eta-1) \\
N_4^b(\xi,\eta) &= N_8^t(\xi,\eta) = \tfrac{1}{4}(1-\xi)(1+\eta)(-\xi+\eta-1) \\
N_9^b(\xi,\eta) &= N_{13}^t(\xi,\eta) = \tfrac{1}{2}(1-\xi^2)(1-\eta) \\
N_{10}^b(\xi,\eta) &= N_{14}^t(\xi,\eta) = \tfrac{1}{2}(1+\xi)(1-\eta^2) \\
N_{11}^b(\xi,\eta) &= N_{15}^t(\xi,\eta) = \tfrac{1}{2}(1-\xi^2)(1+\eta) \\
N_{12}^b(\xi,\eta) &= N_{16}^t(\xi,\eta) = \tfrac{1}{2}(1-\xi)(1-\eta^2)
\end{aligned} \tag{B.16}$$

Shape function of 6-node triangular element:

$$\begin{aligned}
N_1^b(\xi,\eta) &= N_4^t(\xi,\eta) = 1-\xi-\eta \\
N_2^b(\xi,\eta) &= N_5^t(\xi,\eta) = \xi \\
N_3^b(\xi,\eta) &= N_6^t(\xi,\eta) = \eta
\end{aligned} \tag{B.17}$$

Shape functions of 12-node triangular interface element:

$$
\begin{aligned}
N_1^b(\xi,\eta) = N_4^t(\xi,\eta) &= (1-2\xi-2\eta)(1-\xi-\eta) \\
N_2^b(\xi,\eta) = N_5^t(\xi,\eta) &= (2\xi-1)\xi \\
N_3^b(\xi,\eta) = N_6^t(\xi,\eta) &= (2\eta-1)\eta \\
N_7^b(\xi,\eta) = N_{10}^t(\xi,\eta) &= 4(1-\xi-\eta)\xi \\
N_8^b(\xi,\eta) = N_{11}^t(\xi,\eta) &= 4\xi\eta \\
N_9^b(\xi,\eta) = N_{12}^t(\xi,\eta) &= 4\eta(1-\xi-\eta)
\end{aligned}
\tag{B.18}
$$

Appendix C

C.1 Source code of subroutine for Generalized Maxwell model in Midas FEA

```
program extra
!----------------------------------------------------------------------
!
!  Testing procedure for Midas USS
!
!----------------------------------------------------------------------
IMPLICIT NONE
INTEGER :: NS ! NUMBER OF STRESS COMPONENT
INTEGER :: INFM_STEP(5) ! STEP INFORMATION
INTEGER :: ID ! MATERIAL ID OF CURRENT ELEMENT
INTEGER :: NUV ! NUMBER OF PARAMETERS
INTEGER :: NUS ! NUMBER OF INTERNAL STATE VARIABLES
INTEGER :: NUI ! NUMBER OF INTEGER INDICATOR VARIABLES
REAL*8 :: DETJ ! DETERMINENT VALUE AT CURRENT INTEGRATION POINT
REAL*8 :: EPS0(6) ! TOTAL STRAIN AT PREVIOUS STEP
REAL*8 :: DEPS(6) ! INCREMENTAL STRAIN
REAL*8 :: COORD(3) ! COORDINATE OF INTEGRATION POINT
REAL*8 :: SE(6,6) ! ELASTIC CONSTITUTIVE MATRIX
REAL*8 :: SIG(6) ! TOTAL STRESS AT PREVIOUS \& CURRENT STEP
REAL*8 :: STIFF(6,6) ! TANGENT STIFFNESS AT CURRENT STEP (OUT)
REAL*8 :: EPSP(6) ! TOTAL PLASTIC STRAIN AT PREVIOUS STEP
REAL*8 :: USRSTA(26) ! INTERNAL STATE VARIABLES
REAL*8 :: USRVAL(11) ! PARAMETERS
INTEGER:: IUSRIND(1) ! INTEGER INDICATOR VARIABLES
REAL*8 :: DTIME ! TIME INCREMENT
integer:: I,J,IT,NSTEP
real*8 :: youn,pois,STAGE
!
```

```
   open(unit=1,file='inp')
   open(unit=2,file='out')
   open(unit=3,file='diag')
   open(unit=4,file='diage')
   open(unit=5,file='diagE')
!   write(unit=*,fmt=*) 'Input n,a,b.'
!   read(unit=*,fmt=*) n,a,b
   NS=6
   ID=1
   NUV=9
   NUS=2
   NUI=1
   read(unit=1,fmt=*) INFM_STEP(1:5)
   read(unit=1,fmt=*) youn, pois
   read(unit=1,fmt=*) EPS0(1:6)
   read(unit=1,fmt=*) DEPS(1:6)
   read(unit=1,fmt=*) EPSP(1:6)
   read(unit=1,fmt=*) SIG(1:6)
   read(unit=1,fmt=*) COORD(1:3)
   read(unit=1,fmt=*) DETJ
   read(unit=1,fmt=*) USRVAL(1:11)
   read(unit=1,fmt=*) USRSTA(1),IUSRIND(1)
   read(unit=1,fmt=*) DTIME,NSTEP

  write(unit=5,fmt='(1p2e13.4)') 0.0,youn
  write(unit=3,fmt='(1p2e13.4)') 0.0,youn*EPS0(1)
  write(unit=4,fmt='(1p2e13.4)') 0.0,EPS0(1)

call stiffi (youn, pois, SE)
   write(unit=2,fmt='("EPS0",1p6e13.4)')  EPS0(1:6)
STAGE=USRVAL(11)-USRVAL(10)
DO I = 1, NS
   SIG(I) = 0.d0
```

```
DO J = 1, NS
   SIG(I) = SIG(I) + SE(I,J)*EPS0(J)
ENDDO
ENDDO

do IT=1,NSTEP

!if (IT.gt.1) then
!DO I = 1, NS
!   DEPS(I) = 0.d0
!ENDDO
!endif

call USRMAT( EPS0, DEPS, EPSP, NS, INFM_STEP, COORD, SE, USRVAL, NUV, \&
USRSTA, NUS, IUSRIND, NUI, SIG, STIFF, ID, DETJ, DTIME)

DO I = 1, NS
EPS0(I) = EPS0(I) + DEPS(I)
ENDDO
   write(unit=2,fmt=’("SIG",1p6e13.4)’)  SIG(1:6)
!   do i=1,6
!   write(unit=2,fmt=’("STIFF",1p6e13.4)’)  STIFF(i,1:6)
!   enddo
  write(unit=3,fmt=’(1p2e13.4)’) USRSTA(1),SIG(1)
  write(unit=4,fmt=’(1p2e13.4)’) USRSTA(1),EPS0(1)
  write(unit=5,fmt=’(1p2e13.4)’) USRSTA(1),USRSTA(2)
enddo
!  write(unit=2,fmt=’(i4,2f16.5)’) j,x,y
!   write(unit=2,fmt=’(2e16.5)’) x,y
!   write(unit=2,fmt=’(’’#Area =’’,1pe16.5)’) area
stop ’Good bye.’
end
```

```
SUBROUTINE USRMAT( EPS0, DEPS, EPSP, NS, INFM_STEP, COORD, SE, USRVAL, NUV, &
USRSTA, NUS, IUSRIND, NUI, SIG, STIFF,ID, DETJ, DTIME)
IMPLICIT NONE
!DEC\$ ATTRIBUTES DLLEXPORT::USRMAT
INTEGER, INTENT(IN) :: NS ! NUMBER OF STRESS COMPONENT
INTEGER, INTENT(IN) :: INFM_STEP(5) ! STEP INFORMATION FOR STAGE, INCREMENT, ITERAT
! ELEMENT, INTEGRATION POINT
! INFM_STEP(1) : STAGE ID
! INFM_STEP(2) : LOAD INCREMENTAL STEP ID
! INFM_STEP(3) : ITERATION STEP ID
! INFM_STEP(4) : ELEMENT ID
! INFM_STEP(5) : INTEGRATION POINT ID
INTEGER, INTENT(IN) :: ID ! MATERIAL ID OF CURRENT ELEMENT
INTEGER, INTENT(IN) :: NUV ! NUMBER OF PARAMETERS
INTEGER, INTENT(IN) :: NUS ! NUMBER OF INTERNAL STATE VARIABLES
INTEGER, INTENT(IN) :: NUI ! NUMBER OF INTEGER INDICATOR VARIABLES
REAL*8, INTENT(IN) :: DETJ ! DETERMINENT VALUE AT CURRENT INTEGRATION POINT
REAL*8, INTENT(IN) :: EPS0(NS) ! TOTAL STRAIN AT PREVIOUS STEP
REAL*8, INTENT(IN) :: DEPS(NS) ! INCREMENTAL STRAIN
REAL*8, INTENT(IN) :: COORD(3) ! COORDINATE OF INTEGRATION POINT
REAL*8, INTENT(IN) :: SE(NS, NS) ! ELASTIC CONSTITUTIVE MATRIX
REAL*8, INTENT(INOUT) :: SIG(NS) ! TOTAL STRESS AT PREVIOUS(IN) CURRENT(OUT) STEP
REAL*8, INTENT(INOUT) :: STIFF(NS, NS) ! TANGENT STIFFNESS AT CURRENT STEP (OUT)
REAL*8, INTENT(INOUT) :: EPSP(NS) ! TOTAL PLASTIC STRAIN AT PREVIOUS STEP
REAL*8, INTENT(INOUT) :: USRSTA(NUS) ! INTERNAL STATE VARIABLES
REAL*8, INTENT(IN) :: USRVAL(NUV) ! PARAMETERS
INTEGER, INTENT(INOUT) :: IUSRIND(NUI) ! INTEGER INDICATOR VARIABLES
REAL*8, INTENT(IN) :: DTIME ! TIME INCREMENT
!REAL*8, ALLOCATABLE :: SEBAR(:,:), DSIG(:), EPS(:), SIGH(:), SIGMI(:,:), DSIGMI(:)
REAL*8 :: SEBAR(6,6), DSIG(6), EPS(6), SIGH(6)
REAL*8 :: SIG_MI(6,5), DSIG_MI(6,5), SIGH_MI(6,5)
INTEGER :: NC, I, J, K
REAL*8 :: E0,E1,ETA1,E2,ETA2,E3,ETA3,E4,ETA4,T0,T1,T,DELTA_T
```

```
REAL*8 :: LAM1,LAM2,LAM3,LAM4,E_MI(5),E_MIH(5),E,LAM_MI(5),E_FIC,E_DMI(5)

E0   = USRVAL(1)
E1   = USRVAL(2)
ETA1 = USRVAL(3)
E2   = USRVAL(4)
ETA2 = USRVAL(5)
E3   = USRVAL(6)
ETA3 = USRVAL(7)
E4   = USRVAL(8)
ETA4 = USRVAL(9)
T0   = USRVAL(10)
T1   = USRVAL(11)
T    = USRSTA(1) + DTIME
USRSTA(1) = T

!-----------------------------------------------------------
! Concrete properties
!-----------------------------------------------------------
! Maxwell model
LAM1 = E1/ETA1
LAM2 = E2/ETA2
LAM3 = E3/ETA3
LAM4 = E4/ETA4
E_MI = [E0,E1,E2,E3,E4]
E    = E0+E1+E2+E3+E4
write(unit=2,fmt=’("E,E_mi_EL",1p6e13.4)’)  E, E_MI(1:5)
LAM_MI = [0.d0,LAM1,LAM2,LAM3,LAM4]
write(unit=2,fmt=’("LAM_mi",1p4e13.4)’)  LAM_MI(2:5)
DELTA_T   = T - T0
write(unit=2,fmt=’("T,DELTA_T",1p2e13.4)’)  T,DELTA_T
!-----------------------------------------------------------
! Elastic part
```

```
!------------------------------------------------------------
! NC - number of Maxwell chains (default 4)
NC = 5

DO I = 1, NS
DO J = 1, NS
SEBAR(I,J) = SE(I,J) / E
STIFF(I,J) = SE(I,J)
ENDDO
ENDDO
!do I=1,6
!write(unit=2,fmt='("SEBAR",1p6e13.4)')  SEBAR(I,1:6)
!enddo
!write(unit=2,fmt='("DEPS",1p6e13.4)')  DEPS(1:6)

DO K = 1, NC
! For each Maxwell chain do

DO I = 1, NS
   SIG_MI(I,K) = 0.d0
DO J = 1, NS
   SIG_MI(I,K) = SIG_MI(I,K) + SEBAR(I,J)*EPS0(J)*E_MI(K)
ENDDO
ENDDO
write(unit=2,fmt='("SIG_MI_EL",1p6e13.4)')  SIG_MI(1:6,K)
ENDDO

!-----------------------------------------
! Visco-elastic part
!-----------------------------------------
E_FIC=E0
DO K = 2, NC
   E_MIH(K) = E_MI(K)*dexp(-LAM_MI(K)*DELTA_T)
```

```
   E_FIC = E_FIC + E_MI(K)*dexp(-LAM_MI(K)*DELTA_T)
   E_MI(K) = (1/DTIME)*(E_MIH(K)*(1-dexp(-LAM_MI(K)*DTIME)))/LAM_MI(K)
ENDDO
USRSTA(2)=E_FIC
write(unit=2,fmt='("E_mi",1p5e13.4)')  E_MI(1:5)
write(unit=2,fmt='("E_fic",1pe13.4)')  E_FIC
!write(unit=2,fmt='("exp",1p5e13.4)')  dexp(-LAM_MI(1:5)*DELTA_T)

DO I = 1, NS
   SIGH_MI(I,1) = SIG_MI(I,1)
   SIGH(I) = SIG_MI(I,1)
DO K = 2, NC
   SIGH_MI(I,K) = SIG_MI(I,K)*(dexp(-LAM_MI(K)*DTIME)-1)
   SIGH(I) = SIGH(I) + SIGH_MI(I,K)
ENDDO
write(unit=2,fmt='("SIGH_MI(I)",1p4e13.4)')  SIGH_MI(I,2:5)
ENDDO
write(unit=2,fmt='("SIGH",1p6e13.4)')  SIGH(1:6)

!DO I = 1, NS
!   DSIG(I) = 0.d0
!DO J = 1, NS
!   DSIG(I) = DSIG(I) + E_FIC*SEBAR(I,J)*DEPS(J)
!ENDDO
!   SIG(I) = SIG(I) + DSIG(I) + SIGH(I)
!ENDDO

DO I = 1, NS
   DSIG(I) = 0.d0
DO K = 1, NC
   DSIG_MI(I,K) = 0.d0
DO J = 1, NS
   DSIG_MI(I,K) = DSIG_MI(I,K) + E_MI(K)*SEBAR(I,J)*DEPS(J)
```

```
ENDDO
   DSIG(I) = DSIG(I) + DSIG_MI(I,K) + SIGH_MI(I,K)
ENDDO
   SIG(I) = SIG(I) + DSIG(I)

write(unit=2,fmt='("DSIG_MI",1p5e13.4)')  DSIG_MI(I,1:5)
ENDDO
write(unit=2,fmt='("DSIG",1p6e13.4)') DSIG(1:6)
write(unit=2,fmt='("SIG",1p6e13.4)')  SIG(1:6)

END

subroutine stiffi ( youn, pois, d)
!**********************************************************************
!     Elastic stiffness operator for
!     3D D(6,6) with strains Exx,Eyy,Ezz,Gxy,Gxz,Gyz
!**********************************************************************
implicit none
integer :: i
double precision :: youn,pois,d(6,6)
double precision :: c2,c,cm,cp
!
call rset (0.0d0, d, 36)
c2 = youn/(1.0d0+pois)
c  = c2/(1.0d0-2.0d0*pois)
cm = c*(1.0d0-pois)
cp = c*pois
d(1,1) = cm
d(2,1) = cp
d(3,1) = cp
d(1,2) = cp
d(2,2) = cm
d(3,2) = cp
```

```
d(1,3) = cp
d(2,3) = cp
d(3,3) = cm
do i = 4,6
d(i,i) = 0.5d0*youn/(1.0d0+pois)
enddo
end

subroutine rset( rval, rar, n )
!
implicit double precision (a-h,o-z)
dimension  rar(n)
!
rv = rval
do i = 1,n
rar(i) = rv
enddo
return
end
```

Appendix D

D.1 Algorithm of stress update in CS analysis

The formulas for a mechanical analysis are presented below, where stages of structure erection are taken into account with changing geometry of the FE model, its topology and boundary conditions. Although in the MIDAS package (and also in DIANA) algorithms formulated for any non-linearity are available, attention is focused on linear materials, for which

$$\boldsymbol{\sigma} = \boldsymbol{D}^e(\boldsymbol{\epsilon} - \boldsymbol{\epsilon}_0) + \boldsymbol{\sigma}_0 \tag{D.19}$$

where $\boldsymbol{\sigma}$ is stress tensor, $\boldsymbol{D}^e$ is Hooke's operator, $\boldsymbol{\epsilon}$ is strain tensor, $\boldsymbol{\epsilon}_0$ and $\boldsymbol{\sigma}_0$ are initial strain and initial stress tensors, respectively. In a considered stage of analysis the two last tensors are used to include the material condition at the end of the previous stage. Since the analysis is performed for a process changing in time, and potentially nonlinear, it has an incremental character. For each stage of the analysis the process time is assumed and divided into a required number of increments. This derivation is limited to static conditions and increasing effective loading results in increasing deformation and stresses (cross-sectional forces).

In every time increment the Newton-Raphson method is used [DIANA FEA, 2020]

$$\boldsymbol{K}\Delta\boldsymbol{a} = \boldsymbol{f}_{ext} - \boldsymbol{f}_{int} \tag{D.20}$$

where

$\boldsymbol{K}$ – global stiffness matrix,

$\boldsymbol{a}$ – vector of nodal displacement increments (from which strain increments are derived via interpolation),

$\boldsymbol{f}_{ext}$ – current external forces,

$\boldsymbol{f}_{int}$ – current internal forces.

Assuming that increments $\Delta\boldsymbol{u}$ are small enough, we can calculate strain increments $\Delta\boldsymbol{\epsilon}$ from the linear elasticity equation and write down equation (D.19) for increments

$$\Delta\boldsymbol{\sigma} = \boldsymbol{D}(\Delta\boldsymbol{\epsilon} - \Delta\boldsymbol{\epsilon}_0) + \Delta\boldsymbol{\sigma}_0 \tag{D.21}$$

with $\boldsymbol{D} = \boldsymbol{D}^e$. However, equation (D.21) can also represent the tangent relationship for nonlinear material and $\Delta\boldsymbol{\epsilon}_0$ and $\Delta\boldsymbol{\sigma}_0$ are initial strain and initial stress increments, respectively (for example $\Delta\boldsymbol{\epsilon}_0$ can be the strain increment resulting from shrinkage or thermal expansion).

The total values of displacement, strain and stress at the current moment of time $t + \Delta t$ are calculated respectively by summation of the values at the previous instant t and proper increments:

$$\boldsymbol{u}^{t+\Delta t} = \boldsymbol{u}^t + \Delta\boldsymbol{u}, \quad \boldsymbol{\epsilon}^{t+\Delta t} = \boldsymbol{\epsilon}^t + \Delta\boldsymbol{\epsilon}, \quad \boldsymbol{\sigma}^{t+\Delta t} = \boldsymbol{\sigma}^t + \Delta\boldsymbol{\sigma} \tag{D.22}$$

The current external forces are as follows:

$$\boldsymbol{f}_{ext} = \boldsymbol{f}_g + \boldsymbol{f}_t + \boldsymbol{f}_u \tag{D.23}$$

where

$\boldsymbol{f}_g$ – equivalent mass forces (forces representing self-weight)

$\boldsymbol{f}_t$ – equivalent surface forces (nodal forces computed by integration of the load distributed on the model surface)

$\boldsymbol{f}_u$ – force vector resulting from kinematic loads, for example support settlements, computed as

$$\boldsymbol{f}_u = \boldsymbol{K}\boldsymbol{a}_d \tag{D.24}$$

where $\boldsymbol{a}_d$ – vector of imposed nodal displacements.

The respective internal force components are computed as:

$$\boldsymbol{f}_{int} = \boldsymbol{f}_\sigma + \Delta\boldsymbol{f}_\sigma - \Delta\boldsymbol{f}_\epsilon \tag{D.25}$$

where

$\boldsymbol{f}_\sigma$ – internal forces caused by total strain reached in previous stages,

$\Delta\boldsymbol{f}_\sigma$ – effect of incremental stresses,

$\Delta\boldsymbol{f}_\epsilon$ – effect of incremental strains.

They are computed from the following equations:

$$\boldsymbol{f}_\sigma = \sum_e \boldsymbol{T}^T \int_{v^e} \boldsymbol{B}^T \boldsymbol{\sigma} \mathrm{d}V \tag{D.26}$$

$$\Delta\boldsymbol{f}_\sigma = \sum_e \boldsymbol{T}^T \int_{v^e} \boldsymbol{B}^T \Delta\boldsymbol{\sigma}_0 \mathrm{d}V \tag{D.27}$$

$$\Delta\boldsymbol{f}_\epsilon = \sum_e \boldsymbol{T}^T \int_{v^e} \boldsymbol{B}^T \boldsymbol{D} \Delta\boldsymbol{\epsilon}_0 \mathrm{d}V \tag{D.28}$$

in which summation is performed over elements active in a current stage of analysis, $\boldsymbol{T}$ is topology and transformation matrix, $\boldsymbol{B}$ is the matrix of discrete kinematic relations.

If the problem is nonlinear then $\boldsymbol{f}_{\sigma}$ is a nonlinear function of $\Delta\boldsymbol{u}$ and in the Newton-Raphson algorithm iterations are necessary to obtain balance, in which the condition $\boldsymbol{f}_{ext} - \boldsymbol{f}_{int} \cong 0$ is met with sufficient accuracy.

Interface model influence on simulated behaviour of concrete-concrete composite pre-stressed girder with insight into time effects and cracking

by Łukasz Jarno

Summary

The thesis presents the influence of the interface numerical model on the flexural and shear behaviour and on the load-bearing capacity of a composite pre-stressed girder made of high-strength concrete connected with normal-strength concrete. The Finite Element Method is used for numerical simulations.

The pre-stressed composite bridge girder made of HSC with bridge deck made of NSC was selected in order to examine its transient and long-term behaviour. The experimental research performed by W. Choi at State University of North Carolina, Raleigh was a motivation and provided the research object for the assessment of such composite girder. The considered structural element is the composite girder with the geometry based on Choi's experiments and a wider deck. The research takes into account construction stages and two nonlinear effects: creep or inelastic interface between the girder and the deck. Moreover, the experimental cracking response is simulated.

The key factor of load-bearing capacity of such composite girders is the contact zone between the two connected concretes. In order to select an appropriate method of modelling the contact, a simple calculation model is first generated, consisting of two solid cubes with plane interface elements between them. Different types of interface constitutive relations are applied in the interface elements to simulate sliding and opening.

To properly characterize creep the following material models have been adopted: the analytical model from code guidelines and the Generalized Maxwell model based on visco-elasticity. Using Midas FEA software, the main analysis is performed for the composite beam model with the 1.5 meter broad deck and the span of 12.5 m between the supports. Four types of analysis are carried out: first a cracking simulation using the Total Strain Crack model, then a construction stage analysis representing the construction sequence, then a similar analysis with time-dependent effects, in particular creep, and finally an analysis neglecting the creep, but taking into account the nonlinear interface response of the girder-slab connection.

The results of the calculations of the composite beam led to the following conclu-

sions:

1. The results of one-step static computations of the girder under consideration differ strongly from the results of the construction stage analysis. The simulations of such girders using standard FEM algorithms can lead to unrealistic results.

2. There is a significant difference between the load bearing capacity of two different types of the connection zone, i.e. the standard adhesion-friction interface and the use of additional stitching reinforcement in the connection zone. The stitching reinforcement strongly influences the behaviour of the composite girder.

3. The application of more complex (multi parameter) rheological models of concrete allows for a better use of load-carrying capacity of the considered structural element. The standards and creep models they contain lead to more conservative design which results in a higher level of safety, but reduced economic efficiency. When advanced rheological models are employed, the designer can exploit the material strength in a better way. Such creep models also allow one to reproduce the whole history of variable loading acting on the element and this is not possible when simple code models based on the creep coefficient are used.

Wpływ modelu interfejsu na symulowane zachowanie się zespolonych dźwigarów sprężonych typu beton-beton z uwzględnieniem efektów reologicznych i zarysowania

Łukasz Jarno

Streszczenie

Głównym celem niniejszej pracy doktorskiej jest ocena wpływu modelu numerycznego interfejsu na zachowanie przy zginaniu i ścinaniu oraz na nośność zespolonego dźwigara sprężonego wykonanego z betonu o wysokiej wytrzymałości (HSC) połączonego z betonem o normalnej wytrzymałości (NSC). W symulacjach prowadzonych metodą elementów skończonych (MES) z uwzględnieniem etapów konstruowania dźwigara badane są także aspekty reologiczne, w szczególności pełzanie betonu. W ananlizie założono liniowe zależności kinematyczne, sprężyste zbrojenie i cięgna sprężające.

We współczesnym świecie inżynierii lądowej często wymagane jest łączenie zaawansowanych koncepcji, takich jak konstrukcje zespolone, naprężenie wstępne, materiały o wysokiej wytrzymałości itp., aby spełnić wysokie wymagania dotyczące konstrukcji. Jednym z takich kompleksowych rozwiązań inżynierskich jest prefabrykowany sprężony dźwigar mostowy wykonany z betonu o wysokiej wytrzymałości w połączeniu z płytą pomostową z betonu o normalnej wytrzymałości, wykonywaną na budowie. Ten rodzaj dźwigara łączy najlepsze cechy konstrukcji zespolonych, sprężonych i zaawansowanych materiałów. Zespolony element betonowy jest budowany przez połączenie dwóch różnych elementów betonowych, zintegrowanych ze sobą różnymi rodzajami połączeń. Celem projektowania i budowy takich elementów jest zapewnienie jak najlepszej współpracy dwóch betonów ze względu na jej znaczenie dla nośności dźwigara.

Badania eksperymentalne przeprowadzone przez W. Choi na Uniwersytecie Stanowym Karoliny Północnej w Raleigh były motywacją i dostarczyły obiektu badawczego do oceny dźwigara kompozytowego. Badania eksperymentalne miały na celu ocenę zachowania takich zginananych sprężonych zespolonych dźwigarów betonowych. W badaniu przetestowano trzy typy dźwigarów z wylewaną na mokro płyta o szerokości 1.5 m lub 0.3 m lub bez płyty. W niniejszej pracy doktorskiej wykonano badanie symulacyjne belki z szerszą płytą z uwzględnieniem etapów budowy i dwóch nieliniowych efektów: pełzania lub oddziaływania dźwigara z płytą. Ponadto odtwarzany jest eksperymentalny proces zarysowania.

Obecnie metoda elementów skończonych jest uznawana za ugruntowaną i wygodną technikę komputerowej symulacji złożonych problemów z różnych dziedzin: inżynierii lądowej (w tym geomechaniki), inżynierii mechanicznej, inżynierii nuklearnej, inżynierii biomedycznej, hydrodynamiki, ciepłownictwa, itp. Dzieje się tak, ponieważ MES jest potężnym narzędziem do przybliżonego rozwiązywania równań różniczkowych opisujących różne zjawiska fizyczne i procesy. Główna część rozprawy poświęcona jest zatem analizie modeli MES sprężonego dźwigara mostowego, w tym etapów budowy, specyficznego zachowania konstrukcji kompozytowej i efektów reologicznych. W kontekście niniejszych badań dokładność modelu wyjściowego jest weryfikowana na podstawie wyników eksperymentalnych (stosowana jest zatem idealizacja pękania), a następnie przeprowadzane są bardziej zaawansowane symulacje obliczeniowe w celu zbadania złożonych zjawisk, w szczególności wpływu modelu strefy kontaktu belki sprężonej z płytą na zachowanie dźwigara pod obciążeniem.

Istotnym aspektem analizy jest zatem strefa kontaktu w konstrukcji zespolonej beton-beton. Jest to kluczowa kwestia, jeśli chodzi o nośność dźwigara zespolonego. Dlatego dużą część pracy poświęcono temu zagadnieniu. Analizę połączeń rozpoczęto od omówienia głównych właściwości przekroju zespolonego oraz zjawisk zachodzących w strefie kontaktu. Najpierw opisano najważniejsze zjawiska adhezji i tarcia. Następnie przeanalizowano zachowanie się prętów zbrojeniowych uczestniczących w przenoszeniu wzdłużnego ścinania w strefie zespolenia (tzw. zbrojenie zszywające). Następnie przedstawiono elementy skończone typu interfejsowego wykorzystywane w modelowaniu konstrukcji kompozytowych oraz omówiono opcje ich właściwości. Elementy reprezentujące styk betonów HSC i NSC zostały wprowadzone do metody elementów skończonych, aby uwzględnić zależność między wektorem przemieszczenia względnego dwóch stron interfejsu, a wektorem oddziaływań normalnych i stycznych. Wybór odpowiedniego typu zachowania interfejsu jest ważny dla prawidłowej symulacji kontaktu beton-beton.

W celu określenia odpowiedniej reprezentacji styku stworzony został prosty model obliczeniowy składający się z dwóch elementów sześciennych, pomiędzy którymi znajdują się płaskie elementy interfejsu. Różne modele konstytutywne interfejsu zostały zastosowane w tych elementach, aby sprawdzić ich zachowanie. Przeprowadzana została nieliniowa analiza statyczna. W pierwszej kolejności wykorzystano model tarcia, który wywodzi się z plastyczności Mohra-Coulomba dla elementów ośrodka ciągłego. Następnym analizowanym modelem styku był model "zazębiania" się kruszywa. Koncepcja tego modelu polega na tym, że siłę przyczepności zwiększa kruszywo użyte w mieszance betonowej. Aby opisać to numerycznie zastosowano dwufazowy model Walravena. Następnie poddano analizie model połączenia wciętego, które w analizie belki nie zostało zastosowane ze względu na stopień skomplikowania geometrii. Ostatni sprawdzany model polega na zastosowaniu zbrojenia zszywającego. Stalowy pręt umieszcza się w środku kostek połączonych interfejsem i odpowiednio łączy z nimi.

W celu uwzględnienia efektów reologicznych (które są bardzo ważne ze względu na różny wiek łączonych betonów) wprowadzany został model lepkosprężysty betonu. Przy użyciu uogólnionego modelu Maxwella, zasady superpozycji dla zachowania lepkosprężystego betonu pod ciągłym obciążeniem i postaci spektralnej funkcji charakterystycznej reprezentującej właściwości materiału, zostało wyprowadzane i zaprogramowane w zastosowanym pakiecie oprogramowania 3D Midas FEA przyrostowe sformułowanie liniowej lepkosprężystości dla niestarzejącego się materiału. Model został przetestowany w 1D oraz 3D.

Badany dźwigar zawiera strzemiona i jest wstępnie sprężony. Został zamodelowany jako swobodnie podparta belka, obciążona aż do zerwania splotów sprężających czyli do zniszczenia. Główna analiza została wykonana dla modelu belki o rozpiętości 12,5 m między podporami, z płytą o szerokości 1.5 m. Dla modelu dźwigara przeprowadzono szereg obliczeń.

Do oceny zarysowania modelu belki wykorzystuje się model zwany Total Strain Crack, dostępny w pakiecie Midas FEA i opisany krótko w załączniku do pracy. Aby zobaczyć możliwości predykcyjne aproksymacji problemu metodą elementów skończonych, model zarysowania został zastosowany do modelu początkowego w celu sprawdzenia rodzajów uszkodzeń, wzorców pęknięć itp. Wyniki tej symulacji zostały porównane z wynikami eksperymentów przeprowadzonych przez Choi'a.

Wpływ procesu budowlanego jest oceniany na podstawie analizy etapowania konstrukcji. Wykonano symulację pełzania betonu podczas etapowania. Aby pokazać długoterminowe zachowanie modelu, wprowadzono również dodatkowy etap o czasie trwania 10000 dni. Następnie porównano wyniki symulacji dla analizowanego dźwigara zespolonego uzyskane z zastosowaniem uogólnionego modelu Maxwella z wynikami uzyskanymi przy użyciu funkcji pełzania zdefiniowanych w zaleceniach CEB-FIP.

Po wykonaniu analizy reologicznej dokonano oceny wyników w kolejnych etapach dla modelu ze strefą połączenia reprezentowaną przez interfejsy. Na podstawie analizy sprawdzane jest maksymalne ugięcie i maksymalne naprężenie rozciągające. Analizowane jest również zachowanie podczas wzdłużnego ścinania. Przedstawiono i omówiono analizę etapu budowy z elementami interfejsu w celu zbadania wpływu różnych typów modelowania strefy kontaktu na zachowanie i nośność konstrukcji zespolonej.

Niniejsza praca pozwoliła na wyciągnięcie następujących wniosków:

1. Wyniki jednoetapowych obliczeń statycznych rozpatrywanego dźwigara znacznie odbiegają od wyników analizy etapowania konstrukcji. W rzeczywistości dla wszystkich konstrukcji sprężonych konieczne jest zastosowanie analizy etapu budowy, a nie jednoetapowej analizy statycznej, ponieważ każda konstrukcja sprężona jest budowana w kilku fazach, a każdy etap należy traktować jako oddzielny krok analizy i historia poprzednich kroków ma znaczący wpływ na kolejne kroki.

2. Istnieje znacząca różnica pomiędzy nośnością dwóch różnych typów strefy połączenia. W szczególności zastosowanie dodatkowego zbrojenia zszywającego w interfejsie ciernym silnie wpływa na zachowanie dźwigara zespolonego. W tym kontekście oczekuje się, że wpływ połączenia wciętego (o wiele trudniejszego do wykonania w praktyce i nieuwzględnianego w obecnej analizie dźwigara zespolonego) byłby jeszcze silniejszy.

3. Zastosowanie bardziej złożonych (wieloparametrowych) modeli reologicznych betonu pozwala na lepsze wykorzystanie nośności rozważanego elementu konstrukcyjnego. Normy i modele pełzania, które zawierają, są bardziej konserwatywnej konstrukcji, co skutkuje wyższym poziomem bezpieczeństwa, ale zmniejszoną efektywnością ekonomiczną. Kiedy zastosowane są zaawansowane modele reologiczne, projektant może lepiej wykorzystać wytrzymałość materiału. Takie modele pełzania pozwalają również odtworzyć całą historię obciążeń zmiennych w czasie działających na element, co nie jest możliwe w przypadku stosowania prostych modeli normowych opartych na współczynniku pełzania.